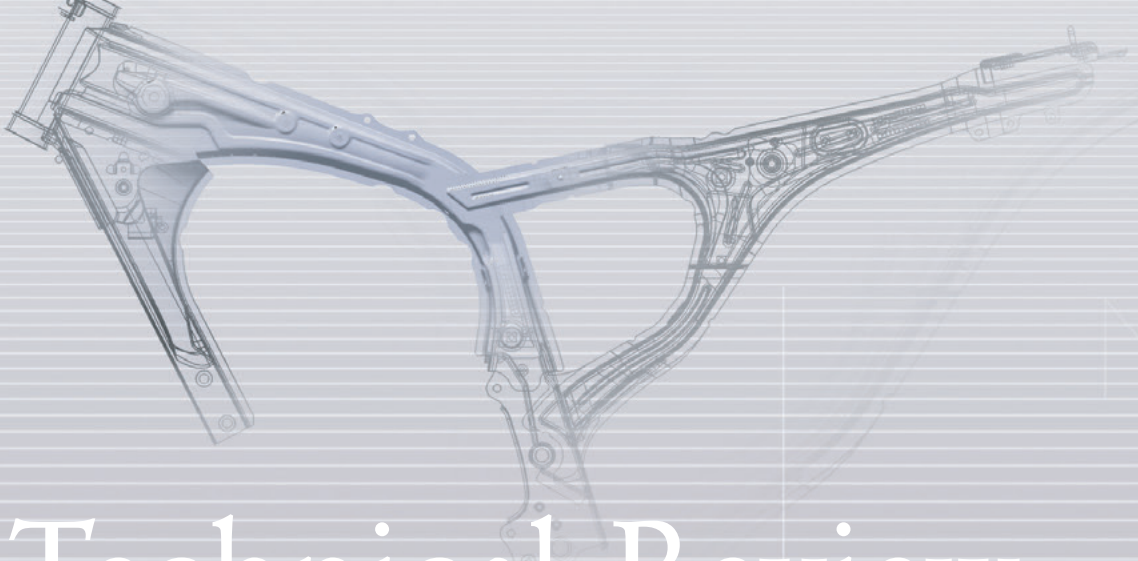
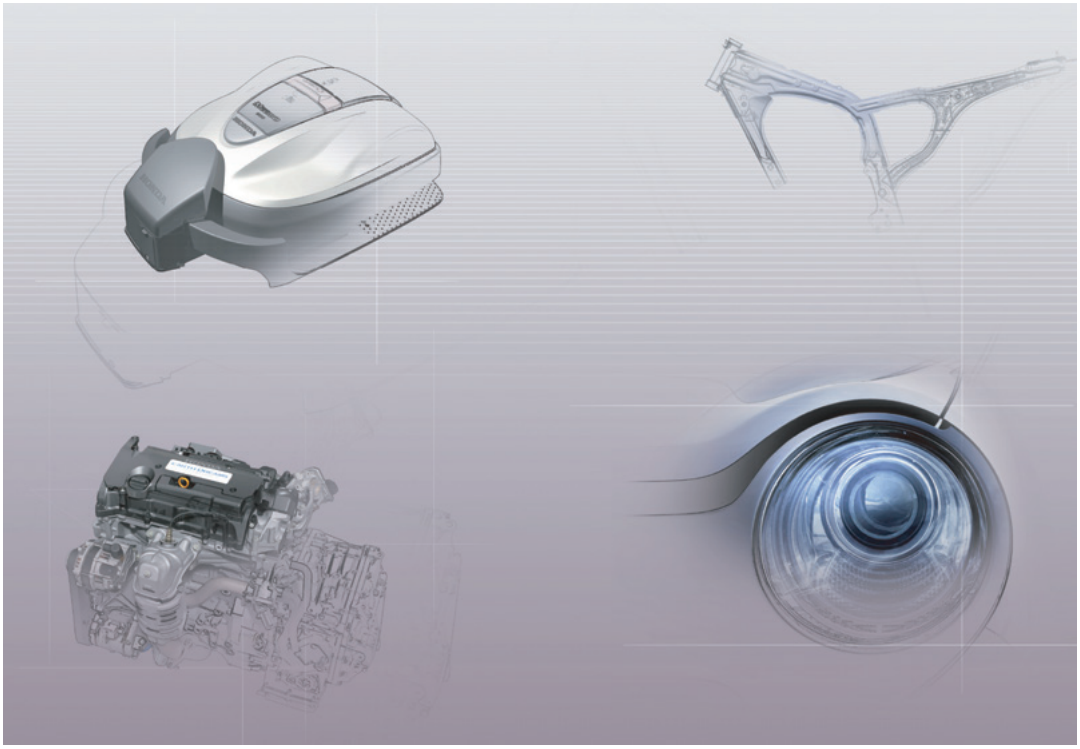


Honda R&D

Technical Review

October 2013
Vol.25 No.2



Comment on the Cover

Motorcycles and scooters, cars and trucks, general purpose products…Few companies can claim to be engaged in developing such a wide range of modes of mobility.

The fact that I could be involved in a lot of things and it sounded so interesting was the big push for me to join Honda.

We seek to go on creating fascinating products that will make people catch their breath.

Using our latest technologies as horizontal and vertical lines, the cover design of this edition provides an image of the technological details provided within its pages.

We hope that you will take this opportunity to learn about the many exciting new technologies born from Honda's commitment to excellence.



Automobile R&D Center
Masahiro Sagawa

Technical Review

October

2013

Honda R&D

CONTENTS

Introduction of new technologies

Styling Design of New N-ONE . . . . . Shinichiro KANAYAMA・Takao ISHIKAWA
. . . . . Masayuki TOGAWA・Yasuko SAITO 1

Development of New V6 3.5 L Gasoline Engine . . . . . Nobuo SUZUKI・Yasutaka HAYASHI・Kazuya ISHIKI
. . . . . Atsushi SATO・Tatsuhito ESAKI・Satoshi WATANABE 9

Development of New 2.4 L Direct-Injection Gasoline Engine
. . . . . Yasuhiro MOTOHASHI・Kenji KUBOTA・Nobuyuki AKAISHI
Kazuya ISHIKI・Takashi IWAMOTO・Masakazu KINOSHITA 17

Development of New 2.0 L Gasoline Engine for Accord Hybrid
. . . . . Akiyuki YONEKAWA・Osamu WATANABE
Noritaka SEKIYA・Naohiro ISHIKAWA 27

Development of SPORT HYBRID i-MMD Control System for 2014 Model Year Accord
. . . . . Hirohito IDE・Yoshihiro SUNAGA・Naritomo HIGUCHI 33

Development of Motor and PCU for a SPORT HYBRID i-MMD System . . . . . Jiro KUROKI・Hiroshi OTSUKA 42

Development of Li-ion Battery for SPORT HYBRID
. . . . . Yoshikazu OHNUMA・Koichi TAKAHASHI・Tsuyoshi MATSUDA 49

Development of Robotic Lawnmower Miimo . . . . . Toshiaki KAWAKAMI・Hiroshi KOBAYASHI
. . . . . Makoto YAMAMURA・Shuhei MARUYAMA 54

Development of ECOWILL PLUS Micro-cogeneration Unit with Autonomous Operation Function
for Generating Electricity during Power Outages
. . . . . Masanori TAKEISHI・Yoshinori NAKAGAWA
Atsumu NAOI・Nobuyuki SASAKI 60

Flat Belt Test System for Suspension and Tire Measurement
. . . . . Tomonori SAKAI・Kaoru KUSAKA・Yuji SATO 66

Development of Stamped Frames Made of High-tensile Steel Plates with Light Weight
and High Production Efficiency for Small Motorcycles
. . . . . Hideaki NAKAGAWA・Masahiko TAKENAKA 73

Development of Short Pitch Resistance Spot Welding Technology
. . . . . Hisayasu OOKA・Atsushi SUZUKI・Mitsushige GOTO
Keita OTSUKA・Yasumasa OKADA 85

Application of Model-based Development to MICU
. . . . . Noboru UJIGAWA・Shuhei KINOSHITA・Masayuki YAMAZAKI 92

Design Appearance Evaluation Tool for Non-prototype Development
. . . . . Daisuke IDE・Ryosuke SAITO・Hajime KUBO 99

Report of Field Test Results Using Electric Vehicle and Plug-in Hybrid Vehicle Prototypes
. . . . . Yoshitaka TAKASUKA・Toru KIMURA・Junya TUNEISHI
Akihito OHTSU・Naoki FUJIHARA・Yoshiko TAKAHASHI 105

Technical papers

Research on Combustion Improvement Techniques by Intake Valve Offset and Squish Effect
. . . . . Takamori SHIRASUNA・Hideki SAITO・Tomokazu NOMURA 115

Technique for Prediction of Automotive Transmission Lubrication Performance
. . . . . Daiki SAEGUSA・Shinji KAWAI 131

Study of Seal Structure of High-differential-pressure Water Electrolysis Cell
. . . . . Nobuyuki KAWASAKI・Eiji HARYU・Hiroyuki ISHIKAWA
Koji NAKAZAWA・Masanori OKABE 137

Development of Steel for High-strength Crankshaft by Precipitation Strengthening of Mn-nitride
. . . . . Hiromasa TAKAHASHI・Hiroki MASUDA
Shigefumi NISHITANI・Motoki TAKASUGA 145

Development of Waterborne Primer Applicable to Different Plastics in Motorcycles
. . . . . .Tomoyuki INOUE・Akiko TANAKA
Shinsuke MOCHIZUKI・Masanobu INOUE 154

Research on Photo-degradation Behavior of E-coat
. . . . . Keisuke KOJIMA・Takamasa AOKI・Takeshi OGAWA 165

Study of High Smooth Electrodeposition Coating That Enables Primer Process-less Paint System
. . . . . .Katsuyoshi KANEKO・Toshikazu HIROBE
Yusuke KAWADA・Tatsumasa HIDAKA 172

Identification of Mechanism of Transmission of Flow-induced Noise through Glass for
Vehicle Interior Noise Reduction
. . . . . KeiAMBO・Kazuya MORISHITA
Takashi YOSHINO・Minoru TERAMURA 177

Styling Design of New N-ONE

Shinichiro KANAYAMA* Takao ISHIKAWA*
Masayuki TOGAWA* Yasuko SAITO*

ABSTRACT

Following the grand concept of "One's MINI TOURER," the N-ONE was developed as a new basic Japanese car with cruising performance and a package in which four adults could take a long drive in comfort, and that pursued high quality and friendly design to surpass small cars while staying within the kei car specification.

The design concept was expressed as "timeless N design," and the N-ONE is intended to be used affectionately for many years as a new basic car. To that end, the design effort achieved "simplicity" along with a "high-quality sense" that does not feel like the kei car class.

The styling themes of the exterior are "friendly," "comfortable," and "usable," while those of the interior are "exhilarating," "enriching," and "usable." The colors and fabric were also developed to bring out these characteristics.

1. Introduction

Since entering the automobile market in 1963 with a kei car, Honda has offered unique products unlike those of any other manufacturer. Among them, the N360 was born as Honda's first kei car bringing together modern design, far better cruising than other cars, a comfortable interior space even when driving long distances, and a high level of safety. The N360 encouraged Japanese society to become more motorized and spurred a boom in private car ownership so that many users experienced the car-owning life for the first time. The N-ONE was developed to carry on this intention of the N360.

As Honda set about to develop its third model in the N Series, it decided to target young people and empty nesters (those whose children are now grown). This is in distinction to the N BOX which was geared toward families with young children. When Honda researched its target users, it found that these users' high level of environmental awareness led them to want high quality they could use for many years. Among the empty nesters in particular, Honda found that more and more were downsizing from sedans and small cars to kei cars. It also found that the area over which people drive their kei cars, which previously consisted of shopping, commuting, and other short trips, is expanding as user activities grow more diverse.

Thus Honda selected three keywords for the N-ONE: "timeless N design" for the high-quality sense to win over downsizers, "comfortable tourer performance" for the excellent cruising and comfortable interior space that make long trips possible, and "safe driving performance" for a high level of safety achieved. It then developed "One's MINI TOURER" to be the best personal car for each customer (Fig. 1).

Honda also set premium specifications to provide even higher quality design and cruising to satisfy customers looking for the value of a high-end car.



Fig. 1 Grand concept

* Automobile R&D Center

2. Design Concept

To realize a new basic car as a kei car surpassing a small car, Honda chose “timeless N design” as the N-ONE’s design concept.

To achieve a car that owners could drive with affection and pride throughout the years, Honda aimed for friendliness, intuitiveness, and simplicity that is never dull, along with a high-quality design that does not feel like the kei car class, so that drivers would accept it as their first car (Fig. 2).

From the start of development, it also aimed to achieve a design built for customization, so that owners could easily change the impression the car makes to suit their tastes.

Honda defined its premium specification concept as “modern premium,” aiming for a design that is of higher quality and euphoria than a normal car.



Fig. 2 Overview of N-ONE

3. Package Layout

To achieve “One’s MINI TOURER,” Honda aimed to create a “mini tourer package” that offers a form designed for high-speed, long-distance cruising, more spaciousness than a small car despite fitting within the kei car size specification, and everyday utility.

3.1. Both Trapezoid Form and Comfortable Space

To achieve a form that embodies excellent cruising with a low center of gravity, the designers selected a vibrant trapezoid form that emphasizes the slope of the tailgate in side view and gives a look of stability even when traveling at high speed. They moreover achieved a top-of-class effective interior length by taking advantage of the superiority of the N series’ innovative platform. Thus they realized a space in which four adults could pass time comfortably, balanced with a sufficient luggage compartment. As a result, there is more space from front to back than in a small car, enough so that passengers in the rear seat can cross their legs, and at the same time, a luggage compartment large enough to hold four adults’ luggage for an overnight trip (Fig. 3).

3.2. Everyday Utility

To enhance everyday utility, the designers adopted the N Series’ innovative platform for the luggage compartment area, and used a rear seat that can be arranged a variety of ways (a 5:5 split) with the same one-motion dive-down and tip-up mechanism as the N BOX.

When in dive-down mode, the luggage compartment length is a top-of-class 1560 mm, making the luggage compartment large enough to hold two mountain bikes with their front tires removed (Fig. 4). There is 39 L of underfloor storage space beneath the trunk, where car maintenance supplies, soiled items, and anything else the user does not want to be seen can be kept out of sight. The ground height of the tailgate opening is a class-lowest 575

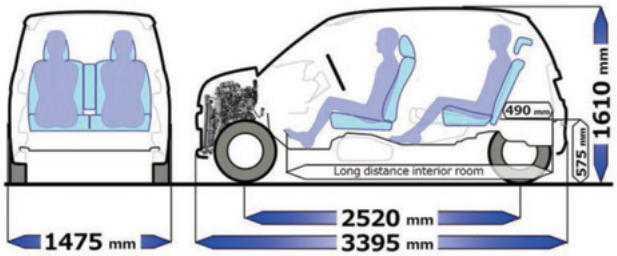


Fig. 3 Package layout

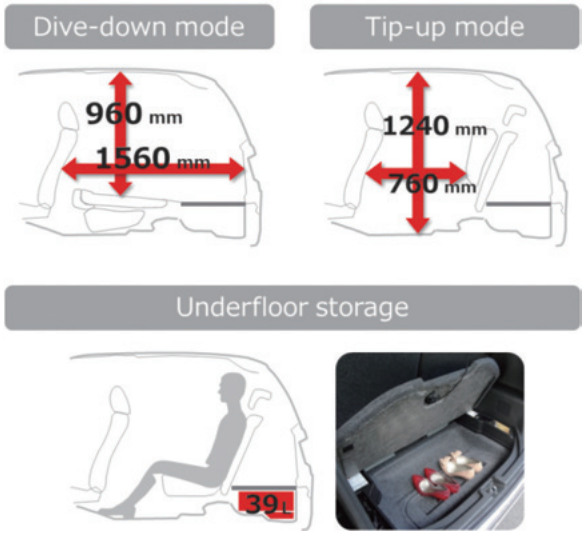


Fig. 4 Utility of rear seat and trunk

mm, which is level with the luggage compartment floor and makes it easy to load and unload heavy luggage.

In terms of handling, the designers moved the A pillar toward the back, giving a wide field of vision in front. The result is a commanding view and good visibility of traffic in the oncoming lane in the corner. Moreover, the horizontal beltline from the front window to side window creates a good field of vision for handling even when moving in reverse (Fig. 5).

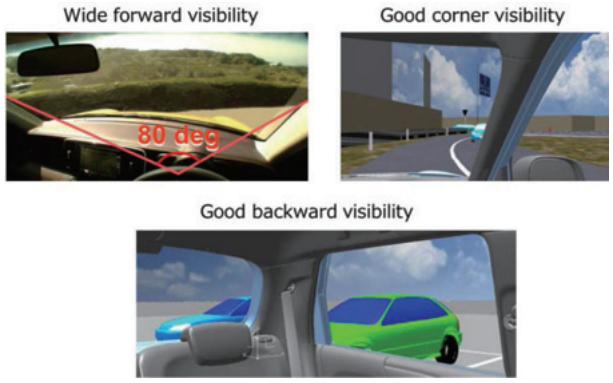


Fig. 5 Good visibility

4. Exterior Design

4.1. Exterior Design Concept

The exterior design pursues simplicity and high quality as a new vehicle directly descended from the N360, so that the car feels familiar to drivers who will use it with affection over many years. Three keywords guided the design process: friendly, comfortable, and usable (Fig. 6).

Aspects that express “friendly” include a simple silhouette with few elements, such as a child’s drawing of a car, and charming round headlights.

“Comfortable” is expressed by the thick, strong front mask and side body and by the stable-looking trapezoid form.

The design becomes more “usable” by using a panoramic cantilever window graphic to ensure an excellent field of vision and by heaping up the profile above the headlights, making the front edge of the engine hood easy to see and helping to ensure excellent handling.

In front view, the fender projects outward from the short but thick and sturdy front mask to express dynamism and comfort. Moreover, the headlights are contained within the grille, emphasizing the wide look and expressing strength and dynamism. The license plate is located in the center, giving the car a symmetrical face.

The side view is characterized by simplicity with few elements, a moderately sloped tailgate, and a roof that slopes forward to give a vibrant feel. Fenders project out from the four corners of the thick body creating a stable-looking trapezoid form. Additionally, the sharp character lines and the modulating surfaces that fill in the space between them express a three-dimensional look, and sense of quality within the width allowed by kei car specifications.

The rear view emphasizes a look of stability with a trapezoid form from which the rear fenders project. The rear combination lamp has a rectangular motif with a simple, friendly-looking form (Fig. 7).

4.2. Lighting Design Concept

The headlights consist of tubular projector units in circular outer forms. This represents the eyes of a human face, and presents an energetic, youthful expression. The position lamps use light guiding bodies that emit rings of light creating an iconic show of lighting that makes the car recognizable as an N-ONE even at night. The HID specifications use escaped light from the projector to illuminate the circumference of the projector creating a higher sense of value without greatly adding to cost.

The rear combination lamps have a friendly-looking rectangular outer form. This is emphasized by the tail lamps and stop lamps, which use light guiding bodies to illuminate the rectangular perimeter, for lighting that is as iconic as in the front (Fig. 8).



Fig. 6 Exterior design concept



Fig. 7 Exterior rendering

4.3. Grille Design Concept

The grille design projects a high-quality, wide look by containing the headlights within the glossy black outer form with a large surface area reminiscent of the N360. Moreover, with the grille's wide, relatively flat surface, it is possible to easily and effectively decorate it with decals and customize it to meet customers' different needs (Fig. 9).

4.4. Exterior Design of Premium Grade

The exterior design of the premium grade of the N-ONE is based on a theme of higher quality and euphoria than anything else in the kei car class. The front achieves both cruising enjoyment and quality with sharp and wide-looking bumpers and a plated, wide-open grille. From the side to the rear, there is plated molding running from the lower part of the doors to the rear bumper enhancing the look of quality. At the same time, the tailgate spoiler, providing both stylish design and aerodynamic performance ensures cruising euphoria. Finally, the large-diameter 15-inch aluminum wheels create a sporty design that accentuates the joy of cruising (Fig. 10).



Fig. 10 Exterior design of premium grade

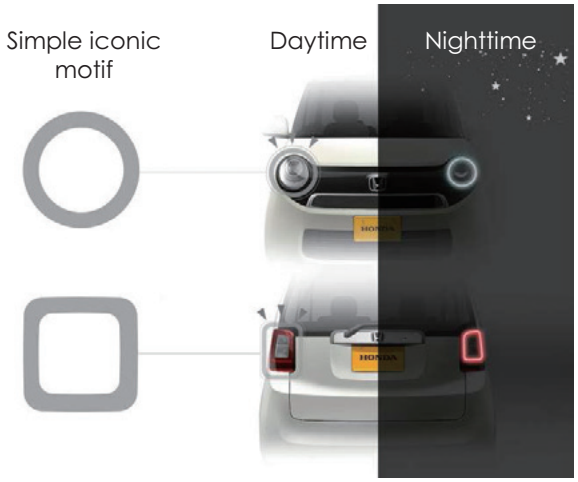


Fig. 8 Lighting image



Fig. 9 Grille design

5. Interior Design

5.1. Interior Design Concept

The interior design features a simple, intuitive motif that drivers can use with affection over many years. Details are very carefully crafted so that the interior has a look of exhilaration and high quality. Three keywords guided the design process: exhilarating, enriching, and usable (Fig. 11).

"Exhilarating" is expressed by shaping the overall interior with a simple structure and intuitive motif, creating a neat and comfortable space.

"Enriching" is achieved by expressing a sense of deliberateness, with a form that has a three-dimensional look with modulations. The aim was to create a high texture that does not feel like the kei car class.

"Usable" is achieved by plentiful utilities, and a



Fig. 11 Interior design concept

comfortable audio system built around the front seat.

The instrument panel has a horizontally aligned motif that keeps the center from sticking out too far so that occupants do not sense a boundary between the driver's seat and front passenger's seat. And the greater depth of the panel helps to create a form that gives a spacious feel and adds to the sense of exhilaration (Fig. 12).

The instrument panel upper section, which tends to draw the occupants' line of vision, has a wide decoration running from left to right enhancing the sense of texture. This decoration slopes toward the occupants giving them a sense of being enveloped and enhancing comfort during high-speed cruising.

The instrument panel and doors have a two-tone color scheme creating a visually refined look.

Using the instrument panel upper section, with its extra depth that expresses spaciousness, the designers added wide, highly usable trays that are accessible to both driver and passenger. Below the instrument panel are convenient open trays in three places: driver's side, passenger's side, and center. These emphasize the horizontal layout and a sense of lightness.

The seats have a placid and clean motif and express quality with their three-dimensional form. They are also designed with hold to envelop the occupant, which creates a form that is comfortable and not tiring even on long drives (Fig. 13).



Fig. 12 Interior rendering



Fig. 13 Seat design

The audio system is divided into the monitor and controls. The monitor is made easier to see by placing it on the upper far side of the instrument panel where there is minimum eye movement. Placing the controls closer to the passenger makes them easier to use (Fig. 14).

5.2. Interior Design of Premium Grade

The interior design of the premium grade is based on a theme of higher quality, poise, and elation than anything else in the kei car class. The premium grade has exclusive interior coloring, decorative patterns, and fabric. The interior as a whole is coordinated using the elaborate graphics of the meters and the violet-colored lighting that is combined with the center lower tray (Fig. 15).



Fig. 14 Audio design





Fig. 15 Interior design of premium grade

6. Color and Fabric Design

6.1. Exterior Color

The lineup consists of a rich selection of vibrant exterior colors so that customers can choose their favorites and use their cars with affection over many years. Between the normal and premium grades, 11 colors are available, ranging from the standard basic colors to casual and bright fun colors and premium colors for a high-quality, mature

feel. Therefore customers are able to choose colors to suit their own tastes (Fig. 16).

There are also five two-tone color patterns borrowed from the N BOX+, which draw out the individuality of the N-ONE even more attractively (Fig. 17).

Innocent Blue Metallic, a new color in the normal grade, presents an image of pure blue composed of layers of air and water. It is meant to appeal universally across the generations and eras. The color appears to be a solid one at first glance, but has a somewhat yellowish hue. The overall impression aims to feel nostalgic to older drivers and impressive and fresh to younger ones.

Premium Blue Moon Pearl, a new color in the premium grade, presents an image of the calm twilight sky. It is intended as a high-quality and urban color (Fig. 18).



Fig. 16 Exterior color line-up



Fig. 17 Two-tone roof line-up

6.2. Interior Color

The intent of the normal grade's interior color is to provide an atmosphere a person could stay with for a long period of time, one which would give feelings of relief and calm as soon as the door was opened to go inside. Thus a bright beige with restrained chroma was chosen as the base tone creating an impression of neatness and friendliness overall. Dark brown is used for the instrument panel and door lining. The contrast gives this two-tone scheme an enriching, high-quality feel. There is also a color variation with a unified black interior that creates a feel of tight fearlessness and providing for the needs of a wider range of customers.

The seat fabric has a detailed houndstooth check pattern in a design to be appreciated with affection by both sexes, no matter the generation or age (Fig. 19).



Fig. 18 New colors





Fig. 19 Interior color variations

The instrument panel upper section is decorated with a glossy finish that seeks to enhance the texture. This decorative element provides accent for the interior as a whole and achieves a high-texture interior that does not feel like the kei car class (Fig. 20).

The premium grade's interior has a two-tone color scheme combining burgundy (a deep red) with a black base tone, creating a poised, modern look.

The instrument panel upper section and door lining are decorated with a black wood grain pattern for a look of high quality.

The seat fabric is embossed with a quilted look which brings out a three-dimensional, high-quality feel. The same type of fabric is used for the door lining to enhance the enriching feel (Fig. 21).



Fig. 20 Instrument panel plating



Fig. 21 Premium interior color

7. New Appeal Initiative

As a first-time experiment, Honda wrote a Design Point Book; a kind of guide to the N-ONE's design to explain to more customers the car's attractiveness in an intuitive way (Fig. 22).

This is not to give a difficult technical explanation of the design. Rather, it is like a storybook, primarily visual and with as little text as possible, so that even a child or a person not particularly interested in cars can understand it. The Design Point Book was written to convey those things that a catalog cannot: the thinking of the people who made it, and Honda's attitude toward craftsmanship. The purpose of this is to encourage even more affection for the car among customers.

The content begins with the background story of the N-ONE, and is divided into five topics: form, good feeling, sense of confidence, goodness, and fun. It gives a very understandable explanation of the car's modeling and safety; topics that otherwise tend to seem difficult.

To begin with, the book gives background to the birth of the N360, its impact on society, and so on. The "form" section explains how the interior and exterior were designed to leave an indelible impression with just one look. The "feel good" section covers packaging (e.g., the spaciousness and excellent visibility) and cruising performance. "Sense of confidence" covers safety performance, such as the good



Fig. 22 N-ONE design point book

handling and passive safety functions. “Goodness” takes a different tone from the other pages to describe the exacting modeling and highly textured surface finishing. “Fun,” the final section, talks about the exterior colors and the fun of choosing from the wide selection of colors, as well as the fun of using the N-ONE’s customizable features and its various utilities.

The book uses a variety of photos, illustrations, and a humorous tone to keep the reader interested, while maintaining a unified feel to all the above content.

8. Conclusion

The N BOX, the first vehicle in the N Series, went beyond the ordinary kei car to feature minivan-like spaciousness. The N BOX+, the second vehicle in the series, offered utility unprecedented in kei cars. As a “new basic Japanese car” to surpass small cars and as the third vehicle in the series, the N-ONE is a perfect fit in the N Series of vehicles that exceed customer expectations.

Developed with the design concept of “timeless N design,” the N-ONE has achieved a design that can be used with affection over many years, regardless of changes in the times and in spite of the conventional hierarchy.

It is Honda’s sincere hope that the N-ONE, developed as above, will be more than just a “thing” people own. Rather, it is hoped the car will be a “just-for-you” vehicle, one that becomes a beloved part of the family, stays part of the family a long time, and carries with it many memories.

■ Author ■


Shinichiro KANAYAMA


Takao ISHIKAWA


Masayuki TOGAWA


Yasuko SAITO

Development of New V6 3.5 L Gasoline Engine

Nobuo SUZUKI* Yasutaka HAYASHI** Kazuya ISHIKI*
Atsushi SATO* Tatsuhito ESAKI** Satoshi WATANABE*

ABSTRACT

A new V6 3.5 L gasoline engine was developed with the goal of simultaneously reducing CO_2 emissions and achieving the driving enjoyment inherent to vehicles. The DI VTEC VCM system that is the key technology of this engine integrates variable valve timing lift and a variable cylinder system with a direct injection system. This increased the maximum output by 3.3% and reduced the fuel consumption rate by 20.1% compared to the previous model. A 2014 model year ACURA RLX equipped with this new engine, enhanced NV performance that expands the 3-cylinder drive area, and vehicle body technologies that increase fuel economy achieved fuel economy enhancement of 29% in Environmental Protection Agency highway mode and 18% in city mode compared to the previous model.

1. Introduction

As expectations increase for enhanced environmental performance of automobiles, Honda is aiming to reduce CO_2 emissions of its products sold around the world by 30% compared with 2000 levels, by the year 2020. The domains of new next-generation technology that pursue driving enjoyment characteristic of Honda products with a base of good environmental performance, and achieve a high balance of both driving quality and fuel economy have been designated EARTH DREAMS TECHNOLOGY. Figure 1 shows the EARTH DREAMS TECHNOLOGY domain lineup, which includes 0.66 L to 3.5 L-class gasoline engines, a small diesel engine, K-Car to medium vehicle-class CVT, an electric vehicle (EV) powertrain, and a hybrid series of powertrains. The gasoline engines achieve both high output performance and low power consumption by further advancing Honda's original VTEC technology, increasing thermal efficiency, and reducing friction.



Fig. 1 Domains of EARTH DREAMS TECHNOLOGY

The newly developed V6 3.5 L engine achieves both enhanced fuel economy and high output by integrating a high-output type Variable valve Timing and lift Electronic Control (VTEC) system that has been used according to the concepts of the vehicles in which it has been mounted thus far, with a Variable Cylinder Management (VCM) system[(1)] that enables 3-cylinder drive, and also by adopting cylinder Direct Injection (DI). This paper reports on the new technology used in this new V6 3.5 L engine.

2. Development Goals

The new engine was developed with the following goals to achieve both the high product appeal and environmental performance enabling use in a mid-size luxury sedan.

(1) Securing top-class output competitiveness
(2) Achieving top-class Environmental Protection Agency (EPA) mode fuel economy
(3) NV performance befitting a mid-size luxury sedan

3. Overview of Engine and Applied Technology

The VCM system is a technology for reducing the fuel consumption of V6 engines. The VCM system treats a V6 engine as two 3-cylinder engines, and instantly stops

* Automobile R&D Center
** HONDA R&D AMERICAS, INC.

Table 1 Engine specifications

Engine code	J35Y4 (new)	J37A
Displacement (cm^3)	3471	3664
Bore x stroke (mm)	89 x 93	90 x 96
Valve train	SOHC VTEC with VCM	SOHC VTEC
Compression ratio	11.5:1	11.2:1
Fuel system	Direct injection	Port injection
Max. power (kW/rpm)	231 / 6500	224 / 6300
Max. torque (Nm/rpm)	369 / 4500	368 / 5000
Redline (rpm)	6800	6800
Fuel grade	Premium recommended	Premium mandatory

inlet and exhaust valve drive for one bank consisting of three of the six cylinders in accordance with the driving status, propelling the vehicle with only the remaining three cylinders. Then, when the accelerator is pressed or a high load is otherwise applied, the engine instantly returns to 6-cylinder drive. This simultaneously achieves a high balance of both the power of large displacement and the low fuel consumption of small displacement.

The new engine uses a newly designed valvetrain and combustion chamber shape to accommodate DI VTEC VCM adoption. Intake efficiency is secured by adopting VTEC and DI, and low-speed torque is secured by reducing knock, which increases the torque. The V6 layout with a bank angle of 60° that is advantageous in terms of first-order rotational vibration, and the compact and lightweight framework structure are carried over from the previous model. Figure 2 shows the external appearance of the engine, and Table 1 lists the major engine specifications.

This paper describes the VTEC VCM system and DI system that are the key technology of this engine. In addition, it also describes the friction reduction technology and VCM applied technology that contribute to enhancing fuel economy, and the mode fuel economy enhancement effects.



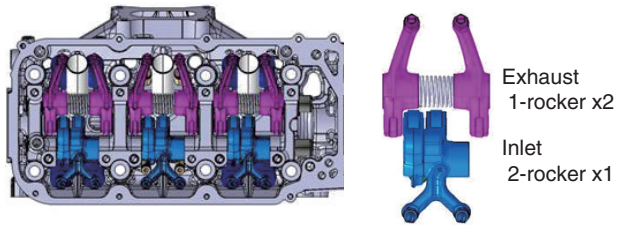
Fig. 2 J35Y4 engine

4. Key DI VTEC VCM Technology

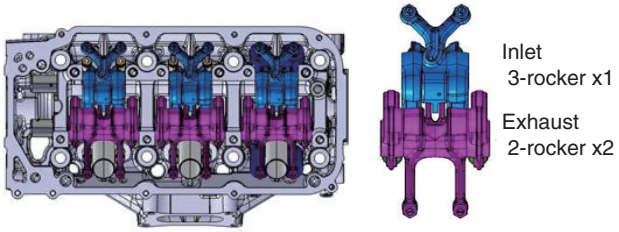
4.1. VTEC VCM System

Figure 3 shows the VTEC VCM system used in this engine. Three-cylinder drive is supported by locating VTEC rocker arms in the V-engine's front bank that constantly performs driving [Fig. 3(a)], and VTEC VCM rocker arms with a new structure in the rear bank [Fig. 3(b)].

The drive mode is switched according to information such as the engine speed, load, vehicle speed, and throttle opening. Figure 4 shows a diagram of the rear bank oil circuit. The newly developed system consists of two different spool valves: spool valve A that controls the hydraulic pressure for VCM switching; and spool valve B



(a) Front bank: VTEC



(b) Rear bank: VTEC and VCM

Fig. 3 VTEC VCM structure

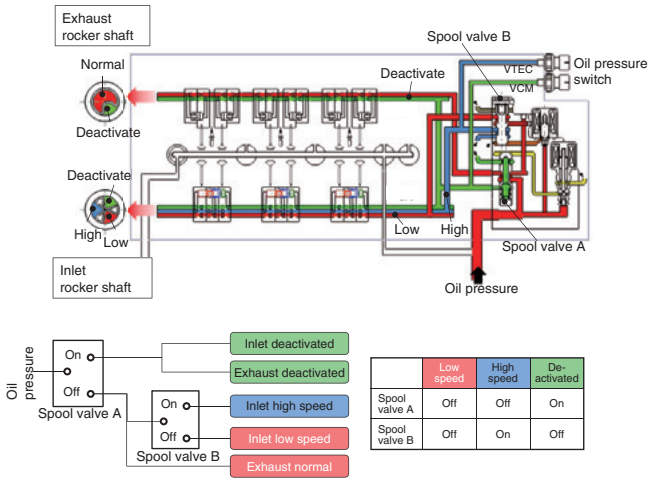


Fig. 4 VTEC VCM oil path system

that controls the hydraulic pressure for VTEC switching between low-speed and high-speed operation. Hydraulic pressure is supplied to the rocker arms, the synchronizing piston pins move, and the rocker arms connect and disconnect according to the switching of these spool valves.

4.1.1. Coaxial synchronizing piston pin structure

Figure 5 shows the differences between the newly developed VTEC coaxial synchronizing piston pin structure and the conventional structure. The conventional structure located the synchronizing piston pin for VTEC switching and the synchronizing piston pin for VCM switching on different axes[(2)]. However, the increase in inertia weight due to locating the synchronizing piston pins on different axes increases the friction loss, which affects fuel economy, so a newly developed 3-stage coaxial synchronizing piston pin structure was adopted that uses hydraulic-hydraulic switching. This was done by incorporating a hollow outer pin and solid inner pin into the mid rocker, and realizes three different types of valve lift by extending and sliding these pins using hydraulic pressure.

Figure 6 shows an overview of VTEC VCM lift change-over. In the initial state, hydraulic pressure is applied to path 2 and the outer and inner pins of the mid rocker are pressed apart, so the low-speed rocker and mid rocker are connected and low-speed cam drive results. During cylinder deactivation, hydraulic pressure is applied to path 1 and the low-speed rocker pin is pushed out, so the low-speed rocker and the mid rocker are disconnected and valve drive stops. When a request to switch to the high-speed cam is issued, hydraulic pressure is applied to path 3 to push out the high-speed rocker pin, so all three high-speed, mid and low-speed rockers are connected and high-speed cam drive results.

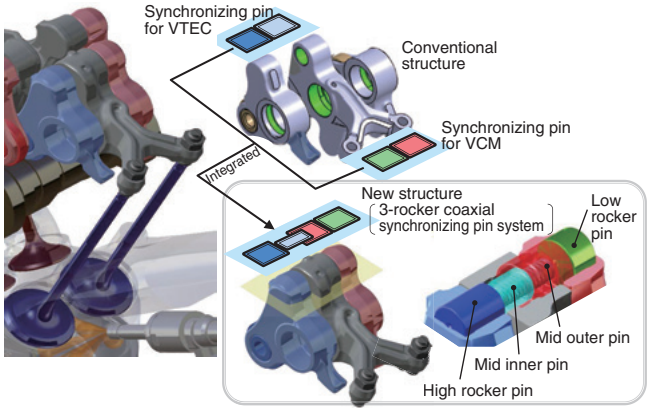


Fig. 5 Synchronizing pin structure

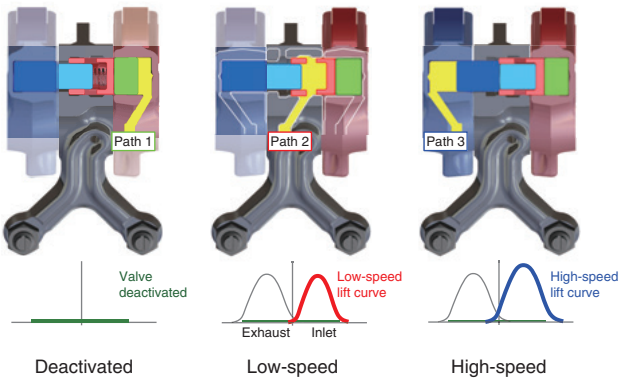


Fig. 6 Valve lift change over

Figure 7 shows the results of measuring valve bounce behavior relative to engine speed. Adoption of the new synchronizing piston pin structure suppressed the increase in weight and enabled stabilizing of valvetrain behavior up to 7000 rpm without increasing the valve spring load.

The adoption of a structure that connects all three rockers even when driving with the high-speed cam enabled stabilizing of the low-speed cam behavior during high-speed operation without adding a new lost motion spring.

The conventional structure in which the three rockers are always connected requires that hydraulic pressure be applied to two paths. In contrast, this coaxial synchronizing piston pin mechanism requires that hydraulic pressure be applied to only one of three paths, which reduces the oil path volume and oil leak amount compared to the conventional mechanism.

4.1.2. Switching responsiveness

The switching responsiveness of the VCM system is an important factor for realizing a linear drive feeling. The volume, diameter and length of the oil path, the introducibility of hydraulic pressure to the synchronizing piston pin, the oil leakage amount, and other factors that affect the switching responsiveness were optimized with the aim of immediately boosting the pressure in each part of the oil path to the supplied hydraulic pressure or returning to low pressure in accordance with the VCM switching signal.

Figure 8 shows an example of the results of measuring the pressure-receiving characteristics of the synchronizing piston pin and optimizing the oil channels. In the initial development stages, a delay occurred in the pin load relative to the rise in hydraulic pressure in the oil path (black line in Fig. 8). Therefore, the introducibility of oil to the

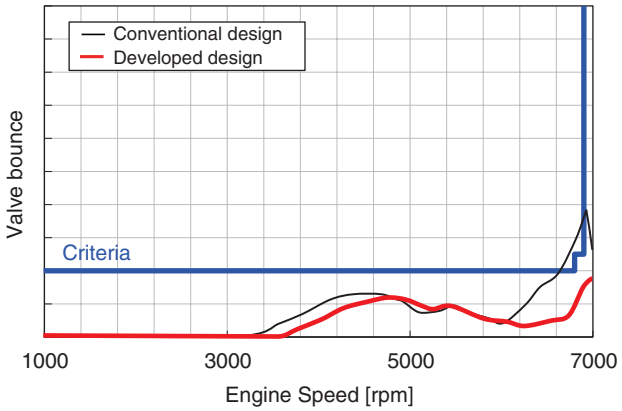


Fig. 7 Valve bounce behavior

pin was enhanced by expanding the inflow area and adding a cross groove to the synchronizing piston pin. This enabled shortening of the reaction time (red line in Fig. 8).

Figure 9 shows the structure of the 3-way spool valve. Use of a 3-way valve enabled lowering of the hydraulic pressure applied in the valve deactivation state by leading the oil to the drain, and to immediately raise the hydraulic pressure on the operating side when switching from the valve deactivation state to the normal operating state. This system achieved high switching responsiveness by reviewing the detailed drain path and spool valve structures, and realized control that stops fuel injection in sync with the inlet and exhaust valve operation stop timings.

4.2. DI System

The combustion chamber shape, head port shape and intake manifold were specially designed to accommodate DI system adoption.

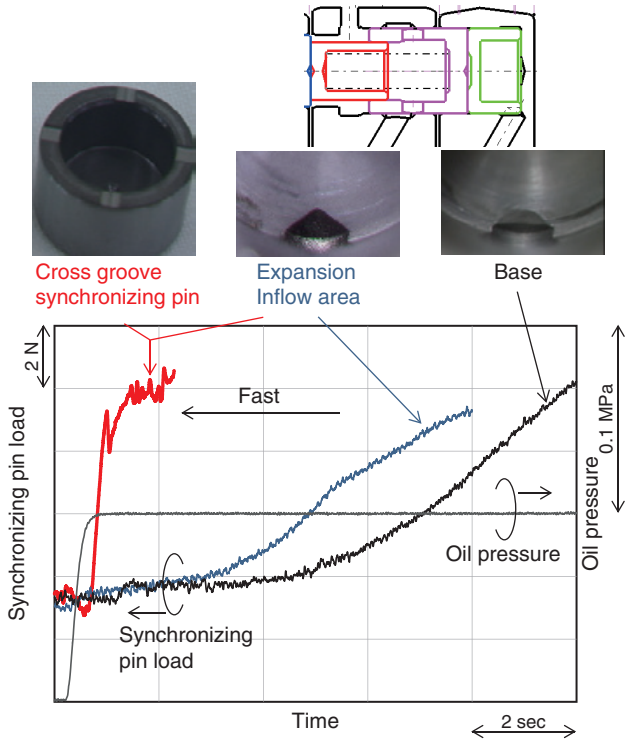


Fig. 8 Decrease of reaction time

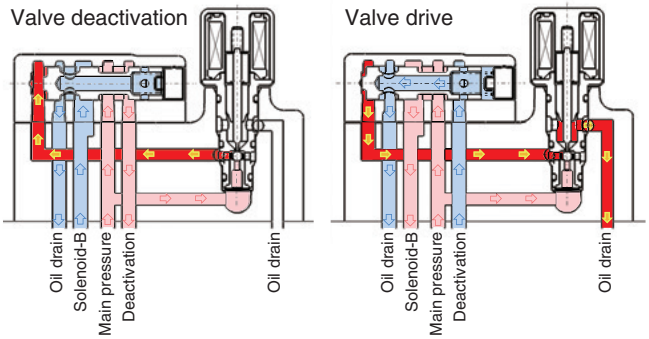


Fig. 9 3-way spool valve drain system

Figure 10 shows the DI combustion system that uses technical elements shared with the new 2.4 L engine. A multi-hole DI injector is located on the intake side of the combustion chamber, and produces strong tumble flow that forms a homogenous air fuel mixture for homogenous combustion. The shallow cavity in the piston crown is used together with split injection to stabilize combustion when warming up the catalyst.

The fuel system uses a compact package that fits between the V banks as shown in Fig. 11 in consideration of collision safety and reduction of noise to the outside of the vehicle. Fuel supply to the front and rear banks was integrated to a single plunger-type pump located at the end of the camshaft on the rear head side to minimize friction loss when driving the high-pressure fuel pump.

The sizes and positions of the orifices inside the fuel pipe were optimized to suppress the fuel pressure fluctuation when the drive mode switches. Figure 12 shows the fluctuation inside the fuel pipe when switched between 6-cylinder drive and 3-cylinder drive. Optimization of the orifice positions and sizes suppressed the fuel pressure fluctuation before and after switching, with the result that A/F control could be rationalized by equalizing the fuel injection amount.

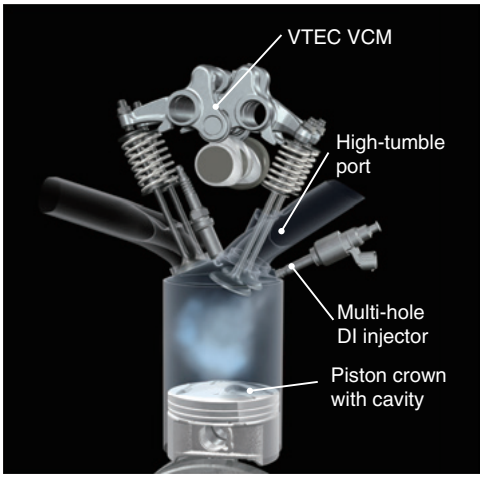


Fig. 10 DI combustion system

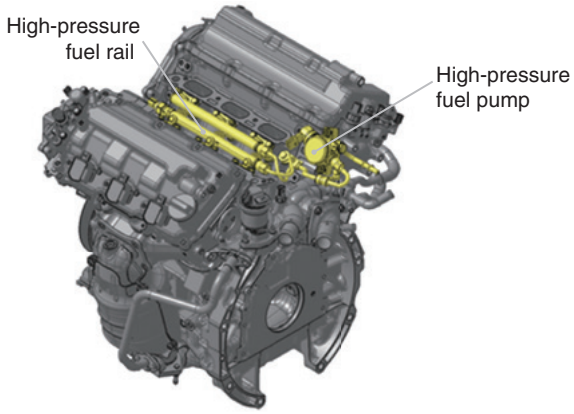


Fig. 11 DI system layout

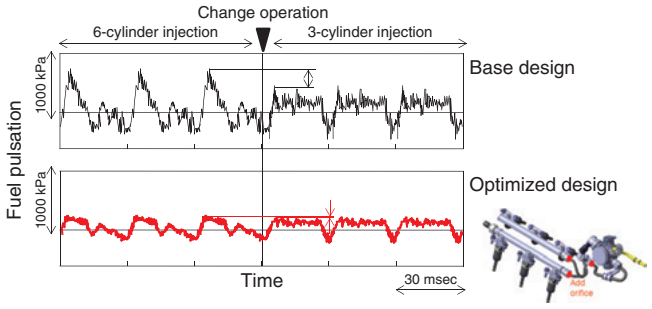


Fig. 12 Reduced fuel pressure fluctuation

5. Power Output

Figure 13 shows the output characteristics of the new V6 3.5 L engine. Adoption of new technology such as the DI VTEC VCM system and reduction of the intake and exhaust pipe resistance achieved a maximum output of 231 kW, which is 3.3% higher than that of the previous model, while downsizing the displacement. Torque characteristics equal to those of the 3.7 L engine of the previous model could also be achieved.

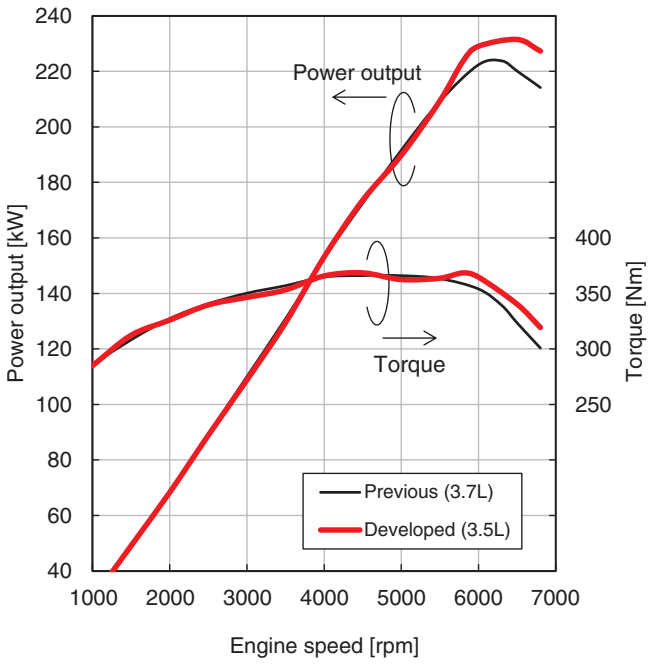


Fig. 13 Engine performance

6. Fuel Economy Enhancement Technology

6.1. Friction Reduction Technology

The cooling control spacers (CCS) and 2-stage relief structure of the oil pump shown in Fig. 14 are the key friction reduction technology used in this engine, and are described below.

First, the CCS are described. CCS are mounted in locations subject to high piston thrust force inside the cylinder water jacket with the aim of reducing friction by optimizing the water flow and expanding the cylinder inner diameter. Figure 15 shows the results of calculating and analyzing the water flow inside the cylinder block water jacket with and without CCS. These results show that CCS reduce the cooling water flow speed in the lower part of the sleeve, and increase the head cooling water distribution ratio and flow speed in the area near the combustion chamber, which requires active cooling due to the heat generated by combustion.

Figure 16 shows the change in the cylinder wall

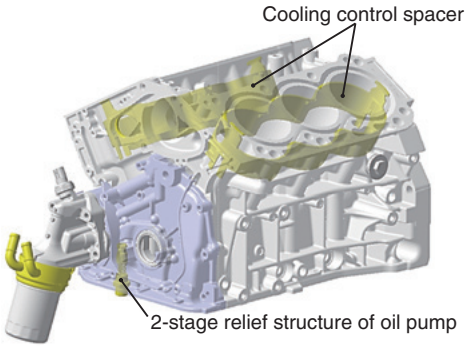


Fig. 14 Friction reduction technology

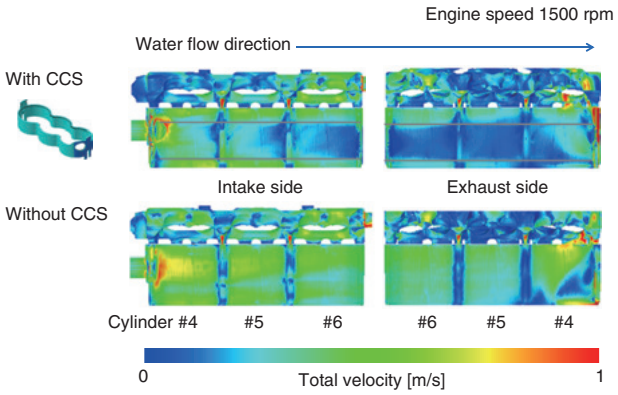


Fig. 15 Water flow speed distribution

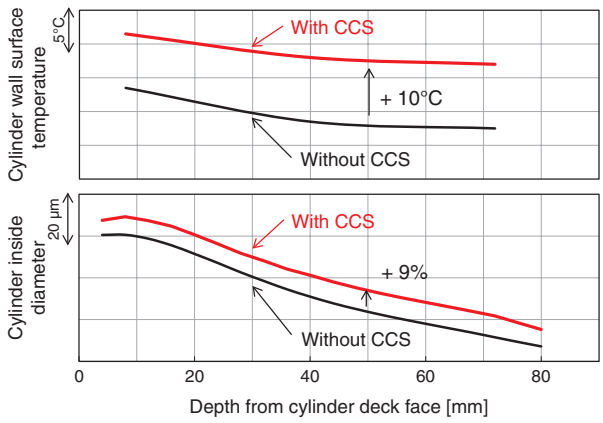


Fig. 16 Effect of CCS on cylinder wall temperature and cylinder inner diameter

temperature and cylinder inner diameter with and without CCS. Rationalization of the water flow inside the cylinder block water jacket increased the cylinder wall surface temperature by approximately 10°C and expanded the cylinder inner diameter by 9%. This reduced the sliding friction of the piston and piston ring, and achieved Brake Specific Fuel Consumption (BSFC) enhancement effects of 0.8%.

Next, the 2-stage relief structure of the oil pump is described. This structure is intended to reduce the oil pump drive torque by optimizing the hydraulic pressure characteristics at slow and mid-engine speed.

Figure 17 describes the relief structure. The conventional relief structure (1-stage relief) has a structure where the relief valve strokes and oil is discharged from a relief hole in the housing when hydraulic pressure of the set valve pressure or more is applied [Fig. 17(a)].

In contrast, the 2-stage relief structure enables 2-stage relief by adding a lubrication groove in the upper part of the relief valve and the housing upstream from the relief hole. Two-stage relief operates as follows. First, the relief valve begins its stroke when hydraulic pressure of the set valve pressure or more is applied. Oil passes through the lubrication groove formed by the valve and housing upstream from the relief hole, and is discharged from the relief hole. As the hydraulic pressure rises and the valve stroke progresses, the lubrication groove is blocked and the 1st-stage relief stops. When the hydraulic pressure rises further to the 2nd-stage valve pressure or more, oil is discharged from the 2nd-stage relief hole [Fig. 17(b)].

Figure 18 shows the hydraulic pressure characteristics at slow and mid-engine speed and the effect due to adoption of the 2-stage relief oil pump relief structure. As a result of optimizing the hydraulic pressure characteristics, hydraulic pressure reduction effects of 25% and oil pump drive torque reduction effects of 35% could be obtained.

Other friction reduction technology included thorough measures to reduce mechanical friction such as application of a molybdenum pattern coat to the piston skirts, reduction of piston ring tension, use of low-torque oil seals and low-viscosity engine oil, and reduction of auxiliary belt tension. These measures achieved BSFC enhancement effects of 4% at 1500 rpm.

6.2. Fuel Consumption

Figure 19 shows the BSFC measurement results. Enhancement of thermal efficiency due to adoption of the DI system, together with the above-mentioned friction reduction technology, achieved BSFC enhancement effects of 5.2% during all-cylinder drive at the mode center of gravity of 1500 rpm, compared with the previous model. Furthermore, the pumping loss reduction effects yielded BSFC enhancement effects of 20.1% during 3-cylinder drive.

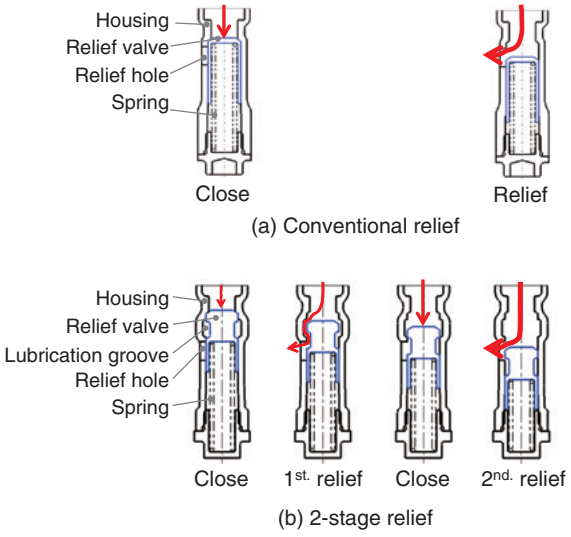


Fig. 17 Relief structure of oil pump

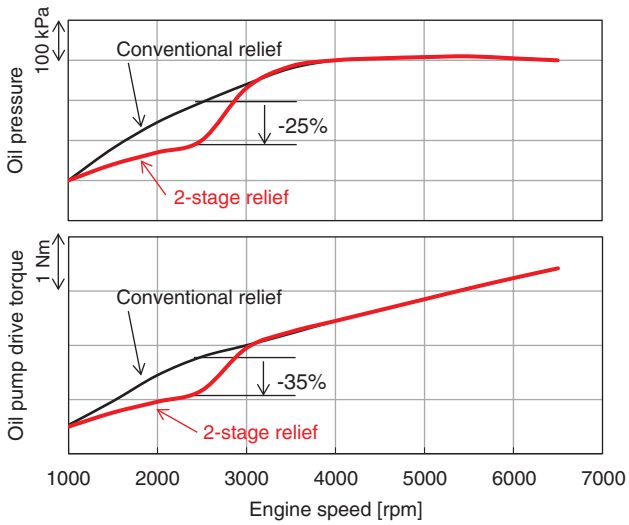


Fig. 18 Effect of 2-stage relief structure

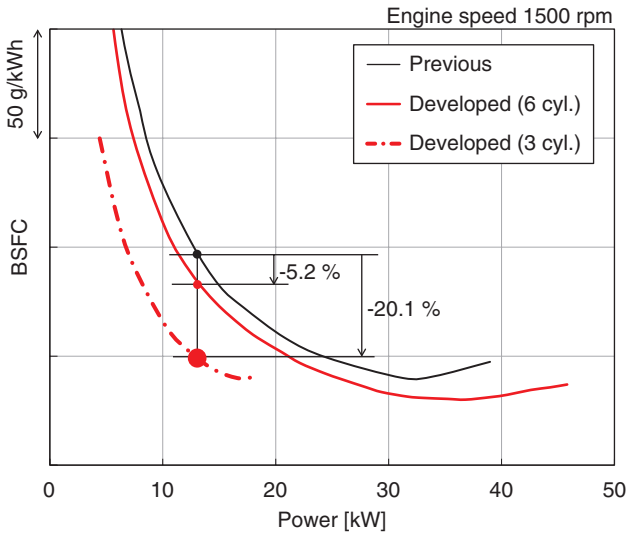


Fig. 19 BSFC characteristics

7. VCM Applied Technology

7.1. Enhancement of ACM Characteristics

There are concerns that the NV performance in a completed vehicle may drop during 3-cylinder drive as a result of increased vibration amplitude due to halving of the base vibration order with the reduction in firing cylinders, and a rise in the combustion pressure due to the increased amount of work per cylinder. However, the 2014 model year ACURA RLX equipped with this engine is the ACURA flagship sedan and is categorized as a mid-size luxury sedan, so higher NV performance is required. The authors set the high target value of 3 dB lower than that of existing models, and aimed for NV levels that make 3-cylinder drive unnoticeable to not only the driver but also the passengers.

For these reasons, the active control engine mount (ACM) capacity was expanded and the characteristics were enhanced.

ACM realizes high anti-vibration performance that makes 3-cylinder drive unnoticeable by absorbing vibration. This is done by building actuators into the bottoms of the liquid-sealed mounts that support the front and back of the engine, and extending and retracting these actuators in-phase and in-sync with the engine vibration[3]. This system achieved the required ACM setoff displacement performance, which is determined from the maximum torque that can be used during cylinder deactivation, by raising the ACM drive voltage output. Figure 20 shows a comparison with the previous model.

In addition, the NV characteristics of the transmission torque converter, exhaust system and steering system were also enhanced. Figure 21 shows the steering vibration level and engine torque during 3-cylinder drive. This shows that the conflicting elements of NV performance enhancement and expansion of the 3-cylinder drive torque could be simultaneously achieved.

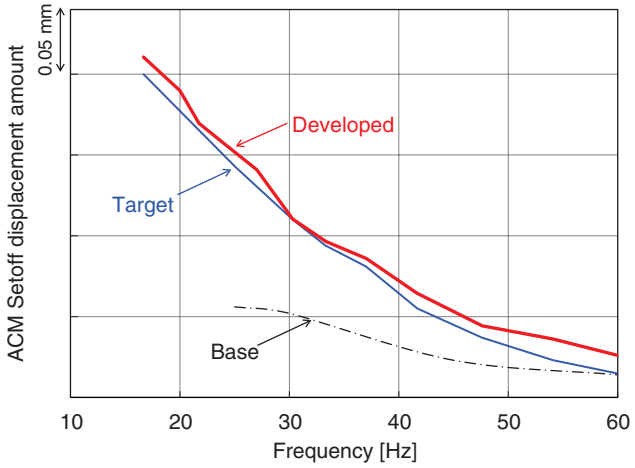


Fig. 20 Characteristics of ACM

7.2. Investigation of Gear Ratio

High-power performance is required of the RLX. However, there is the issue that when using a high-torque engine with comparatively large displacement, the load required for city driving is low, and the increased pumping loss results in a noticeable drop in fuel efficiency. The VCM system addresses this issue by enabling shifting from a low-load operating point to a more efficient high-load operating point, making it possible to simultaneously achieve both high-power performance and high fuel efficiency. The transmission gear ratio was optimized to more effectively increase the frequency of 3-cylinder drive. Figure 22 shows the relationship between the gear ratio and the 3-cylinder

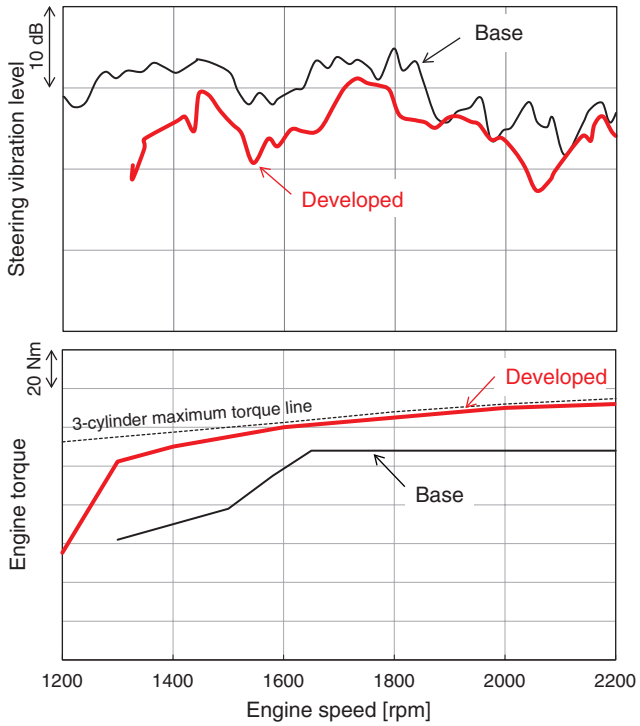


Fig. 21 Steering vibration of enhanced engine torque

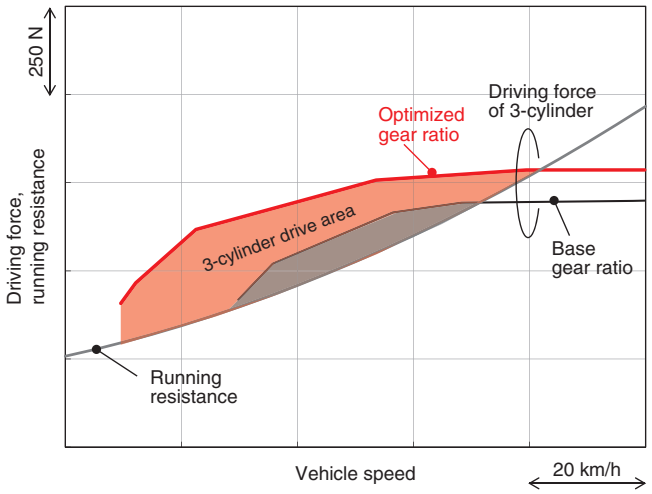


Fig. 22 Optimization of transmission gear ratios

Table 2 EPA mode fuel economy

	Highway (mpg)	City (mpg)	Combined (mpg)
2012 model year RL	24	17	20
RLX	31	20	24
Improvement	+29%	+18%	+20%

drive area. The vehicle speed range in which 3-cylinder drive can be performed was expanded by establishing a lower gear ratio than the base gear ratio.

Figure 23 shows VCM operation in EPA highway mode. The new engine features higher 3-cylinder torque, enhanced NV performance due to ACM enhancement, and an optimized transmission gear ratio, enabling 3-cylinder drive during most of highway mode.

7.3. Fuel Economy of a Vehicle

In addition to introduction of the technology described above, thorough body measures were taken to reduce the energy required to propel the RLX equipped with this engine. These measures include reducing the weight of each part to reduce the vehicle body weight, enhancement of bearings, brakes and tires to reduce rolling resistance, and aerodynamic enhancement. As a result, fuel economy was enhanced by 29% in EPA highway mode and 18% in city mode compared to the 2012 model year RL (Table 2).

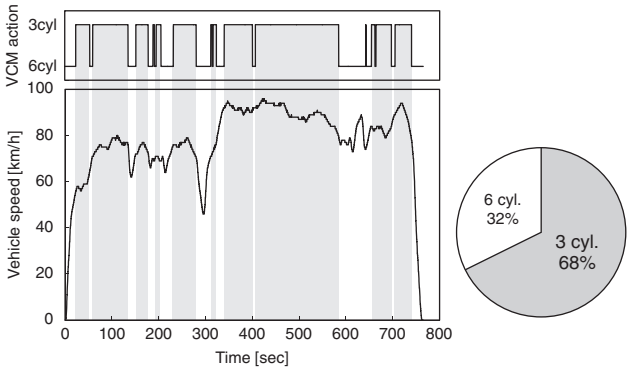


Fig. 23 VCM action of EPA highway mode

8. Conclusion

The new V6 3.5 L engine enhances combustion and pumping loss with the DI VTEC VCM system, adopts friction reduction technology and VCM applied technology, and has a downsized displacement. This produced the following results.

(1) The maximum output was increased by 3.3% and torque characteristics equal to those of the previous model were also obtained, while downsizing the displacement.
(2) Fuel consumption was enhanced by 5% during 6-cylinder drive and 20% during 3-cylinder drive compared to the conventional engine. In addition, the fuel economy of an actual vehicle was enhanced by 29% in EPA highway mode and 18% in city mode.
(3) Expansion of the ACM capacity enhanced NV performance during 3-cylinder drive while at the same time expanding the 3-cylinder drive torque range.

References

(1) Noguchi, K., Fujiwara, M., Segawa, M., Sawamura, K., Suzuki, S.: Development of V6 i-VTEC Engine with Variable Cylinder Management, Honda R&D Technical Review, Vol. 16, No. 1, p. 85-92
(2) Okui, S., Kishi, T., Ishikawa, N., Hanada, K.: Development of 3-state i-VTEC VCM Engine for CIVIC Hybrid, Honda R&D Technical Review, Vol. 18, No. 2, p. 44-51
(3) Matsuoka, H., Mikasa, T., Nemoto, H.: Development of Active Control Engine Mount, Honda R&D Technical Review, Vol. 15, No. 2, p. 209-214

■ Author ■


Nobuo SUZUKI


Yasutaka HAYASHI


Kazuya ISHIKI


Atsushi SATO


Tatsuhito ESAKI


Satoshi WATANABE

Development of New 2.4 L Direct-Injection Gasoline Engine

Yasuhiro MOTOHASHI* Kenji KUBOTA* Nobuyuki AKAISHI*
Kazuya ISHIKI* Takashi IWAMOTO* Masakazu KINOSHITA*

ABSTRACT

A new 2.4 L i-VTEC 4-cylinder direct injection gasoline engine reconciling low CO_2 emissions performance with high power has been developed as part of a next-generation Honda engine series. The new engine employs a direct injection system provided with a high-pressure multi-hole injector positioned between the inlet valves. The inlet head port, combustion chamber shape, injector spray, and fuel injection control were optimized in order to realize homogeneous air-fuel mixture formation and enhanced combustion. Together with the reduction of friction through the modification of the engine framework, these innovations made it possible to realize a 4% increase in maximum power, a 12% increase in maximum torque, and a 5% or more increase in unit fuel efficiency. The use of this engine in the 2013 model year Accord, together with the employment of a high-efficiency CVT and modification of the vehicle body, has made it possible to realize an 11% increase in the EPA fuel economy label value and an emissions level corresponding to the LEV II SULEV level in the California Air Resources Board regulations. In addition, the use of a new engine framework that was reduced in weight while realizing stiffness in the areas necessary for noise and vibration performance made it possible to balance weight savings with the realization of an equivalent or higher level of noise and vibration performance than the previous engine.

1. Introduction

As concern over the protection of the environment increases, in the field of engine development attention is being focused on environmental performance technologies, as exemplified by the realization of increased fuel efficiency and reduced exhaust emissions, as an important agenda. At the same time, the driving pleasure offered by vehicles is also viewed as an important factor, and the development of groundbreaking technologies that reconcile dynamic performance with environmental performance is being pushed ahead. Honda has developed a K24 2.4 L 4-cylinder i-VTEC direct injection engine as a new 4-cylinder 2.4 L-class engine. The new engine adds in-cylinder direct injection ("direct injection" below) to the existing i-VTEC mechanism[(1)-(4)] in order to realize increased fuel efficiency, reduced exhaust emissions, and high power. This paper will discuss the new technologies employed in the new engine and its achieved performance.

2. Development Goals

Based on Honda's concept of EARTH DREAMS TECHNOLOGY, revolutionary next-generation technologies that seek to balance further contribution to the realization of a low-carbon society with driving pleasure, the following targets were set for the development of the new engine in an attempt to reconcile environmental performance in the form of increased fuel efficiency and reduced emissions with dynamic performance offering driving pleasure:

(1) Dynamic low- and mid-speed torque to realize driving pleasure in the standard driving range
(2) Top-class fuel economy
(3) Emissions level satisfying the LEV II SULEV standard
(4) A balance between increased quietness and reduced weight

3. Overview of Engine and Applied Technologies

Figure 1 shows an external view of the engine, and Table 1 shows the main specifications of the new engine and a conventional 2.4 L engine. The core engine technology adopted in order to realize the development goals was in-cylinder direct injection, in an attempt to reconcile power performance with environmental performance by increasing charging efficiency and thermal efficiency against conventional port injection.

* Automobile R&D Center

Table 1 Engine specifications

Item	Developed	Previous
Engine code	K24W	K24Z
Cylinder configuration	In-line 4-cylinder	In-line 4-cylinder
Bore × Stroke (mm)	87 × 99.1	87 × 99
Displacement (cm^3)	2356	2354
Compression ratio	11.1	10.5
Valve train	DOHC i-VTEC 16-valve	DOHC i-VTEC 16-valve
Valve diameter (mm) IN/EX	36/30	36/31
Cylinder offset (mm)	8	0
Fuel injection	Direct injection	Port injection
Fuel	Regular	Regular
Max. power (kW/rpm)	138/6400	132/6500
Max. torque (Nm/rpm)	245/3900	218/4300

Changes to the structure of the engine framework made it possible to realize an equivalent or higher level of noise and vibration performance than a conventional engine while reducing weight and increasing compactness. In the main drive system, the oil supply mechanism for the crank pin was increased in efficiency and friction reduction technologies were applied. The cylinder head was integrated with the exhaust manifold in order to reduce exhaust emissions and increase compactness. The modification of the configuration of the valvetrain mechanism reduced the valve angle despite the use of a conventional i-VTEC mechanism, and increased the compactness of the combustion chamber (Fig. 2), thus increasing the specific surface area of the combustion chamber, resulting in increased combustion efficiency. The shapes of the inlet head port and the combustion chamber were changed to realize the high level of flow motion necessary for homogeneous mixture formation. In the cam valve system drive mechanism, the positioning of a high-pressure pump drive cam for direct injection at the end of the exhaust cam and the use of a new chain tensioner mechanism have increased the reliability of the chain and reduced friction.



Fig. 1 K24W i-VTEC direct-injection engine

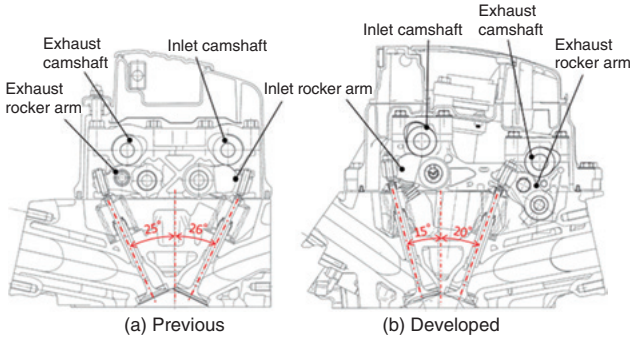


Fig. 2 Configuration of valvetrain and combustion chamber

4. Direct Injection System

4.1. Overview of Direct Injection System

Figure 3 shows an overview of the direct injection fuel supply system. In addition to realizing increased performance levels by means of high-pressure multi-stage fuel injection, this high-pressure fuel injection system was developed with consideration of sharing components with a V6 3.5 L engine, the present engine being the first in a series development. A compact packaging with the same ease of vehicle fitting as the port injection system used in the conventional system was realized.

A six-hole multi-hole injector was positioned between two inlet valves, and the form of the spray was optimized for stronger tumble motion, realizing stable combustion with minimal cycle fluctuation due to the formation of a homogeneous air-fuel mixture.

A high-pressure plunger pump able to pressurize the fuel to a maximum of 20 MPa was positioned at the end of the exhaust-side camshaft using a roller tappet. The use of optimum settings for four cam profiles and the realization of high-accuracy control have made it possible to realize fuel pressure control with high flexibility and good injector fuel spray performance. The optimization of the orifices in the fuel pipes has enabled the system to follow changes in fuel pressure during transient operation, helping to realize high-accuracy air-fuel ratio (A/F) control.

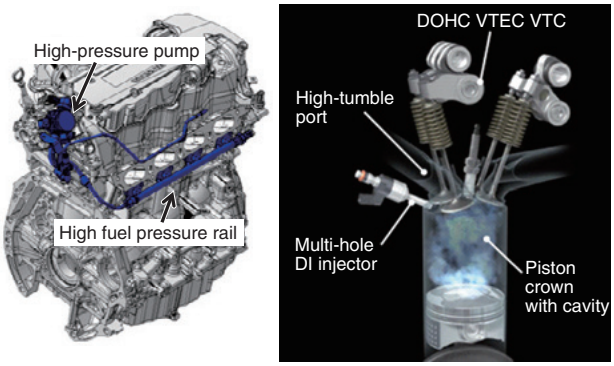


Fig. 3 High fuel pressure direct-injection system

4.2. Direct Injection Combustion Technologies

The concept established in order to achieve the goal of a balance between environmental performance and power established for the new engine was to realize stoichiometric combustion by means of homogeneous air-fuel mixture formation, with a focus on increasing charging efficiency, reducing knock and reducing exhaust emissions by means of direct injection. The high-flow motion inlet head port, multi-hole injector, and high-pressure fuel system were the core elements in the realization of homogeneous air-fuel mixture formation. Performance was improved and stable combustion was realized through the application of split injection, in order to enhance combustion and reduce soot emissions, and the realization of homogeneous mixture formation by means of more precise fuel injection control.

4.2.1. High-flow motion inlet head port

In order to realize homogeneous air-fuel mixture formation when using direct injection, it is necessary to increase the level of flow motion in the cylinders, but this reduces the relative flow rate coefficient, leading to the issue of balancing stronger flow motion with the high flow rate necessary for the realization of high power in a naturally aspirated engine. In order to balance these antagonistic performance elements, maximal use was made of the VTEC mechanism to optimize the balance between tumble and the flow rate coefficient in each cam lift range in order to satisfy the differing performance targets for each engine speed range. In concrete terms, the development aimed at a balance between a high tumble characteristic in the VTEC low-speed cam lift range, in order to realize a high level of flow motion in the low engine speed range, in which the flow energy of the intake air is low, and the high flow rate necessary to the realization of high power in the VTEC high-speed cam lift range. In order to attain this goal, in addition to modifying the shape of the inlet head port, a shroud was added to the combustion chamber. Figure 4 shows the shape of the combustion chamber with its shroud, while Fig. 5 shows the change in flow around an inlet valve produced by the shroud.

The shroud is formed on the outer circumference of the combustion chamber inlet valves, and controls the flow approaching the inlet-side sleeve. This makes the flow on the spark plug side the dominant flow, strengthening tumble mainly during low to medium lift, as shown in Fig. 6, thus realizing a high level of flow motion in the VTEC low-speed cam range. As Fig. 7 shows, because the effect of the shroud is minimal in the high lift range, and does not produce a decline in the flow rate coefficient, it is possible to realize a high flow rate coefficient in the VTEC high-speed cam range. In addition, tumble in the high lift range has been enhanced through the use of an inlet head port shape that significantly curbs the reduction in the flow rate coefficient, making it possible to realize, in collaboration with VTEC, a high level of flow motion across the entire range and the high flow rate coefficient necessary for high power. Figure 8 shows the tumble ratio produced by the inlet head port shape and the addition of the shroud wall and its effect on the flow rate coefficient. The enhancement of tumble by means of modification of the shape of the inlet head port normally involves a tradeoff, resulting as it does in a decline in the flow rate coefficient. The use of the shroud, however, has made it possible to balance both parameters in relation to the correlation line for the tradeoff between them.

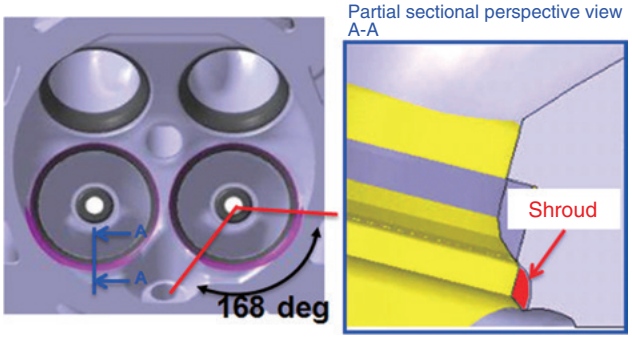


Fig. 4 Combustion chamber shape with shroud

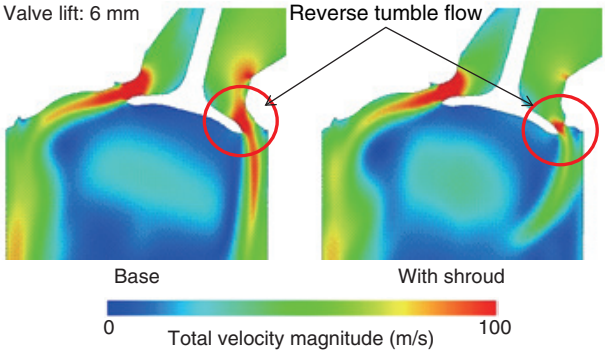


Fig. 5 Influence of shroud on air flow around inlet valve

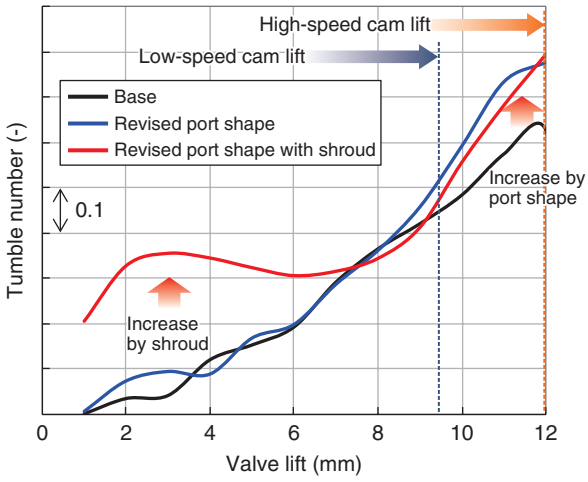


Fig. 6 Tumble flow intensity characteristics

4.2.2. Spray characteristic of direct injection injector

A six-hole multi-hole injector was employed as the direct injection injector. The spray characteristics of the injector were optimized. The position of the injector holes has a significant effect on formation of a homogeneous air-fuel mixture, in-cylinder flow motion and on the wetting of the cylinder walls. It was therefore necessary to attempt to realize a spray characteristic optimized for the strong in-cylinder flow motion achieved via the modification of the inlet head port. In selecting the injector spray characteristics, in addition to basic performance parameters such as power and fuel efficiency, combustion stability at low temperatures, soot production, and oil dilution were also taken into consideration as issues for direct injection. The spray characteristic was optimized on this basis using CFD and engine tests. Figure 9 shows the spray patterns employed in the study. Studies were conducted on Pattern A, designed for a high level of diffusion; Pattern B, designed to achieve a high level of flow motion via the effect of the spray in assisting flow motion; and Pattern C, designed to reduce wetting of the sleeve.

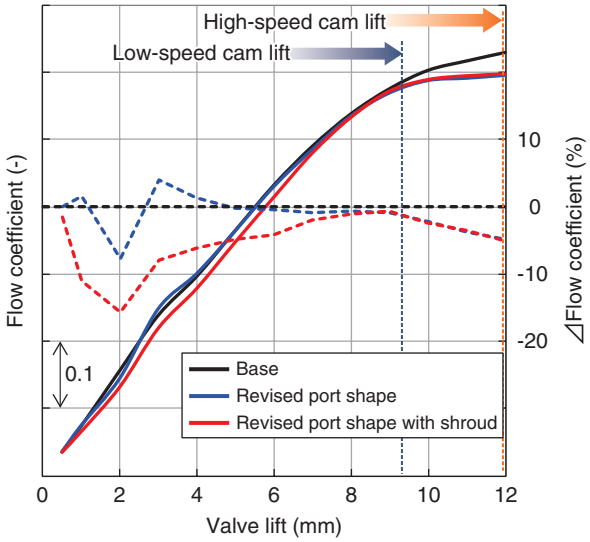


Fig. 7 Flow coefficient characteristics

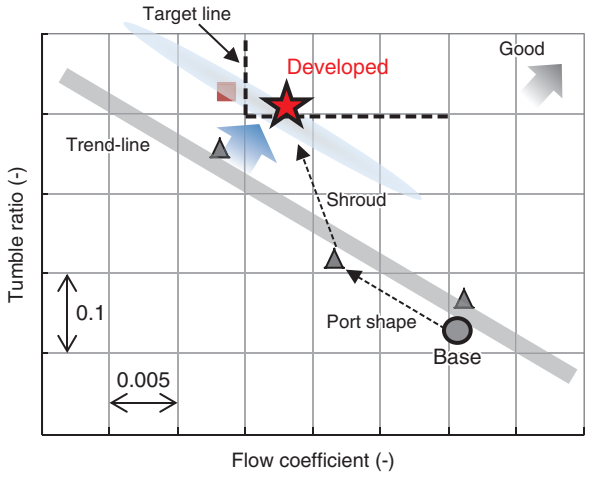


Fig. 8 Relationship of flow coefficient and tumble ratio

Table 2 Test results for difference in injector spray position

	Pattern A	Pattern B		Pattern C	
WOT power	Base	+	1% Increase		Equivalent
BSFC	Base		Equivalent		Equivalent
Combustion stability	Base	+	Better		Equivalent
Exhaust soot	Base		Equivalent	-	Increase
Oil dilution	Base	+	3% Reduction	+	2% Reduction

Figure 10 shows CFD results for the three injector configurations for (a) tumble ratio, (b) homogeneousness of air-fuel mixture, and (c) amount of wetting of the sleeve and pistons. Table 2 shows an overview of representative test results. A variety of changes, for example in combustion,

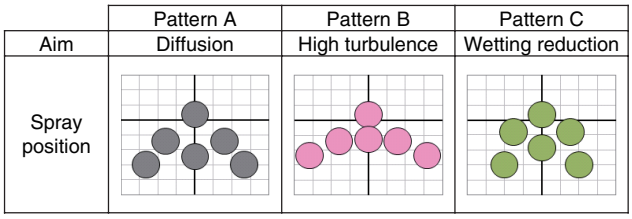


Fig. 9 Injector spray position

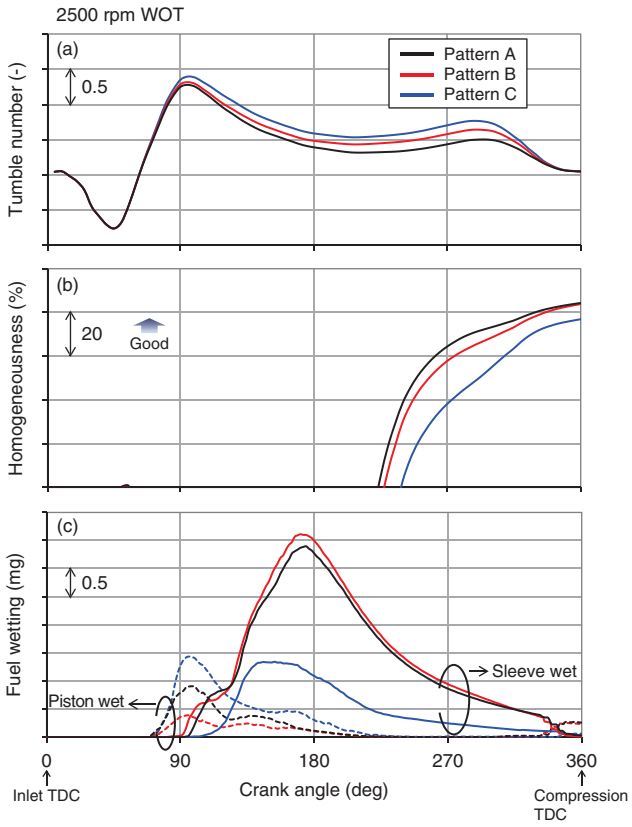


Fig. 10 CFD results for difference in injector spray position

were observed in both the CFD and engine test results. In comparison to Pattern A, Pattern B increased power at WOT due to an increased tumble ratio, and an increase in combustion stability was observed. While an increase in the tumble ratio was observed for Pattern C, no increase in power or change in combustion were obtained due to a decline in the homogeneousness of the air-fuel mixture, thought to be due to concentration of the spray in the center. An increase in soot production due to increased wetting of the pistons was also observed. Oil dilution was reduced for both Patterns B and C, but wetting of the sleeve increased in CFD results for Pattern B, and a correlation could therefore not be observed. The positions in which wetting of the sleeve occurred were isolated. Figure 11 shows results of wetting of the sleeve on the inlet and exhaust sides at bottom dead center during the inlet stroke and for oil dilution in the actual engine. A correlation can be observed between results for the amount of wetting of the sleeve on the inlet side and for oil dilution in the engine. This is thought to be because the temperature of the sleeve on the inlet side is low and there is little evaporation following wetting, and this tends to contribute to dilution. Based on the results discussed above, Pattern B was selected as the configuration of holes producing the optimum spray for the engine in development.

4.2.3. Direct fuel injection timing and injection pressure control

A number of methods of maximally realizing the merits of direct injection – greater freedom in injection timing, and the achievement of increased power and fuel efficiency through the use of multi-stage fuel injection – are available, including reducing the injection period by increasing fuel pressure and setting maximum and minimum injection amounts by increasing the range of fuel pressure control. A system using high fuel pressure and with a wide fuel pressure control range was therefore applied in the new engine. The range of fuel pressure control in the engine is 3.5 MPa to a maximum of 20 MPa, and cooperative control is applied to optimize injection timing and the number of injections in response to operating conditions including engine speed and engine load. CFD was used to study the effect of the high-fuel-pressure split injection realized through the optimization of fuel pressure and injection timing. Figure 12 shows changes in (a) the kinetic energy of turbulence in the cylinder, (b) A/F close to the spark plug, and (c) the homogeneousness of the air-fuel mixture in the cylinder. With the use of split injection, in-cylinder flow motion has been strengthened by the second injection at the commencement of the compression stroke, and increased stability of A/F close to the spark plug and increased homogeneousness of the mixture can be observed.

To maximize the effects of split injection, the fuel injection pressure, the timing of the first and second injections, and the ratio of splitting were optimized. Figure 13 shows the results of tests of optimized split injection in an actual engine. For a single injection, advancing the injection timing tends to increase combustion stability, but an increase in soot production due to increased wetting of the pistons becomes an issue, necessitating the use of high-accuracy injection timing settings. In the case of high-fuel-pressure split injection, robustness in relation to

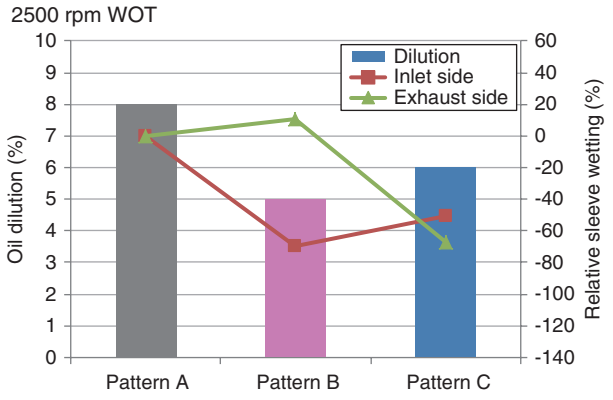


Fig. 11 Fuel wetting and oil dilution

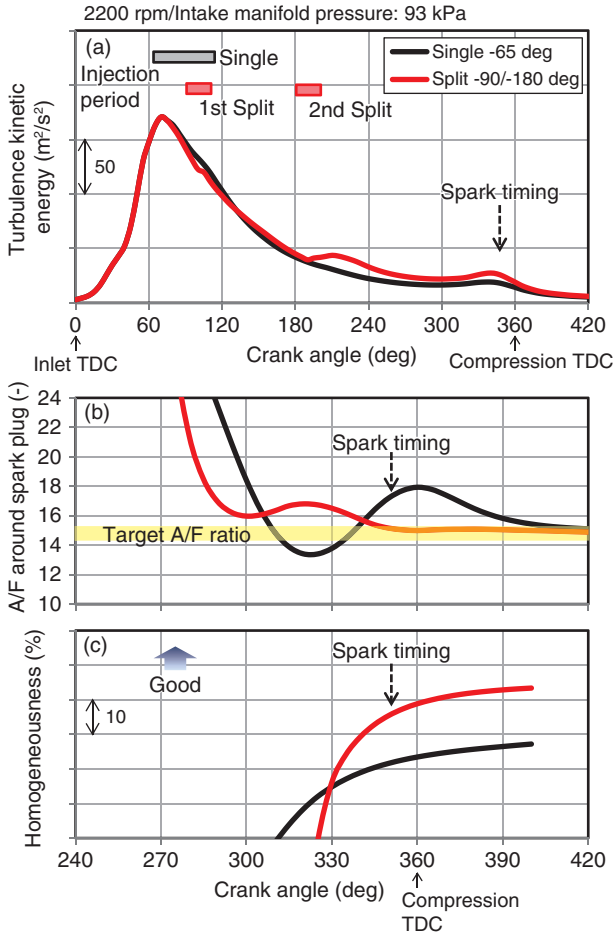


Fig. 12 CFD results for differences in injection control

soot production is increased, making it possible to increase combustion stability without increasing soot emissions. Flexibility in injection timing settings is also increased. These factors, in combination with the realization of increased combustion speed, have resulted in a reduction of more than 1% in fuel consumption (BSFC).

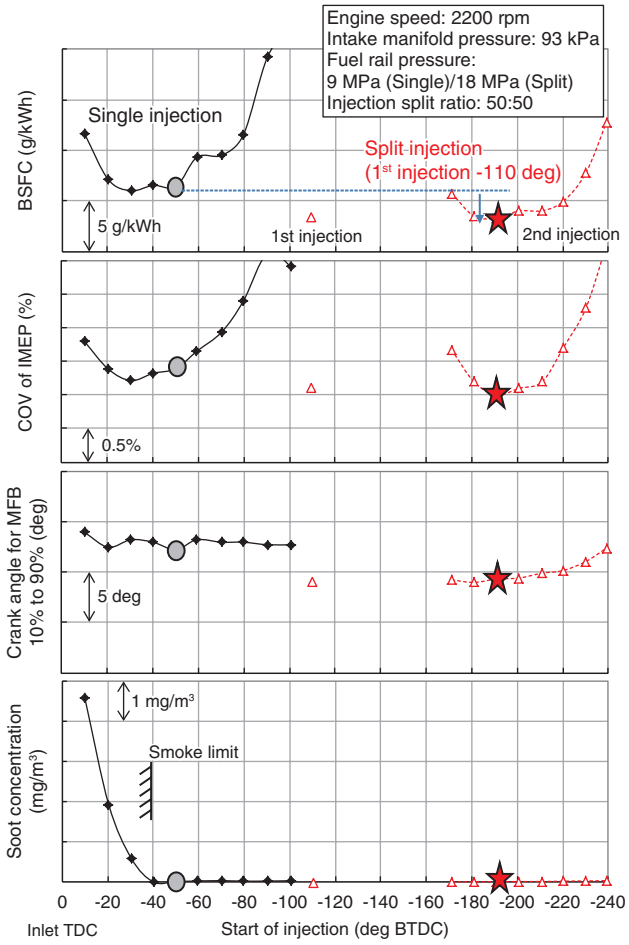


Fig. 13 Effect of fuel pressure and injection timing control

5. Technologies for Increased Power

Development of the new engine aimed towards the realization of a power characteristic in which low- to mid-speed torque was increased in order to boost dynamic performance in the standard operating range. The technologies employed to increase power are discussed in this section. In the direct injection system, in addition to an inlet head port designed to realize both a high level of in-cylinder flow motion and a high flow rate coefficient, high power was realized by increasing charging efficiency and reducing knock through optimization of the injector spray and injection control. Figure 14 shows the increase in power realized through the use of direct injection.

Figure 15 compares the power characteristics of the developed engine and the previous engine. The developed engine increases low-speed torque by 10% or more, maximum torque by 12%, and maximum power by 4% against the previous engine due to the application of the direct injection system discussed above and the following technologies designed to increase power:

(1) Use of an intake manifold with a built-in resonator to increase low- to mid-speed torque
(2) Realization of increased inlet and exhaust efficiency through the shape of the inlet head port, the integration of the exhaust manifold with the cylinder head, and the optimization of valve timing
(3) Reduction of knock through the use of a high-flow-motion port, increased compactness in the combustion chamber, and modification of the cooling system
(4) Friction reduction technologies

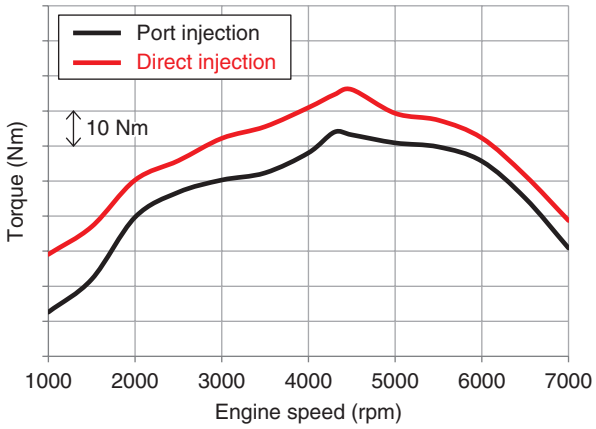


Fig. 14 Effect of direct injection

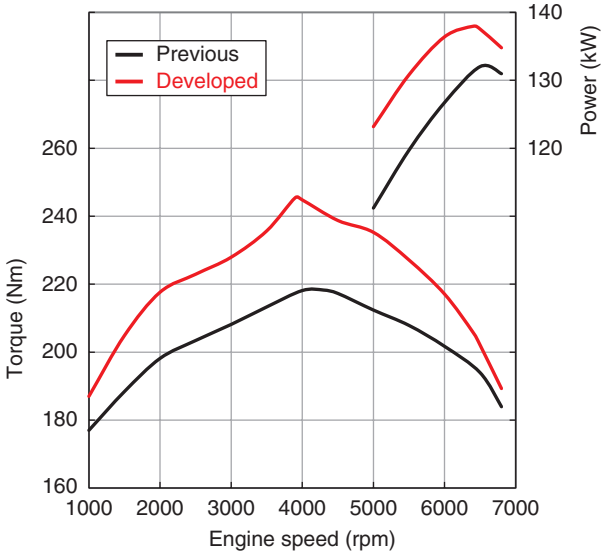


Fig. 15 Engine performance

6. Technologies for Increased Fuel Efficiency

6.1. Friction Reduction Technologies

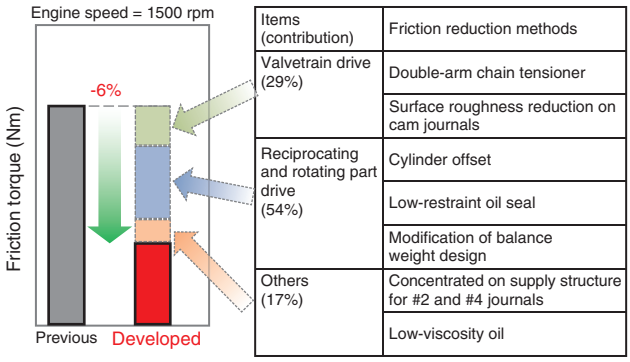
As Fig. 16 shows, the following technologies were applied to reduce friction by means of modification of the basic framework: the application of a double-arm chain tensioner, reduction of the surface roughness of the cam journals, optimized cylinder offset, the use of low-restraint oil seals, modification of the shape of the balance weight, the use of a concentrated supply configuration for journals #2 and #4, and the use of low-viscosity oil. The use of these friction reduction technologies has reduced friction by 6% against the previous engine.

6.2. Unit Fuel Consumption

Figure 17 shows BSFC characteristics at an engine speed of 1500 rpm. As a result of the application of the friction reduction technologies discussed above and the increased combustion efficiency achieved by means of direct injection, in addition to the optimization of split direct injection control in the high-load range, unit fuel consumption has been reduced by 5% or more against the previous engine.

6.3. Fuel Efficiency in an Actual Vehicle

The use of a new CVT made it possible to reduce engine speed while driving and freely set engine speed. Powertrain control was optimized with consideration of the enhanced torque characteristic achieved by means of direct injection, the BSFC characteristic, and the transmission efficiency of the transmission. As Fig. 18 shows, it was possible to reduce engine speed against the previous AT model in LA4 mode, increasing fuel efficiency. In addition to the increased fuel efficiency achieved by means of these innovations in the powertrain, the application of a number of measures including enhancing the aerodynamics of the vehicle body, reducing weight, and reducing rolling resistance has made it possible for the developed engine to increase EPA fuel efficiency by 11% against the previous engine, realizing the top-class fuel economy of 30 mpg.



Items (contribution)	Friction reduction methods
Valvetrain drive (29%)	Double-arm chain tensioner
	Surface roughness reduction on cam journals
Reciprocating and rotating part drive (54%)	Cylinder offset
	Low-restraint oil seal
	Modification of balance weight design
Others (17%)	Concentrated on supply structure for #2 and #4 journals
	Low-viscosity oil

Fig. 16 Friction reduction technologies

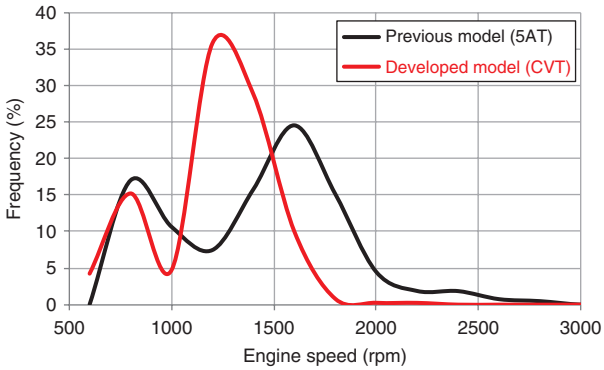


Fig. 18 Engine speed frequency in LA4 mode

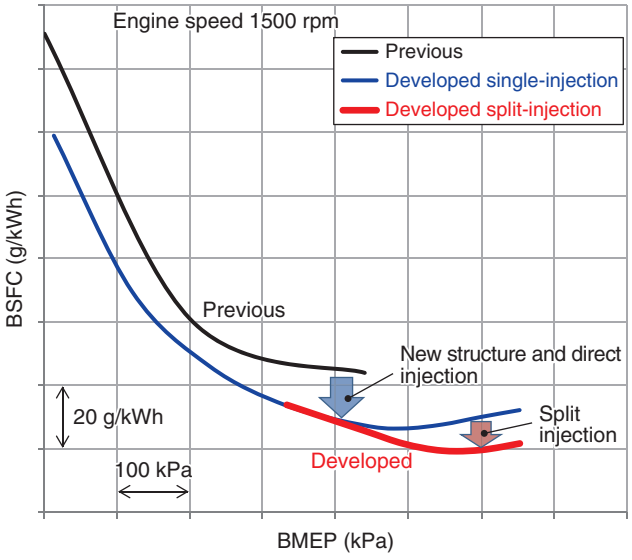


Fig. 17 BSFC characteristic

7. Technologies to Reduce Exhaust Emissions

7.1. Overview of Technologies to Reduce Exhaust Emissions

In order to conform to the SULEV category of the US LEV II regulations, one of the world's most stringent exhaust emissions standards, the following technologies were applied in the new engine in an attempt to reduce feed-gas emissions and increase the efficiency of exhaust gas after-treatment:

- Reduction of feed-gas emissions through optimization of direct injection combustion and modification of combustion chamber
- Enhancement of catalyst purification efficiency through modification of exhaust gas flow
- Use of a new catalyst balancing low cost and high performance

7.2. Enhancement of Exhaust Gas Flow

In order to make maximal use of the purification efficiency of the catalyst while controlling catalyst degradation, it is necessary to introduce the exhaust gas to the catalyst in a uniform manner. The shape of the front cone is important in realizing this goal. The use of front exhaust rather than the rear exhaust employed in the previous engine increased the flexibility of design of the front cone, making it possible to introduce a more uniform exhaust gas flow to the close-coupled catalyst, as shown in Fig. 19. It was also possible to install the Universal Exhaust Gas Oxygen sensor in the optimal position, helping to enable the realization of more accurate A/F control.

7.3. Low-precious-metal Catalyst

Reduction of the amount of precious metals used in the catalyst, in particular rhodium (Rh), which is produced in only extremely small quantities, was studied in order to contribute to the preservation of global environment and resources. Rh displays good performance in the purification of exhaust gas. Substitution of palladium (Pd), which increases the speed of absorption and desorption of oxygen, for part of the Rh in the newly developed catalyst made it possible to reduce the amount of precious metals, and particularly Rh, in the catalyst overall. Figure 20 shows a comparison of the amount of precious metals used and emissions performance for the previous and the newly developed catalysts. Despite the fact that it uses 22% less precious metals and 50% less Rh than the previous catalyst, the new catalyst achieves a higher level of purification performance. This has made it possible to conform to the SULEV category of the US-LEVII regulations while using a reduced amount of precious metals and Rh than the previous catalyst.

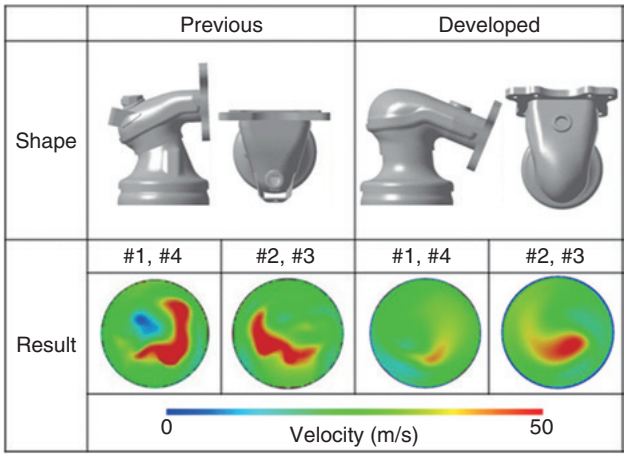


Fig. 19 Front gas feed distribution

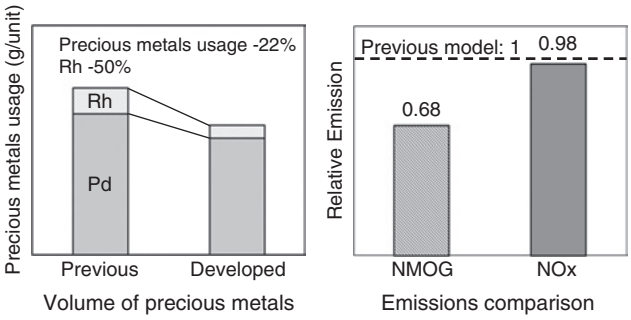


Fig. 20 Comparisons of volume of precious metals and emissions

8. Technologies for Reduction of Noise and Vibration

A transfer path analysis using principal component regression (PCR-TPA)[5, 6], a technique used to analyze phenomena such as cabin noise during acceleration, was applied to the new engine in an attempt to balance NV performance with weight savings. The transfer paths for engine vibration produced by combustion excitation force can be broadly divided into three:

(1) A transfer path from the combustion chamber directly to the cylinder head.
(2) A transfer path to the cylinder block, via the pistons.
(3) A transfer path to the lower block integrated with the crank bearings and surface of the outer wall, via the crankshaft.

Cylinder head vibration, cylinder block vibration, crank bearing vibration, and engine vibration at the engine mounts were measured simultaneously and a PCR-TPA was conducted. Figure 21 shows the analysis results for the ratio of contribution to transfer. The results of the analysis showed that the ratio of contribution of the areas around the crank bearings to the transfer of vibration to the engine mounts was high, while other parts displayed a low contribution.

Based on these results, the same lower block configuration integrated with the crank bearings and the exterior wall by means of the rudder frame employed in the previous engine was used in the new engine to help ensure stiffness around the bearings. In addition,

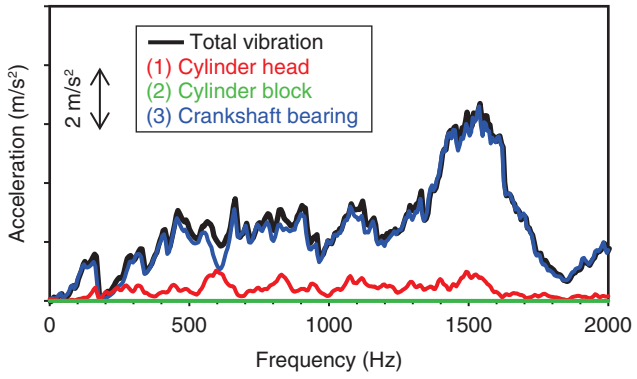


Fig. 21 Effect on PCR-TPA vibration transfer

as shown in Fig. 22, the weight of the cylinder block, which displayed a low contribution to the transfer of vibration, was reduced by 10%. Figure 23 shows the positioning of maximum power and the reduction of weight of the cylinder block in the developed engine against the previous engine. The realization of a balance between high stiffness and reduced weight, as described above, made it possible to achieve noise and vibration performance equal to or higher than the previous engine (Fig. 24), while reducing the weight of the engine framework by 6%.

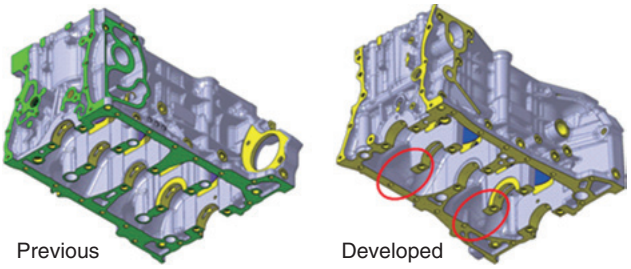


Fig. 22 Cylinder block weight reduction

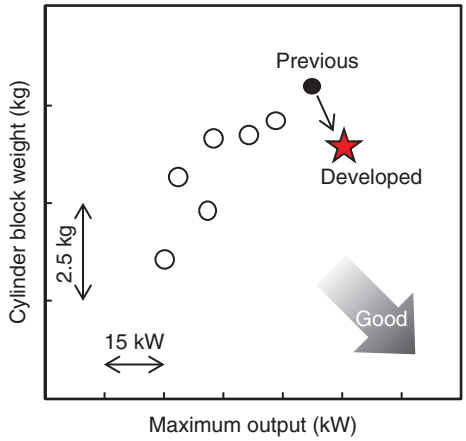


Fig. 23 Cylinder block weight and maximum output

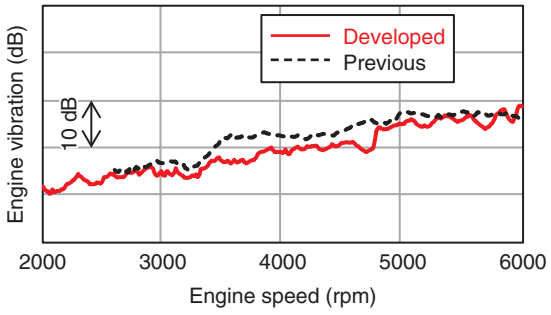


Fig. 24 Vibration level at end of engine mount bracket under full load

9. Conclusion

In the development process of a new 4-cylinder 2.4 L direct injection engine, CFD was employed to study the specifications of direct injection combustion technologies, resulting in the realization of enhanced combustion by means of optimization of the inlet head port, combustion chamber shape, the injector spray, and injection control. In addition to direct injection combustion technologies, the use of a new framework made it possible to employ friction reduction technologies and emissions reduction technologies, producing the following results:

(1) The new engine has achieved a 10% increase in low-speed torque, a 12% increase in maximum torque, a 4% increase in maximum power, and a 5% increase in unit fuel efficiency against the previous engine.

(2) The reduction of engine speed with the use of a CVT and the optimization of the engine operating line, in addition to the enhancement of unit fuel efficiency, helped to enable the achievement of a EPA top-class fuel economy of 30 mpg.

(3) The reduction of feed gas emissions and the optimization of the exhaust system in the new engine made it possible to realize US LEV II SULEV-level emissions performance.

(4) In line with modification of the engine framework, a high level of stiffness was efficiently realized in combination with a reduction in weight by means of analysis of contribution to vibration transfer, with the result that the engine was increased in compactness and reduced in weight by 6% against the previous engine while realizing an equivalent or higher level of noise and vibration performance.

References

(1) Niizato, T., Hayashi, A.: Development of New 2.0L Lean-burn Engine, Honda R&D Technical Review, Vol. 12, No. 2, p. 45-54

(2) Seko, K., Taga, W., Torii, K., Nakamura, S., Akima, K., Sekiya, N.: Development of 1.8L i-VTEC Gasoline Engine for 2006 Model year Honda CIVIC, Honda R&D Technical Review, Vol. 18, No. 1, p. 8-15

(3) Kohda, Y., Suganami, T., Kobayashi, H., Ogawa, K.: Development of High-performance and Low-emission Direct Injection Gasoline Engine, Honda R&D Technical Review, Vol. 16, No. 1, p. 39-46

(4) Kawaguchi, R., Yamamoto, K., Kayaba, T., Kojima, S., Shinkai, T., Asame, K.: Development of 2.4 L i-VTEC Gasoline Engine for 2008 Model Year ACCORD, Honda R&D Technical Review, Vol. 20, No. 1, p. 27-34

(5) Sakamoto, A., Ozaki, M.: Interior Sound Enhancement of Vehicle Acceleration for New Model ACCORD - Transfer Path Analysis Using Principal Component Regression Method -, Honda R&D Technical Review, Vol. 19, No. 2, p. 67-71

(6) Noumura, K., Yoshida, J.: Method of Transfer Path Analysis for Interior Vehicle Sound Using Principal Component Regression Method, Honda R&D Technical Review, Vol. 18, No. 1, p. 136-141

■ Author ■


Yasuhiro MOTOHASHI


Kenji KUBOTA


Nobuyuki AKAISHI


Kazuya ISHIKI


Takashi IWAMOTO


Masakazu KINOSHITA

Development of New 2.0 L Gasoline Engine for Accord Hybrid

Akiyuki YONEKAWA* Osamu WATANABE*
Noritaka SEKIYA* Naohiro ISHIKAWA*

ABSTRACT

We developed a new 2.0 L gasoline engine for an Accord hybrid. This engine achieved remarkable fuel efficiency, and complied with the SULEV20 regulation for the first time in the world for an Accord plug-in hybrid in North America. The mechanical compression ratio was set to 13 and improvement in thermal efficiency was aimed at by adopting the Atkinson cycle and cooled EGR. Applying a VTEC system to the intake valve-train, we set up the output cam and the fuel economy cam. The output cam has narrow duration and is used as needed at the time of starting and high-output. The fuel economy cam has wide duration and is used during normal driving. By controlling air-intake closed-valve timing in combination with VTC, the fuel economy cam can acquire the maximum effect of the Atkinson cycle. The minimum specific fuel consumption attained was 214 g/kWh, equaling a 10% improvement in fuel consumption compared to the mass-production 2.0 L engine.

Moreover, we also aggressively tackled engine weight saving. A lightweight forged crankshaft was adopted, and the piston design was optimized, and lightweight press-type rocker arms were applied to the exhaust valve-train. As a result, the newly developed DOHC engine attained 4.7% weight savings over the mass-production 2.0 L SOHC engine.

1. Introduction

In the evolution of global motorization, providing products that are considerate of the environment is a responsibility of automobile companies. Each manufacturer performs various approaches for reduction of the CO_2 discharged from a car, such as fuel cell electric vehicles (FCV), electric vehicles (EV), hybrid electric vehicles (HEV), and the use of downsized turbocharged engines. Honda has been selling HEV that have Integrated Motor Assist (IMA) systems. This system has the advantages of being simple, compact and lightweight, and suitable for small cars. At the end of 2012, Honda announced the Accord plug-in hybrid, a vehicle fitted with a new two-motor hybrid system. This system increases motor power, and can be applied in medium-sized vehicles. A new 2.0 L gasoline engine was developed simultaneously in order to improve fuel efficiency[(1)]. This paper will discuss the main technologies employed in the new engine, in addition to weight-saving measures and electric VTC.

2. Development Goals

The following aims were set for the development of an exclusive engine for a hybrid car.

(1) Low fuel consumption: Improved fuel efficiency in the hybrid operating range
(2) Reduced weight: Weight equivalent to or less than a mass-production SOHC 2.0 L engine despite changing to DOHC
(3) Emission performance: Conformity with SULEV 20 standard of the plug-in hybrid (PHEV) specification for the North American market
(4) Quietness: Equivalent NV performance to an upper-mid-class sedan

3. Main Specifications and Performance

3.1. Engine Specifications

Figure 1 shows an external view of the newly developed engine, and Table 1 compares its specifications with those of a mass-production 2.0 L engine. The new engine is DOHC, and has a VTEC system and electric valve timing control (EVTC) on the intake side. For the exhaust side, we adopted press-type rocker arms with Hydraulic Lash Adjusters (HLA). Since it is lightweight, it was possible to set high positive acceleration of the valve lift curve, thus reducing loss in the expansion stroke. A high-tumble port has been employed in order to realize stable EGR combustion, and the intake valves have been increased in diameter by 1 mm in order to make

* Automobile R&D Center

Table 1 Engine specifications

Engine Type	Developed	Current
Cylinder configuration	Inline 4	Inline 4
Bore x Stroke (mm)	81 × 96.7	81 × 96.9
Displacement (cm^3)	1993	1998
Valvetrain (intake)	VTEC and E-VTC	VTEC
Valvetrain (exhaust)	Finger rocker arm (with HLA)	Rocker arm (with rocker shaft)
Number of valves	4	4
Valve diameter (mm) Intake/exhaust	33/26	32/26
Cylinder offset (mm)	6	12
Crank journal diameter (mm)	50	55
Compression ratio	13.0	10.6
EGR system	Cooled	Hot
Water pump	Electric	Mechanical
Fuel injection type	Port injection	Port injection
Fuel	Regular	Regular
Maximum power	105 kW	115 kW
Maximum torque	165 Nm	192 Nm
Emission regulation	SULEV20	EURO5

up the decline in the flow coefficient. The cylinder offset has been modified, and the height of the cylinder block has been reduced in order to reduce weight. The diameter of the crank journal has been reduced in order to reduce friction and weight. The compression ratio was set to 13, and applied the Atkinson cycle and cooled EGR. The use of an electric water pump and the removal of the accessory belt have reduced friction loss. With consideration of a balance between cost and fuel efficiency, a port injection system was chosen.

3.2. Power Performance

Figure 2 shows the power performance of the engine. The engine realizes a maximum power of 105 kW at 6200 rpm and a maximum torque of 165 Nm at 4500 rpm.

3.3. Fuel Consumption Performance

Figure 3 shows the distribution of brake specific fuel consumption (BSFC). The yellow line shows operation in hybrid drive mode, and the area surrounded by the white broken lines is the engine drive mode operation area[2]. The engine achieves a BSFC of 214 g/kWh at an operating point of 2500 rpm/120 Nm. In addition, in comparison of BSFC in equivalent horsepower to a mass-production 2.0 L engine, it increased by 10% across the entire operating range (Fig. 4).

3.4. Emissions Performance

Figure 5 shows the new engine's exhaust system. The engine uses a new control[1] that utilizes the characteristics of the hybrid system in order to efficiently warm up the two catalysts by adjusting the amount of power generated after engine start. Feed emissions are also reduced to a low level through the use of output cams with narrow opening angles at engine start. As a result, the PHEV specification for the North American market is the first vehicle to conform to the SULEV 20 standard (Fig. 6).



Fig. 1 New 2.0 L gasoline engine for Accord Hybrid

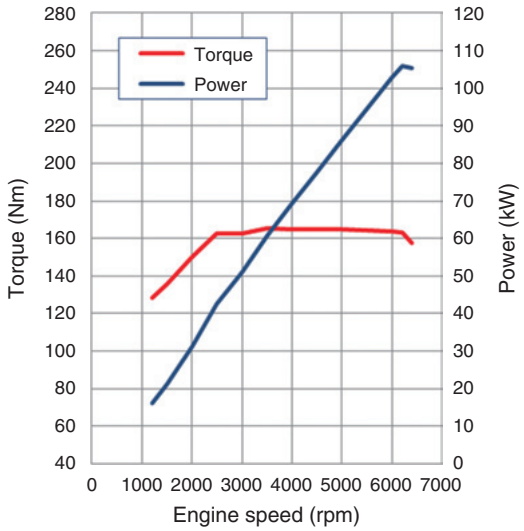


Fig. 2 Engine performance

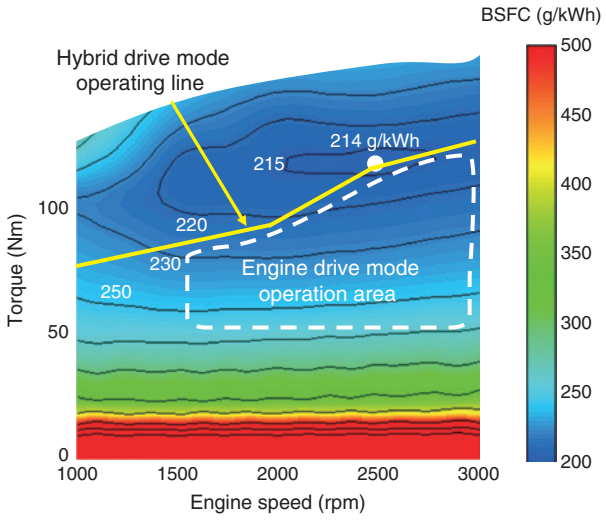


Fig. 3 Fuel consumption performance

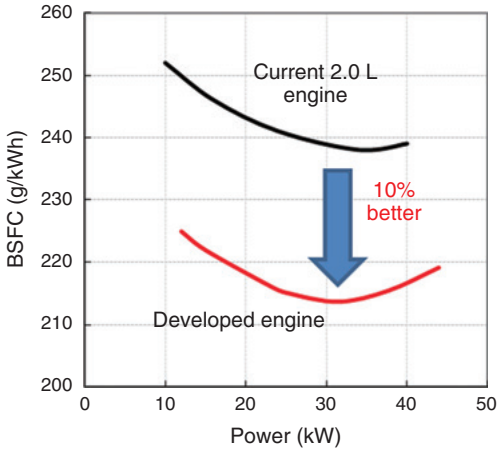


Fig. 4 Improvement of fuel consumption

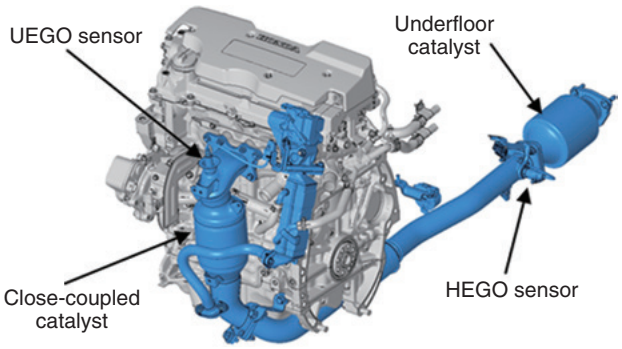


Fig. 5 Exhaust system

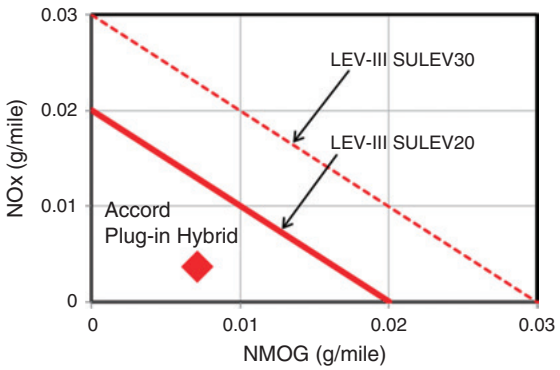


Fig. 6 SULEV20 regulation and emission performance

4. Main Engine Technologies

4.1. VTEC

Figure 7 shows the configuration of the VTEC system used in the intake-side valvetrain. The system uses three cams and three rocker arms for each cylinder. The two cams at the sides (shown as blue) are called output cams, and the center cam (shown as green) is called a fuel economy (FE) cam. When the output cams are in operation, the synchronized pins are not engaged, and the rocker arms act independently. When the FE cams are in operation, the synchronized pins are engaged, and the rocker arms are coupled by the pins. In order to make it possible to switch between output and FE cam operation in the low-speed range, the system uses a form of VTEC in which both the engaged and non-engaged states of the synchronized pins are controlled by oil pressure[3].

Figure 8 shows the valve lift curve when the output cams and the FE cam are in operation, and Fig. 9 shows the operating ranges of the cams. The opening angle of the output cams is narrow, 196° in the 1 mm and higher lift range, and these cams are used at loads close to wide-open throttle and at engine start. The opening angle of the FE cams is wide, 240° in the 1 mm and higher lift range, and these cams are used in operating states where fuel efficiency is demanded.

4.2. Cooled EGR

The high-load range, in which BSFC is low, is the main operating range for engines used in series hybrid vehicles. This makes it expedient to use cooled EGR,

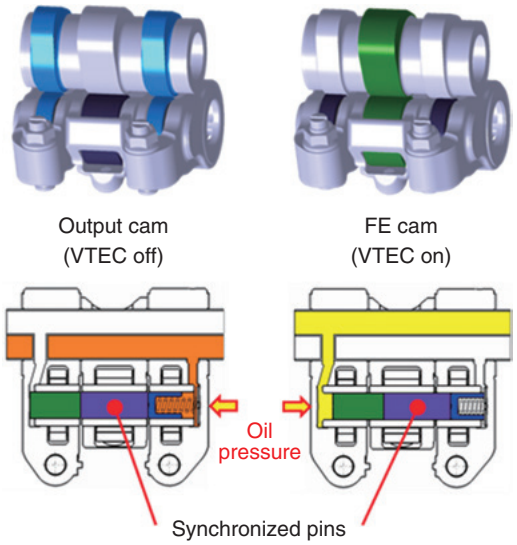


Fig. 7 VTEC structure and pin action

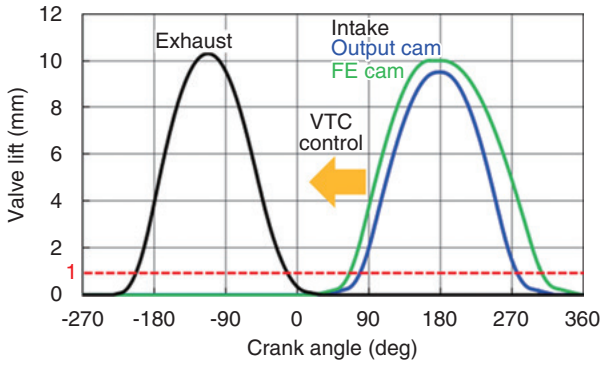


Fig. 8 Valve timing

which makes it possible to reduce knocking, in order to improve fuel efficiency[4]. However, cooled EGR slows down combustion, and can result in a decline in combustion stability. A high-tumble port was used in the new engine in order to increase combustion speed and assist in controlling these effects (Fig. 10). The shape of the side of the port was modified and an edge shape added to the lower section in order to strengthen tumble flow by helping to ensure that the main flow occurred on the exhaust side of the combustion chamber. Figure 11 shows simulation results for the flow in the cylinders. The results show that the flow from between the valves along the wall on the intake side has been reduced. In addition, the edge shape separates the flow, with the result that the main flow flows strongly along the exhaust side, creating a strong tumble flow within the cylinder. As a result, the tumble ratio has increased from 0.73 to 1.40. Figure 12 shows the results of tests to verify the effect of the new port. The increased combustion stability realized by means of the high-tumble port has resulted in reduced covariance in indicated mean effective pressure (IMEP). The innovations applied to the new port have helped to achieve a 5 g/kWh reduction in indicated specific fuel consumption (ISFC).

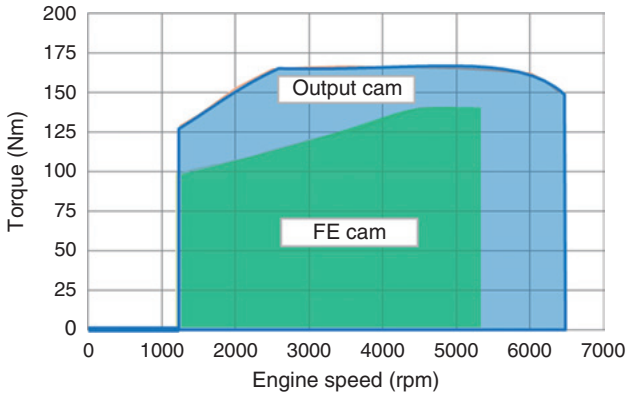


Fig. 9 VTEC operation

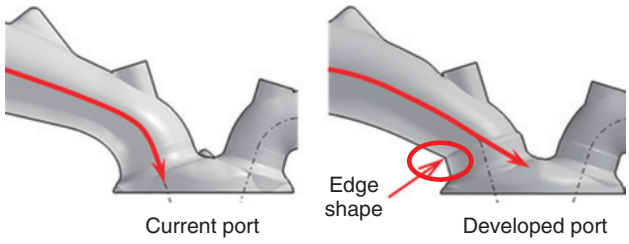


Fig. 10 High-tumble port shape

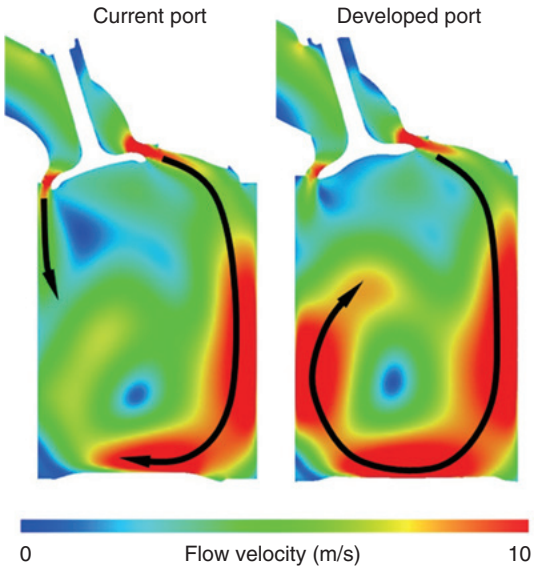


Fig. 11 Flow simulation result

4.3. Weight Reduction Technologies

The reduction of weight is also an important element in increasing automotive fuel efficiency. Hybrid vehicles are fitted with heavy batteries, increasing the importance of reducing weight in other areas. The reduction of weight was therefore also focused on in the development of the new engine.

4.3.1. Crankshaft

As Fig. 13 shows, an extra angled forging process has been applied to the crank counterweights in order to form a dent shape. This is the first time this technology has been applied. This has realized a weight savings of 3.7 kg in combination with the reduction of the journal diameter from 55 mm to 50 mm and the reduction of the number of counterweights from eight to four.

4.3.2. Pistons

Since assistance by a motor can be used in a hybrid car, the output torque required of an engine could be low as that of the same displacement gasoline engine. As a

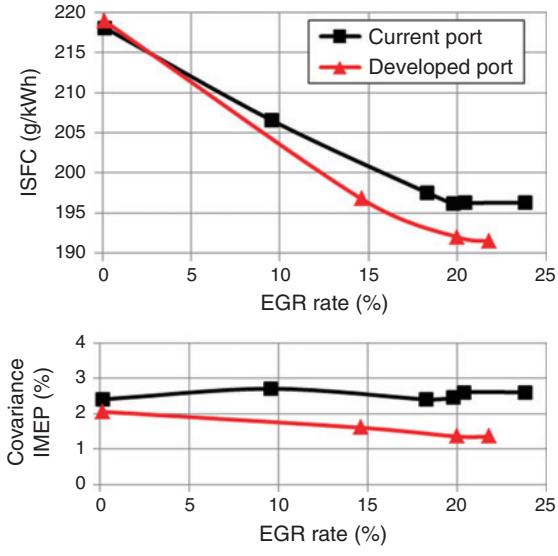


Fig. 12 Effect of high-tumble port

result, the maximum pressure in the cylinders can be set up lower. Pressure has been reduced from 7.9 MPa in the mass-production 2.0 L engine to 5.6 MPa in the developed engine. The compression height and piston pin diameter and length were newly set based on this characteristic, resulting in a weight savings of approximately 61 g per cylinder and 246 g for the entire engine (Fig. 14). The weight savings achieved in this section also contributed to improved fuel efficiency through reduced friction.

4.3.3. Exhaust-side sheet-metal rocker arms

To reduce weight and to assist in maximizing the effect of the Atkinson cycle achieved through lift curve settings, HLA and sheet-metal rocker arms were employed in the exhaust-side valvetrain (Fig. 15). This type of valve train is 1.3 kg lighter than Honda's conventional rocker shaft-type valve train.

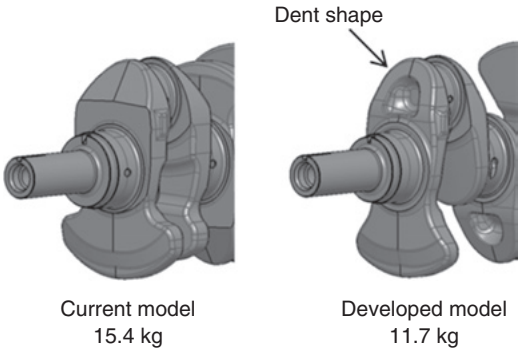


Fig. 13 Crankshaft design

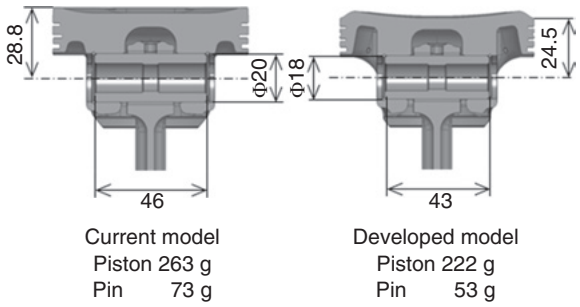


Fig. 14 Piston design

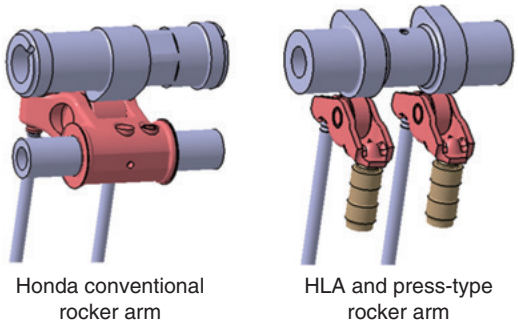


Fig. 15 HLA and rocker arm

4.3.4. Electric water pump

The use of an electric water pump (Fig. 16) has made it possible to do away with the accessory belt, reducing weight by 1.3 kg.

The technologies described above have reduced the weight of the engine by 4.7% against the previous engine, despite changing to DOHC.

4.4. Electric VTC

The developed engine employs idling-stop in order to improve fuel efficiency. However, because the mechanical compression ratio is high at 13, a significant amount of vibration was generated by compression pressure during cranking when the engine is restarted using the output cams, and this had a negative impact on NV performance. Retarding the intake valve close-timing (IVC) at engine start is an effective means of addressing this issue, therefore electric VTC was applied in the new engine. Figure 17 shows the operation and effect of electric VTC.

Figure 17 shows the rise in engine speed at IVC 76 deg (red) and IVC 96 deg (blue). At IVC 76 deg, vibration generated in the resonance range at under 600 rpm continues over 600 rpm. By contrast, at IVC 96 deg, engine speed increases smoothly. This indicates that the cause of the decline in NV performance at engine start is the powertrain torsional mode that occurs under 600 rpm. Modifying the resonance frequency by means of structural measures is too difficult, so the source of the vibration was controlled by means of decompression through retardation of the IVC. Next, the details of the method are described.

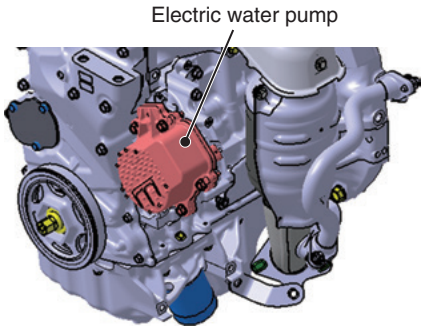


Fig. 16 Electric water pump

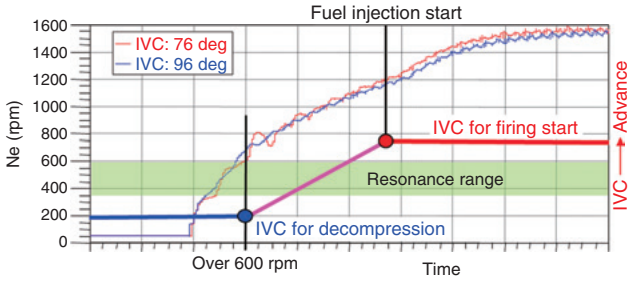


Fig. 17 Effect of electric VTC

When the engine is stopped, VTC maximally retards the IVC (96 deg) and waits for engine restart. When the engine exceeds 600 rpm, which is beyond the resonance range, VTC advances the IVC to 76 degrees for the initiation of fuel injection. These operations control the source of vibration, making it possible to realize the necessary NV performance.

Because this series of operations takes place before the increase in engine speed, it would be challenging to realize using a standard oil pressure-type VTC. The application of electric VTC has made it possible to realize the high level of NV performance demanded from an upper-mid-class sedan, without sacrificing power or emissions performance.

5. Conclusion

The application of the technologies discussed above has resulted in the development of a competitive engine for use in a hybrid system. The development can be summarized as follows:

(1) The application of the Atkinson cycle and cooled EGR, in combination with VTEC, has made it possible to realize a maximum power of 105 kW and a BSFC of 214 g/kWh (a 10% improvement over the previous engine).
(2) The application of weight-saving technologies including a forged crankshaft has reduced the weight of the developed engine by 4.7% against the previous engine despite changing to DOHC.
(3) The PHEV specification for the North American market is the first vehicle to conform to the SULEV 20 standard.
(4) The application of electric VTC and the retardation of IVC in order to reduce vibration at engine start made it possible to realize the high level of NV performance demanded from an upper-mid-class sedan, without sacrificing power or emissions performance.

References

(1) Yonekawa, A., Ueno, M., Watanabe, O., Ishikawa, N.: Development of New Gasoline Engine for ACCORD Plug-in Hybrid, SAE Technical Paper 2013-01-1738 (2013)
(2) Higuchi, N., Sunaga, Y., Tanaka, M., Shimada, H.: Development of a New Two-Motor Plug-In Hybrid System, SAE Technical Paper 2013-01-1476 (2013)
(3) Okui, S., Kishi, T., Ishikawa, N., Hanada, K.: Development of 3-stage i-VTEC VCM Engine for CIVIC Hybrid, Honda R&D Technical Review, Vol. 18, No. 2, p. 44-51
(4) Kawamoto, N., Naiki, K., Kawai, T., Shikida, T., Tomatsuri, M.: Development of New 1.8-Liter Engine for Hybrid Vehicles, SAE Technical Paper 2009-01-1061 (2009)

■ Author ■


Akiyuki YONEKAWA


Osamu WATANABE


Noritaka SEKIYA


Naohiro ISHIKAWA

Development of SPORT HYBRID i-MMD Control System for 2014 Model Year Accord

Hirohito IDE* Yoshihiro SUNAGA* Naritomo HIGUCHI*

ABSTRACT

A highly efficient two-motor hybrid system named SPORT HYBRID Intelligent Multi-Mode Drive was developed and mounted in the 2014 model year Accord to meet global demands for CO_2 reduction. The control system switches the three drive modes of "EV drive," "Hybrid drive" and "Engine drive" according to the driving conditions. Together with hybridization, this helped to enhance fuel economy by 39%. In addition, cooperative control between components was developed that supports the large system configuration, and helped to achieve both reliability and driving performance. Installation of this system and control technology in an Accord plug-in hybrid achieved an EV driving range of 13 miles and fuel economy of 115 MPGe (Charge Depleting mode) and 46 mpg (Charge Sustaining mode). Furthermore, sufficient driving performance was also maintained while observing the constraints required to secure reliability.

1. Introduction

Demands are increasing further on the automotive industry to reduce the environmental load, such as by reducing CO_2 emissions. The Integrated Motor Assist (IMA) system, which is lighter in weight and more compact, has been proposed as one method for addressing this issue. In addition, zero emission systems such as fuel cell EV systems and battery EV systems have also been proposed. Enhancements such as even higher hybrid system efficiency and longer zero emission cruising ranges are urgently needed to further reduce the environmental load in the future. A new two-motor hybrid system called SPORT HYBRID Intelligent Multi-Mode Drive (SPORT HYBRID i-MMD) was developed to meet these demands[(1)]. This hybrid system features higher efficiency than previous hybrid systems, and also provides power performance enabling use in mid-size sedans. In addition, this system also increased the zero emission cruising range of the SPORT HYBRID i-MMD Plug-in that is equipped with a large-capacity battery and a plug-in charging function.

This paper describes the goals and features of the newly developed two-motor hybrid system using the SPORT HYBRID i-MMD Plug-in as an example. In addition, this paper also discusses the control system that contributed to increasing efficiency and securing vehicle reliability, and the performance achieved by an actual vehicle.

2. Development Goals

The previous IMA system made use of the characteristics of a lightweight and compact hybrid system to achieve enhanced fuel economy mainly in compact cars. However, similar enhancements in fuel economy are also needed for mid-size sedans and larger classes to reduce the environmental load in the future. Therefore, the two-motor hybrid system SPORT HYBRID i-MMD was newly developed with the aim of high efficiency. This system switches the three modes of EV drive, Hybrid drive and Engine drive according to the driving conditions, and has the following features compared to the IMA system.

(1) Expanded EV driving range and higher efficiency
(2) Expanded area enabling highly efficient engine operation
(3) More efficient recovery of deceleration energy

As a result, it is thought that this system can achieve good fuel economy. However, the system configuration is larger than that of the IMA system, and coordinated operation is needed to maintain sufficient driving performance while observing the various constraints for securing reliability. Therefore, a control system was developed that simultaneously realizes both fuel economy and driving performance by performing the appropriate control for the system in accordance with various environmental and driving conditions.

* Automobile R&D Center

3. Overview of System

3.1. Overall Configuration

Figure 1 shows the major components of the SPORT HYBRID i-MMD system. An electric coupled CVT comprising two motors (motor and generator) and a clutch is built into the transmission case and located inside the engine room together with a newly developed Atkinson cycle engine optimized for HEV[2]. A Power Control Unit (PCU) incorporating a voltage control unit that boosts the Li-ion battery voltage, a motor control unit used to control the motor[3] and generator, and an inverter is located above the electric coupled CVT. An Intelligent Power Unit (IPU) consisting of a Li-ion battery, a DC/DC converter, and a battery control unit that controls the Li-ion battery and DC/DC converter is located behind the rear seat. The plug-in hybrid vehicle is also equipped with a dedicated high-capacity Li-ion battery and high-output onboard charger, enabling city driving in EV drive mode with a range of 10 miles or more.

3.2. Overview of Powertrain

Figure 2 shows an overview of the powertrain, which consists of an inline 4-cylinder 2.0 L engine and an electric coupled CVT unit. This Atkinson cycle engine employs VTEC, electric VTC and cooled EGR, and friction has been reduced, enabling achievement of both high output of 105 kW and 10% higher efficiency in terms of Brake Specific Fuel Consumption (BSFC) compared to the previous 2.0 L engine. The motor achieves high output of 124 kW and high efficiency of 96% (max.) by increasing the voltage with a booster and making use of reluctance torque. Table 1 lists the major specifications of the powertrain.

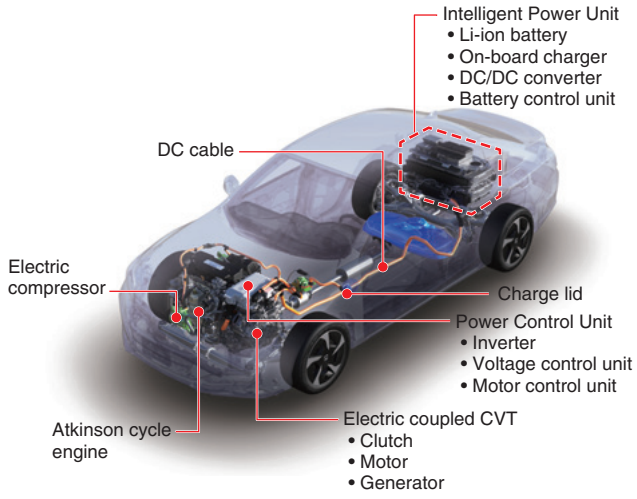


Fig. 1 Overall system configuration

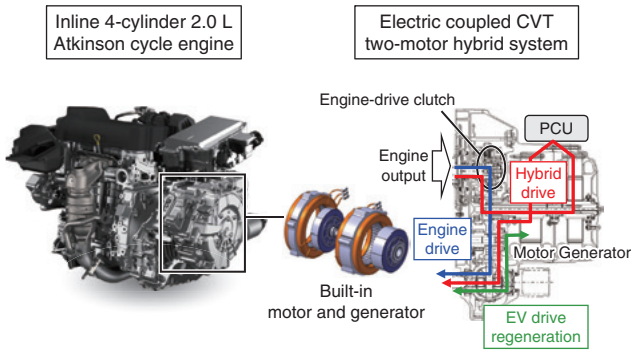


Fig. 2 SPORT HYBRID i-MMD powertrain

Table 1 Specifications of hybrid powertrain

Engine	Type	L4 DOHC Atkinson
	Max. power [kW]	105
	Max. torque [Nm]	165
Motor	Type	Interior permanent magnet synchronous motor
	Max. power [kW]	124
	Max. torque [Nm]	307
	Max. speed [rpm]	12584
	Max. voltage [V]	700

3.3. Overview of Plug-in Hybrid Operation

Figure 3 shows an overview of plug-in hybrid operation.

Plug-in hybrid operation is classified into the following two modes.

The first mode is called Charge Depleting mode (CD mode). This mode mainly performs EV drive using the electric energy stored in the Li-ion battery by plug-in charging. CD mode expands the EV drive operation range and secures a 13-mile EV range by setting a high threshold for engine start as shown in Fig. 3.

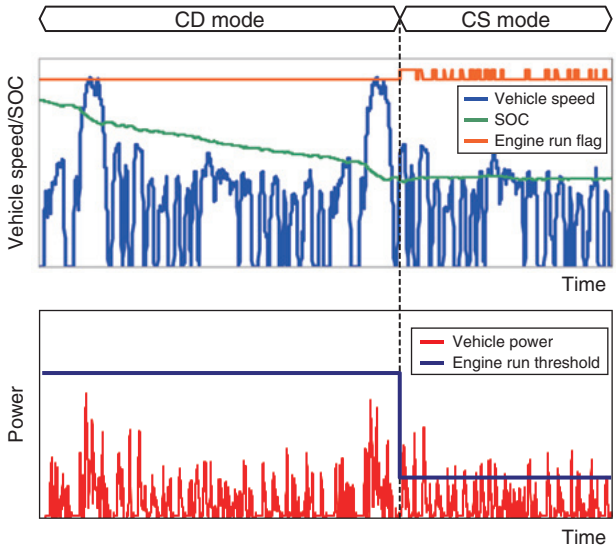


Fig. 3 Plug-in hybrid operation

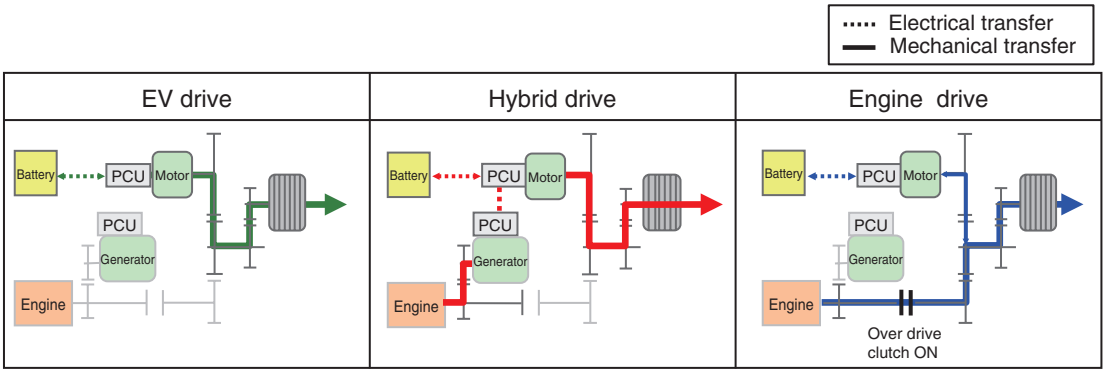


Fig. 4 SPORT HYBRID i-MMD operation modes

The second mode is called Charge Sustaining mode (CS mode). In this mode, when the State of Charge (SOC) of the Li-ion battery falls below the specified value, the vehicle is propelled using gasoline as the energy source so that the SOC stays within the specified range. In other words, the vehicle functions as a hybrid vehicle.

3.4. Overview of Drive Modes

Figure 4 shows the types of drive modes of the SPORT HYBRID i-MMD system. This system has three drive modes, and the system efficiency is enhanced by selecting the appropriate drive mode according to the driving conditions.

The first mode is called EV drive mode. In this mode, the vehicle is propelled by the motor using the electric power stored in the Li-ion battery.

The second mode is called Hybrid drive mode. In this mode, the engine power is converted to electric power by the generator, and the vehicle is propelled by the motor using this electric power (the system operates as a series hybrid). When the generator produces less electric power than is consumed by the motor, the shortage is compensated by discharge from the Li-ion battery. When excess electric power is generated by the generator, it is charged to the Li-ion battery.

The third mode is called Engine drive mode. In this mode, the engine and axles are coupled at fixed gear ratios using a clutch, and the wheels are driven directly by the engine (the system operates as a parallel hybrid). In this case the motor performs assist and charging functions, and power is discharged from the Li-ion battery (assist) or charged to the Li-ion battery.

4. Control System

4.1. Control System Configuration

Figure 5 shows the block diagram of the SPORT HYBRID i-MMD system. The control units for the power train components comprising the engine, electric coupled CVT with built-in motor and generator, PCU, and IPU communicate through a Controller Area Network (CAN) with a redundant design. In addition, related components such as an electric servo brake[4] and a full-electric compressor for air conditioning communicate through the CAN, and cooperative control is performed according to the environmental and driving conditions. Power management control, and in particular control related to fuel economy performance and driving performance under various constraints, is described below.

4.2. Major Goals of Power Management Control

The major goals of power management are to:

(1) Enhance fuel economy in each drive mode;
(2) Enhance fuel economy by switching the drive modes; and
(3) Secure driving performance under various constraints.

Regarding (1) and (2), fuel economy performance can be enhanced by taking into account the acceleration and deceleration intent of the driver and the constraints and efficiency characteristics of each component. Regarding (3), for example when the constraint of a battery power limit arises, driving performance is secured by performing cooperative control between the components so that any excess or shortage of electric power relative to the motor output is compensated by the generator output. The control methods used to achieve the above targets are described below.

4.3. Enhancement of Fuel Economy Performance in Each Drive Mode

The SPORT HYBRID i-MMD system modes that operate the engine are Hybrid drive mode and Engine drive mode. Fuel economy performance in each mode is mainly governed by the thermal efficiency of the engine. This means that the keys to enhancing fuel economy are how to more efficiently operate the engine, and how to increase the efficiency of the overall system. An overview of engine operation in these two modes is described below.

4.3.1. High-efficiency operation in Hybrid drive mode

In Hybrid drive mode, there is no mechanical transmission path from the engine to the wheels. That is to say, there is no constraint on rotational speed between the vehicle velocity (which is proportional to the motor speed) and the engine and generator. This means that the engine speed can be set arbitrarily relative to the vehicle speed. Therefore, control is basically performed so that the engine operating point traces the minimum BSFC line determined uniquely relative to the engine output. Furthermore, the engine output is adjusted toward operation points with higher efficiency on the blue minimum BSFC line as shown in Fig. 6. At this time, any excess or shortage of generated electric power relative to the motor output is compensated by the battery energy.

4.3.2. High-efficiency operation in Engine drive mode

In Engine drive mode, the engine and wheels are coupled via a fixed reduction gear, so the engine speed is determined uniquely with respect to the vehicle speed. The relationship between the engine speed and the torque when cruising on a flat road is shown by the dashed line in Fig. 6. Engine drive mode is used in the high-speed cruising area, but when driving on a flat road the engine operating point deviates to the low torque side of the minimum BSFC line. In this case, the engine torque is increased so that the engine operates at a more efficient operating point, and this increase in torque is absorbed by the regeneration operation of the motor. Conversely, under conditions where the engine operating point deviates to the high-torque side of the minimum BSFC line, the engine torque is reduced and the difference is compensated by motor drive. In this manner, control is performed to converge the engine operating point to the higher-efficiency area by motor regeneration and motor drive.

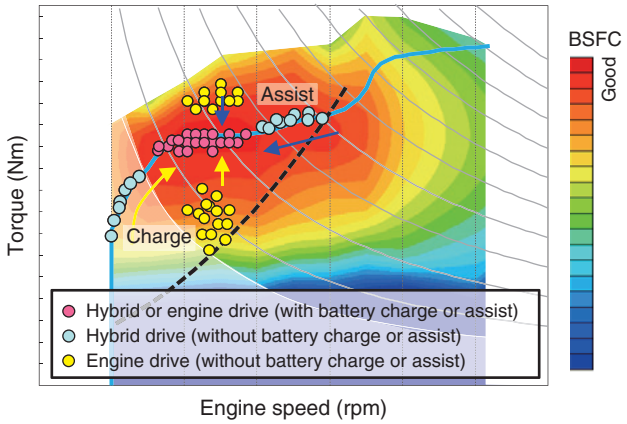


Fig. 6 Engine operating point

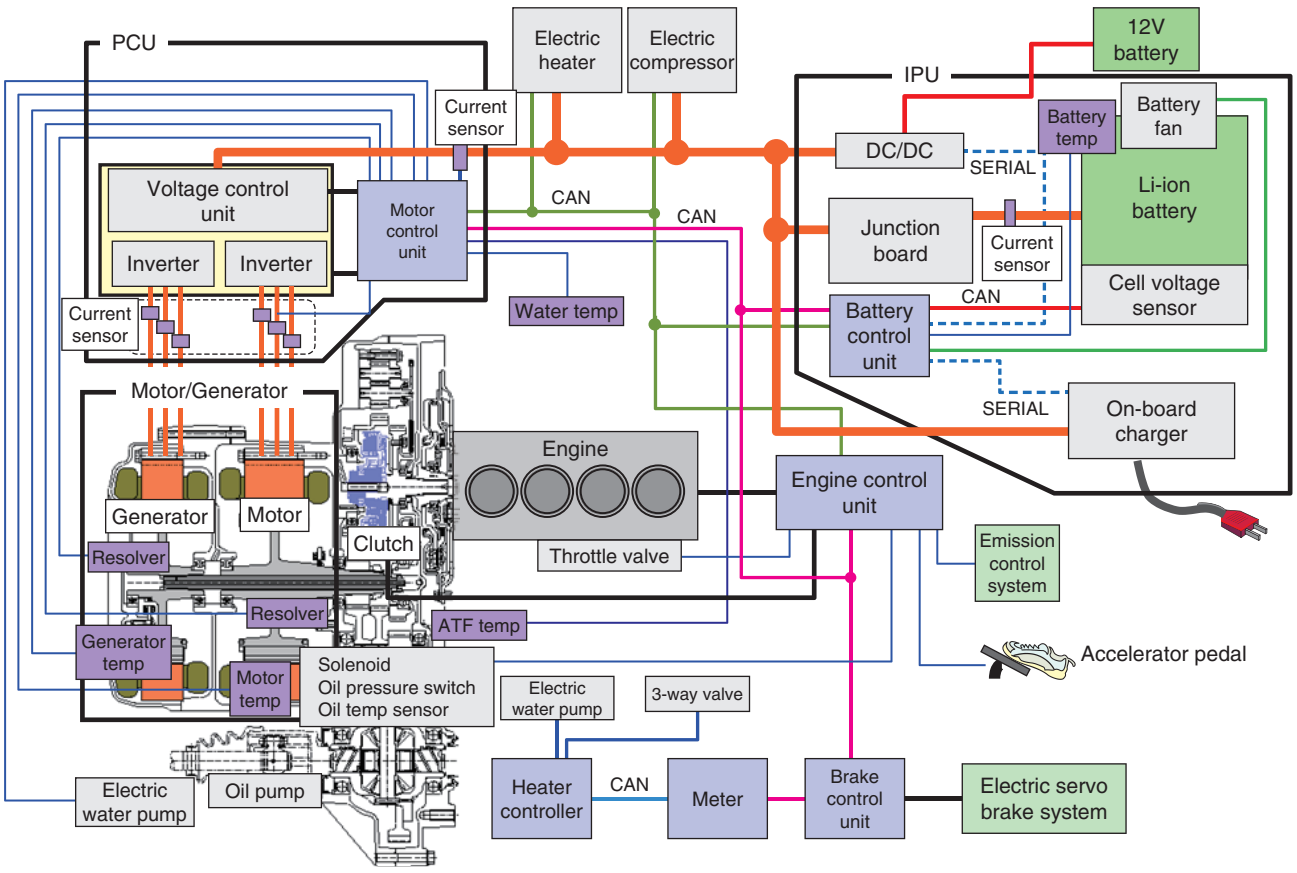


Fig. 5 Block diagram of SPORT HYBRID i-MMD system

4.4. Enhancement of Fuel Economy Performance by Switching the Drive Mode

In order to enhance vehicle fuel economy, it is necessary to enhance the thermal efficiency of the engine as described in 4.3. above, and at the same time increase the efficiency of the overall system by increasing the energy transfer efficiency from the engine output to the axle output. The SPORT HYBRID i-MMD system achieves higher efficiency by switching the drive mode.

Figure 7 shows an overview of switching the drive mode according to the vehicle speed in CS mode, and Fig. 8 shows the driving force diagram and the drive mode operating areas. EV drive mode is mainly selected in the range from launch to city and other low-speed driving in order to avoid a drop in fuel economy due to low-load engine operation. When driving at medium speeds, fuel economy is enhanced by performing intermittent operation that switches between EV drive and Hybrid drive or between EV drive and Engine drive as appropriate in consideration of the balance between the thermal efficiency of the engine and the Li-ion battery charge/discharge loss. When driving at high speeds, Hybrid drive mode or Engine drive mode is selected as appropriate to achieve the highest energy transfer efficiency.

4.4.1. Switching between EV drive and Hybrid drive (Engine drive)

Mode switching called intermittent operation is performed as appropriate in the driving power area where EV drive can be selected. In this case, the Li-ion battery is charged during Hybrid drive (or Engine drive), and then operation switches to EV drive using the accumulated electric energy. Figure 9 shows the fuel economy enhancement effect due to switching between EV drive and Hybrid drive.

This shows that in consideration of the balance between the thermal efficiency of the engine and the Li-ion battery charge/discharge loss, fuel economy enhancement effects of up to approximately 50% can be obtained in the low driving power range by performing intermittent operation, compared to the case when the engine always operates (Battery charge 0 kW line in Fig. 9). Conversely, the fuel economy enhancement effect of intermittent operation decreases and fuel efficiency instead tends to drop in the high driving power range. Therefore, the EV drive area was determined in consideration of the fuel economy enhancement effect.

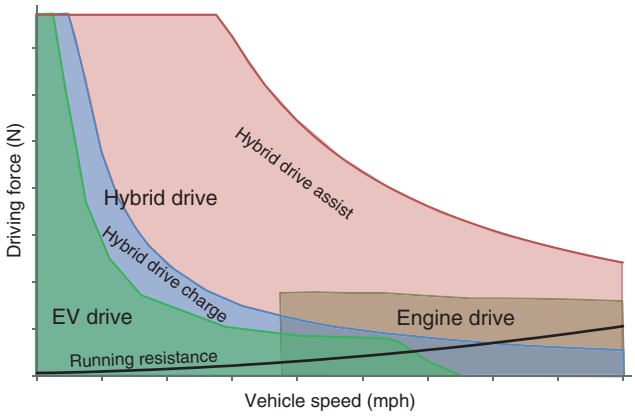


Fig. 8 Operating area of three driving modes (CS mode)

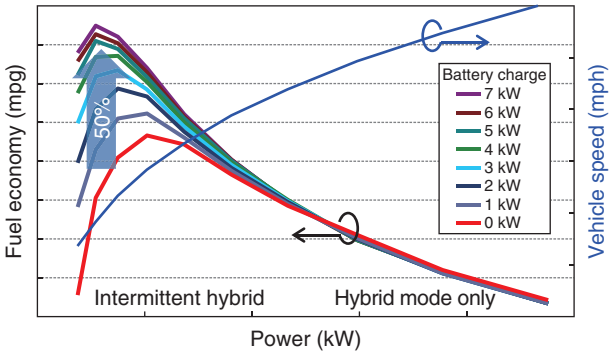


Fig. 9 Fuel economy enhancement of intermittent operation

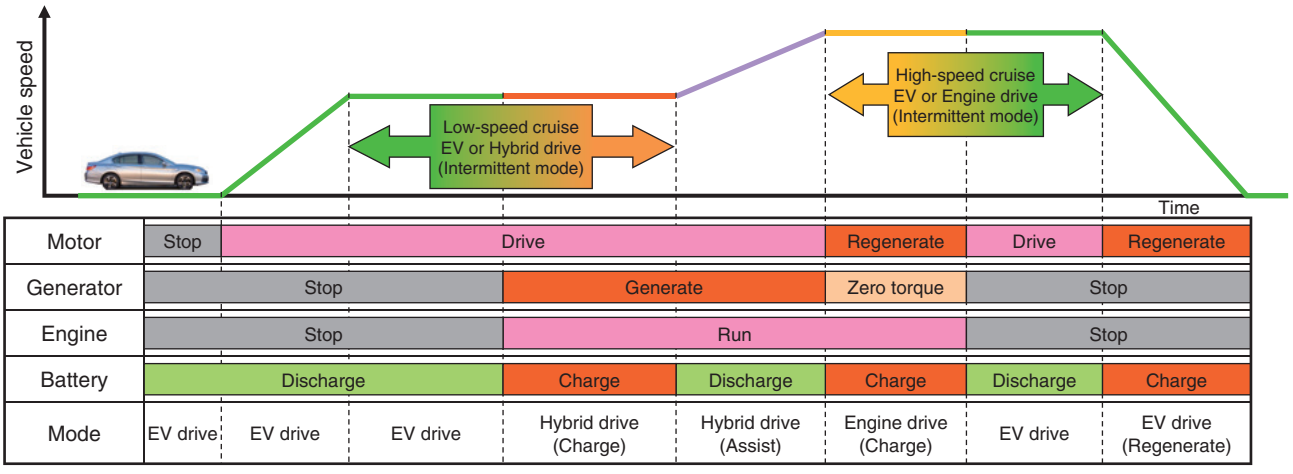


Fig. 7 CS mode operation

4.4.2. Switching between Hybrid drive and Engine drive

Figure 10 compares the Hybrid drive and Engine drive fuel economy.

The colored area in Fig. 10 indicates the area in which Engine drive provides better fuel economy, and the white area indicates the area in which Hybrid drive provides better fuel economy. The black line indicates the driving resistance when driving on a flat road. This shows that when accelerating gently from cruising, Engine drive mode has a higher energy transfer efficiency than Hybrid drive mode, so fuel economy performance is up to 12% better. Conversely, Hybrid drive mode provides better fuel economy performance in areas with a higher driving load. Therefore, Hybrid drive mode and Engine drive mode are switched based on these relationships.

4.5. Securing Driving Performance under Constraints

The SPORT HYBRID i-MMD system consists of various components, and each component is subject to constraints in order to secure reliability. For example, these constraints include a motor torque limit, generator torque limit, and battery power limit. In particular regarding the battery power limit, accurate control is demanded from the viewpoint of securing Li-ion battery durability, and this limit is known to greatly influence the driving performance of a system using a series hybrid. Therefore, cooperative control between each component to support various environmental and operating conditions is described below using the battery power limit as an example.

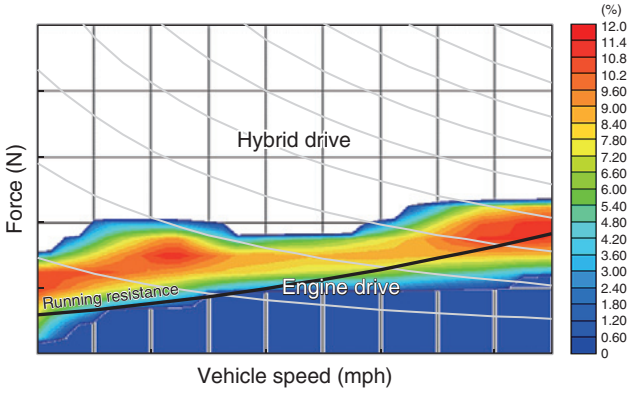


Fig. 10 Comparison of fuel consumption of hybrid drive and engine drive

The power management control obtains the acceleration and deceleration intent of the driver (accelerator and brake pedal operations) and the power and torque limit information from each component, and performs the appropriate cooperative power control within the limit range. Under conditions where the battery power is limited, such as in low-temperature environments, and the acceleration and deceleration intent cannot be satisfied by battery power alone, power management control selects Hybrid drive mode and accurately balances the motor, generator and engine outputs to both satisfy the battery power limit and achieve sufficient driving performance. Figure 11 shows the block diagram of this control.

Power management control first calculates the target vehicle driving force from the acceleration and deceleration intent of the driver and the motor torque limit requirement. Next, it calculates the target engine power that matches the sum of the target motor power calculated from the target vehicle driving force and the target battery power calculated from the energy management control. The target engine power is corrected as necessary by the battery power regulator. After that, the target engine speed and target engine torque are calculated from the corrected target engine power. Here, the target engine speed and torque values select the point at which the engine efficiency is maximized. Finally, the engine power, generator power and motor power are corrected in consideration of various constraints including the battery power limit. This control system

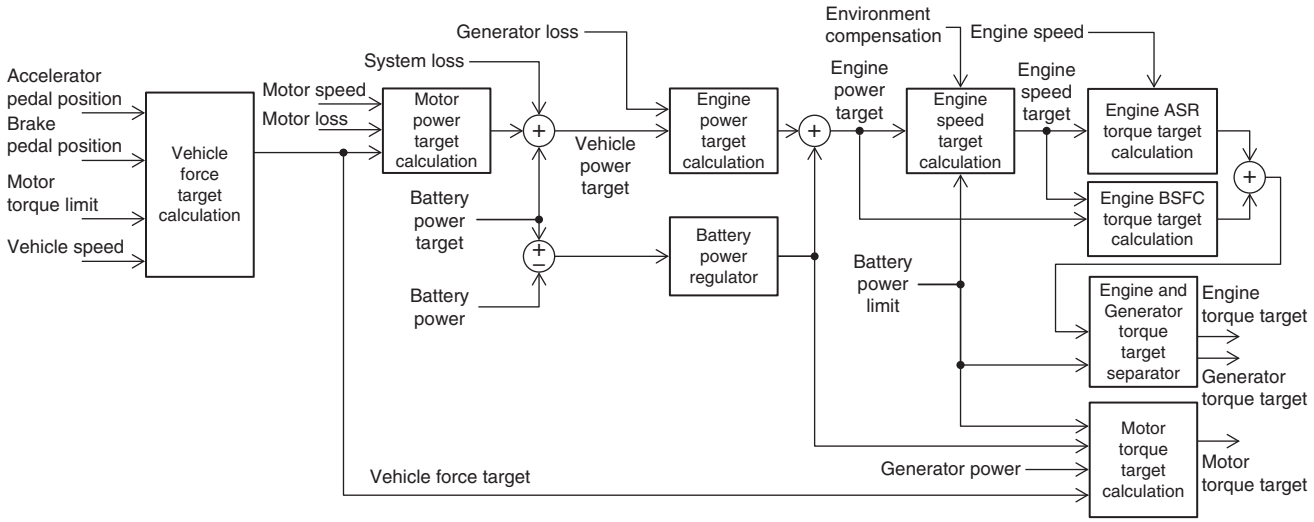


Fig. 11 Power management control

configuration balances the acceleration and deceleration intent of the driver, the battery SOC convergence properties, the battery power limit performance, and the constraints of other components.

In addition, the motor and generator power calculated as noted above are accurately corrected with rapid response so that the battery power limit can be satisfied even when the battery power is greatly limited, such as at extremely low temperatures or when the power fluctuates sharply due to sudden acceleration or deceleration.

At extremely low temperatures, the battery power is strictly limited to help secure battery durability. To maintain sufficient driving performance with this limit, the motor and generator need to output power in excess of 100 kW, and accurate control that can maintain this power balance within a battery power limit of several kW or less is also needed. In addition, when accelerating or decelerating rapidly on low-μ road surfaces such as snow-covered roads, wheel-spin and tire-lock occur, and the resulting fluctuation in motor speed produces rapid changes in the motor power. This means that rapid response control is also required that can maintain the power balance within the limit even in these types of situations. The power correction method used to achieve both high accuracy and rapid response is described below.

4.5.1. Estimation of battery power

Rapid response battery power control requires battery power information with little delay or dead time, so the battery power is estimated swiftly. The battery power can be measured from the Li-ion battery voltage sensor and current sensor. However, there are also the sensor delay factors, battery capacitor characteristics, the characteristics of the capacitors and reactors inside the PCU, the communication delay between each control unit, and other factors. This means that there are delay and dead time characteristics between the motor and generator power fluctuation recognized by the control units and the battery power fluctuation. Those delay and dead time characteristics cannot be ignored for the rapid control response requirement, so the battery power is estimated indirectly from the motor and generator power and other loss information. Figure 12 shows the high-voltage components of this system.

Regarding these high-voltage components, the battery power P_{bat} is the sum total of the motor and generator input power P_{mot} and P_{gen}, the motor and generator inverter loss P_{invmot} and P_{invgen}, the boost loss P_{vcu}, the DC/DC converter loss P_{dcdc}, and the air conditioner and heater loss P_{ac}. Therefore, the power equation shown in Eq. (1) below is constantly satisfied.

$$P_{bat} = P_{mot} + P_{gen} + P_{invmot} + P_{invgen} + P_{vcu} + P_{dcdc} + P_{ac} \quad (1)$$

Equation (1) shows that the battery power can be estimated by compensating the various losses based on the motor and generator power. The input power to the motor and generator can be measured by a phase-current sensor and a boosted-voltage sensor. The motor and generator inverter loss and the boost loss can be estimated using the nominal values determined from the prescribed parameters. The DC/DC converter loss information and the air conditioner and heater loss information are obtained from the respective control units via the CAN. The controller estimates the battery power from this information. Figure 13 shows the configuration of this controller.

4.5.2. Power compensation for battery power control

Accurate battery power control with a rapid response is performed using the estimated battery power calculated as described above. It was noticed that battery power fluctuation mainly occurs due to motor and generator power fluctuation, and that the power is correlated with the torque. Therefore, a configuration was selected that controls the battery power by compensating the motor and generator torque command values calculated by power management control. In addition, the estimated battery power contains some error due to factors such as temperature characteristics and manufacturing error, so this error needs to be compensated. Therefore, the effects of this error are removed by calculating the deviation between the actual battery power and the estimated battery power, and compensating the battery power limit value based on the calculated deviation. Figure 14 shows this controller configuration using the generator torque compensation side as an example.

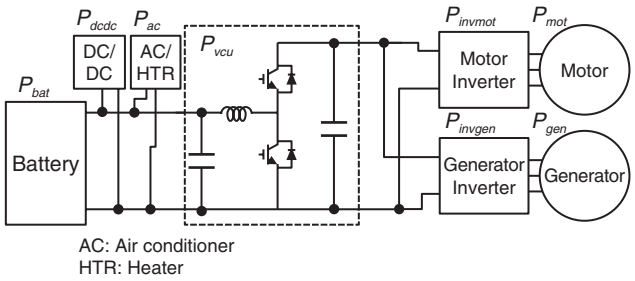


Fig. 12 High-voltage component

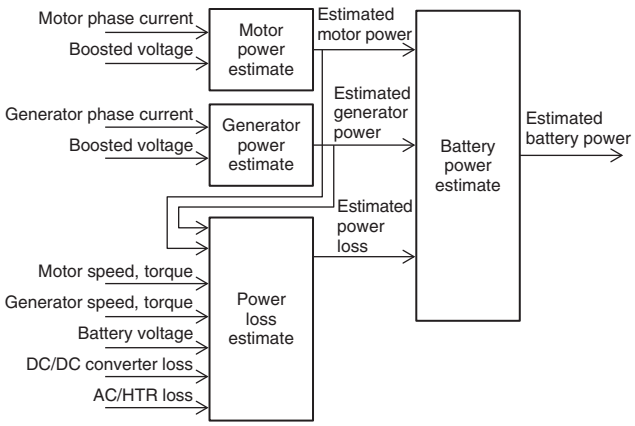


Fig. 13 Battery power estimator

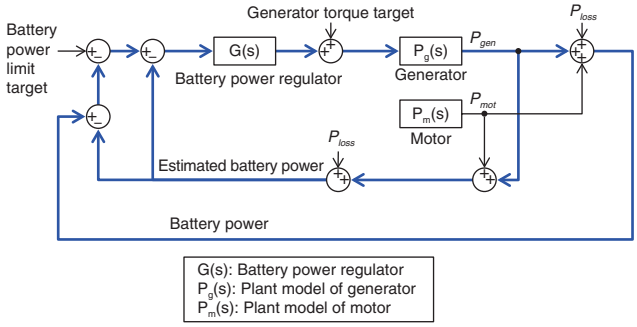


Fig. 14 Closed loop of battery power limit to battery power

A closed loop is formed between the battery power and the battery power limit value as indicated by the blue arrows in Fig. 14. Therefore, the battery power can be converged to within the power limit value range by adding the regulator G(s) between the battery power and the battery power limit value, and compensating the motor torque and generator torque calculated by power management control.

5. Performance Achieved by an Actual Vehicle

Figure 15 shows the fuel economy enhancement effect of the SPORT HYBRID i-MMD Plug-in system compared to a current gasoline engine vehicle. Compared to the current gasoline engine vehicle, the SPORT HYBRID i-MMD Plug-in system enhanced fuel economy in the EPA fuel economy measurement modes by 104% in City mode, 35% in Highway mode, and 70% in Combined mode, and achieved fuel economy of 46 mpg. Figure 16 shows the breakdown of this 70% fuel economy enhancement effect. This control contributed to the 39% enhancement in fuel economy due to hybridization. In addition, a 13-mile EV range and fuel economy of 115 MPGe were achieved in CD mode.

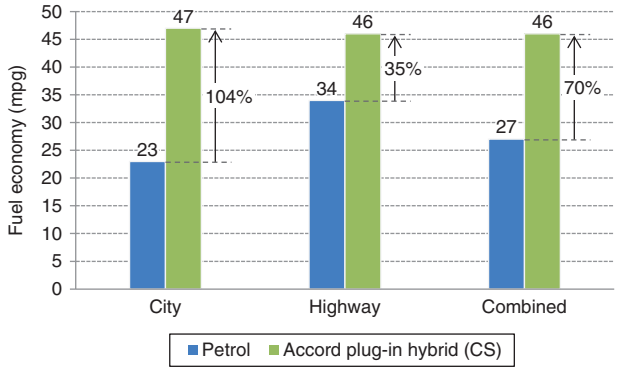


Fig. 15 Comparison of fuel economy

Figure 17 shows the results for highway driving that includes acceleration and deceleration (US06 mode) under a constraint (battery power limit). These results confirmed that the power shortage relative to the motor output under the battery power limit can be compensated by adjusting the generation level of the generator, maintaining sufficient driving performance while converging the battery power

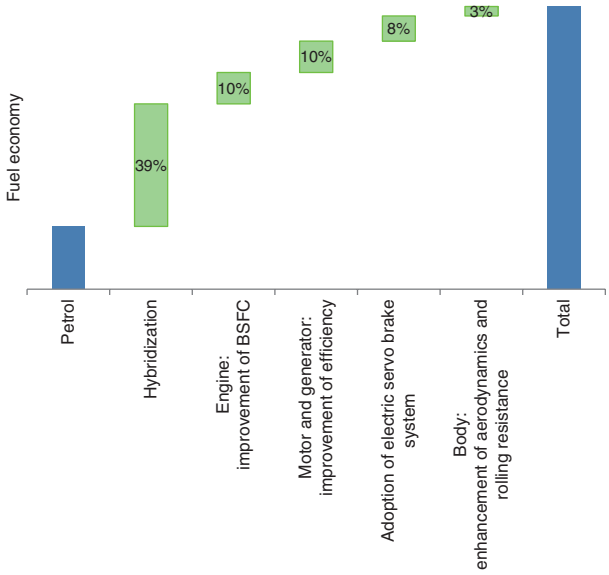


Fig. 16 Contributions to fuel economy enhancement of proposed SPORT HYBRID i-MMD Plug-in system

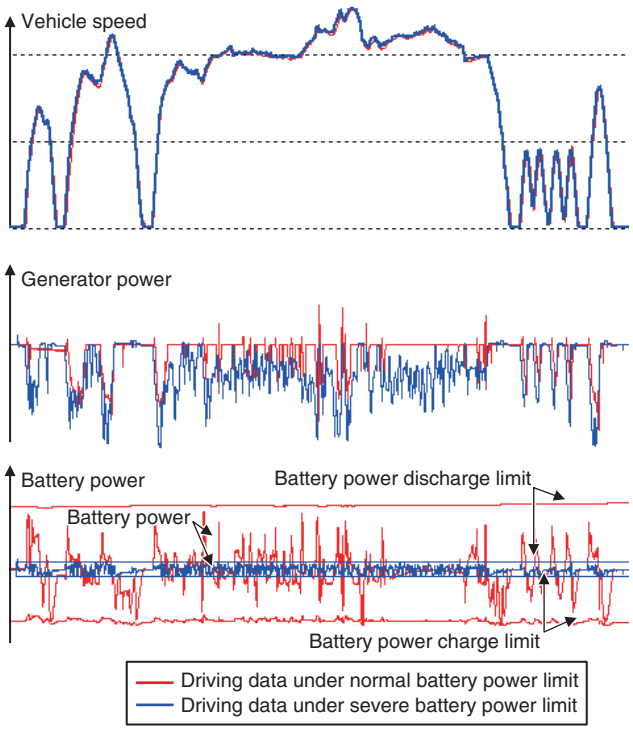


Fig. 17 Power management in US06 mode

to within the limit range. In addition, Fig. 18 shows the battery power behavior when the motor power changes suddenly during wheel spin and sudden braking. This confirmed that the battery power is similarly converged to within the limit range even in these types of situations. The motor and generator power exceeds 100 kW under the above conditions, but the battery input/output power is converged to a range of several kW or less.

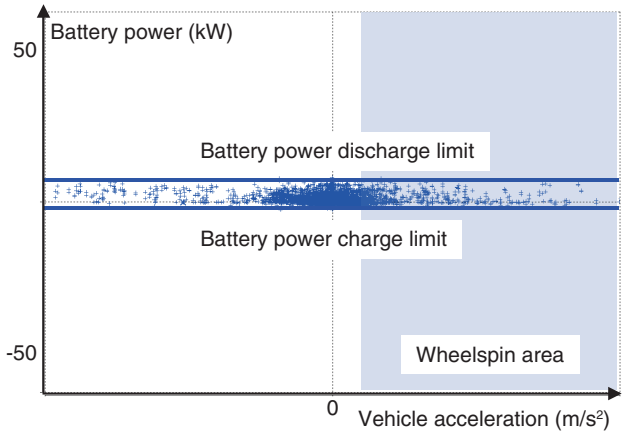


Fig. 18 Vehicle acceleration and battery power

6. Conclusion

A control system was developed for the two-motor hybrid system SPORT HYBRID i-MMD, and achieved the following performance when mounted in the 2014 model year Accord.

(1) The new control system contributed to a 39% increase in fuel economy by switching three drive modes as appropriate according to the driving conditions, and by enhancing the thermal efficiency of the engine and the energy transfer efficiency. In addition, the following fuel economy performance was achieved.
EV range: 13 miles
CD fuel economy: 115 MPGe
CS fuel economy: 46 mpg

(2) When driving with a battery power limit, cooperative control between each component enabled maintaining of sufficient driving performance while converging the battery power to within the limit range.

References

(1) Higuchi, N., Sunaga, Y., Tanaka, M., Shimada, H.: Development of a New Two-Motor Plug-In Hybrid System, SAE 2013-01-1476 (2013)

(2) Yonekawa, A., Ueno, M., Watanabe, O., Ishikawa, N.: Development of New Gasoline Engine for ACCORD Plug-in Hybrid, SAE 2013-01-1738 (2013)

(3) Kuroki, J., Otsuka, H.: Development of Motor and PCU for Two-Motor Hybrid System, Honda R&D Technical Review, Vol. 25, No. 2, p. 42-48

(4) Ohkubo, N., Matsushita, S., Ueno, M., Akamine, K., Hatano, K.: Application of Electric Servo Brake System to Plug-In Hybrid Vehicle, SAE 2013-01-0697 (2013)

Author


Hirohito IDE


Yoshihiro SUNAGA


Naritomo HIGUCHI

Development of Motor and PCU for a SPORT HYBRID i-MMD System

Jiro KUROKI* Hiroshi OTSUKA*

ABSTRACT

A highly efficient SPORT HYBRID Intelligent Multi-Mode Drive system was developed in order to achieve a balance between the joy of driving and measures to address climate change and energy issues. The developed power train is composed of the engine, an electric coupled CVT with a built-in motor and generator, a Power Control Unit, and an Integrated Power Unit. The built-in motor was given higher torque, higher output, and higher efficiency by using reluctance torque and raising the voltage. The Power Control Unit was made more compact and power was increased by enhancing the unit's heat dissipation performance, and it was made more efficient by using a low-loss chip. As a result, the motor achieves maximum torque of 307 Nm and maximum output of 124 kW, while the Power Control Unit achieves a voltage increase of 700 V and total output of 400 kVA. The Power Control Unit including the motor achieved a maximum efficiency of 96%.

1. Introduction

In order to address climate change and energy issues, there is demand for motor vehicles with lower emissions and better fuel economy. Honda has responded to these expectations by developing the Integrated Motor Assist (IMA) system[1] installed in models such as the INSIGHT, CR-Z, FREED HYBRID, and FIT HYBRID, and by taking steps to reduce fuel consumption.

Honda has also been developing fuel cell electric vehicles[2] and battery electric vehicles (EV) as highly advanced zero emission vehicles. A fuel cell EV uses hydrogen as fuel, causing it to react with oxygen in the air to generate electricity and provide driving power. A battery EV uses electricity stored in batteries for driving power. It has the advantage of not emitting exhaust gases when operating, but one issue faced by the battery EV is that it has a limited driving range compared to an Internal Combustion Engine Vehicle (ICEV). At present, there are also not many hydrogen stations or charging facilities, and more widespread use will be limited until the infrastructure is developed.

A 2014 model year Accord Plug-in Hybrid was developed in order to resolve these issues. The batteries can be charged from household power or other such sources, enabling EV operation for commuting, shopping, and other such everyday short-range uses. When the remaining battery capacity diminishes, the vehicle can use the energy in gasoline to operate in hybrid mode, so the driving range is not limited by battery capacity.

The developed vehicle described here is equipped with the newly developed SPORT HYBRID Intelligent Multi-Mode Drive (SPORT HYBRID i-MMD) system[3], which has a higher electric transmission ratio. The motor and Power Control Unit (PCU) were given enhanced performance and efficiency to achieve higher dynamic performance as well as fuel consumption of 115 MPGe (Charge Depleting mode: CD) and 46 mpg (Charge Sustaining mode: CS) and EV range of 13 miles. This Paper will describe the technology of the newly developed motor and PCU.

2. SPORT HYBRID i-MMD System

Figure 1 shows the SPORT HYBRID i-MMD system power train. The motor and generator are built into the case of the electric coupled CVT. The PCU is located above it. The engine is a 2.0 L Atkinson cycle engine developed for hybrid electric vehicle use.

Figure 2 shows the three operating modes of the SPORT HYBRID i-MMD system, namely (1) EV drive mode, in which the vehicle is driven by the motor

* Automobile R&D Center

using battery energy; (2) hybrid drive mode, in which the mechanical energy of the engine is converted into electrical energy to drive the vehicle using the motor; and (3) engine drive mode, in which the vehicle is driven using the engine.

Figure 3 shows a section view of the electric coupled CVT and the transfer paths under the various modes. The motor torque is transferred by means of gears to the driving shaft. In EV drive mode, the vehicle is driven using the motor, and the engine and generator are shut off. In hybrid drive mode, the engine torque is transferred to the generator and converted to electrical energy that is used by the motor to drive the vehicle. In engine drive mode, the overdrive clutch built into the electric coupled CVT is engaged and the engine torque is transferred to the driving shaft.

The modes are selected so as to minimize fuel consumption under various operating conditions. EV drive mode is used when starting the vehicle under low load. Hybrid drive mode is used when under high load or when accelerating. Engine drive mode is used when cruising at high speeds. In this system, the motor is used both for driving the vehicle and for regeneration, while the PCU performs both electric power conversion and voltage control.

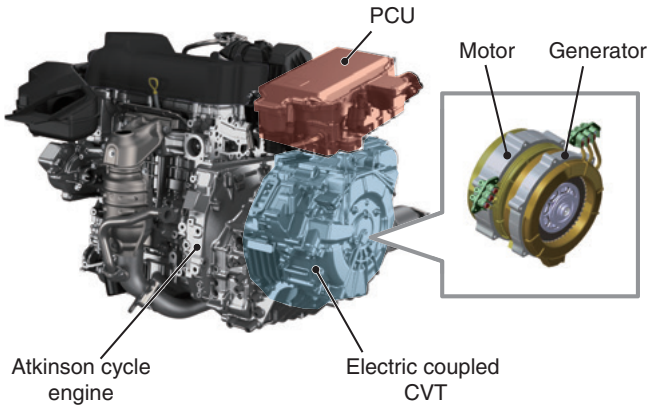


Fig. 1 Hybrid power train

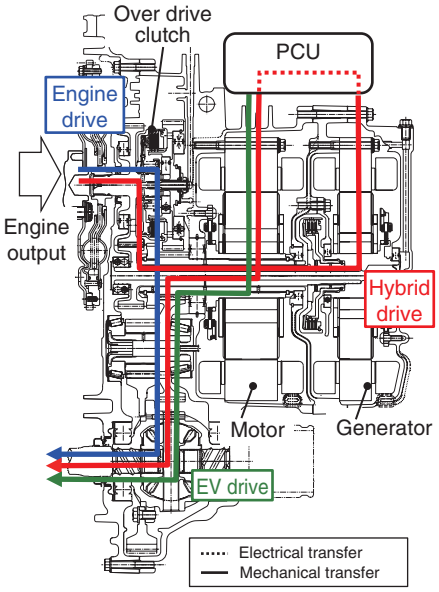


Fig. 3 Section of electric coupled CVT

3. Motor

Under the SPORT HYBRID i-MMD system, the motor is required to drive the vehicle throughout its driving force range. The vehicle's acceleration performance and maximum speed depend on the motor torque, output characteristics, and maximum rotor speed, while motor efficiency has a large influence on fuel consumption. Therefore a high-torque, high-output, high-efficiency motor is called for. At higher maximum motor speeds, rotor strength becomes an issue, so that measures to reduce stress are needed. Furthermore, higher motor output is accompanied by increased motor heat generation, so that a cooling system is needed in order to assure stable driving force. In order to achieve the 115 MPGe (CD) fuel consumption and higher dynamic performance that are performance targets for the vehicle, the motor was developed with the target performance values shown in Table 1.

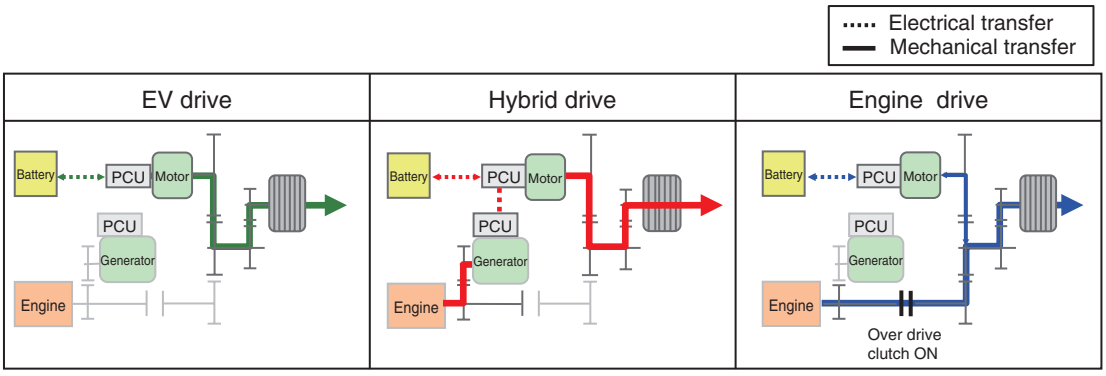


Fig. 2 Operation modes

Table 1 Target performance of motor

Max. torque	307 Nm
Max. power	124 kW
Max. speed	12584 rpm
Max. motor and PCU efficiency	96%

3.1. Enhancement of Motor Efficiency

Figure 4 shows the torque characteristics of the motor together with the high-efficiency area of the conventional motor and the operating areas when operating normally. As to ways in which the motor is used, there is high frequency of operation in the low-load area when city driving. When cruising at high speed, the vehicle will be in engine drive mode and the motor will be running in the vicinity of zero torque. Meanwhile, the conventional motor has the high-efficiency area in the high-output range and the motor is not making effective use of the high-efficiency area.

An enhancement of efficiency in the low-load area was aimed at in order to enhance efficiency during normal operation. Losses in the motor can be divided into copper loss, which occurs in the coil, and iron loss, which occurs in electrical steel. In the low-load area, a higher proportion of loss consists of iron loss, and in order to enhance efficiency in the low-load area, iron loss has to be reduced. In order to reduce iron loss in the low-load area, it is effective to reduce the mass of electrical steel and to reduce magnetic flux. These aims were achieved by using reluctance torque and raising the voltage.

3.2. Making Use of Reluctance Torque

Reluctance torque is torque that uses the magnetic salience of the rotor[4]. In general, flux passes readily through iron but does not pass readily through air and magnets. A greater difference in how readily a material passes flux results in a greater magnetic force of attraction. If this force could be used, then motor torque could be increased without increasing magnet torque; greater compactness would enable reduction in the mass of electrical steel; and reduction in magnetic flux would achieve a reduction in iron loss.

The developed motor is of the interior permanent magnet synchronous type, and a distributed winding was selected as the winding type for the stator. Figure 5 shows a section view of the motor. In order to maximize the reluctance torque effect, the magnets are placed in V-shaped arrangements. When the angle α in the V-shape is smaller, the torque increases. However, this also results in an increased torque ripple that may cause louder motor sound. Angle α was determined in consideration of motor torque and torque ripple. Figure 6 shows the torque at different current phase angles. The current phase angle indicates the timing of the alternating current with respect to the rotor position. When the current phase is 0 degrees, the magnet torque is at its maximum. The developed motor reaches maximum torque when the current phase is 55 degrees. A magnet circuit was achieved in which the maximum torque is 82% greater than the magnet torque and the ratio of reluctance torque is high.

3.3. Raising the Voltage

When the motor operates at high speed, a flux weakening current[4] is generated. Also, below a certain voltage, the generated output is limited by an inductance component in the coil. In order to reduce iron loss, the coil windings were increased to the area where the magnetic flux density of the electrical steel becomes saturated when the maximum current passes through it, the torque was increased the weight of the electrical steel was reduced. There are issues, however, of an increase in inductance

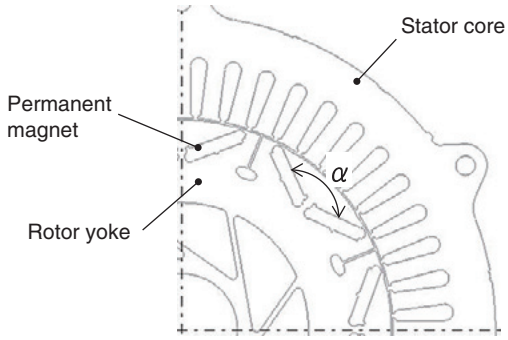


Fig. 5 Profile of motor core

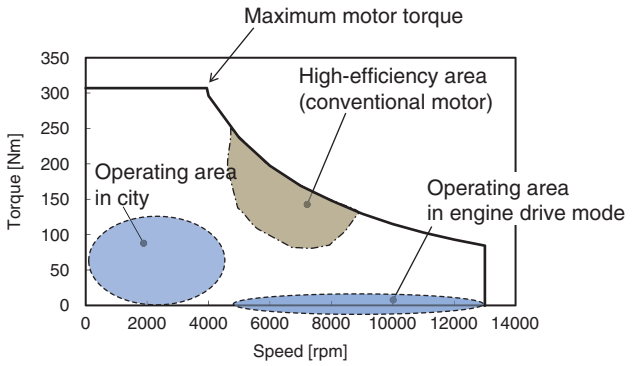


Fig. 4 Motor torque characteristics and operating area

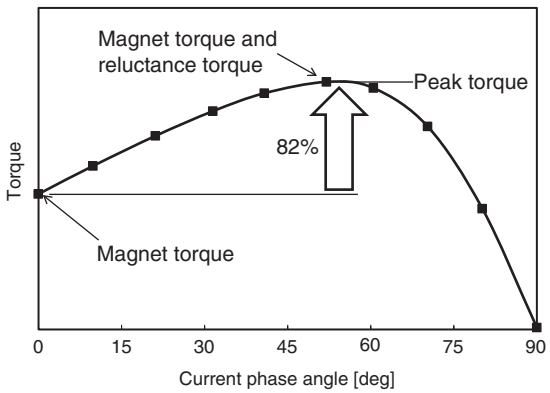


Fig. 6 Torque at different current phase angles

and decrease in output. The voltage was raised in order to resolve these issues. Figure 7 shows the motor voltage and torque characteristics. The voltage increase is carried out by the voltage control unit (VCU) that is built into the PCU. With an applied voltage of 700 V, compared to 300 V, the output increases by 50% or more, achieving a maximum output of 124 kW without enlarging the motor body.

3.4. Increasing Rotor Speed

When the motor's rotor reaches a high rotation speed, the rotor needs to be stronger, and that strength becomes an issue. At high speeds, there is an increase in the centrifugal force of the magnets in a radial direction. This causes high stress to occur in the center ribs at the centers of the V-shaped magnets and in the side ribs at either side of them. One effective way of reducing the stress is to increase the width of each rib, but this results in increased flux leakage from the magnets that become ineffective for torque, and the motor torque is reduced.

In order to resolve these issues, slits were made in the rotor yoke structure. Figure 8 shows the results of stress analysis during rotor rotation.

A slit structure was adopted, and the use of low-rigidity steel in the vicinity of the slits resulted in a 53% reduction of the stress that concentrates in the side rib on the outside of the magnets, and this achieved an increase in speed without increasing the thickness of the side ribs.

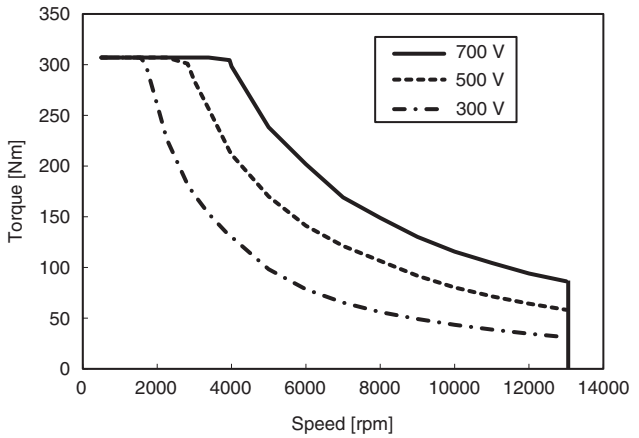


Fig. 7 Motor voltage and torque characteristics

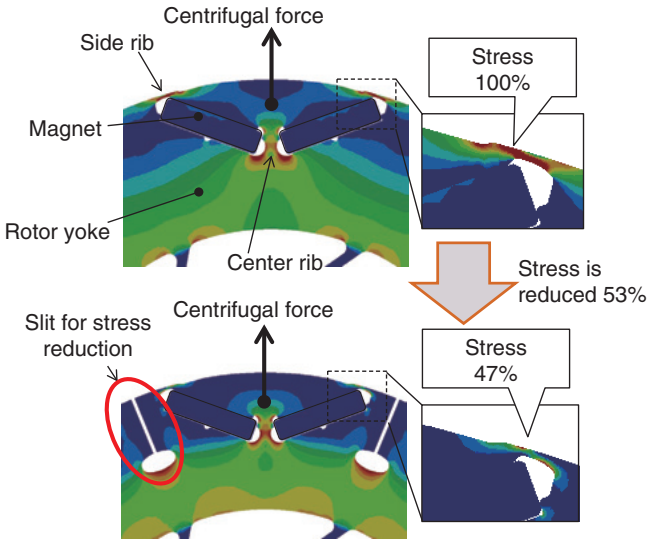


Fig. 8 Comparison of simulated stress distribution

3.5. Motor Cooling System

An oil cooling system was constructed for stable motor operation. Figure 9 shows the cooling system and Fig. 10 shows the structure of the motor cooling system. The heat originating in mechanical loss inside the electric coupled CVT as well as in copper loss and iron loss occurring in the motor is taken into the cooling medium of automatic transmission fluid (ATF) and transported to the ATF cooler to be released. The motor is cooled by ATF that is dripped from a pipe located above the coil. Construction of this cooling system enabled stable actuation of the motor.

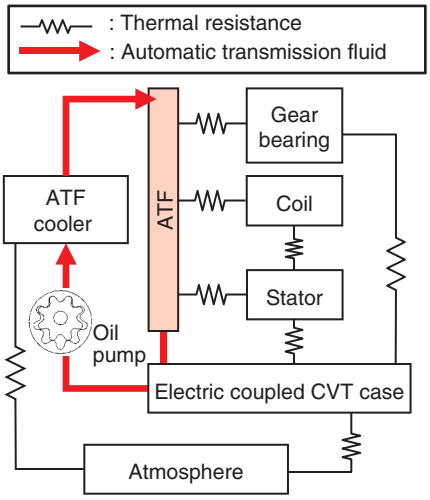


Fig. 9 Cooling system

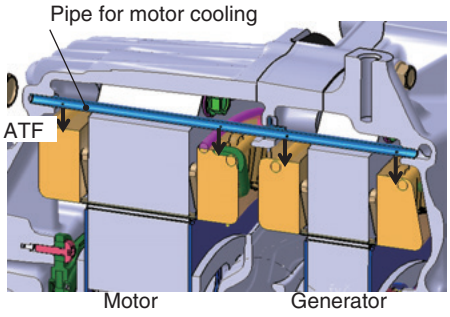


Fig. 10 Structure of motor cooling system

4. PCU

The PCU performs the function of electric power conversion for the batteries, motor, and generator, and it affects motor output and fuel consumption. The size and

Table 2 Target performance of PCU

PCU total max. output	400 kVA
System voltage	700 V
Max. motor and PCU efficiency	96%
PCU volume	11.5 L

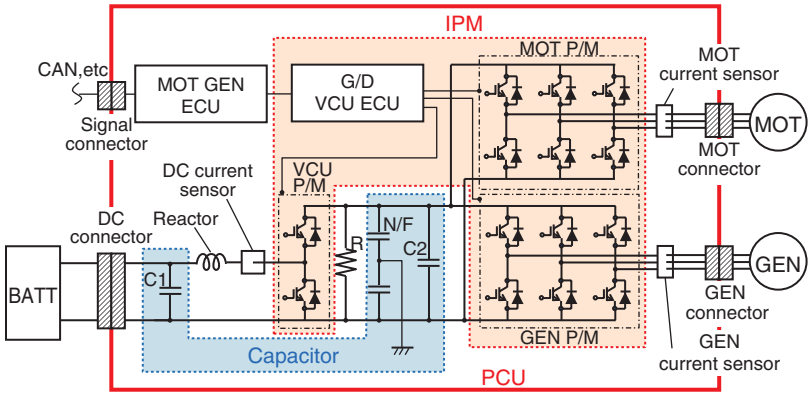
installed location of the PCU also affect cabin space. In order to provide cabin space equal to that in conventional gasoline-powered vehicles, the PCU has to be installed in the engine compartment together with the 12-V battery for the vehicle's electrical system. In order to achieve the target output and fuel consumption for the vehicle as well as to assure cabin space, a PCU that provides higher output, greater efficiency, and greater compactness is needed. The PCU was developed with the performance target values shown in Table 2.

4.1. Enhancement of PCU Output and Compactness

Figure 11 shows a block diagram of the PCU. Figure 12 shows the internal configuration of the PCU. The PCU components include an intelligent power module (IPM), ECUs to control the motor and generator, capacitors, a reactor, and current sensors. The IPM is composed of a power module (P/M) that converts electrical current by switching, a gate driver (G/D) for switching control, and an ECU for VCU control. Placing P/M, G/D, VCU ECU for the motor, generator, and VCU in an integrated package achieves common use of parts and greater compactness. For the capacitors, functional integration of secondary smoothing capacitors for the motor, generator, and VCU, together with integrated packaging of primary smoothing capacitors and noise filters for the VCU, achieved greater compactness. Higher output capability was also implemented by enhancing the heat dissipation of the IPM and using high-voltage connectors with high-current capability for the DC and three-phase sections.

4.2. Enhancing the IPM for Higher Output and Greater Compactness

Figure 13 shows a configuration diagram of the IPM.



BATT: Battery MOT: Motor GEN: Generator R: Resistor
C1: Smoothing capacitor 1 C2: Smoothing capacitor 2 N/F: Noise filter

Fig. 11 Block diagram of PCU

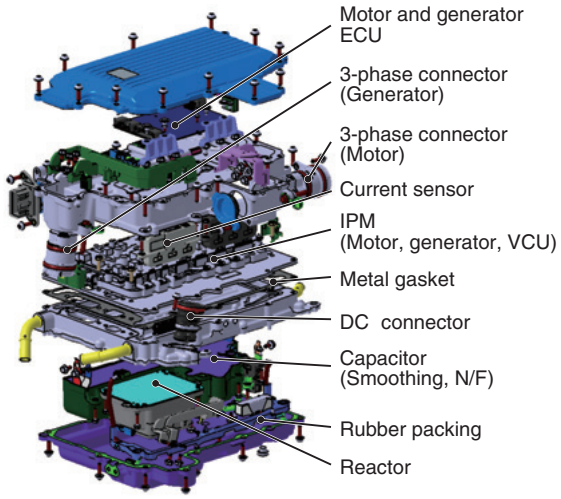


Fig. 12 Configuration of PCU

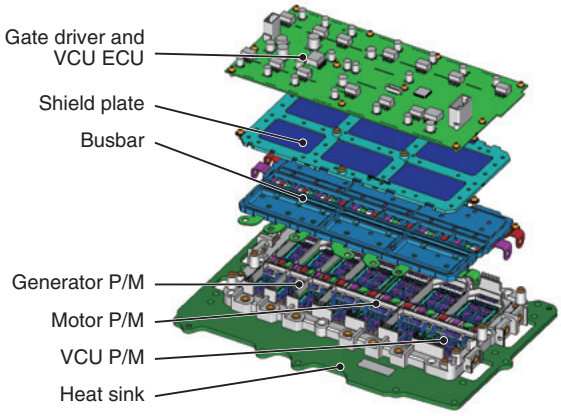


Fig. 13 Configuration of IPM

The IPM consists of P/M, G/D, and VCU ECU for the motor, generator, and VCU, heat sinks, and so on. When the voltage or current applied to the P/M is increased, the chips inside the P/M generate more heat. Even though more chips are needed, increasing their number also increases the volume of the PCU. In order to achieve the targets for increased output and decreased PCU volume, the heat dissipation of the P/M was increased and the temperature and number of the chips were reduced.

Figure 14 shows the structure of the P/M substrate. The conventional substrate structure has an insulating substrate and heat-dissipating plate connected by solder, and the substrate connected to the heat sink by thermal compound placed between them. The heat-dissipating structure adopted here eliminates the heat-dissipating plate and thermal compound, instead connecting the insulating substrate directly to the heat sink by means of solder for a direct cooling-type P/M. In the case of a direct cooling structure, the linear expansion differential between the insulating substrate and the heat sink causes greater stress on the solder than in the conventional structure, but the structure here uses high-strength lead-free solder to assure durability equal to that of the conventional structure. The adoption of a direct cooling structure achieves a 24% enhancement of heat-dissipation performance and, as shown in Fig. 15, fewer chips and greater compactness.

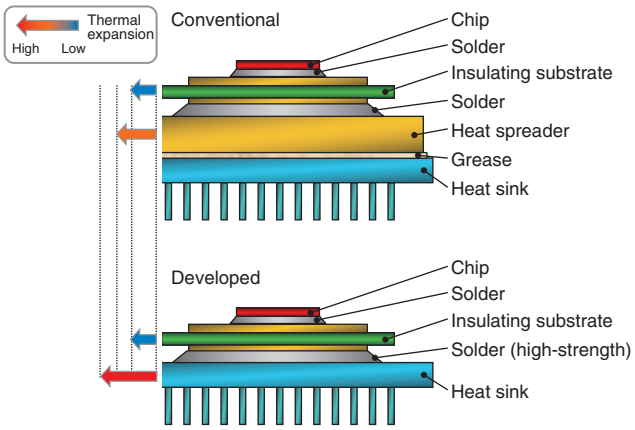


Fig. 14 Structure of P/M substrate

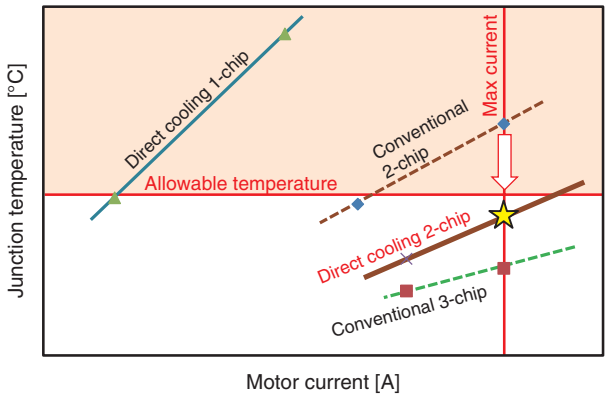


Fig. 15 Comparison of P/M substrate characteristics

4.3. High-Voltage Connectors with High-Current Capability

Figure 16 shows the internal terminal structure of the DC and three-phase connectors that attach to the PCU. A conventional terminal structure has a male terminal that fits against a contact area on the female terminal side and was clamped in one direction to provide the contact area. Here, however, the male terminal was made into a cylinder that fits into a contact area on the female terminal side with a cross-section that has a circular arc and is clamped toward the center so that the number of contacts (the contact area) is increased. These measures were able to halve the contact resistance, support the higher output resulting from the increase in current, and make the PCU compact enough to install in the engine compartment. Compared to conventional connectors, the weight and volume per ampere were reduced 30% while doubling the allowable current.

4.4. Enhancing the IPM for Higher Efficiency

An Insulated Gate Bipolar Transistor (IGBT) capable of high-power, high-speed switching was adopted as the switching device for the IPM. IGBT performance is one of the factors with a large influence on PCU efficiency. The IPM in this system implements loss reduction on the IGBT. The IGBT adopted here has the P-base localized in the surface structure and the gate placed differently (Fig. 17). This

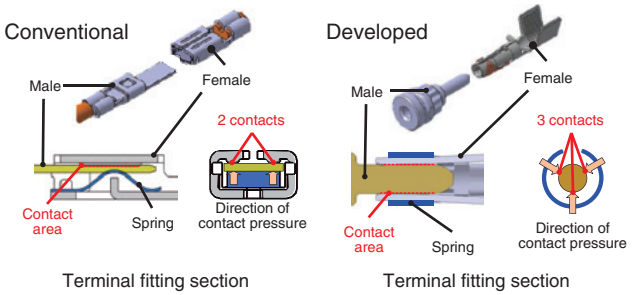


Fig. 16 Structure of high-voltage connector

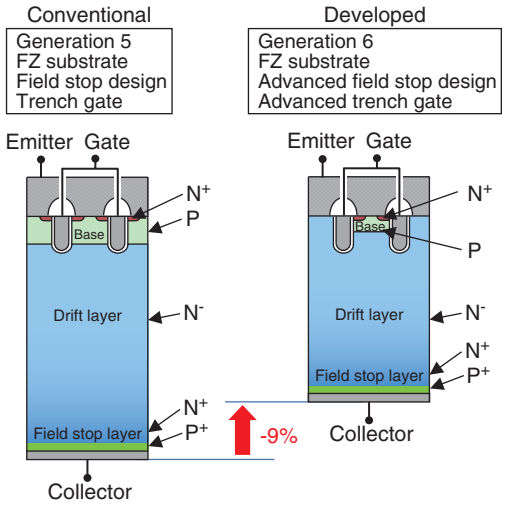


Fig. 17 Structure of IGBT

structure does not lose the carrier collection effect while enhancing the turn-on di/dt controllability and enabling application of the low-resistance N-drift layer. This limits oscillation during turn-off while achieving a 9% reduction in the thickness of the device and a 20% enhancement in loss characteristics[5].

5. Performance

Figure 18 shows the achieved motor performance and motor efficiency with the PCU. Using a PCU that achieves maximum output of 400 kVA and a voltage increase to 700 V, the motor achieves maximum torque of 307 Nm, maximum output of 124 kW, and maximum speed of 12584 rpm. The motor and PCU together achieve a maximum efficiency of 96%. In addition, controlling the voltage to maximize the high-efficiency area expands the high-efficiency area into the large low-load area, achieving enhanced efficiency in the normal operating area.

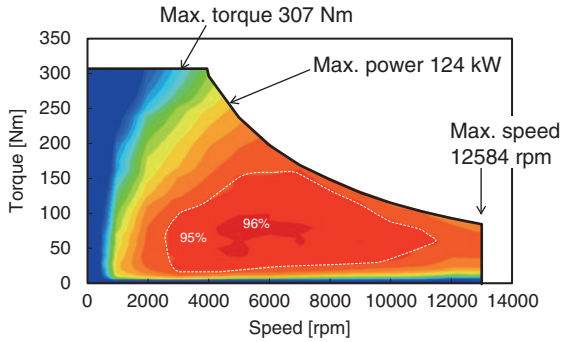


Fig. 18 Motor performance and efficiency with PCU

6. Conclusion

The motor and PCU were developed in order to achieve a balance between the joy of driving and measures to address climate change and energy issues. This achieved the following:

(1) Motor given higher torque, higher output, and higher efficiency by using reluctance torque and raising the voltage
(2) Higher rotor speed achieved by rotor slit construction that reduces stress
(3) Stable actuation of the motor achieved by oil cooling system
(4) Increased system voltage to 700 V by installation of VCU, and higher PCU output by enhancing IPM heat dissipation and adopting high-voltage connectors with high-current capability
(5) Enhanced PCU compactness by increasing IPM heat-dissipation performance and unifying parts with identical functions
(6) Enhanced IPM efficiency and compactness by adopting low-loss IGBT

Adoption of the above technologies achieved maximum torque of 307 Nm, maximum output of 124 kW, and maximum motor speed of 12584 rpm in the motor, and output of 400 kVA and volume of 11.5 L for the PCU, together with efficiency of 96% for the motor and PCU combined.

References

(1) Hotrie, T., Kishi, T., Hasegawa, O.: Development of IMA System for New CIVIC Hybrid, Honda R&D Technical Review, Vol. 18, No. 1, p. 16-21
(2) Matsunaga, M., Fukushima, T., Ojima, K., Kimura, K., Ogawa, T.: Fuel Cell Powertrain for FCX Clarity, Honda R&D Technical Review, Vol. 21, No. 1, p. 7-15
(3) Ide, H., Sunaga, Y., Higuchi, N.: Development of SPORT HYBRID i-MMD Control System for 2014 Model Year Accord, Honda R&D Technical Review, Vol. 25, No. 2, p. 33-41
(4) Morimoto, S., Ueno, T., Takeda, Y.: Wide Speed Control of Interior Permanent Magnet Synchronous Motor, T. IEE, Vol.114-D, No. 6, p. 668-673 (1994)
(5) Onozawa, Y., Nakano, H., Otsuki, M., Yoshikawa, K., Miyasaka, T., Seki, T.:Development of the next generation 1200V trench-gate FS-IGBT featuring lower EMI noise and lower switching loss, in Proc. 19th ISPSD, p.13-16 (2007)

■ Author ■



Jiro KUROKI



Hiroshi OTSUKA

Development of Li-ion Battery for SPORT HYBRID

Yoshikazu OHNUMA* Koichi TAKAHASHI* Tsuyoshi MATSUDA*

ABSTRACT

A lithium-ion battery was developed to meet the performance required by Honda SPORT HYBRIDs.

The surface area of the electrode was expanded and the amount of active material applied was increased to enhance cell performance. This achieved 63% higher output at -10°C and 26% higher output and 6% higher capacity at 25°C compared to the previous cell. In addition, mounting compatibility with existing vehicles was realized by keeping the same cell outline dimensions and voltage behavior. The module length in the cell stacking direction was reduced by 7% compared to the previous structure by changing the materials and shapes of the end plates and frames, and by changing the structure used to hold the cells.

1. Introduction

Petroleum resource reserves are finite, and there are concerns over depletion. In addition, the continuous evolution of technology to increase automobile fuel efficiency is also necessary from the viewpoint of effective use of resources. However, customer demands for automobile product appeal are diversifying, and the need to provide driving enjoyment on a par with conventional automobiles remains high even for low-fuel-consumption vehicles.

Hybrid electric vehicles (HEV) are typical low-fuel-consumption vehicles, and are equipped with traction motors, dedicated batteries and other devices in addition to internal combustion engines. The combination of these devices reduces automobile fuel consumption by increasing the combustion efficiency of the internal combustion engine and by recovering deceleration energy. In addition, acceleration performance can also be realized that makes use of motors with responsiveness and torque characteristics that differ from those of an internal combustion engine.

Honda has developed and sold HEV equipped with an Integrated Motor Assist (IMA) system classified as a parallel type. The IMA system features light weight, a compact size and low cost, and cumulative worldwide sales had reached the one million unit mark as of the end of September 2012.

In addition, the company has created a lineup of three SPORT HYBRID systems as part of its EARTH DREAMS TECHNOLOGY, which is next-generation power train technology that realizes both excellent driving performance and high fuel efficiency. These are the one-motor SPORT HYBRID Intelligent Dual-Clutch Drive (SPORT HYBRID i-DCD), the two-motor SPORT HYBRID Intelligent Multi-Mode Drive (SPORT HYBRID i-MMD), and the three-motor SPORT HYBRID Super Handling - All Wheel Drive (SPORT HYBRID SH-AWD). The company aims to expand this lineup successively in the future in accordance with the demanded characteristics.

The IMA system used nickel metal hydride (Ni-MH) batteries since the 1999 model year Insight, but was changed to lithium-ion batteries (LIB) from the 2011 model year Civic Hybrid. LIBs feature 33% higher output and 30% lighter weight compared to Ni-MH batteries of the same voltage, which helps to further increase fuel efficiency[(1)].

IMA systems sold thus far have been designed with the engine as the main source of motive power and motors as auxiliary power sources, so the motor output was small and the battery output and capacity were also just enough to satisfy the required performance. However, the SPORT HYBRID lineup that will be expanded in the future are systems that also enable driving with only the motor, so even higher battery capacity and output will be required in the future. In addition, mountability should be enhanced by reducing the battery size to enable mounting in a wide range of models.

This development aimed to develop an LIB with a performance and size suitable for SPORT HYBRIDs that can also be mounted in a wide range of models. Furthermore, an additional goal was to realize specifications compatible with existing vehicles that use the IMA system.

* Automobile R&D Center

2. Development Goals

The smallest unit of a battery is called a cell, and multiple cells bundled in series are called a module. In addition, multiple modules connected in series are called a pack, with the number of modules connected in series varying in accordance with the voltage required by the system (Fig. 1).

Cell performance needs to be enhanced while maintaining the same outline dimensions and voltage characteristics in order to secure both the high performance required for SPORT HYBRIDs and compatibility with existing vehicles. Therefore, this development investigated methods of increasing the output density and capacity density, while using the same cell outline dimensions and active materials at the positive and negative electrodes as those of the previous cell.

A goal for module development was to enhance mountability by reducing its size. but the cell outline dimensions were not to be changed, so a smaller module size was realized by changing the shapes of components other than the cells.

The following three points were set as development goals when developing an LIB for SPORT HYBRID systems.
(1) Increased cell output and capacity
(2) Cell compatibility with existing vehicles
(3) Reduced module size

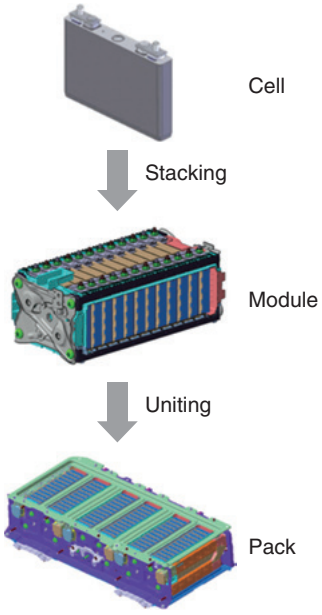


Fig. 1 Battery components for HEV

3. Cell

3.1. Cell Configuration

Figure 2 shows the structure of the cell mounted in the battery. The LIB consists of positive and negative electrodes made by coating metal foil with active materials, current collectors that connect the positive and negative electrodes with the respective terminals, an electrolysis solution consisting of an organic solvent and an electrolyte, a separator that functions to hold the electrolysis solution and insulate the electrodes from each other, and a container that encloses the aforementioned components.

3.2. Enhanced Cell Performance

The surface area of the electrodes was expanded to achieve the development goal of increased cell output.

Output is calculated as the product of the current and the closed circuit voltage. The size of the allowable battery current I can be expressed by Eq. (1)[2].

$$I = n\,F\,A\,k\,C_M\,C_E \exp\left(n\,\alpha\,F\,\eta\,/\,RT\right) \quad (1)$$

n: number of electrons participating in the battery reaction, F: Faraday constant, A: effective surface area of the electrode, k: reaction rate constant, C_M and C_E: Concentrations of the electrode and the substance reacting with the electrode, α: transmission coefficient, η: overpotential, R: gas constant, T: absolute temperature

Equation (1) indicates that the current flowing to the electrode increases together with the effective surface area of the electrode A, and that cell output can be increased without changing the active materials at the positive and negative electrodes.

The thickness of the substrates onto which the active materials are coated and the thickness of the separator were reduced and the electrode length was increased in order to expand the surface area of the electrode. In addition, reducing the separator thickness shortened the distance between the positive and negative electrodes, which suppressed the cell internal impedance[3], and the use of additives to form the film on the electrode surface also helped to increase the output.

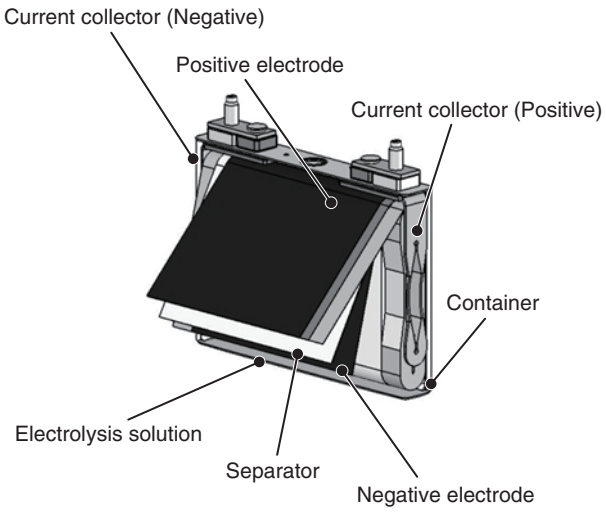


Fig. 2 Construction of cell

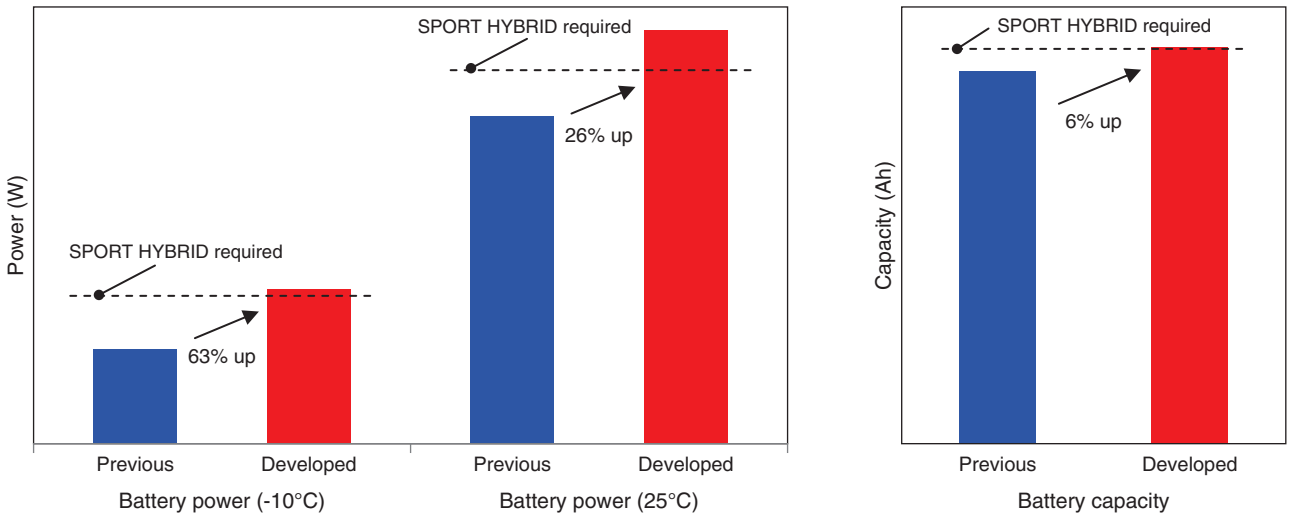


Fig. 3 Comparison of battery performance

The amount of active materials applied to the positive and negative electrodes was increased to achieve a higher cell capacity. The capacity is proportional to the amount of active materials applied[4], so the positive and negative electrode substrate thickness and the separator thickness were reduced to secure space, and the amount of active materials applied to the positive and negative electrodes was increased to increase the cell capacity.

As a result of the above methods, the developed cell achieves 63% higher output at -10°C and 26% higher output and 6% higher capacity at 25°C compared to the previous cell. These enhancements enabled achievement of the required performance targets for SPORT HYBRID systems (Fig. 3).

Enhanced cell performance was achieved by expanding the surface area of the electrode and increasing the amount of active materials applied. However, the volume of the cell container and the characteristics of the active materials at the positive and negative electrodes are the same as those for the 2011 model year Civic Hybrid. This means that the cell outline dimensions and voltage characteristics are also the same as those for the 2011 model year Civic Hybrid, so cell mounting compatibility was also achieved.

4. Module

4.1. Module Configuration

Figure 4 shows the construction of the module. The module consists of cells, which are the smallest battery unit, holders that position the cells and secure insulation and cooling air channels between the cells, springs that hold the cells, end plates, and frames.

Modules require strength sufficient to withstand external stress such as oscillation of the cell and the module itself due to vibration while driving, and internal stress such as cell expansion.

4.2. Reduced Module Size

Cast magnesium end plates were used to reduce the weight of modules mounted in the 2011 model year Civic Hybrid, and each module consisted of 10 stacked cells.

The developed module assumed application to a wide range of models, and size reduction was set as a goal. In addition, the number of stacked cells was increased by two cells to 12 cells per module in order to mount the optimum quantity for SPORT HYBRID systems. This increased the stack length, which greatly increased the torsional displacement.

The frames were changed to box structures positioned on the four corners of the end plates, and a four-point cell holding structure was also used to suppress the cell torsional displacement and disperse the coupling stress between the frames and end plates (Fig. 5).

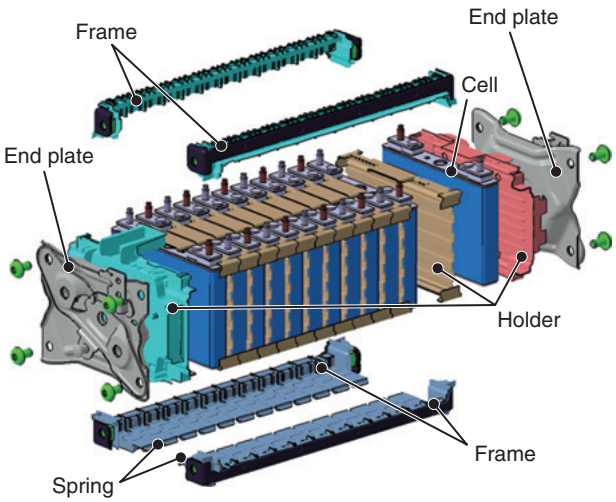


Fig. 4 Construction of module

These measures kept the maximum stress on the end plates and frames within the limits and successfully addressed the issues produced by increasing the number of cells.

The end plates were changed from cast magnesium to steel plates and the thickness was reduced in order to reduce the module size (Fig. 6). As a result, the end plate thickness could be reduced by 37%. Note that the increase in module component weight (excluding the cells) due to the change in end plate materials was offset by changing the materials and shapes of the frames and holders, and the same module component weight was achieved as that of the modules mounted in the 2011 model year Civic Hybrid.

The number of developed modules mounted can be changed in accordance with the demands of the hybrid system. Six of the developed modules are mounted in the SPORT HYBRID i-MMD 2014 model year Accord Hybrid (Fig. 7), and reducing the module size achieved a 7% reduction in length in the cell stacking direction compared to the previous structure.

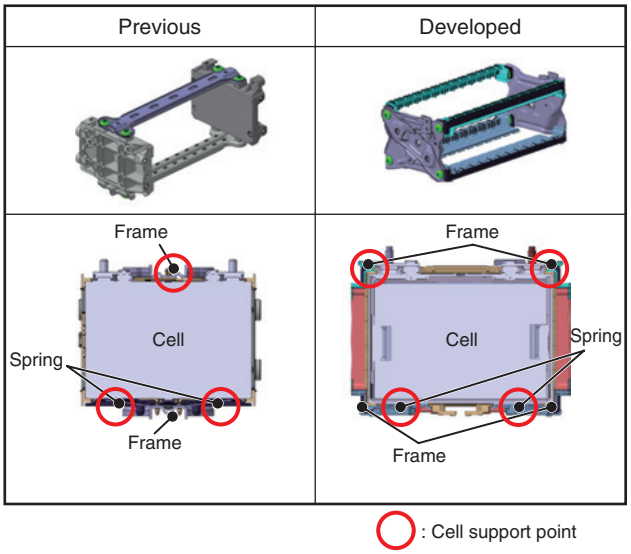


Fig. 5 Cell support points

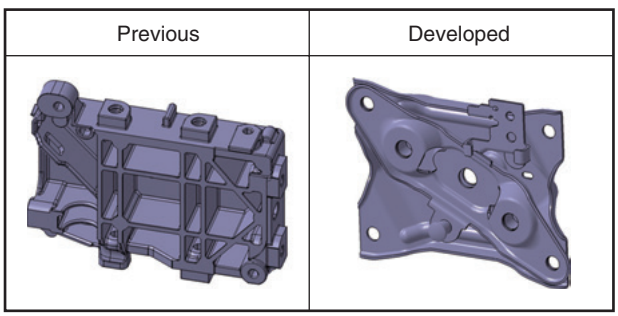


Fig. 6 Module end plate

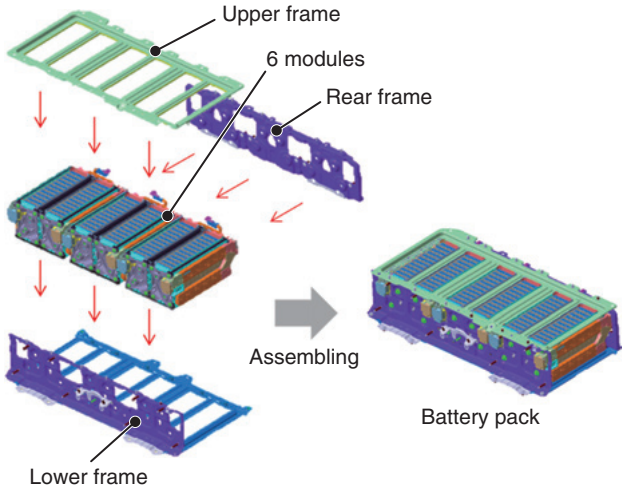


Fig. 7 Battery pack for 2014 model year Accord Hybrid

5. Conclusion

An LIB was developed for the SPORT HYBRID lineup, and the three set development goals were achieved to the following degrees.

(1) Increased cell output and capacity
The electrodes were lengthened, the surface area of the electrodes was increased, and the amount of active materials at the positive and negative electrodes was also increased. This resulted in 63% higher output at -10°C and 26% higher output and 6% higher capacity at 25°C compared to the previous cell, which achieved the performance required by SPORT HYBRID systems.

(2) Cell compatibility with existing vehicles
Cell output and capacity were increased without changing the active materials at the positive and negative electrodes, so the voltage characteristics are the same as those of existing vehicles. In addition, the cell outline dimensions were not changed, so cell compatibility with existing vehicles was achieved.

(3) Reduced module size
Changing the end plates from cast magnesium to steel plates enabled reducing the length in the cell stacking direction by 7% compared to the previous structure, and achieved a smaller module size.

The developed product is scheduled for successive adoption from the 2014 model year Accord Hybrid.

References

(1) Komoda, S., Nishida, Y., Maruno, N.: Development of Lithium ion Battery System for Hybrid System, 2011 JSAE Annual Congress Proceedings, No. 107-11, p. 1-4

(2) Takamura, T., et al.: Denchi Hanno no Kihon, Niji-denchi no Kaihatsu to Zairyo, CMC Publishing Co.,Ltd., p. 3-5, (2002) (in Japanese)

(3) Sato, N., Sakai, T.: Richiumu-ion Denchi no Dosa Genri to Tokucho, Jidosha-yo Dai-yoryo Niji Denchi, CMC Publishing Co.,Ltd., p. 68-75, (2003) (in Japanese)
(4) Ogumi, Z.: Separeta no Kihon Kino to Yokyu Tokusei, Saishin Niji Denchi Zairyo no Gizyutsu, CMC Publishing Co.,Ltd., p. 100-101, (2002) (in Japanese)

■ Author ■


Yoshikazu OHNUMA


Koichi TAKAHASHI


Tsuyoshi MATSUDA

Development of Robotic Lawnmower Miimo

Toshiaki KAWAKAMI* Hiroshi KOBAYASHI*
Makoto YAMAMURA* Shuhei MARUYAMA*

ABSTRACT

Development of the robotic lawnmower Miimo was pursued in response to people's need to make their lawn look nice without spending time and effort on it. The product was developed on the three concepts of giving people a sense of security about letting it do the work, making it simple for people to use, and allowing people to spend their time in comfort.

In order to enable the lawnmower to continue its work automatically without imposing a burden of labor on the customer, the unit was given the capability to recognize its work area, to automatically recharge its battery, and to avoid obstacles it might encounter. In order to maintain an attractive-looking lawn, the product assures finish quality by adopting movement patterns that cause the mower to work through the entire area thoroughly, a mowing method with a mulching system that distributes mown grass over seedbed soil, and movement patterns that avoid leaving ruts. Because the product works automatically, a conceptual approach of functional safety was built into the system so that there will be nothing to worry about even if someone other than the user approaches the machine.

1. Introduction

Honda brought the HR21 walk-behind lawnmower to the market in 1978. The HR21 established the qualities of ease of use and reliability, giving Honda lawnmowers a foothold in the European and American markets.

With the worldwide aging of populations and heightening of environmental awareness in recent years, Honda has worked actively as a leading global corporation to seek greater environmental compatibility in such things as simpler garden maintenance and reduction of garden waste. Unlike the maintenance of garden trees and flowers, people see mowing lawns as hard work and have sought lawnmowers that require less time and trouble in order to ensure their leisure time.

This paper introduces the robotic lawnmowers Miimo 300 and Miimo 500 (Miimo), which were developed in response to people's desire to have attractive-looking lawns without spending time and labor on them. Figure 1 shows the external appearance of the Miimo, and Table 1 shows the basic specifications.

Sales in the robotic lawnmower market have been trending upward consistently and rapidly, going from about 10000 units annually in the European market in 2006 to 90000 units annually in 2012. The major lawnmower manufacturers in Europe have also been actively participating in the market. Figure 2 shows the changes in the annual number of robotic lawnmower units sold in Europe.

Table 1 Basic specifications

Name			Miimo300	Miimo500
Model			HRM300	HRM500
Overall length		mm	645	
Overall width		mm	550	
Overall height		mm	275	
Wheelbase		mm	300	
Mass		kg	11.5	11.8
Wheel diameter	Front wheel	mm	100	
	Rear wheel	mm	200	
Running speed (Forward)		$m \cdot s^{-1}$	0 - 0.55	
Trimming width		mm	220	
Trimming height		mm	20 - 60	
Blade rotating speed		min^{-1}	2200	
Blade type (number of blades)			Swing-back type (3 blades)	
Motor performance	For driving	W	10.8 x 2	
	For mowing	W	25.3	
Battery	Type		Li-ion	
	Capacity		22.2V x 1.8Ah	22.2V x 3.6Ah
Transformer output current		A/VA	2.3 / 60	



Fig. 1 Robotic lawnmower Miimo

* Power Products R&D Center

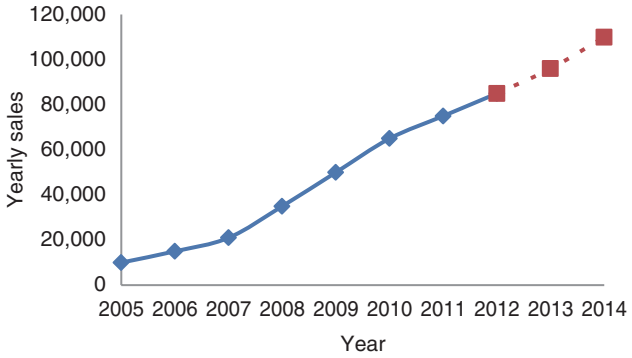


Fig. 2 Prediction of European robotic lawnmower market growth

2. Development Goal

Development of the Miimo followed the three product concepts of giving people a sense of security about letting it do the work, making it simple for people to use, and allowing people to spend their time in comfort. These were pursued with the following objectives:

(1) Definite capability to continue work without imposing a burden of time and effort
(2) Works with a high quality of finish to maintain an attractive-looking lawn
(3) Reliability as a gardening partner

3. Miimo Configuration

The Miimo is made up of a transformer that converts commercial electric power to supply as safety extra-low voltage (SELV) or lower, a docking station for recharging, and the mower that runs and mows automatically. The docking station is also able to output a signal to a wire that marks the working area boundary. Figure 3 shows the configuration.

The mower powertrain is made up of three motors that drive the blade and the two rear driving wheels, the battery that serves as power supply, and the electronic control unit (ECU). The mower is also equipped with a display unit, which shows the mower's status and allows input of settings, and sensors that enable independent operation. Figure 4 shows the mower components.

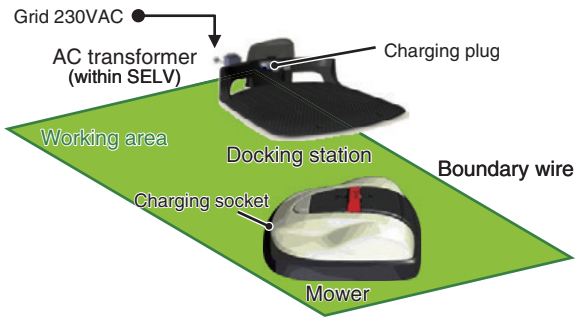


Fig. 3 Miimo configuration

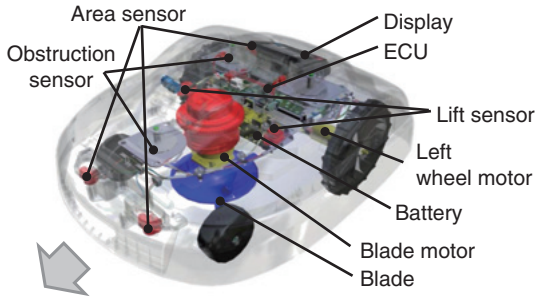


Fig. 4 Mower components

4. Technology for Automatic Operation

4.1. Functions for Continuous Performance of Work

In order to perform work automatically, the robotic lawnmower needs functions for recognition of the work area, assurance of power supply, and ability to continue working even in the presence of obstacles.

4.1.1. Detection of work area

In order for the robotic lawnmower to work automatically, it needs to recognize the area where it is to perform its mowing work. As it is essential that the mower not move outside that area, the area where the Miimo is supposed to work is outlined with an electric wire.

The mower has permission to work only inside that wire, and it is configured so that when it reaches the wire while working, it turns back without crossing over the wire. When the wire is broken or when the mower is placed outside the wire, the mower will stop.

A method of detecting magnetic field changes was adopted in order to recognize whether it is within the area. Specifically, this is done by sending a current pulse from the docking station in a clockwise direction through the wire that marks the area boundary. When this is done, the downward magnetic field intensifies while the current is increasing, and diminishes while the current is decreasing on the inside of the wire. On the outside of the wire, the magnetic fields change inversely with the inside.

This minute change in the magnetic field is amplified and filtered to enable the mower to recognize the inside and outside of the work area. Figure 5 shows the receiver circuit and Fig. 6 shows the waveform after amplification.

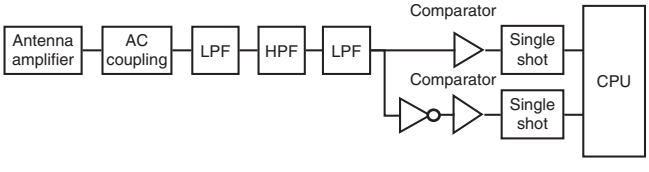


Fig. 5 Area signal receiving circuit

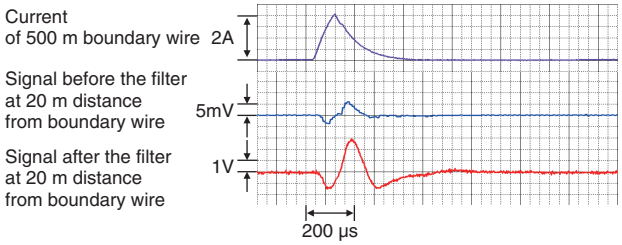


Fig. 6 Current of boundary wire and received signal

4.1.2. Li-ion battery

The Miimo uses a battery as its power supply while it is mowing. The mower carries on work according to a set-up by the user, but when the battery charge becomes low while the mower is working, the mower is set to return to the docking station automatically to recharge itself.

Li-ion batteries were adopted for their weight and service life. Figure 7 shows the change in capacity of single-cell Li-ion and NiMH batteries in charge-discharge cycle testing.

In order to simplify the circuit, voltage balance control between cells is not implemented. Deterioration of cell voltage balance is mitigated by limiting charging so that the battery does not receive a full charge. This also has the effect of mitigating degradation. As a further measure to mitigate degradation, charging is stopped when the battery reaches 60% capacity so as not to stay on standby in a high-capacity state. The battery is then charged to 100% capacity before starting work.

The battery pack also has a built-in battery management system (BMS) that monitors overcurrent in the battery pack as well as overvoltage and low voltage for each cell. The battery is further equipped with a precharge function for when the battery is discharged to a low-voltage state.

Figure 8 shows the change in battery pack capacity from charge-discharge cycle testing. It was confirmed that the battery pack retained 70% or better capacity after 1500 cycles, which is equivalent to two years of use, without cell balance control.

4.1.3. Avoidance of obstacles

When the mower collides with an obstacle, it stops moving forward and then bypasses the obstacle before continuing its automatic work. If the mower has been lifted off the ground, it then stops not only its drive wheels but also its mower blade. Once it is returned to ground level, either through a bypassing maneuver, it then continues with its automatic work.

4.2. Functions for Maintaining Attractive-Looking Lawns

In order to maintain attractive-looking lawns, the lawnmower needs to work thoroughly throughout the entire area. In order to produce an attractive-looking finish, a mowing system suited to continuous operation is needed, and footprints also have to be taken into consideration.

4.2.1. Straight-forward movement control

The Miimo movement while working is straight forward. When it reaches the area boundary, it turns and again moves straight forward until it reaches the boundary. The Miimo needs to repeat this operation to move over the entire work area and cover it thoroughly. In order for the Miimo to work on wet sloping lawns that are slippery, it needs to move straight forward on this kind of surface, as well. Otherwise it will not be able to climb to the top of a slope nor work efficiently over the entire area.

In order for the Miimo to move straight forward under these circumstances, straight-forward movement control is implemented. The straight-forward movement control detects angular velocity and measures it cumulatively so that even if the Miimo slips, it will sense the deviation in direction, apply fuzzy logic control to the magnitude of the turn, and regain straight-forward movement.

4.2.2. Mower movement patterns

In order to maintain a large lawn in an attractive condition, it is important to mow the entire area thoroughly. If it were to mow each area in order like a walk-behind lawnmower operated by a human being, there would be no wasted motion. Depending on the shape of the work area, however, a regular movement pattern could result in the mower moving repeatedly across some parts of the determined path. It was therefore decided to adopt both a reciprocating working pattern suited to mowing a single section of lawn area and a random pattern for thoroughly

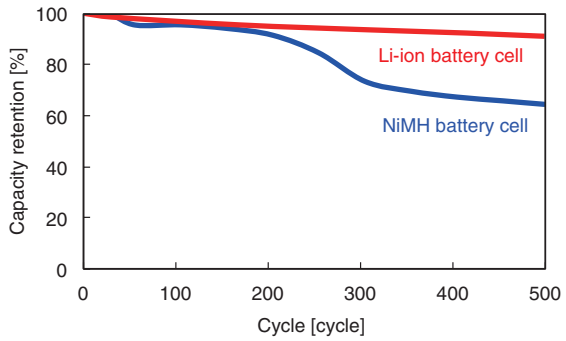


Fig. 7 Cell battery cycle performance

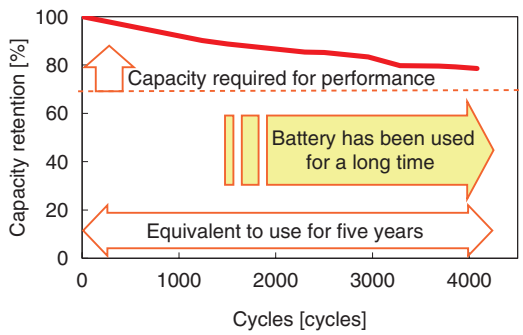


Fig. 8 Battery pack cycle performance

mowing a larger area with a more complex shape.

Making wider-angled turns allows the mower to follow the area boundary more easily. Acute-angled turns characteristically allow the mower to travel to the center of the area more easily. In deciding the random turning pattern, the range of acute-angled and wide-angled turns was taken as a parameter. In addition, values for movements that would efficiently cover variously shaped work areas were simulated. The model was made up of movement patterns, mower body model, and area model. The model outputs the movement area and uneven patches. A parameter optimization tool was applied to these output results to derive optimal values. Figure 9 shows a conceptual diagram of the simulation. Figure 10 shows confirmed area models.

Three patterns supporting a variety of different lawn shapes were configured.

(1) The random pattern is effective over large areas and was optimized by simulation.
(2) The directional pattern works in a reciprocating manner that concentrates operation in a designated zone.
(3) The mixed pattern is capable of well-balanced work that combines the random and directional movement.

Figure 11 shows a conceptual diagram of the movement patterns.

Figure 12 shows the motion capture results for the Miimo movement filling in the mowing area. Every mode yielded results as obtained in simulation. Areas that have been mowed only once are shown in yellow, and areas mowed two times or more are in red.

4.2.3. Mulching work

The mown grass is reduced to minuscule fragments and scattered over the seedbed soil at the grass roots. This mulching process allows the mown grass to decompose quickly, making practical use of it as fertilizer.

The mowing component has a fan structure by which the mown grass is distributed equally. This enhances its mulching value. Figure 13 shows the structure of the mowing component.

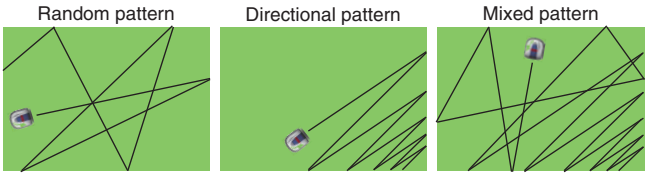


Fig. 11 Movement pattern

Mowing time [min]	5	10	15	20	25	30
Random pattern						
Mowing area [%]	51	73	84	91	95	97
Directional pattern						
Mowing area [%]	47	74	87	94	97	98
Mixed pattern						
Mowing area [%]	49	72	84	91	95	98

Fig. 12 Grass cutting in each pattern

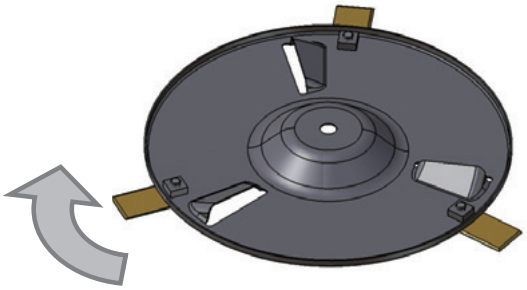


Fig. 13 Mowing part structure

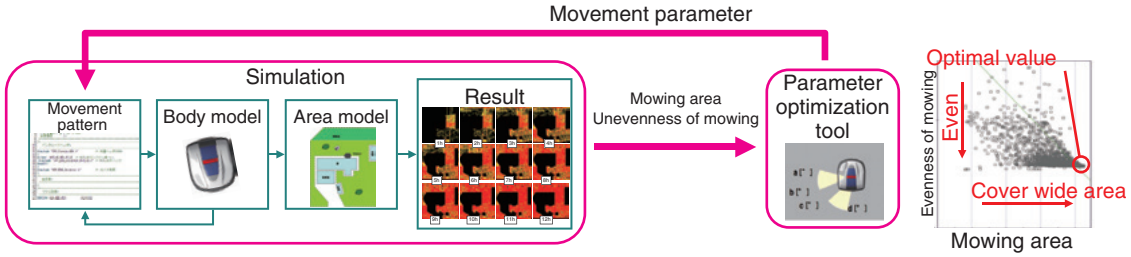


Fig. 9 Movement pattern simulation

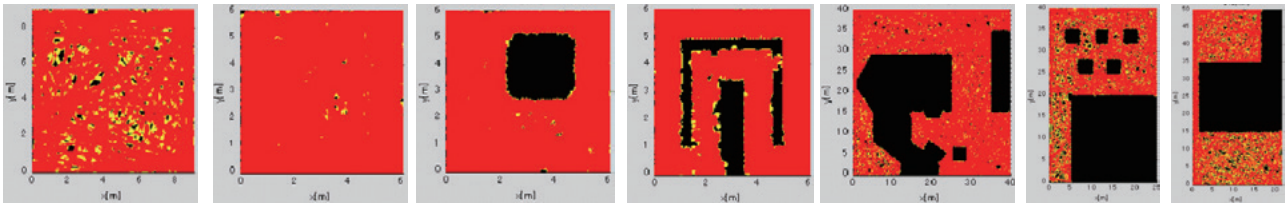


Fig. 10 Area model

Figure 14 shows the results from flow field analysis of the effect of the fan using computer-aided engineering (CAE), and Fig. 15 shows the dispersibility. It has been confirmed that dispersibility is assured.

4.2.4. Return movement

The flow of mowing operation by the Miimo is as follows:

(1) When the configured work starting time arrives, the mower moves away from the docking station and moves to the designated area.
(2) The mower begins working in the designated area.
(3) When the battery charge becomes low, the mower stops working and returns to the docking station.
(4) At the docking station, the mower charges to 100%.
(5) When the charging ends, the mower again moves to the designated area.
(6) The mower begins working again in the designated area.
(7) When the configured work ending time arrives, the mower returns to the docking station.

This includes movement from the docking station to the designated area and movement to return to the docking station. The important point about movement to the docking station is that return is definitely needed in order for the automated work to continue. The Miimo is therefore programmed to start the return movement while it still has adequate power to return.

These movements are made along the boundary wire around the work area. The Miimo does not mow grass during this movement, so a shorter distance makes for greater efficiency. Another concern is that repeated movement over the same places will cause ruts to develop. In order to reduce the distances traveled, therefore, the Miimo is configured to return by the reverse of the route it took when moving to the designated area. Figure 16 shows a conceptual diagram of return. The reasoning here is that the Miimo is configured to start work after traveling 40 m in an anticlockwise (ACW) direction. In this case, therefore, it is likely that when it is time to return, the Miimo will be in the area where it started working, so that returning to the docking station by a clockwise (CW) movement can reduce the movement distance in many cases.

In order to keep from always traveling over the same places, the Miimo also has the ability to shift its route slightly each time it moves. When the Miimo is not configured to move to a designated area, it will return to the docking station by alternating CW and ACW directions.

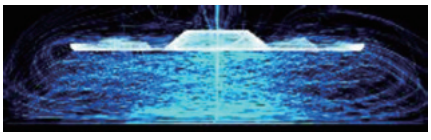


Fig. 14 Grass diffusion simulation



Fig. 15 Dispersibility by fan

Table 2 Stop functions

Functions	Description
Manual stop switch detection	Blade motor and wheel motor are stopped by pushing a stop switch
Lift detection	Lift sensor detects when user lifts up mower, and then it stops blade motor and wheel motor.
Tilt detection	When tilt sensor observes limit angle of inclination, blade motor and wheel motor are stopped.
Rollover detection	Rollover sensor monitors mower. Rollover sensor detects the rollover of mower, and then it stops blade motor and wheel motor.
Detection of area interior	Area sensor detects pulse from boundary wire and constantly monitors the status of inside/outside the area. Area sensor stops blade motor and wheel motor when pulse is not detected due to disconnection or short circuit of boundary wire.
Obstruction detection	Wheel motor stops at time of collision. After mower collides with person or obstruction, obstruction sensor maneuvers the mower to avoid them.

4.3. Functions for worry-free use

The robotic lawnmower carries out its work automatically even if no controlling person is present to supervise. When no person is present to supervise the robotic lawnmower's work, however, the possibility exists that someone other than the owner will unexpectedly approach the mower. This possibility had to be taken into consideration when developing the robotic lawnmower.

4.3.1. Functional safety

The stop functions shown in Table 2 are implemented in the Miimo by redundant design. The Miimo has been made capable of stopping even if there is a malfunction in the components for the stop function, and it is also made capable of detecting such a malfunction. The switches and sensor inputs are configured as dual systems, so that the Miimo will stop even with detection from only one side, and the system can compare one side with the other to detect malfunctions. The motor stoppers are also dual systems, so that the motors can be stopped even if only one of the stoppers operates, and feedback on the operating status of the stoppers enables detection of malfunctions.

In order to enable people to use the Miimo with a sense

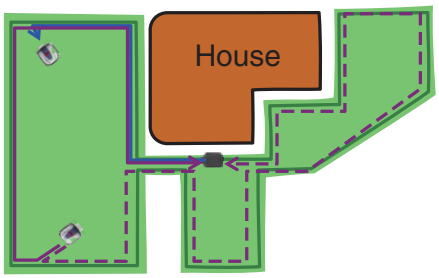


Fig. 16 Concept of return

of security, the working part that rotates and cuts grass has been positioned so that it is difficult to access and thus be touched. It is also capable of detecting collisions in every direction, and is able to detect being lifted up at any point around the periphery. This is achieved by mounting the cover onto the frame that holds the working components so that the cover can freely move laterally, longitudinally, and vertically in relation to the frame. Figure 17 shows the collision detection mechanism. Figure 18 shows the lift detection mechanism.

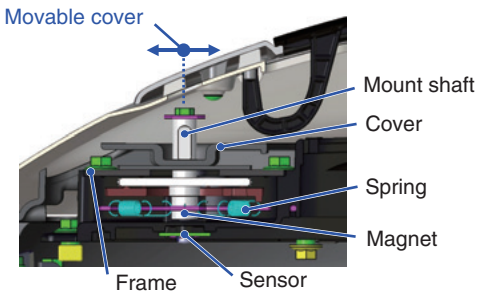


Fig. 17 Structure of collision detector

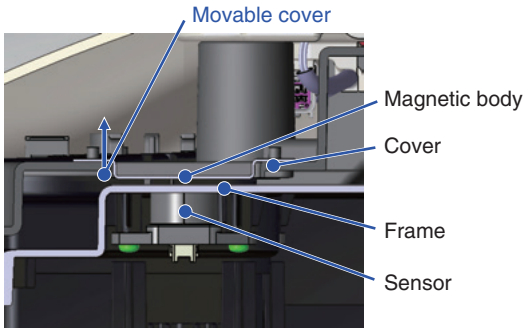


Fig. 18 Structure of lift detector

5. Conclusion

The development of this robotic lawnmower yielded the following results.

(1) Area detection enables the mower to continue working within the set working area without leaving that area. It is capable of working for extended periods without greatly reducing battery life. Further, if there is an obstacle in the working area, the mower can avoid it and continue working. The certainty of these results has been assured.

(2) The mower's straight-forward movement control and movement patterns enable it to work throughout the entirety of the working area. It is able to assure the finish quality of its work by mulching, and move without making excessive wheel tracks. These capabilities enable the mower to maintain an attractive-looking lawn.

(3) The mower incorporates the conceptual approach of functional safety and is able to detect collisions from all directions as well as to detect when it is lifted up anywhere around its periphery. This has produced a working machine that can be used with a sense of safety and security.

■ Author ■


Toshiaki KAWAKAMI


Hiroshi KOBAYASHI


Makoto YAMAMURA


Shuhei MARUYAMA

Development of ECOWILL PLUS Micro-cogeneration Unit with Autonomous Operation Function for Generating Electricity during Power Outages

Masanori TAKEISHI* Yoshinori NAKAGAWA*
Atsumu NAOI* Nobuyuki SASAKI*

ABSTRACT

A micro combined heat and power generation (micro-cogeneration) unit for residential use has been developed that can be used during power outages by manually starting a gas engine. This unit is equipped with a recoil starter as a device that enables starting without a battery or other auxiliary power during power outages. Start control for autonomous operation was established to enable engine start by recoil. In addition, currently sold cogeneration units output at 200 V in order to connect with the grid power, but the developed unit also has a dedicated 100 V output terminal for autonomous operation so that the generated power output from the unit can be used directly by electrical equipment during autonomous operation.

These technologies enabled development of a micro-cogeneration unit with autonomous operation function for generating electricity during power outages that maintains the same size and performance of currently sold micro-cogeneration units.

1. Introduction

Combined heat and power generation systems use a generator to generate electricity, and also recover and use the heat produced by the power generation process. These systems are viewed as an effective means of reducing CO_2 emissions, and have been widely used for some time centering on large-scale private industrial power generating facilities that also serve as heat sources.

Figure 1 shows an image of installation of a combined heat and power generation system for residential use in Japan.

Honda applied its engine and inverter generator technologies developed for power products, and released a micro combined heat and power generation unit (hereafter, micro-cogeneration unit) for residential use within Japan in 2003[(1)]. This was followed by the release of a second-generation model in 2006, and a third-generation model (hereafter, 2011 model year unit) that employs an extended expansion linkage engine (EXlink) to achieve even higher efficiency and a more compact size in 2011[(2)].

Since the Great East Japan Earthquake, Japan has experienced planned power outages and also a number of large-scale power outages due to natural disasters. As a result, the need has increased for equipment that supports power outages in Japan.

This paper introduces a micro-cogeneration unit for residential use with autonomous operation function for generating electricity during power outages. This is the ECOWILL PLUS configuration that adds a recoil starter function to the 2011 model year unit. Figure 2 shows an external view of the ECOWILL PLUS. (ECOWILL PLUS is a registered trademark of Osaka Gas Co., Ltd.)

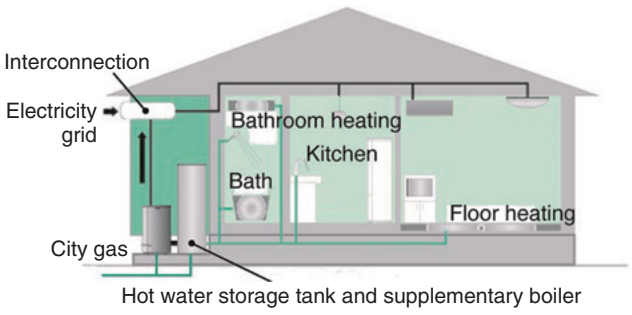


Fig. 1 General view of micro-cogeneration system

* Power Products R&D Center



Fig. 2 Micro-cogeneration unit with autonomous operation function for generating electricity during power outages

2. Development Goals

When developing the new unit, the goal was to add a starter function for autonomous operation with the minimum changes while maintaining the same size and performance as the 2011 model year unit currently being mass produced. Therefore, specifications were created that maintain the same normal operation performance as the 2011 model year unit, and also enable manual starting so that autonomous operation can be started to reliably supply electricity during power outages. In addition, the unit is connected to the grid power (commercial power), so single-phase 3-wire AC 100 V/ 200 V is output during normal operation. However, the electrical equipment assumed to be used during power outages is AC 100 V, so single-phase 2-wire AC 100 V is output[(3)].

3. Main Specifications and Features

3.1. System Configuration and Specifications

Figure 3 shows the structure of the newly developed micro-cogeneration unit, and Table 1 lists the main specifications.

Compared to the 2011 model year unit, the developed unit features a recoil starter and a dedicated output terminal for autonomous operation (maximum output 980 VA).

3.2. Starting Method during Power Outages

Micro-cogeneration units require external power to start up the starter motor when starting the engine. In contrast, the engine must be started without external power in order to perform autonomous operation for generating electricity during power outages. Therefore, possible starting devices during power outages include the following.

- A recoil starter such as often used in general-purpose engines

Table 1 Specifications

Output	Electricity	Grid connection	1000 W
		Autonomous operation	980 VA
	Heat		2500 W
Heat recovery			75°C hot water
Efficiencies (LHV)	Electricity		26.30%
	Heat		65.70%
Dimensions (L × W × H)			580 mm × 298 mm × 750 mm
Mass			76.0 kg
Noise	Grid connection		43 dB(A) / 1 m (JIS B 8627-1)
	Autonomous operation		47 dB(A) / 1 m (JIS B 8627-1)
Starting system	Grid connection		Starter generator
	Autonomous operation		Recoil starter
Engine	Type		GFV110 (EXlink)
	Displacement (Comp./Exh.)		110 cm^3 / 163 cm^3

Table 2 Comparison list

Item	Recoil starter	Starter motor	Starter generator
Power source	None (Manual)	Battery	Battery
Usability	Good	Good	Good
Mass-production experience	Good general purpose engine	Good general purpose engine	Good cogeneration unit
Installation ability	Fair Need operating space	Good	Good
Maintain-ability	Good	Fair Must replace battery	Fair Must replace battery
Layout feasibility	Good	Fair Need additional space	Fair Need additional space
Conformity to regulation	Good	Good	Good

- A kick-type starter such as used in motorcycles
- A starter motor with a battery such as used in automobiles
- A starter generator with a battery

In consideration of applicability to engine start, the recoil starter and the two methods that use batteries were compared. Table 2 shows the results, and ultimately the recoil starter was selected.

The 2011 model year unit was a more compact unit with little space around the engine, so it was a challenge

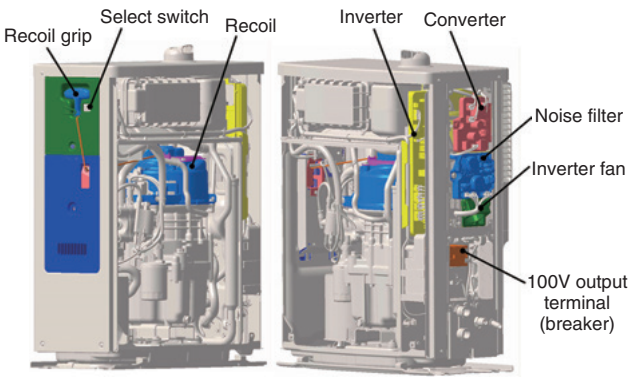


Fig. 3 Structure of micro-cogeneration unit

to mount a recoil starter such as used in general-purpose engines. Therefore, attention was turned to the cooling fan located on top of the alternator, and a new cooling fan and fan cover were developed and integrated with a recoil starter. This enabled mounting of a recoil starter without impairing the cooling function (Fig. 4).

In the recoil operation elements, the recoil grip is stored in the operation panel and protected by the switch panel cover to help prevent noise leaking from inside the engine room via the rope guide and to help prevent mishandling and tampering (Fig. 5).

3.3. Inverter for Autonomous Operation

The inverter of the current model connected to the grid power performs single-phase 3-wire AC 200 V output. However, when generating power by autonomous operation, both a grid connection output terminal and a separate dedicated output terminal are required to obtain domestic certification[4]. In addition, when performing autonomous operation, a dedicated inverter is required to produce high-quality AC 100 V output that can be used by general electric appliances at the dedicated outlet.

An inverter was therefore developed that enables both grid connection output and autonomous output. Also, when performing AC 100 V output, the current value is approximately twice that during normal operation, so the amount of heat generated by the surface-mounted devices on the inverter increases. For this reason, a compact electric fan that operates to cool the inverter only during autonomous operation was adopted.

3.4. Flow of Electricity during Autonomous Operation

Power needs to be supplied from a dedicated output terminal during autonomous operation, so recoil starting is performed after switching the plug of the hot water storage tank from the outlet for grid connection operation to the outlet for autonomous operation during power outages (Fig. 6).

Figure 7 shows the flow of electricity during normal operation and during power outages.

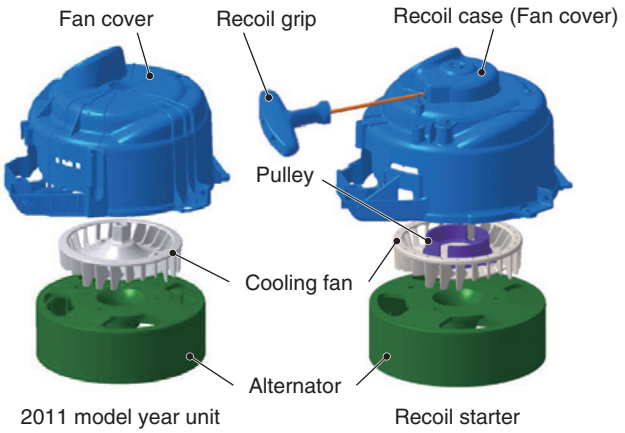


Fig. 4 Recoil starter

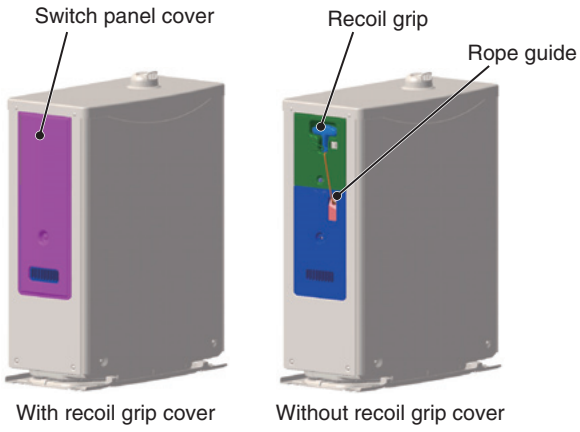


Fig. 5 Position of recoil grip

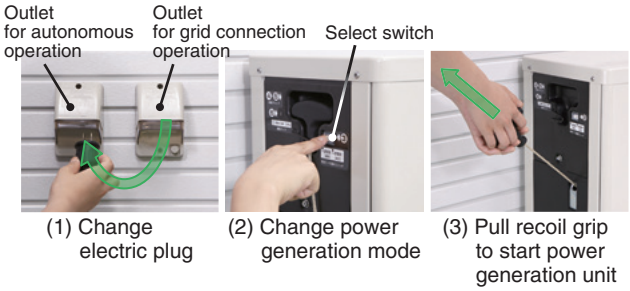


Fig. 6 Starting procedure

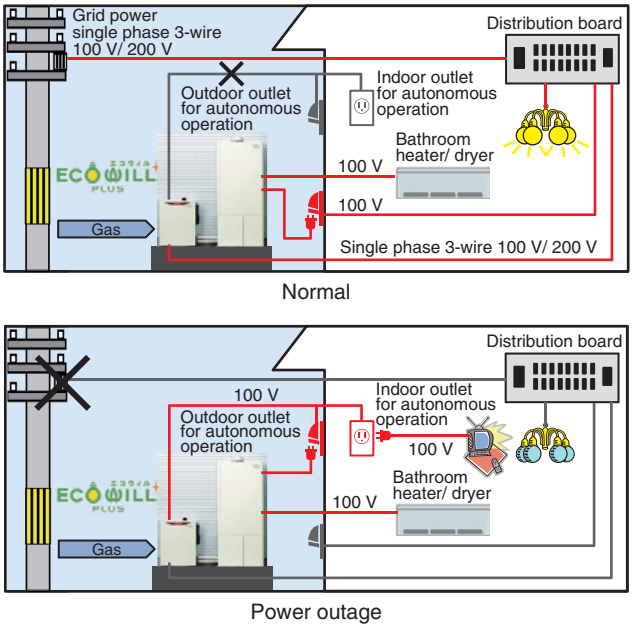


Fig. 7 Flow of electricity

4. Key Technologies

4.1. Recoil Starter

4.1.1. Required performance

The items required of the recoil starter are as follows.

- Durability in an engine room internal temperature (approximately 80°C) environment
- Able to be pulled even by someone operating the recoil starter for the first time

4.1.2. Method of achievement

The operating load and the rotating speed, that is to say the rope stroke, are conflicting requirements. However, due to the goals of this development, it was necessary to add a recoil starter function without changing the size of the enclosure. Therefore, the maximum pulley diameter that can be housed inside the cooling fan without impairing the engine cooling function was investigated. The flow of the cooling wind was analyzed (Fig. 8), and the results showed that the optimal maximum pulley diameter was 75 mm. This was then checked using an actual unit, and the results confirmed that equivalent cooling performance could be obtained. This enabled positioning a reel for winding the rope on top of the cooling fan (Fig. 9). The space required to perform the starting operation for autonomous operation was set at 1500 mm based on the installation conditions in the typical operating environment, so the reel diameter was set at 46 mm. This resulted in a required operating load around the 400-N, which is equivalent to the operating load required for a 400 cm^3 class general-purpose engine. In addition, the operating load was reduced by employing a large recoil grip and enhancing operability. Furthermore, the optimum rope pulling direction was derived using human models with 3D data, and the rope outlet shape was designed to reduce rope wear and other issues (Fig. 10).

In consideration of high-temperature degradation characteristics and durability, this development used aramid fiber rope as the recoil rope material instead of the nylon fiber rope used in many general-purpose engines. In addition, the boss of the recoil case that supports the reel receives a large load during the recoil operation. Therefore, strength at high temperatures and long-term durability were secured by making the aluminum recoil case.

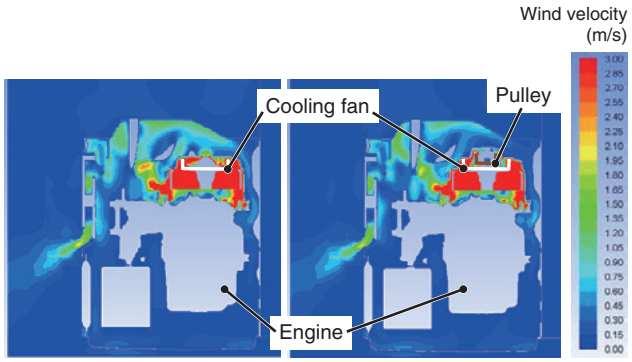


Fig. 8 Flow analysis of cooling wind

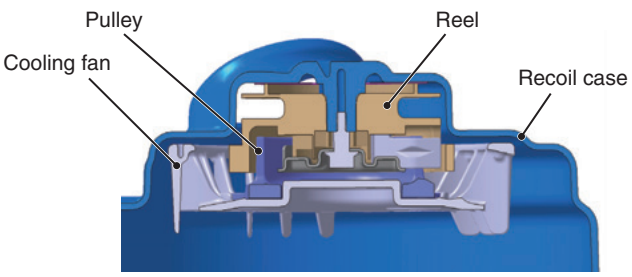


Fig. 9 Structure of recoil

4.2. Start Control for Autonomous Operation

4.2.1. Required performance

Conventional starting used the commercial power supply, and this power was sufficient for ignition. In contrast, during autonomous operation it is necessary to provide the number of ignition times required for engine start by supplying the power required to ignite the spark plugs to the ignition coil for approximately 1 second while the engine is rotating by recoil starting (Fig. 11).

4.2.2. Method of achievement

As mentioned above, it is necessary to provide the number of ignition times required for reliable engine start, so the ECU that controls ignition needed to be started quickly. In addition, it was also necessary to secure stable control power supply in order to provide the required number of ignition times. Therefore, a boost converter was positioned upstream of the ECU (Fig. 12). The boost converter functions when the engine speed exceeds 550 rpm as shown in Fig. 13. As a result, the ECU starts quickly and the ignition-enabled voltage period is lengthened, providing the number of ignition times required for engine start.

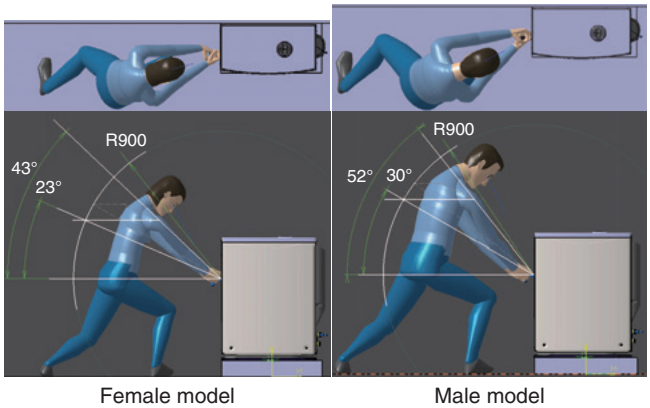


Fig. 10 Human model layout

4.3. Autonomous Operation Control

4.3.1. Required performance

Autonomous operation control requires the certification issue described in section 3.3. and also functions to protect the system against overload.

4.3.2. Method of achievement

Separate circuits were established for grid connection output and autonomous output. Then relays and inter-lock circuits for each output were provided on the circuit board to help prevent incorrect output. Figure 14 shows the block diagram.

In addition to the grid connection protective functions, dedicated protective functions for autonomous operation were added to protect against momentary overload that may occur during autonomous operation, or cases where the output rises gradually until it exceeds the maximum output. These functions operate to protect against low engine speed and momentary overload in the event of overload operation, and the engine is stopped when any of the protective functions has operated. The unit can be used again by disconnecting some of the electrical appliances connected to the outlet to reduce the load and then restarting the engine.

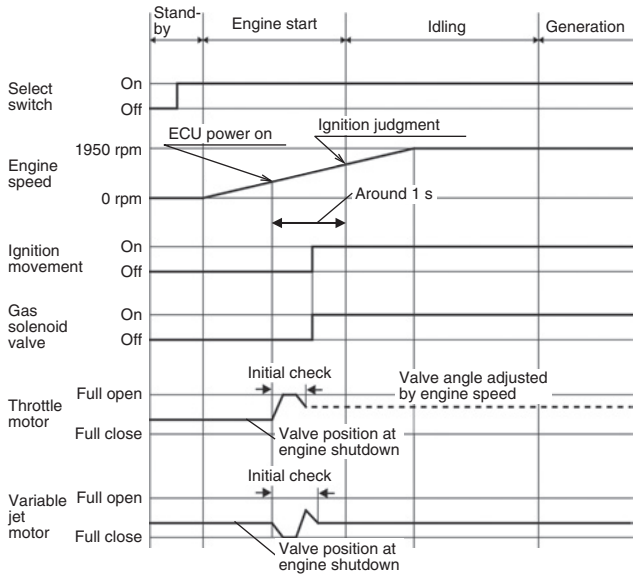


Fig. 11 Starting sequence of autonomous operation

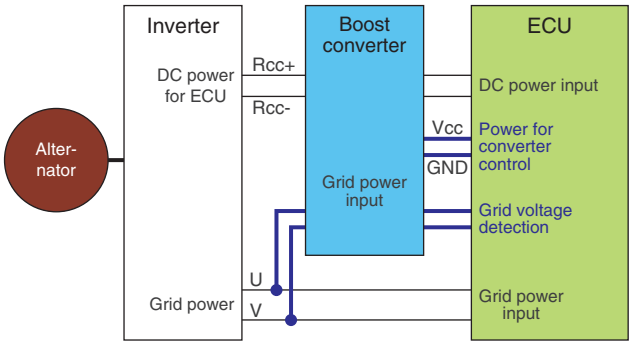


Fig. 12 Diagram of converter

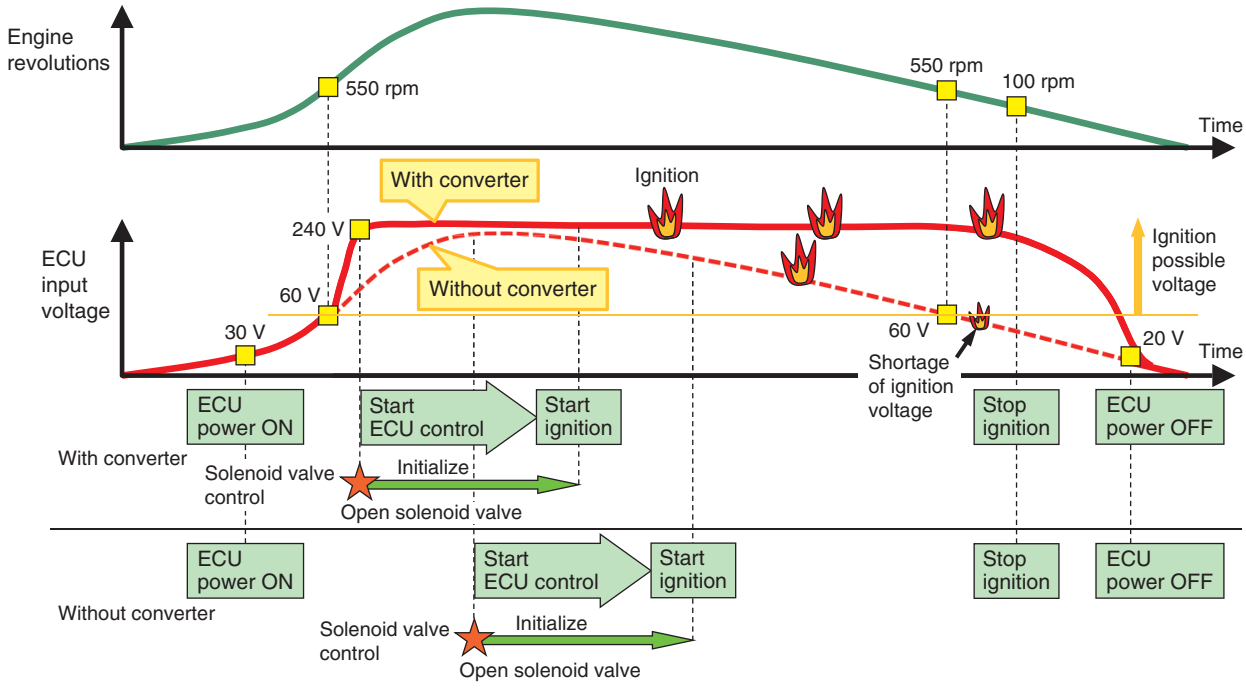


Fig. 13 Ignition timing

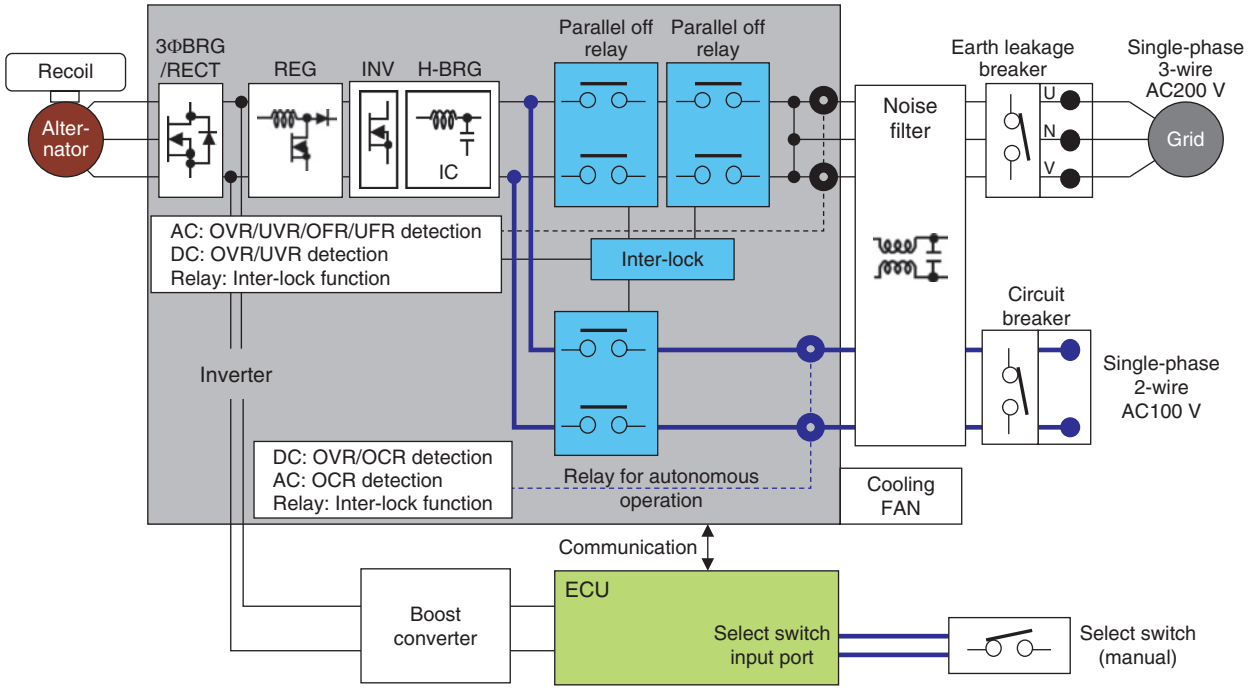


Fig. 14 Cogeneration unit block diagram

5. Conclusion

A micro-cogeneration unit for residential use that is capable of autonomous operation for generating electricity during power outages was developed that maintains the same size and high performance of the 2011 model year unit.

(1) A recoil starter with the durability to enable use whenever necessary was added. The operation load was set to enable starting even by someone operating the recoil starter for the first time, and start control for autonomous operation was established that enables reliable engine start.

(2) The use of Honda's inverter generator technology enabled supply of high-quality power so that electrical appliances with total power consumption of 980 VA or less can be used, even during autonomous operation.

References

(1) Takaishi, T., Ara, M., Togawa, K.: Introduction of Micro Combined Heat and Power Generation Unit for Residential Use, Honda R&D Technical Review, Vol. 15, No. 1, p. 53-58

(2) Takita, Y., Kono, S., Takada, H., Kitsu, K., Naoi, A., Tsuno, K.: Development of Micro Combined Heat and Power Generation Unit with Extended Expansion Linkage Engine, Honda R&D Technical Review, Vol. 23, No. 2, p. 30-38

(3) http://www.honda.co.jp/cogeneration/ecowillplus/

(4) Grid-connected Inverters (Power conditioners) for small distributed generation systems, Japan Electrical Safety & Environment Technology Laboratories (JET): http://www.jet.or.jp/en/products/protection/index.html

■ Author ■


Masanori TAKEISHI


Yoshinori NAKAGAWA


Atsumu NAOI


Nobuyuki SASAKI

Flat Belt Test System for Suspension and Tire Measurement

Tomonori SAKAI* Kaoru KUSAKA* Yuji SATO*

ABSTRACT

A new chassis testing system equipped with flat belt roadways for both left and right vehicle wheels has been developed and put into operation. This system is designed to be capable of comprehensive performance evaluation of vehicle suspension and tires.

Testing of suspension characteristics using actual vehicles requires many work-hours of testing on the proving ground in order to assure measurement accuracy and to reduce deviation from environmental factors. The use of the present system, however, enables enhanced development efficiency by replacing proving grounds test evaluations with testing of the system in a fixed environment and by shortening measurement time.

This test system can be transformed into three measurement modes: the first mode can measure suspension characteristics of the front or rear wheels of a vehicle; the second mode can measure suspension assembly characteristics by testing just a suspension system with tires; and the third mode can measure the characteristics of tires alone.

In actual vehicle testing, the vehicle behavior is measured under the influence of forces generated in both front and rear axles, which are dynamically coupled with each other through the vehicle's motion. It becomes difficult, therefore, to separately analyze the influences of the front and rear axle tire forces on vehicle dynamics. The present test system can measure the component forces and moments of each tire of front or rear axles separately with a vehicle body constrained to the ground, and can provide analytical information to improve vehicle dynamics performance.

1. Introduction

Vehicle developers and manufacturers have been increasingly required to develop more attractive products that achieve a balance between high environmental performance and the qualities of safety, comfort, and driving pleasure. Vehicle performance derives from combinations of a variety of different parts and components, and among various components, tires are one of the few parts that have significant influence across the range of vehicle handling and stability, ride comfort, noise and vibration, and fuel consumption, which are considered elements of chassis performance, and tires have recently been displaying a conspicuous shift toward lower rolling resistance coefficients (hereafter, lower RRC) in conjunction with the call for enhanced fuel economy.

In general, the shift toward lower tire RRC is accompanied by reduction in grip performance. In order to pursue higher chassis performance with such lower RRC tires, therefore, it is of great importance that a quantitative grasp of tire characteristics be obtained and that, on that knowledge, an optimal suspension be designed from the initial stages of the development.

Recently, the vehicle development period has been becoming shorter year by year in order to respond more quickly to customer needs, which are changing with the times. In place of running tests using prototype vehicles, therefore, development methods making use of computer simulation are progressively being introduced. Consequently, there is increasing demand for quantification of the characteristics of vehicle parts and components, including tires and suspensions, which are needed for these methods.

If sole reliance is placed on actual vehicle tests for the measurements that such quantification needs, then many work-hours have to be expended to assure the desired data accuracy in the presence of such disturbance factors as temperature, condition, and slight undulations of the road surface. For example, making quantitative comparisons of slight variations, such as differences in parts specifications, calls for the acquisition of vast quantities of data as well as statistical processing of that data in order to obtain sufficient accuracy as considered necessary for examination. Carrying out quantification for all of the various different parts becomes a serious issue in terms of development efficiency.

In that respect, although test bench measurement is

* Automobile R&D Center

limited by the measurable conditions available to it, it is able to keep variations resulting from disturbance factors and changes in the environment to a minimum, and it is capable of highly accurate and reproducible measurement. This approach is also well suited to quantification of the specifications and characteristics of parts and components for which measurement accuracy offers particular advantages, and when combined with simulation techniques, this approach enables investigation of optimal designs for a variety of different performance parameters.

At every stage of vehicle development, the influence on chassis performance of various parts and components of the chassis should be researched quantitatively in order for development to proceed. What this calls for, therefore, is not just the characteristics of the chassis as attached to the vehicle, but also quantitative characteristics analysis based on analysis of the characteristics of the suspension assembly alone, of the tires alone, and so on. For example, the suspension has stabilizer bars that link the left and right wheels together, and there are configurations that are structurally linked, as typified by the coupled beam suspension. In addition, quantitative analysis of the suspension assembly characteristics with the shock-absorbing function of the suspension included calls for reproduction of undulated road profiles. One example of a method for bench analysis of such characteristics used to date is to perform measurements of a tire mounted against a rotating drum. A drum has curvature, however, so that the contact patch shape of the tire would differ from the shape on the road, so there would be cases in which actual driving characteristics could not be represented.

With the aim of resolving the various issues described above, a suspension and tire test system has been developed. The system enables comprehensive measurement and analysis of chassis performance by the capability to measure the left and right tires of the suspension simultaneously on two flat belts and also by the excitation function of the flat belts. This paper presents an overview of this test system together with an example of measurement results.

2. Overview of the Test System

The present test system has three measurement modes suited to each purpose:
(1) Vehicle test mode (VT mode);
(2) Suspension carrier mode (SC mode); and
(3) Tire stand mode (TS mode).

Figure 1 shows a schematic diagram of the system in VT mode configuration.

When in VT mode, two flat belt units are positioned underneath the vehicle to enable drive-on testing. This is how the basic configuration was designed, so that the floor surface and the upper belt surface would be at the same height. Each flat belt unit is also configured with wobbling and vertical excitation functions so that freely selectable slip angles and vertical input can be applied to the front and rear axes.

The flat belt units are equipped with steel belts that are passed around two cylindrical drums. One of the drums drives the belt, and the other drum performs lateral belt tracking. Air bearings, which have better maintainability, are used in the structure that holds vertical load Fz for the level part of the flat belt. In order to simulate a coefficient of friction (μ) equivalent to an actual road, measurement is conducted with a sheet to which abrasive are bonded affixed to the steel belt surface.

The configuration and specifications for each mode are summarized in the following.

2.1. VT Mode

In VT mode, the front axle or rear axle of the vehicle is positioned over the flat belts, the vehicle body is fixed on a surface plate, and the slip angle and vertical force are applied from the flat belts. The test system specifications are shown in Table 1. Figure 2 shows a photograph of the system with an actual vehicle loaded on it.

In this mode, the system is equipped with six-component wheel force and moment sensors to measure tire forces and with alignment equipment to measure tire position and orientation. This configuration measures forces generated on the tires, including influences from body stiffness and suspension characteristics.

In actual vehicle testing, there is mutual influence between the force on the front axle and the force on the rear axle, and the slip angles of the individual tires and the vertical load on them vary with the vehicle behavior. This makes separate analysis of the front and rear axles, or of the

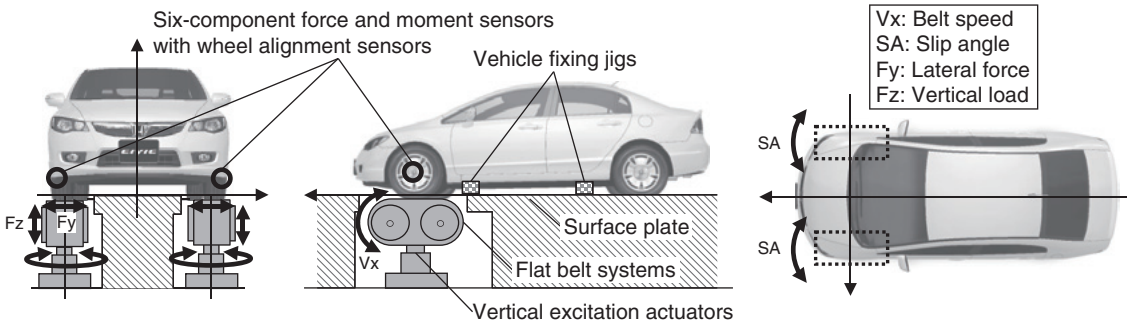


Fig. 1 Configuration of VT mode

Table 1 System specification of VT mode

Vx	0 to 180 km/h
SA	-20 to +20 deg (up to 3 Hz)
Fz	0 to 15000 N (up to 25 Hz)
Fy	-10000 to 10000N

left and right wheels, difficult. When vehicle characteristics do not exhibit the desired performance, therefore, it can be more difficult to determine quantitatively where in the tires, suspension, or body the technical issues are located.

In this mode, the vehicle's front axle or its rear axle can be subjected to individual measurement on the test bench. This enables detailed analysis of the tire forces, such as the influence of body deformation on alignment and the tire forces, including compliance steer functions of the suspension.

In addition, the suspension functions to assure the comfort of vehicle occupants by mitigating shock force from road surfaces, and also functions to keep the tires in contact with road surfaces and maintain vehicle handling and stability performances. Making simultaneous measurements of these areas of performance calls not only for flat roads, but also for input that is equivalent to input from undulating roads. The present test system is equipped with vertical excitation function to enable verification of whether or not the suspension is functioning according to



Fig. 2 Photograph of VT mode

Table 2 System specification of SC mode

Vx	0 to 180 km/h
SA	-20 to 20 deg (up to 3 Hz)
RA	-15 to 15 deg
Fz	0 to 15000 N (up to 25 Hz)
Fy	-10000 to 10000N

design under a variety of different conditions, including vehicle stability and cornering limit performance, on undulating roads as well as under conditions equivalent to flat roads. Furthermore, performance objectives can be replaced with more quantitative indicators by making comparisons between benchmark vehicles and the vehicle under development.

The device specifications also take into account scalability to allow attachment of a steering robot and/or braking robot for testing that simulates a human driver's steering and/or braking operations. This enables clarification of how mounting point stiffness on the suspension, steering gearbox, and steering hanger influences vehicle handling and stability as well as steering torque.

2.2. SC Mode

In SC mode, the suspension system and tires are attached to a fixing jig. Measurement can then be made of forces that include the influence of the suspension assembly in a condition that is not influenced by the stiffness of the body. Test system specifications for SC mode are shown in Table 2. Figure 3 shows a schematic diagram of the system in that configuration, and Fig. 4 shows a photograph of that actual measurement mode.

This mode is similar to the VT mode in that six-component force and moment sensors and alignment equipment are attached to the measured wheels. Not only can this configuration measure the forces generated on each tire, but the other six-component force and moment sensor installed under the fixing jig can also measure the total value of forces generated on the suspension system and tires as a whole.

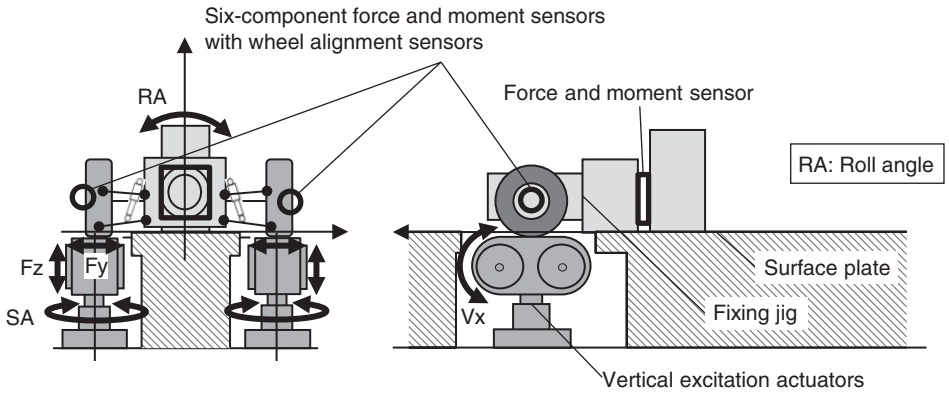


Fig. 3 Configuration of SC mode

In VT mode, measurements of factors that are due to suspension characteristics, such as changes of geometry, response lags, and inputs to steering components, are made in a state that includes body characteristics. In SC mode, however, measurements can be made so as to exclude input from the body. As a result, detailed analysis can be made as to whether the kinematic geometry of the suspension, and its component parts, such as springs, dampers, and every kind of rubber bushing, are functioning as the designers intend, as well as what is contributing to response lag, and other such questions.

It is also the case that, in VT mode, highly accurate sensors and measuring equipment could not readily be installed due to the layout of parts and components on actual vehicles. In SC mode, however, there are not as many constraints on layout. It is anticipated, for example, that highly accurate sensors can be installed to measure input to the steering assembly that is generated by a difference in the tire forces on the left and right wheels, therefore also enabling analysis of the contribution made by steering assembly components to steering force.

2.3. TS Mode

Test system specifications for TS mode are shown in Table 3. Figure 5 shows a schematic diagram of the system in that configuration, and Fig. 6 shows a photograph of it.

Analysis of suspension characteristics calls for comparison of the measurement results obtained from the suspension assembly with tires alone. Measurement of tires alone used to be carried out using flat belt test systems owned by tire manufacturers and independent measurement organizations. Their conceptual approaches to tire measurement differed from each other, however, and there were also differences due to the use of different test systems, so that comparisons could not be made of data under identical conditions. Consequently, measurement of the characteristics of tires alone using the same test system as for VT mode and SC mode will enable highly accurate quantification of the extent to which the suspension brings out the performance of the tire and of how the tire performance is transmitted to the vehicle.

Table 3 System specification of TS mode

Vx	0 to 180 km/h
SA	-20 to 20 deg (up to 3 Hz)
CA	-15 to 15 deg
Fz	0 to 15000 N
Fy	-10000 to 10000N
My	-2800 to 2800 Nm
Fx	-6600 to 6600 N
Slip rate	-100 to 100%

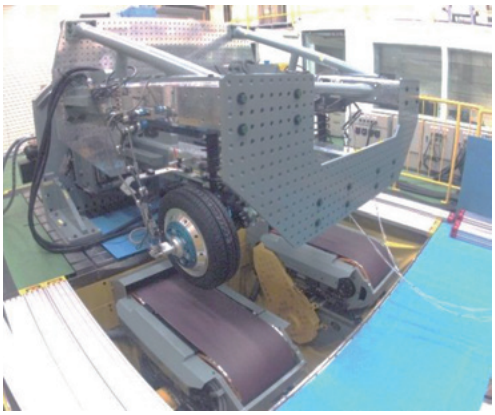


Fig. 4 Photograph of SC mode



Fig. 6 Photograph of TS mode

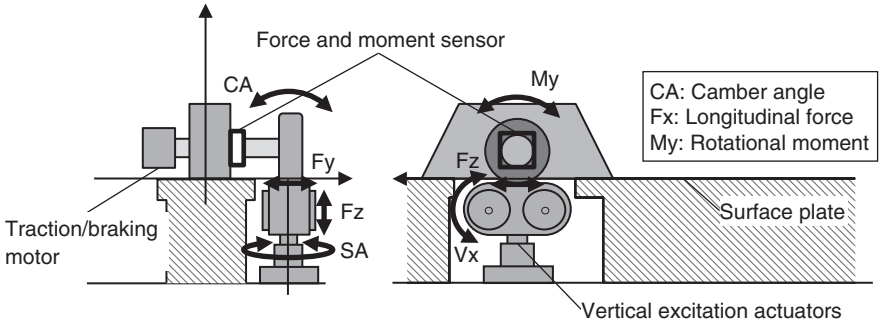


Fig. 5 Configuration of TS mode

In TS mode, the device that applies vertical displacement and camber angle to the tire is combined with the flat belt that applies rolling speed and slip angle, enabling measurement of the characteristics of a tire alone under conditions simulating those in which the tire is used. The system was designed to allow slip angles up to 20 deg and camber angle up to 16 deg with a view to measuring the characteristics of the tire alone under driving conditions that involve a large steering angle such as would result in a vehicle spinning or rolling over.

When measuring braking and acceleration characteristics, the rolling speed of the test tire is controlled by a driving and braking motor, and slip states from -100% (driving) to +100% (braking) are reproduced by causing a speed difference between tire speed and belt speed.

3. Measurement Results

Examples of measurement results obtained from the present system in each mode will be shown below.

3.1. VT Mode

Figure 7 shows a comparison of results from measurement with the front wheels positioned on the flat belts and the tire slip angle applied by wobble in the belt units, and measurement with the same front wheels with vertical excitation simulating an undulating road in addition to the slip angle. Table 4 shows the test conditions.

The horizontal axis in Fig. 7 represents the tire slip angle and the vertical axis represents the cornering force (CF). This shows the resultant CF on the left and right wheels when Fz is increased by causing a vertical stroke of 20 mm and of 40 mm with the vertical stroke set to 0 mm for the suspension with an empty vehicle. The lateral forces when the flat belts are steered to the right and to the left are averaged and treated as the CF. The CF characteristics of the tire alone are known to reach a saturation state at angles from 6 deg to 10 deg, and a saturation state is similarly reached at 10 deg or more

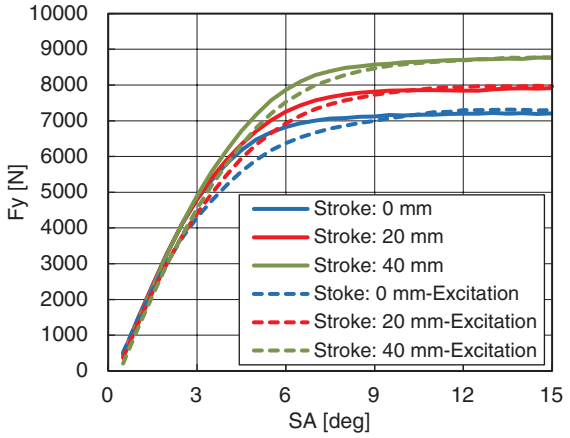


Fig. 7 Cornering force change to slip angle in VT mode with or without vertical excitation

Table 4 Cornering force test conditions in VT mode

Test vehicle	2010 model year JAZZ
Tire	175/65R15 84T
Vx	30 km/h
SA	0 to 12 deg
SA change speed	3 deg/sec
Air pressure	220 kPa
Suspension stroke	0, 20 and 40 mm
Vertical excitation	5 Hz, +/-5 mm

when the vehicle characteristics are included, and this method is expected to be capable of quantification of the suspension with tires as a whole handled in the same way as measurement of the tire alone.

When vertical excitation is applied, the reaction force in the suspension that keeps the tire in contact with the road surface becomes unable to keep up with the excitation, and the force Fz on the tire fluctuates. The coefficient of friction of the tire is dependent on load, so that CF generated with respect to a fluctuating load tends to diminish. The measurement examples here were made in a state that included the suspension characteristics, and the results confirmed that excitation caused a significant reduction in the CF even in the conditions that are observed in ordinary driving.

3.2. SC Mode

Figure 8 shows the results from measurement made

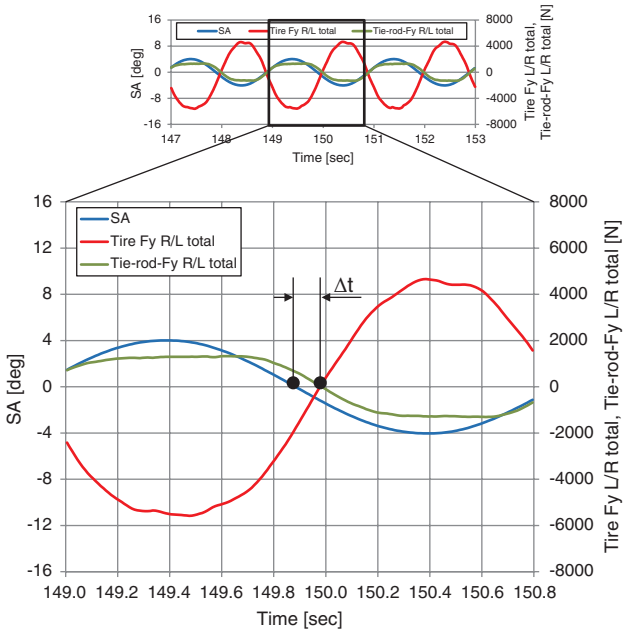


Fig. 8 Time history of cornering force and tie-rod end force

Table 5 Cornering force test conditions in SC mode

Test suspension	2010 model year JAZZ
Tire	175/65R15 84T
Vx	30 km/h
Fz	7000 N
SA change	-4 to 4 deg, 0.5 Hz
Air pressure	220 kPa

with the front suspension assembly fitted to a jig and slip angle input. The test conditions are shown in Table 5.

In the Fig. 8, the horizontal axis is the time and the vertical axis represents the resultant CF on the left and right wheels, the slip angle applied to the suspension assembly, and the resultant force on the steering tie rods at the left and right wheels.

The system was able to confirm the CF response lag Δt, which had been submerged in load variations caused by the undulating road surface and therefore had not been readily susceptible to analysis in actual vehicle testing, the state in which forces on the tie rods reach saturation, and so on.

This approach also enables analysis of the CF on each wheel, which could not be analyzed in actual vehicle testing, and comparison of it with the force on the suspension assembly as a whole can be expected to enable analysis of how each part of the suspension is functioning.

3.3. TS Mode

Figure 9 shows the results from measurement of CF with the tire alone, which is a representative characteristics of the tire, placed against the flat belt and with input of the slip angle. The test conditions are shown in Table 6. With the axes the same as in Fig. 7, the measurement results when Fz of 2 kN, 4 kN, and 6 kN is applied are shown and, as in section 3.1, the average of the left and right SA is treated as the CF.

Table 6 Cornering force test conditions in TS mode

Tire	205/60R16 92H
Vx	60 km/h
Fz	2000, 4000, 6000 N
SA	-12 to 12 deg, 6 deg/sec (triangle)
Air pressure	220 kPa

Table 7 Cornering stiffness test conditions in TS mode

Tire	205/60R16 92H
Vx	10 km/h, 100 km/h
Fz	200 to 7600 kN
SA	1 deg (const.)
Air pressure	220 kPa

Figure 10 shows CF measurements under varying speed and load with changes in the tire temperature. The test conditions are shown in Table 7. The horizontal axis represents Fz and the vertical axis represents CF and tire surface temperature. The CF per unit SA with the slip angle in the vicinity of 0 deg is termed cornering power (CP). This is an important tire characteristic that governs basic performance of vehicle dynamics.

Significantly different CP characteristics are obtained when measurement speed and tire surface temperature change. This makes it a matter of importance, therefore, to create measurement methods for appropriate quantification of tire characteristics based on a grasp of tire speed and temperature under actual driving conditions that change from moment to moment. This applies, for example, to lane changing when driving at high speeds, driving on winding roads at medium speeds, and emergency avoidance maneuvers.

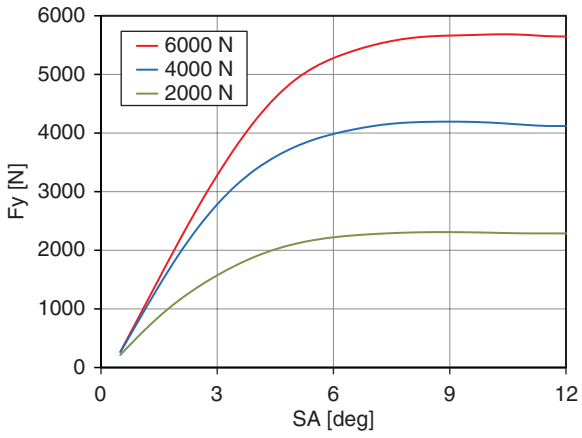


Fig. 9 Cornering force change to slip angle

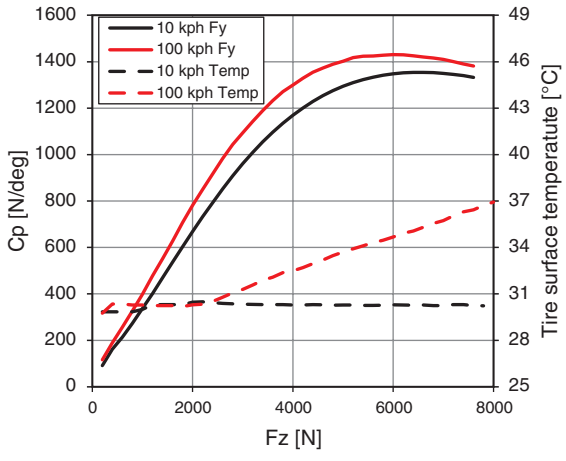


Fig. 10 Cornering stiffness change to vertical load

4. Conclusion

The features of a test system that performs comprehensive performance evaluation of the suspension and tires have been described.

The three test system modes were introduced by examples of how they can be used in development. VT mode was shown through the example of changing CF performance due to vertical excitation simulating an undulating road. SC mode was shown through the example of the relationship between CF and forces on the tie rods. TS mode was shown through the example of tire characteristics that change with a variety of factors.

The use of these test modes enables analysis of tire forces that previously were not readily susceptible to analysis in actual driving as well as highly accurate analysis of individual systems. This can be expected to enable enhanced accuracy of desktop examination using simulation and enhanced accuracy of verification of suspension component parts even at initial stages of development when a completed vehicle cannot be tested. By making the performance of prototype vehicles approach objectives more closely than before from the initial stages, this approach can be anticipated to enable the development of mass-production vehicles with a high level of maturity even with a short period of development.

The verification functions of this test system can also be applied in later development, for example to analyze phenomena that present issues, thus enabling the preparation of appropriate countermeasures. This test device can therefore be expected to perform effectively in the development of chassis performance.

References

(1) Milliken, W. F., Milliken, D. L.: Chapter 8 Force-Moment Analysis, Race Car Vehicle Dynamics, SAE International, p. 293-343 (1995)
(2) The Yokohama Rubber Co. Ltd.: Chapter 4 Tire dynamics of road, Pneumatic Tire Technology, Sankaido, p. 109-150 (1995)
(3) Bridgestone Co.: Chapter 4 Tire characteristic, Section 3 Vehicle Dynamics, Pneumatic Tire Technology, Sankaido, p. 124-158 (2006)
(4) Uno, T.: Section 2 Chassis and Tire dynamics, Vehicle dynamics and Chassis mechanism, Grand Prix Book Publishing Co. Ltd., p. 16-75 (2001)
(5) Abe, M.: Chapter 2 Tire dynamic, Automotive Vehicle Dynamics, Publication Administration of Tokyo Denki University, p. 5-45 (2009)
(6) Pacejka, H. B.: Chapter 1 Tyre Characteristics and Vehicle Handling and Stability, Tire and Vehicle Dynamics - Second Edition, Elsevier, p. 5-60 (2006)
(7) Gillespie, T. D.: Chapter 6 Steady-state cornering, Fundamentals of Vehicle Dynamics, SAE, p. 195-235 (1996)
(8) Reimpell, J., Stoll, H.: Chapter 2 Tyre and wheels, The Automotive Chassis: Engineering Principles, SAE International, p. 72-96 (1996)

■ Author ■


Tomonori SAKAI


Kaoru KUSAKA


Yuji SATO

Development of Stamped Frames Made of High-tensile Steel Plates with Light Weight and High Production Efficiency for Small Motorcycles

Hideaki NAKAGAWA* Masahiko TAKENAKA*

ABSTRACT

A lightweight stamped frame with high production efficiency was developed for application in small motorcycles produced in large numbers. This development was motivated by the challenge to produce the lightest frame in this category of 150 cm^3 displacement motorcycles, and weight reduction was pursued by the application of thin plate material for its production. To ensure the necessary strength and stiffness, high-tensile steel plates were used and the suitable cross-sectional profiles of the frames were newly devised. In the production using high-tensile steel plates, there exist rigorous restrictions in the orientation of parts partitioning, because they are highly resistible against the extension force and the press-forming of the parts with a large depth is considerably difficult. To cope with those restrictions, the forming parts were designed to have limited depths by employing the structure having flanges for welding at the upper and the lower portions of the parts enabling the coupling-type assembly along their horizontal direction while achieving enhancement of the strength, along their cross-sections, in the direction of the main load application. Moreover, the manufacturing time was shortened by normalized manufacturing processes and the simplified parts correction process brought by the application of the separated structure of the frame, which formerly was a mono-bone structure. However, when the stamped frame was constructed with the front-rear separation structure, the yield rate of the parts per plate went down and became an issue because of the complexity of the parts shapes. To cope with this issue, multiple parts blanking, in which multiple parts are cut out at one time, was introduced by adjusting the thicknesses of the yielding plate parts into a few standardized thicknesses. Consequently, the weight reduction was achieved while minimizing the increase in the manufacturing processes and the decrease of the yield rate, even though the frame parts were downsized and divided into a larger number of parts. Through these measures, a 30% reduction in weight and 30% reduction in process time were realized compared to the current stamped frame manufacturing processes, while maintaining the equivalent strength and stiffness of the frame.

1. Introduction

In response to environmental issues such as global warming and air pollution, efforts to reduce CO_2 emissions have become an urgent issue in the area of motorcycles. In particular, the market for small motorcycles is expanding annually in developing countries, and with an increase in the number of units being produced, the reduction of CO_2 emissions at the manufacturing stage is becoming an issue in addition to reductions when the vehicles are running. This makes it necessary to introduce diverse measures to improve fuel economy and rationalize production processes. In the area of frame components, the realization of weight savings is a standard method of improving fuel efficiency. It is particularly essential to realize weight savings in the frame, which represents a high proportion of the complete vehicle. Further, in addition to responding to environmental issues, efforts to reduce the weight of parts and increase the efficiency of manufacturing are necessary from the perspective of the manufacture of cost-competitive products.

Honda is responding to the annually expanding market for small motorcycles in Brazil. As part of these efforts, it was necessary to increase efficiency in the production of the CG series, which is produced in the highest numbers (more than 800,000 units per year as of 2011). The CG series is subjected to severe use conditions, for example being ridden on rough road surfaces and while heavily loaded. It is therefore essential to produce frames possessing sufficient strength and stiffness to resist these conditions. In order to

* Motorcycle R&D Center

satisfy these demands, stamped frames have been used for the series since 1999. These stamped frames were created with a focus on production efficiency, but with the increase in the number of units manufactured, it was necessary to further increase production efficiency.

Honda has realized weight savings in the body frames of various small motorcycles, and its pipe frames have been optimized for their specific use environments[1]. In the case of stamped frames, while efforts have previously been made to realize weight savings, due to factors including restrictions on the yield from the materials, significant outcomes were not obtained. The production of stamped frames is highly dependent on production equipment, and it was therefore also essential to make changes to the production process in order to realize weight savings.

A new, lightweight stamped frame with high production efficiency and able to contribute to the resolution of global environmental issues has been developed with consideration of the use conditions and production demands described above, and it was applied to the CG150 of the 2014 year model that began production in July 2013 (Fig. 1). This paper will discuss the technological specifics of the new frame.



Fig. 1 CG150 2014 model year

2. Development Goals

The following three development targets were set with the CG150, a current production model that uses a stamped frame, as the base model.

(1) A 30% reduction in weight against the current stamped frame
(2) A 30% reduction in production time against the production process for the current stamped frame
(3) Identical performance (strength, stiffness, vibration) to the current stamped frame

3. Issues of Realizing Weight Savings and Technological Approaches

3.1. Status of Stamped Frames and Issues of Realizing Weight Savings

Figure 2 shows the shape of the frame for the CG150, which is currently in production. In order to increase production efficiency, a mono-bone structure produced mainly using spot welding is employed. In this mono-bone structure, the structure from the head pipe to the seat rail is connected as a single unit. Spot welding is a high-productivity coupling method, but it necessitates the use of flanges for coupling, and the weight of the body frame therefore increases by the weight of the flanges. In the case of frames formed by mating stamped materials, because the yield from the material is the major focus in the shape of each individual part, optimization of shape in order to realize weight savings represents a challenge. Combining parts with good yield from material and determining how to use the flanges employed for spot welding structurally were the issues in realizing weight savings. Because of these issues, key points in design included realizing the appropriate direction of division for parts and realizing an efficient arrangement of cross-sections with consideration of the direction of load inputs. However, even when the flanges used for coupling are employed effectively in terms of function, an increase in weight produced by the flanges against a structurally optimized pipe frame is unavoidable. In order to achieve a weight reduction of 30%, it was therefore necessary to consider materials and plate thickness in addition to optimization of the structure.

3.2. Use of Thin, High-tensile Steel Plates and Associated Issues

The use of thin plates is an effective means of realizing weight savings. However, it was necessary to select materials with consideration of maintaining sufficient strength to resist severe use environments and to improve cost competitiveness. The authors therefore examined the potential for employing high-tensile steel plates, which are already used as a method of realizing weight savings in four-wheeled vehicles. Figure 3 shows a graph of material cost against material strength. Because material cost in relation to strength is low for both cold-rolled and hot-rolled high-tensile steel plates, efficient use of these plates is able to reduce material costs. It was therefore decided to employ thin, high-tensile steel plates, aiming to realize a 30% reduction in weight against the current stamped frame.

When the plate material is replaced with thin, high-



Fig. 2 Mono-bone frame of 2013 model year CG150

tensile steel plate, the arising issues are the decline in the frame stiffness, which is caused by the decreased thickness of the steel plate, and the tendency to have a larger stress, which is originated from the enlarged displacement. However, we thought those issues could be overcome by devising countermeasures on structures and the application of thin, high-tensile steel could be feasible.

3.3. Consideration of Frame Structure

In order to help ensure the necessary strength and stiffness using thin plates, a continuous closed cross-section structure was adopted in the main members of the frame. The required cross-section shapes were arranged for the assumed loading direction, and a structure to receive the load by a box shape was adopted. Figure 4 compares the cross-sectional shape of the main members for the current and developed frames. By contrast with pipe frames that use a uniform cross-section, in the case of stamped structures it is possible to freely modify the shape of the cross-section. Making use of this advantage, cross-section shapes were set that would make it possible to realize the necessary strength and stiffness for the required members. Further, the addition of rib structures (forming concave and convex areas on the surface of the plates) made it possible to avoid a decline in stiffness of the surface with the use of thin plates.

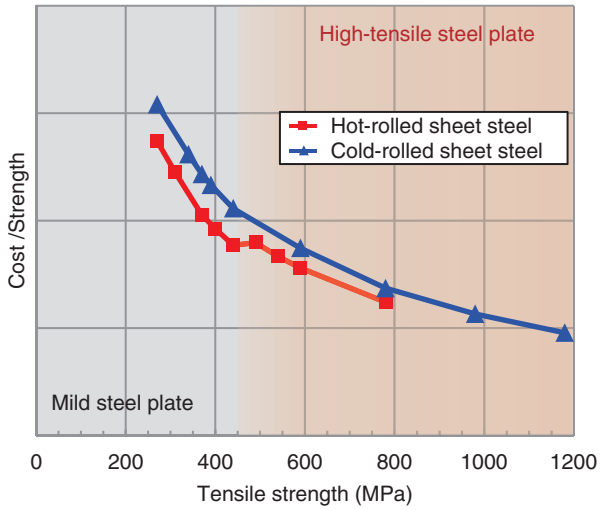


Fig. 3 Cost against strength of steel plate

3.3.1. Approach to realizing stiffness

The employment of a continuous cross-sectional shape would make it possible to realize the required stiffness despite the use of thin plates, but unless a closed cross-section was employed in the connections with other parts, stiffness would decline in these sections. Among the main frame members, the pivot plate uses a three-sided square shape for the fitting of the engine, making it an open section. A member was therefore employed in order to close the cross-section, helping to ensure stiffness. In addition, to prioritize the dimensional stability after welding, the connecting part between the main member and the seat rail adopted a uniting planes mutually. The connection used a square cross-section that helped to ensure stiffness, but when twisting loads were input from the seat rail, the cross-section was prone to deformation into a diamond shape, resulting in a decline in the stiffness of the frame. Two inner gussets were added to the interior of the main member in order to help prevent this deformation. The addition of the gussets helped to control the decline in stiffness due to deformation. Figure 5 shows the structure that closes the opening of the pivot section and the structure used in the main member to respond to deformation. The use of the frame structures described above and the application of thin, high-tensile steel plates made it possible to reduce the thickness of the plates used for the main members from 1.5 mm to 1.2 mm.

3.3.2. Approach to realizing strength

In attempting to realize weight savings, the area that represented an issue in terms of strength was the rear frame structure. The rear frame, in particular the seat rail, receives the load of the passengers, and also receives a high load input from the rear cushion. The use of thin plates increases the level of deformation in the member itself when it receives a load, and stress concentrates in the joint sections connecting the front and rear of the frame. It was therefore necessary to employ cross-sectional shapes that

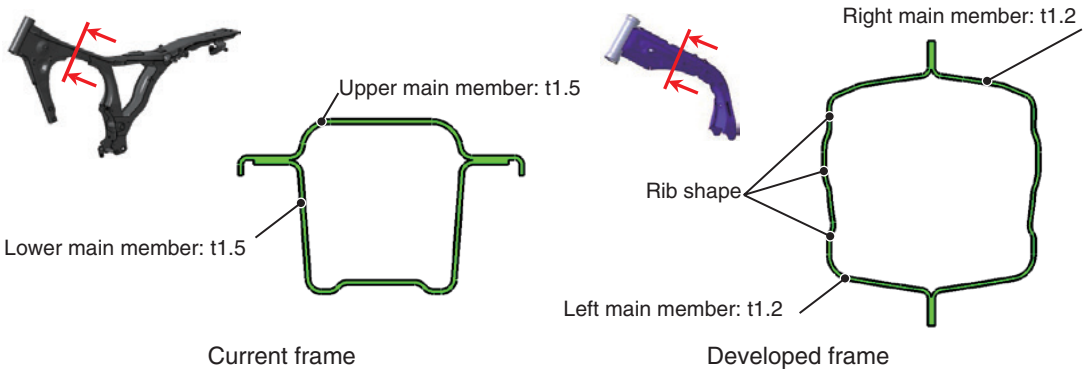


Fig. 4 Comparison of cross-sectional shapes of main members

would disperse this stress in the appropriate positions. The load input direction in the case of the seat rail was clear, with the up-down direction predominating. Due to this, a closed cross-section structure divided between left and right, which would increase the section modulus in the up-down direction, was adopted and welding flanges were positioned in the direction of load (the up-down direction). Figure 6 compares the cross-sections close to the area at which the seat rail supports the rear cushions in the current and the developed frames. By employing the appropriate cross-section structure in the necessary position in this way, it was possible to achieve a level of strength equivalent to that of the current stamped frame. However, because it is challenging to extend high-tensile steel during forming, there are limits to the depth of forming of the part, and it is challenging to realize the sectional modulus in the lateral direction when employing a structure with a left-right division. Members were therefore used in the appropriate positions to connect the left and right sections of the seat rail in order to increase the robustness of the seat rail as a whole against load input in the lateral direction. The application of these measures and the use of 590 MPa-class high-tensile steel sheets have helped to enable the seat rail to receive loads efficiently, and made it possible to employ thin steel plates that reduce the thickness of the seat rail members from 1.5 mm to 1.0 mm.

4. Enhancing the Production Cycle: Issues and Methods of Realization

4.1. Conventional Stamped Frame Production Process

Figure 7 shows the elements of the welding process for the current stamped frame. The overall process is made up of three sub-assembling processes and a main assembling process. There are differences in the times necessary for the sub-assembling processes due to the composition of

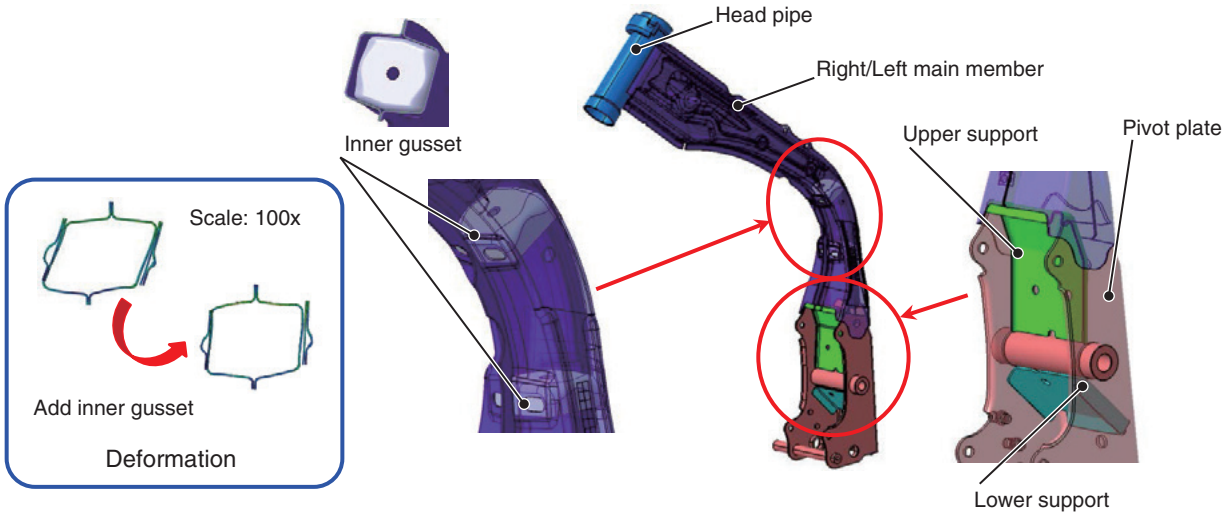


Fig. 5 Structure of main frame parts

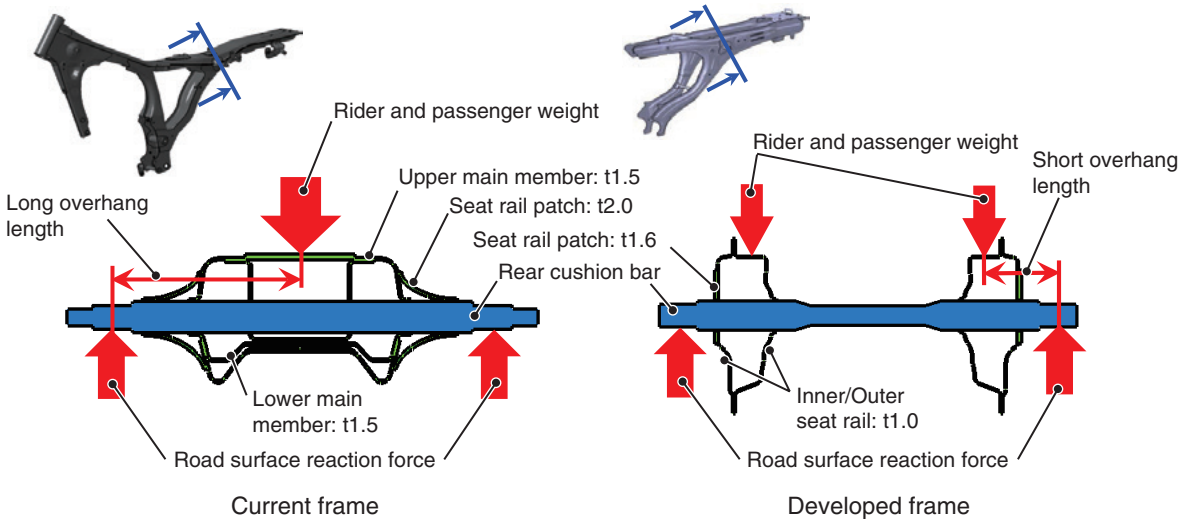


Fig. 6 Comparison of supporting area of rear cushion

the parts, and the time taken is determined by the longer processes. In addition, due to the shapes of the parts produced in the sub-assembling processes, the management and correction of the parts is not completed during these processes, and it is necessary to check the parts during the main assembling process. This means that second and third checks and correction work are necessary. Simplifying management and correction by standardizing process times is therefore an issue in realizing more efficient manufacture of frames in response to the need to increase production. Because the structure of the frame is strongly related to the shapes of the parts produced in the sub-assembling processes and the difference in the times necessary for their assembling, it was necessary to consider changes from the perspective of the frame structure in order to realize high-efficiency production.

4.2. Frame Shape: Changes and Issues

The current stamped frame uses a mono-bone structure in order to reduce the welding processes involved and increase the yield from the material. As indicated in the previous section, in order to respond to the production of an increased number of units, it was necessary to change the shapes of parts in the sub-assembling and main assembling processes to further rationalize production. The issues involved in doing so were resolved by using a frame with a divided front and rear structure, like a pipe frame.

Figure 8 shows the stamped frame with the divided front and rear structure. The front section comprises from the head pipe to the pivot plate. The rear section is made up of the seat rail and the sub-tube and cross-plate that support it. The issue in employing a divided front and rear structure is the increased complexity of the shapes of the parts and a decline in the yield from the material. Generally, the yield from the material is high for frames that use pipes for their main framework. Draw-forming stamped frames have a low yield from material in comparison to pipe frames, but their productivity is higher. It was therefore essential to increase the yield as much as possible in order to maintain cost competitiveness while increasing production efficiency through the use of a stamped frame.

4.3. Increasing Yield from Material: Technological Approaches and Methods of Realization

Increased complexity in the shapes of parts is a factor in reducing the yield from the material employed. For stamped parts, rectangular shapes offer the highest yield from the material, making it possible to use material from the band without waste. If the shapes of the parts become more complex (no longer rectangular) when they are blanked, the yield from the material declines. It is possible to increase the yield from the material by reducing the size of the parts, but this increases the number of parts and also entails more coupling and production processes. When taking production efficiency into consideration, it is necessary not only to increase the yield from the material, but also to minimize the number of parts. In addition, because the frame parts

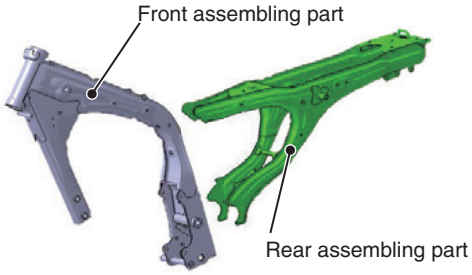


Fig. 8 Frame structure divided between front and rear

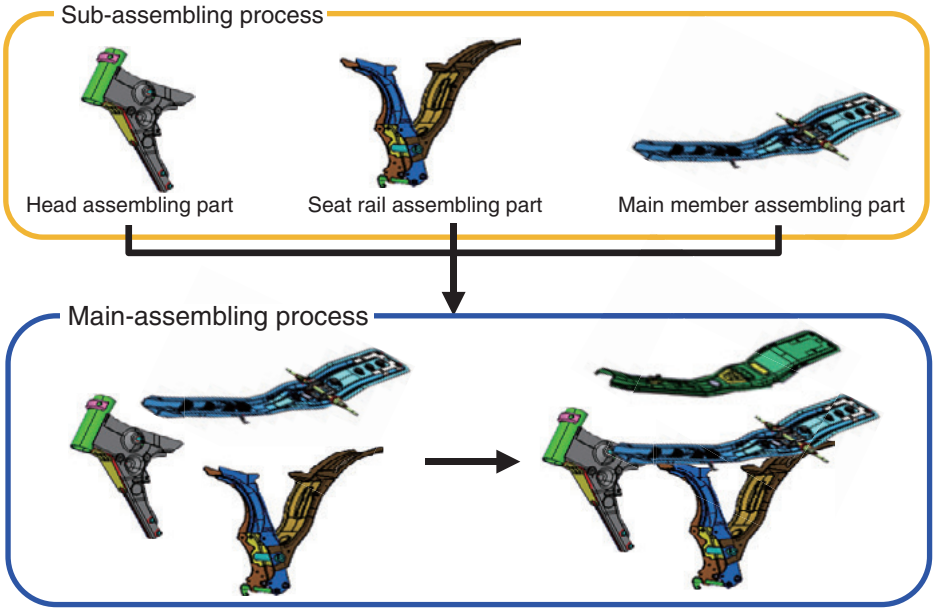


Fig. 7 Flow of welding process for manufacture of current frame

are shaped by draw-forming, it is necessary to remove the sections used to hold the parts during forming in a trimming process following the forming process. Because these trimmed sections are included in the material costs, this represents another factor preventing the yield from the material from being increased. The following two points were therefore focused on in order to increase yield:
(1) The forming method of the products
(2) The blanking process used for the material

4.3.1. Forming method of the products (Use of form-forming without need for trimming)

The application of form-forming, which by contrast with draw-forming does not necessitate trimming following forming, was examined as a means of increasing the yield from the materials. In draw-forming, the part is shaped by applying tension while inducing plastic deformation of the material; form-forming, by contrast, is a type of forming in which bends predominate. Figure 9 shows the draw- and form-forming processes. Form-forming offers a good yield from the material, but compared to draw-forming tends to form wrinkles in the parts, and its degree of freedom of shaping is low. To help prevent the occurrence of wrinkles, it is desirable to use shapes with a minimal difference between the length of the circumference during blanking and during forming. Mating of left and right sides was therefore used to produce parts shapes with lower forming depth than conventional upper-lower mating in order to minimize difference in the length of the circumference as much as possible. A closed cross-section divided between the inner side and the outer side was employed for the seat rail. Figure 10 shows the shapes of the parts. When these parts were draw-formed, the yield from the materials was 53.5%. The application of form-forming, which does away with the need for trimming, increased the yield by 10 points, to 63.7%.

4.3.2. Blanking process (Simultaneous blanking of multiple parts)

Simultaneous blanking of multiple parts, in which small parts are positioned in the spaces left free by large parts, was employed in order to increase the yield from the material during blanking. The major issue in applying this manufacturing method was the necessity to standardize materials and plate thicknesses. In addition, the shapes of the parts being blanked simultaneously and the method of combining the parts are also important factors. The plate thicknesses for the front frame parts were therefore standardized at 1.2 mm and 1.6 mm, and for the rear frame parts at 1.0 mm. This arrangement of thicknesses makes it possible to blank multiple parts simultaneously, as shown in Fig. 11. Figure 12 shows the yield from the material

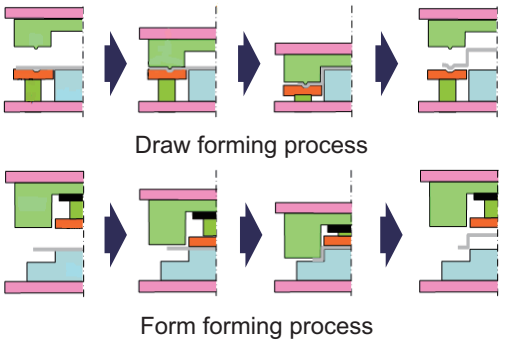


Fig. 9 Comparison of stamp forming process

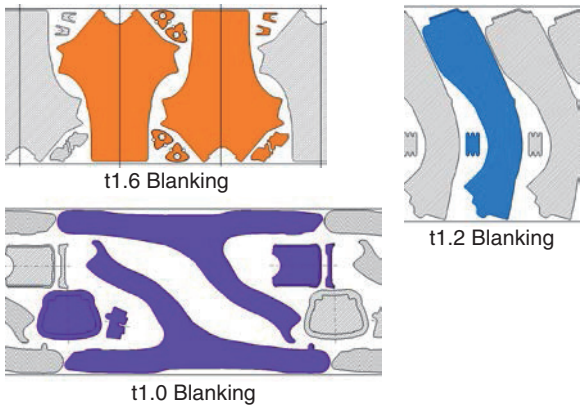


Fig. 11 Simultaneous blanking of multiple parts

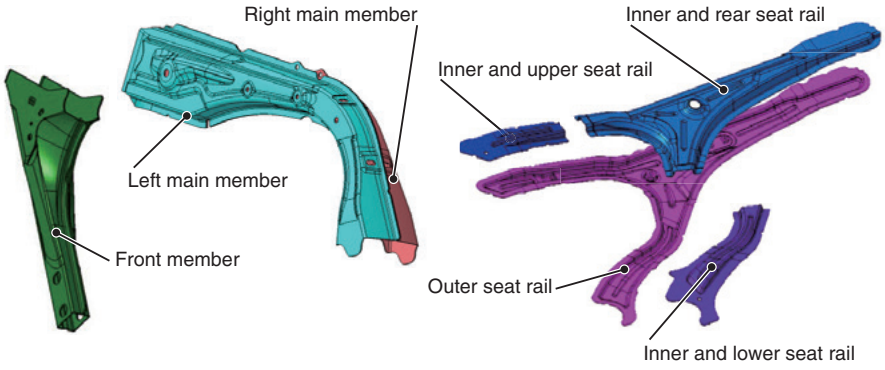


Fig. 10 Shapes of each stamped part

for the current stamped frame and the yield rates obtained for the developed frame when simultaneous blanking of multiple parts and form-forming that does away with the need to trim the part are applied. As the figure indicates, the use of form-forming increases the yield rate by 3.5 points against the current stamped frame, and the addition of simultaneous blanking of multiple parts results in a further increase of 6.5 points. The application of the two methods discussed above increased the yield rate by 10 points against the current stamped frame, making it possible to employ a frame configuration divided between the front and rear while achieving a high yield rate.

4.4. Technologies for Increased Welding Efficiency

As indicated above, the issue in increasing the efficiency of welding was reducing the difference in the time necessary for each welding process. The time necessary for welding is the time for actual welding and the time for incidental operations related to welding. The latter category includes time for movement between processes and time for correction of distortion caused by welding. Spot welding is the main form of welding used in the manufacture of the current stamped frame, but because MIG welding is necessary in numerous sections, a considerable amount of time is needed for incidental operations. In addition, the time needed for the fitting of vibration-absorbing rubbers to the interior of the frame during the main assembling process to help control ringing of the outer plates also adds to the time for processes incidental to welding. In response to these issues, the authors attempted to reduce the time needed for incidental processes through the application of the following three methods:

(1) Reduction of welding points through integration of stamped parts;
(2) Concentration of MIG welding; and
(3) Reduction of number of procedures by doing away with vibration-absorbing rubbers.

4.4.1. Reduction of welding points through integration of stamped parts

The first point that was focused on in the current stamped frame configuration was areas in which left and right parts were mated and coupled by MIG welding. Figure 13 shows the shapes of the current and developed

Material utilization		
Current frame body	Developed frame	
	Form forming	Form forming and simultaneous blanking of multiple parts
58.1%	61.4%	67.9%

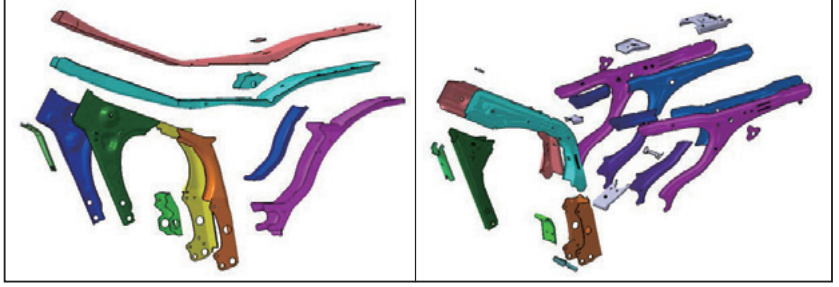


Fig. 12 Comparison of material utilization

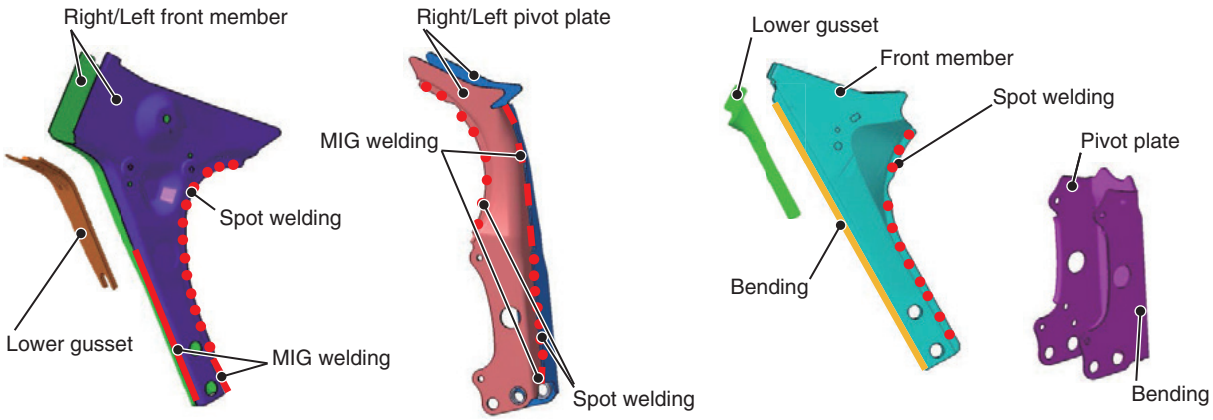


Fig. 13 Structural comparison of integrated parts

parts and the welding points employed. In current parts, the front member is formed with a left-right division; the two sides are connected by MIG welding at the front and spot welding at the rear. In addition, the pivot plate is coupled using spot welding at the front and MIG welding and spot welding at the rear. The potential for doing away with MIG welding and reducing the number of points for spot welding by integrating these two sections in the forming process was investigated. Because the frame uses a structure divided between the front and the rear, it was possible to reduce the size of the pivot and realize a simple three-sided square cross-sectional shape by extending the main member close to the pivot. The front member was integrated through the use of a UO bend. The UO bend is a technique used in the forming of pipes and similar products, in which a flat steel plate is given a U-shaped cross-section in a first procedure, following which the open ends are closed in a second procedure in order to create an O-shaped cross-section. In the present case, the technique was used to create closed cross-sections in integrated stamped parts. The bend employed is a two-dimensional curve, and it is essential that the section to be bent is straight. However, if the section of the front member to be bent is straight, the section that contacts the head pipe becomes pointed, and stress concentrates in this section. The use of a lower gusset to block this sharp section has helped to prevent stress from concentrating and formed a structure that is able to resist load inputs. This made it possible to integrate each of the parts whose new shapes are shown in Fig. 13, doing away with MIG welding and reducing the number of spot welding points by 15.

4.4.2. Concentration of MIG welding

Frames that are manufactured mainly using spot welding are suited to high-speed production. However, due to the limitations of shunting, spot welding is unable to concentrate coupling points in a narrow area. MIG welding was therefore applied to restricted areas of the points at which a closed cross-section was being welded, where stress would be concentrated; the points at which bars or pipes were being coupled; and the points at which a continuous coupling was desired in order to help ensure stiffness (Fig. 14). While the welding length increased at certain points, this helped to prevent complexification of the welding process, and increased production efficiency. In addition, the use of plate members as cross members made it possible to couple them using spot welding.

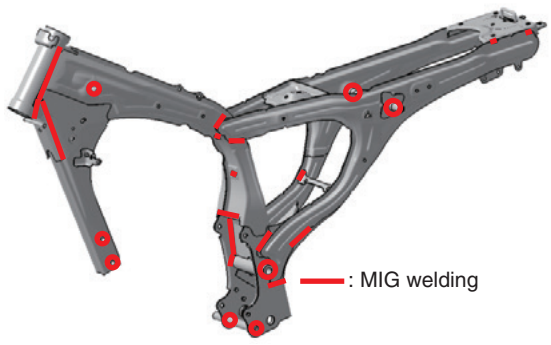


Fig. 14 Points for application of MIG welding

4.4.3. Reduction of number of procedures by doing away with vibration-absorbing rubbers

Because stamped frames are composed of large stamped parts with many flat surfaces, the vibration of the engine causes their surfaces to vibrate like the skins of drums, resulting in ringing in the outer plates. In the current stamped frame, this surface vibration was controlled by the application of vibration-absorbing rubbers to the interior of the body frame, controlling ringing in the outer plates. To make it possible to do away with these vibration-absorbing rubbers, it would be necessary to control surface vibration by means of cross-section shape, the makeup of parts, and structure. Ringing in the outer plates was therefore controlled by reducing the surface area of the members making up the frame and increasing the surface stiffness of each of the members. The use of a structure divided between front and rear for the body frame and a structure divided between left and right for the seat rail in the new frame reduced surface area by 15% against the current frame. In addition, the use of concavities, convexities and curves in the various sections helped to do away with large planar sections, and increased surface stiffness. Figure 15 shows the vibration-absorbing structures used in the current frame, and the concavities and convexities added to various sections in the developed frame. The vibrations were suppressed by installing plates within the parts if there were difficulties in applying reinforcing indents or extrusions because of the necessity for the part to be a flat plane shape due to a requirement in production processes. Figure 16 shows this configuration. The application of these methods has controlled surface vibration structurally, making it possible to entirely do away with the vibration-absorbing rubbers.

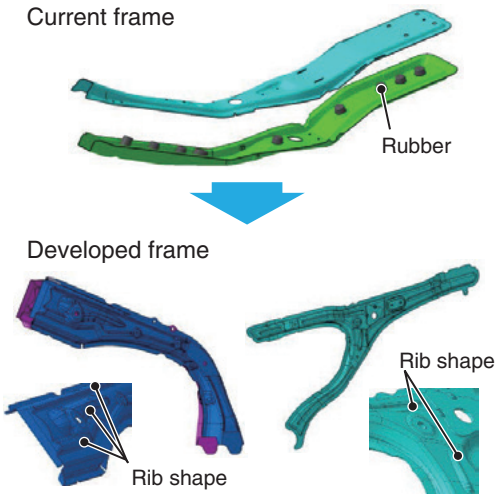


Fig. 15 Rib structure for suppressing surface vibration

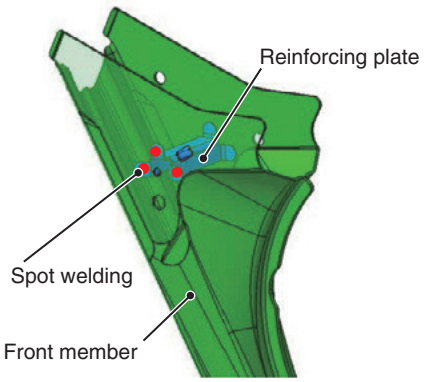


Fig. 16 Internal structure for suppressing surface vibration

5. CAE Verification of Unit Performance

Figure 17 shows the shape of the developed frame. Unit performance for this frame was verified using CAE. A solid model was used in stiffness and strength analyses, while a surface model was used in a vibration analysis.

5.1. Verification of Stiffness

Figure 18 shows a comparison of stiffness values measured with the swing-arm pivot fixed and a lateral load input to the front axle for the current and developed stamped frames. The graph shows lateral stiffness and torsional stiffness with values for the current frame defined as 1. Figure 19 shows deformation diagrams at the time that the measurements were taken. As the comparison of stiffness values indicates, results for the developed frame are almost identical to those for the current frame.

5.2. Verification of Strength

Figure 20 shows a stress distribution diagram produced when the maximum load projected for running on a rough road is input to the rear cushion mounts. As this diagram indicates, the load is dispersed with a good balance through the entire member, with no local concentrations of stress.

5.3. Verification of Reduction of Ringing in Outer Plates due to Vibration

Figure 21 shows a comparison of the vibration level with and without rib reinforcement, focusing on an area with a large cross-section and a broad surface area for sound to radiate from. The figure on the left shows results for the developed frame with rib reinforcement. The figure on the right shows results for an analysis of the same frame without ribs, conducted to provide a comparison. The red

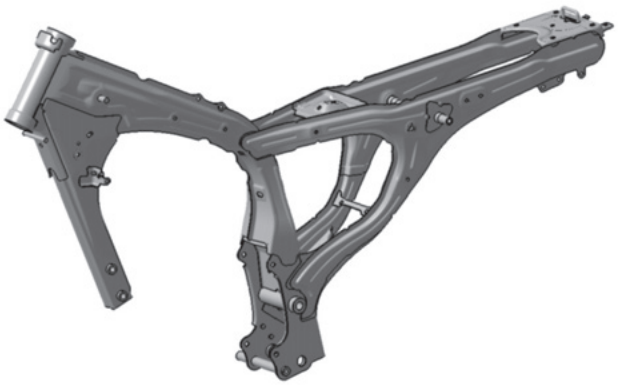


Fig. 17 Shape of developed frame

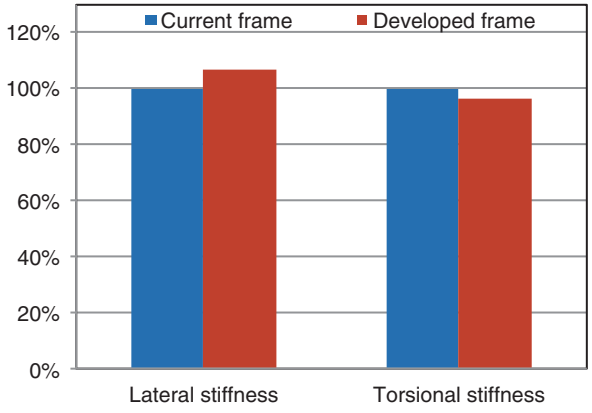


Fig. 18 Comparison of stiffness values



Fig. 19 CAE deformation diagram showing stiffness

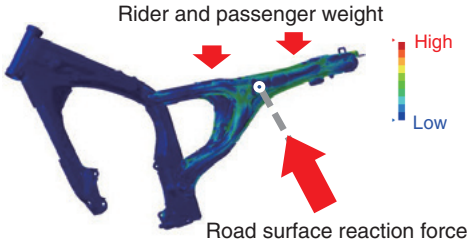


Fig. 20 CAE stress distribution assuming running on rough road

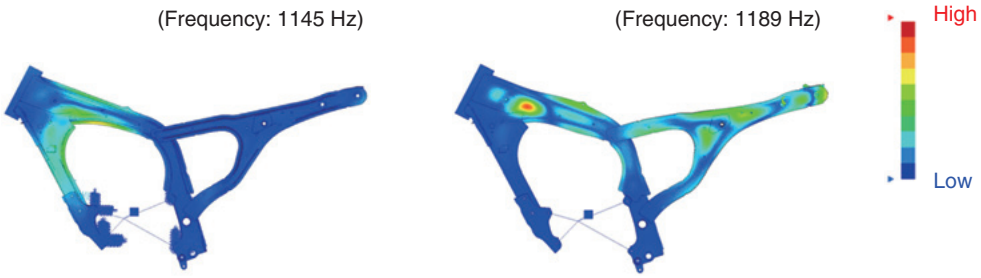


Fig. 21 Confirmation of vibration reduction by eigenvalue analysis of mode shape

areas in the figures show the areas of high amplitude. The results show that while there is significant local vibration of the outer plates in the frame without ribs, in the developed frame the ribs help ensure surface stiffness, controlling ringing in the outer plates produced by surface vibration.

6. Confirmation of Effects

6.1. Weight Reduction Effect

Figure 22 shows the weight reduction effect dividing the current and developed frames into the front frame section and the rear frame section. While the current stamped frame did not employ a structure divided into front and rear, the comparison was conducted with the current frame divided based on the concept of the developed stamped frame. The results of the comparison show that weight reductions of 2 kg were achieved in both the front and rear frames. The result achieved for the rear frame in particular (-33%) indicates that reducing the thickness of the plates had a significant effect. The developed frame is four kilograms lighter than the current frame, at 10 kg to 14 kg, realizing the target for a 30% reduction in weight.

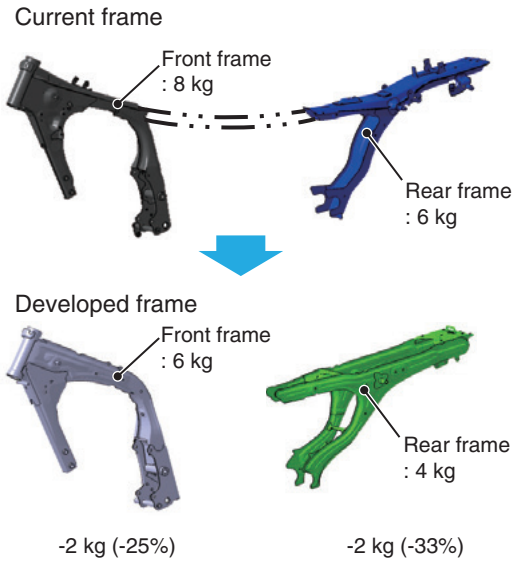


Fig. 22 Weight reduction effect and structural comparison

6.2. Effect of Reduction of Time for Manufacturing Procedures

Figure 23 shows the order of coupling in the sub-assembling and main assembling processes for the frame using the methods described in Chapter 4. Figure 24 compares the length of MIG welding and the number of spot welding points for the current and developed methods, and Fig. 25 compares process time for the current and developed methods. In the developed frame, the total MIG weld length has been reduced by 200 mm, and the replacement of MIG welding by spot welding and other initiatives has reduced the time for incidental procedures by one-half. As a result, while the time for actual welding is the same as for the current stamped frame, the process time is reduced by 30% against the time for the current stamped frame considered as 1.

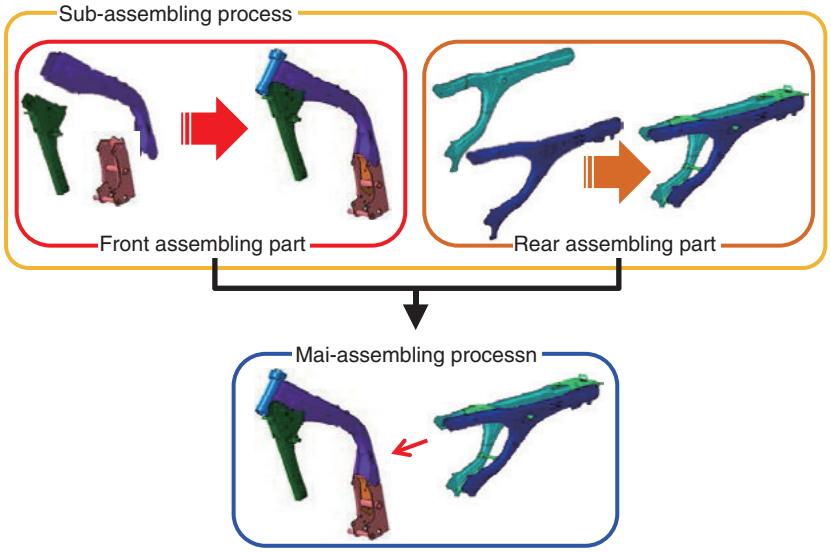


Fig. 23 Flow of welding process for manufacture of developed frame

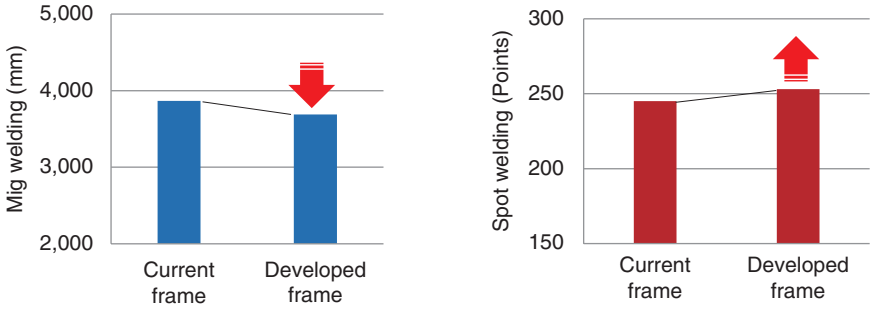


Fig. 24 Length of MIG welds and number of spot welds

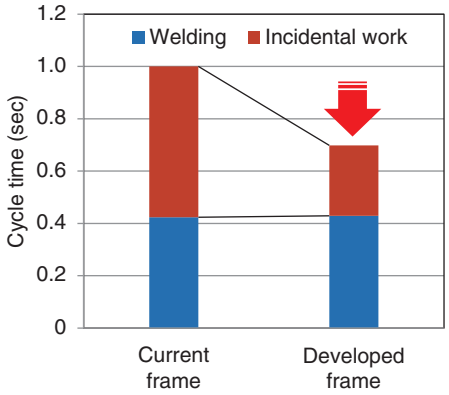


Fig. 25 Reduction of process time

7. Conclusion

A lightweight and high productive efficiency stamped frame for small motorcycles produced in large numbers was developed. The following are the salient points of the development.

(1) Using thin, high-tensile steel plates, stiffness was realized by means of a structure offering a continuous closed cross-section. A closed cross-section divided between left and right, employing a structure having flanges for welding at the upper and the lower portions of the parts, was used for the seat rail; these sections were connected by cross-plates to help ensure strength. By means of these methods, while the developed frame is stamp-formed like the current frame, the plate thickness of the main frame sections has been reduced from 1.5 mm to 1.2 mm, and of the seat rail from 1.5 mm to 1.0 mm, realizing a weight reduction of 4 kg.

(2) The application of simultaneous blanking of multiple parts and form-forming that does away with the need for trimming has increased the yield rate from the material, and made it possible to realize a front-rear divided structure in a stamped frame.

(3) Integrated forming of parts and concentration of MIG welding have made it possible to reduce the length of MIG welds and replace MIG welds with spot welds.

(4) The use of a front-rear divided structure in the frame and a left-right divided structure in the seat rail has reduced surface area by 15%; this, in addition to the use of ribs to reinforce surface stiffness, has made it possible to do away with the vibration-absorbing rubbers previously used.

These innovations have reduced weight by 30% and process time by 30% against the current stamped frame.

References

(1) Honma, H., Itoh, M., Seki, Y., Yamashita, A., Tsuchiya, M.: Establishment of Analysis Method for Weight Reduction Design of Motorcycle Frame Parts, Honda R&D Technical Review, Vol. 18, No. 2, p. 163-168

■ Author ■


Hideaki NAKAGAWA


Masahiko TAKENAKA

Development of Short Pitch Resistance Spot Welding Technology

Hisayasu OOKA* Atsushi SUZUKI* Mitsushige GOTO*
Keita OTSUKA* Yasumasa OKADA*

ABSTRACT

In order to reduce the pitch used in resistance spot welding, it is necessary to quantify the phenomenon of shunting, or short-circuiting of current flow. A technology for predicting the state of current flow using a three-dimensional spot welding simulation was therefore developed. Test results showed that predicted spot weld diameter values when current shunting occurred, corresponded well with measured values. Using this method, it was shown that it was possible to realize sufficiently sized spot welds in short-pitch resistance spot welding by increasing input energy to compensate for heat loss caused by the short-circuiting of the welding current. In addition, an application study of short pitch spot welding showed that a reduced weld pitch of 15 mm in high stress regions reduced peak stress in the weld, making the use of thinner steel sheets possible.

1. Introduction

In response to environmental issues, automotive manufacturers are today actively engaged in developing technologies which increase fuel efficiency and thus reduce CO_2 emissions. In the area of the vehicle body, continuous joining processes using laser welding and adhesives are being employed to reduce sheet thickness and achieve weight savings while still realizing joining strength. However, this increases cost, and the time necessary for the welding process in comparison to resistance spot welding (RSW), a discontinuous joining method.

RSW is a joining method in which an electric current is applied through adjoining metal sheets that are held under pressure by the electrodes. Joule heat (resistive heating) is generated by the transmission of current between opposing electrodes and by the corresponding contact resistance at the interface between the work piece and electrode surfaces, and by the specific resistance of the metal materials through which current is passed. Subsequent melting and joining occurs at the surfaces. If it were possible to reduce the pitch between these spot welding points, the strength of the join would increase proportionally with increase in the area of the joints. However, when the pitch between welds is reduced, a phenomenon termed shunting occurs, in which the current is short-circuited by contiguous welding points (Fig. 1). This results in insufficient heat being generated in the area to be welded, making it challenging to realize the necessary size in the welding point (termed the “nugget diameter” below) to satisfy strength standards. Because of this, it is common to employ a pitch of around 30 mm between spot welds.

In order to realize RSW using a pitch of around 15 mm (short-pitch RSW), it was necessary to elucidate the phenomenon of shunting. A method was therefore developed to predict shunting using a three-dimensional spot welding simulation. Using this method, it was determined that the heat loss due to shunting could be compensated for, by increasing the input energy. The study also showed that it was possible to set welding conditions that would satisfy nugget diameter standards even when conditions such as the thickness, combination, or properties of the sheets differed. This paper will report on these results.

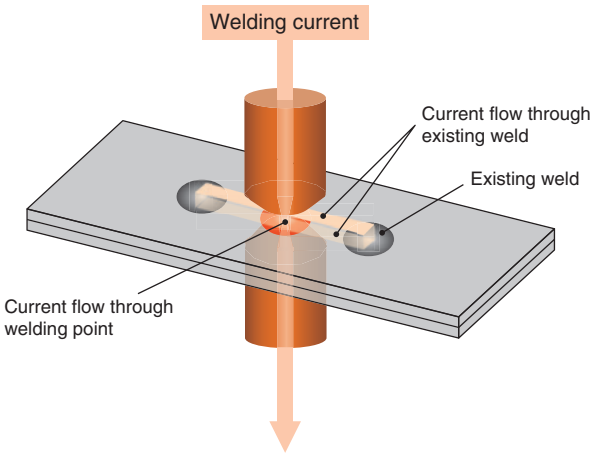


Fig. 1 Phenomenon of current shunt

* Automobile R&D Center

2. RSW Simulation

2.1. Conditions for Study using RSW Simulation

Because the shunting that occurs as a result of short-pitch RSW is a phenomenon that occurs in an infinitesimal range, measurement of the phenomenon in tests represents a challenge. A simulation was therefore used in order to conduct a current path analysis. Spot welding simulation software available on the market is normally used to conduct simulations of nugget formation, and therefore involves analysis of two-dimensional axial symmetry models, making it unable to calculate the phenomenon of shunting. The three-dimensional model shown in Fig. 2 was therefore formulated using a spot welding simulation software, capable of three-dimensional analysis, developed by Nippon Steel & Sumitomo Metal Corporation. Analyses were conducted using this model. A 1/4 model was used based on considerations of symmetry and calculation speed. Contact resistance at the interface between the steel sheets is an important parameter in RSW, and was set with consideration of the effect of contact pressure and the properties of the steel sheets (yield stress, resistivity, and the temperature-dependence of these parameters)[1]. Two sheet combinations were employed for comparison: a mild steel with a lower specific resistance, which was considered would have a significant effect on shunting (Combination A); and a 590 MPa high-tensile steel with a high specific resistance (Combination B). Details of the materials and the spot welding conditions are shown in Table 1.

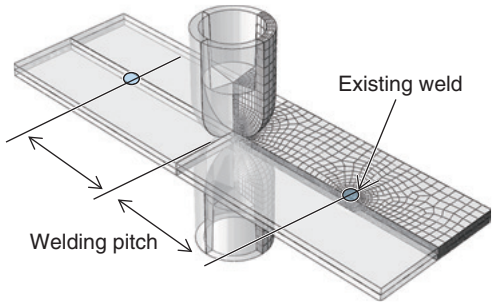


Fig. 2 Analysis model by CAE

Table 1 Spot welding conditions

Sheet combination	A	B
Material	JSC270D	JSC590R
Thickness	1.4 mm	1.0 mm
Electrode force	3.5 kN	3.5 kN
Welding current	7.8 kA	6.2 kA
Welding time	17 cycles	12 cycles
Existing weld diameter	5.2 mm	4.5 mm
Welding pitch	Single weld, 15 mm	

2.2. Verification of Analytic Accuracy of RSW Simulation

First, the analytic accuracy of the simulation was verified. Figure 3 shows the shape of a nugget as determined using the simulation and in a test. The upper frames in each case show simulation results, and the lower frames show test results. Images from the simulation and the test show that in going from a single weld point, for which shunting does not occur, to a welding pitch of 15 mm, results in a reduction in the nugget diameter due to the effect of shunting.

Figure 4 shows simulation and test results for nugget diameter. The tendency for the nugget diameter to decline

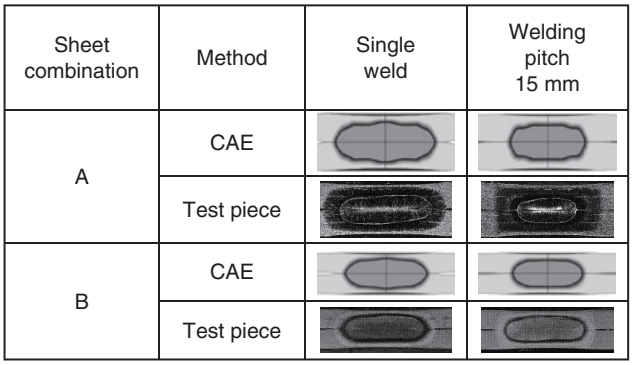


Fig. 3 Results by analysis and experiment of spot welding (cross-sectional images)

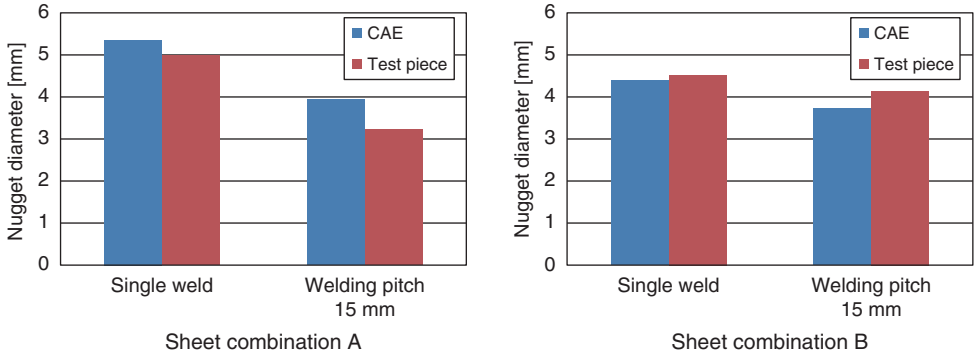


Fig. 4 Results by analysis and experiment of spot welding (nugget diameter)

due to shunting matches in the simulation and test results for both sheet combinations, indicating that it is possible to use the simulation in evaluations.

2.3. Results of Study of Shunting using RSW Simulation

Figure 5 shows simulation results for the distribution of current density during welding of Combination A. Figure 5(a) shows results for a single weld point, for which shunting does not occur, while Fig. 5(b) shows results for a welding pitch of 15 mm. Under the conditions shown in Fig. 5(b), because the current is flowing via the intermediary of the nugget, the current density increases in areas other than the welding point, indicating that shunting is occurring. Figure 6 shows simulation results for the amount of shunting in Combination A. In the case of the single welding point, 100% of the current flows to the welding point [Fig. 6(a)], while in the case of the 15 mm welding pitch, an average of approximately 67% of the current flows to the welding point, indicating that approximately 33% of the current is shunted.

Figure 7 shows the relationship between the amount of time that the current is applied, and the amount of current flowing through the welding point. The amount of current flowing through the welding point declines with time, indicating the amount of shunting increases during the initial three cycles. However, after three cycles the amount of shunting declines. This phenomenon is thought to occur because, up to the third cycle, the heating of the welding point increases its resistance, thus restricting the flow of current through the welding point. It is considered that the current flows more easily after the third cycle because the area in which the current flows, increases with increasing nugget diameter, and the resistance of the welding point declines.

The use of the simulation made it possible to visualize and study the phenomenon of shunting during welding, which is not possible to measure in tests. In addition, it was also possible to study the amount of change in shunting produced by changes in conditions, such as material properties, sheet thickness, and welding conditions.

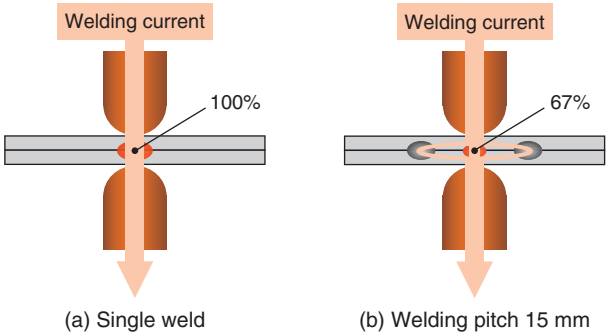


Fig. 6 Measurement of current shunt by CAE

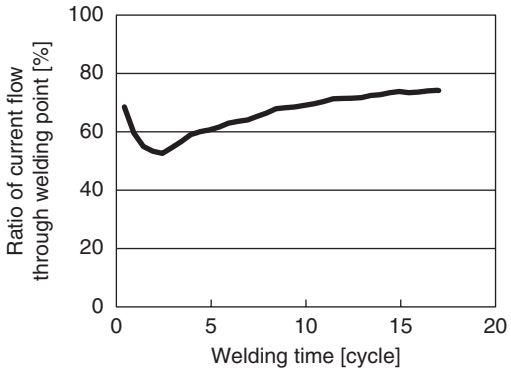


Fig. 7 Relationship between welding time and current shunt

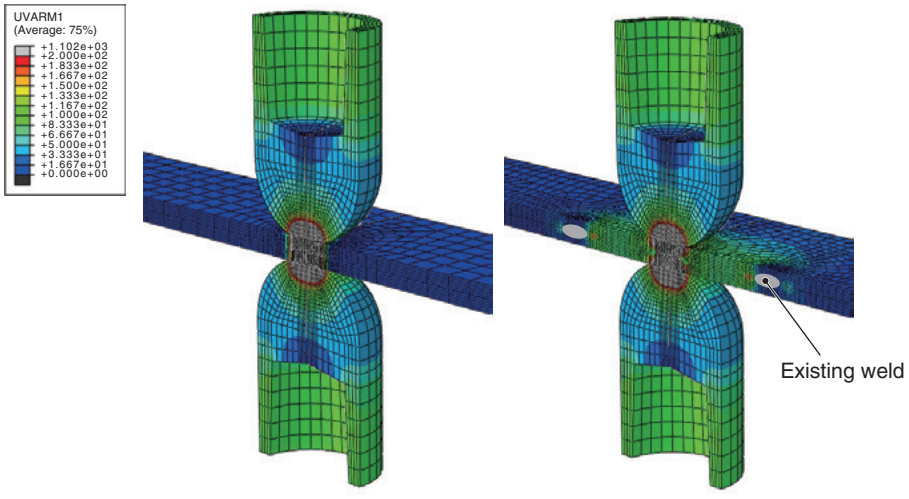


Fig. 5 Results of current density distribution by CAE

3. Method of Setting Welding Conditions

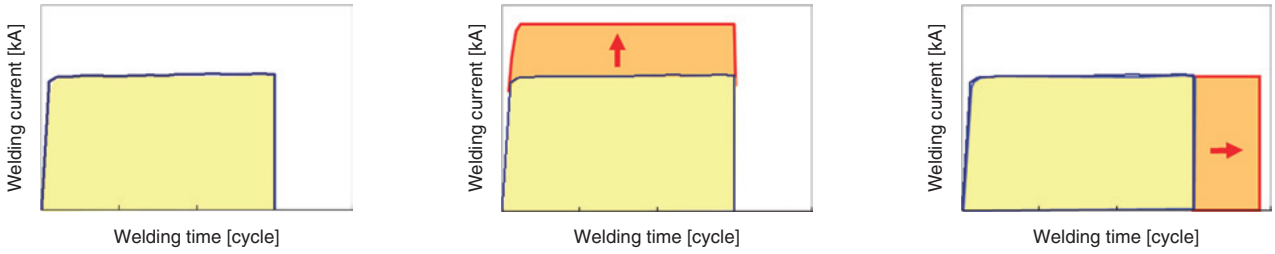
3.1. Study of Method of Compensation via Input Energy

It was conjectured that by increasing input energy in relation to the loss of heat generation resulting from shunting, it would be possible to satisfy nugget diameter standards, as for example, those stipulated by the Japanese Industrial Standards[2]. Figure 8(a) shows a schematic diagram of the current waveform for direct current. The area of the section shaded in yellow is input energy. A variety of methods of increasing input heat can be considered: increasing the input current [Fig. 8(b)], increasing the length of time for which the current is input [Fig. 8(c)], or a combination of the two suffice. The present research conducted a study of both increased welding current and increased welding time methods, using simulations and tests.

Table 2 shows the sheet combination and basic welding conditions. In order to study the effects of increased welding current and increased welding time, welding current and welding time were varied under the basic welding conditions (Fig. 9). Figure 9(a) shows results for increased welding current; results for single weld points are shown as black, and results for a weld pitch of 15 mm are shown as grey. The solid lines show CAE results, while the round points show test results. A decline in nugget diameter due to the effects of shunting under the same current conditions can be observed. However, increasing the welding current, increases the nugget diameter, and enables weld size equivalency to that of the single point weld. In Fig. 9(b) are results for increased welding time, and saturation can be observed from the 14th cycle onwards. The Joule's law equation [Equation (1)] also shows that current, I, has a significant effect on increasing the amount of heat produced, Q. This relationship also suggests the

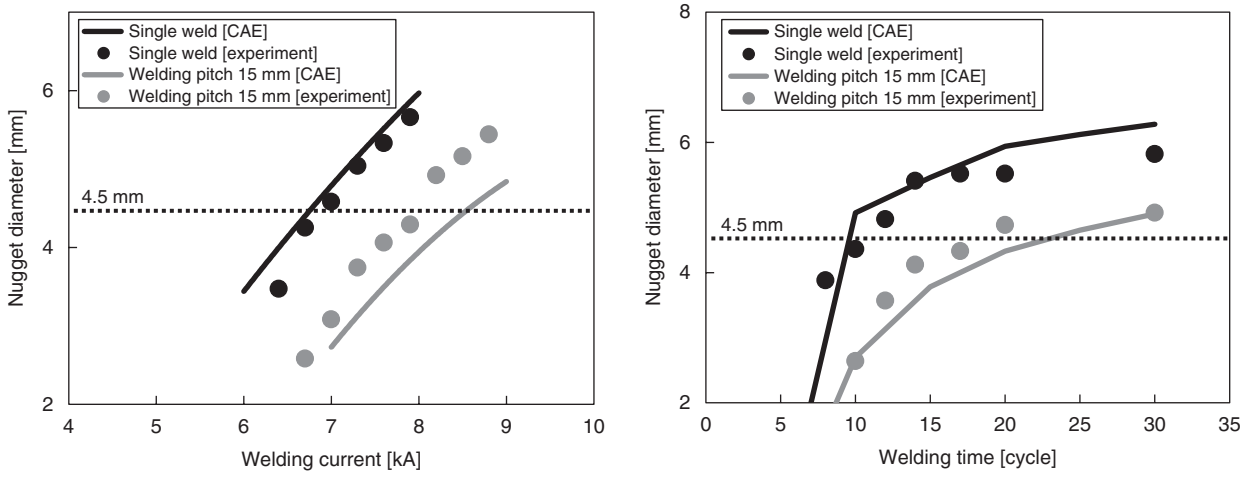
Table 2 Spot welding conditions

Sheet combination	JSC270D
Thickness	1.4 mm
Electrode force	3.5 kN
Welding current	7.6 kA
Welding time	14 cycles



(a) Conventional welding current (b) Increased welding current (c) Increased welding time

Fig. 8 Current waveform



(a) Increased welding current (b) Increased welding time

Fig. 9 Influence of welding current and welding time on nugget diameter

Table 3 Spot welding conditions

Sheet combination	JSC270F	JSC590R	JSC590R
Thickness	0.7 mm	1.4 mm	1.4 mm
Sheet size	30 mm × 100 mm		
Electrode force	3.5 kN		
Welding time	18 cycles		
Welding pitch	Single weld, 15 mm		

effectiveness of increasing current. In addition, increasing the welding time on an actual production line would have an effect on the number of welds that could be made in the process, further suggesting that increased current would be the more effective method of compensating for the loss of heat generation.

$$Q = R \times I^2 \times t \quad (1)$$

Q: Joule heat [J]
R: Resistance [Ω]
I: Current [A]
t: Time [s]

3.2. Study of Short-pitch Resistance Spot Welding Conditions using Sheet Combinations Employed in Actual Vehicles

A simulation analysis was conducted using representative three-sheet spot welding for sheet combinations in general use in vehicle bodies. Table 3 shows the sheet combination and welding conditions, and Fig. 10 shows the welding results.

Comparing single weld points and 15-mm pitch weld points of diameter 4.5 mm and larger, it was predicted that a 2.0 kA welding current increase for the close pitch joints would yield equivalent weld size to that of single point welds.

Tests were conducted based on the simulation results.

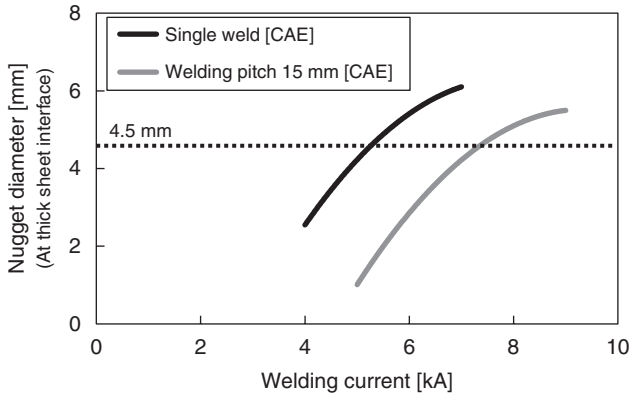


Fig. 10 Infuence of short-circuit on nugget diameter by CAE

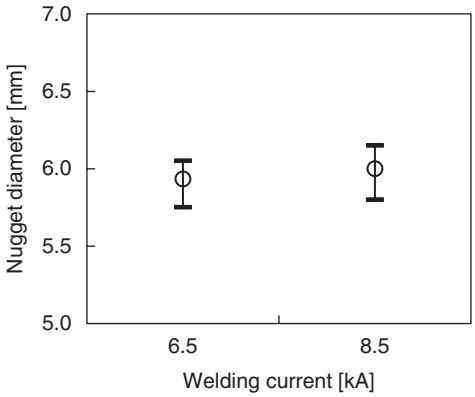


Fig. 11 Infuence of short-circuit on nugget diameter by experiment

For the single weld point, 6.5 kA was set as the welding current that would satisfy the nugget diameter standards. For the 15-mm pitch welds, the welding current was increased by 2.0 kA to 8.5 kA. Tests were conducted under these conditions, and Fig. 11 shows the test results. The nugget diameter for the 15 mm-pitch welds is almost equivalent to the nugget diameter for the single weld.

These results demonstrate that the simulation is able to make predictions for actual sheet combinations, including differing sheet thickness and material properties in three-sheet welds.

Conventionally, sheets of the same combination have been joined under the same welding conditions, but in the case of short-pitch RSW, the effect of shunting due to the welding pitch, the sheet combination, and the welding conditions makes it necessary to optimize the welding conditions in order to satisfy nugget diameter standards.

4. Application to Actual Vehicle

A study was conducted in order to determine which areas of an actual vehicle short-pitch RSW would be effectively applied. A CAE analysis was conducted, focusing on areas in which spot welding discontinuities were prone to occur under strength and durability conditions due to the stress concentration. Figure 12 shows the structure of the front damper housing. Figure 13(a) shows

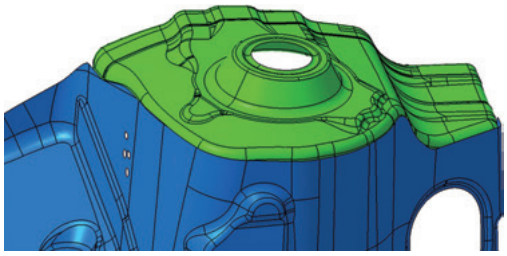
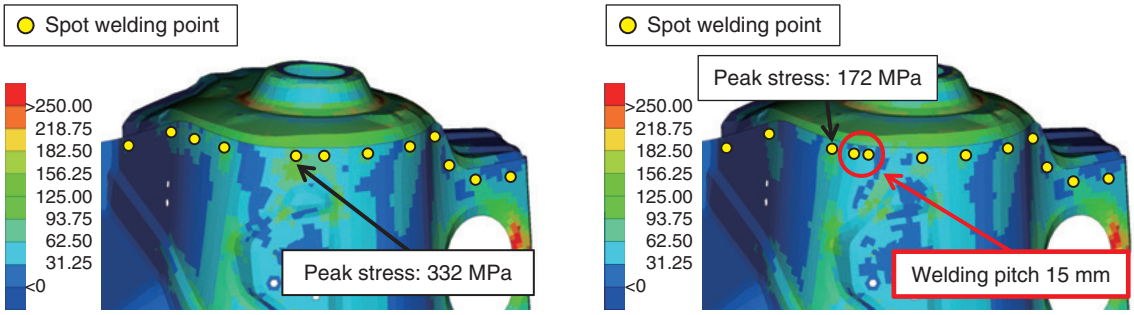


Fig. 12 Front damper housing structure



(a) Normal pitch (b) Short pitch

Fig. 13 Stress distribution

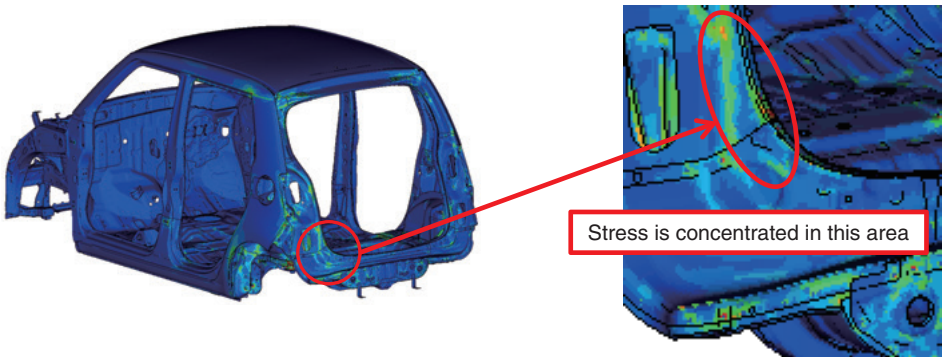


Fig. 14 Result of stress analysis by torsion test

the stress distribution in the structure with input from the damper. The input is particularly strong at the corners of the structure. A maximum stress of approximately 332 MPa is generated on the welding points used in conventional RSW. The use of short-pitch RSW in the corners of the damper housing disperses stress, reducing the maximum stress on the spot weld points by 48% [Fig. 13(b)]. Consequently, even if the sheets were reduced in thickness (to achieve a weight savings of approximately 13%), the stress target of 250 MPa at the spot weld points would be satisfied. This study changed the position of the welding points, but did not change the number of welding points. It would, therefore, be possible to achieve weight savings and reduce material costs through sheet thickness reduction, without increasing process costs associated with additional welding points.

In an entire vehicle body, stress concentrates particularly in the corners of the door openings and the tailgate, which are large open sections. Figure 14 shows the results of a stress analysis using a torsion test with input to the left rear damper. In the future, studies will be conducted concerning application of short-pitch RSW to areas of this type.

5. Conclusion

The development of a short-pitch RSW technology produced the following outcomes.

(1) Using a three-dimensional resistance spot welding simulation, the phenomenon of shunting was elucidated, and it was shown that the amount of shunting could be predicted even when sheet thickness, sheet combination, material properties, welding conditions, and other parameters differed.

(2) The study showed that heat loss due to shunting in short-pitch RSW could be compensated for, by appropriately inputting energy. In addition, it was demonstrated that it was possible to set welding conditions in order to realize a stable nugget diameter even when sheet thickness, sheet combination, material properties, and other parameters differed.

(3) In order to test the applicability of the method to vehicle bodies, short-pitch RSW was used in the areas of the body in which stress becomes high under the conditions employed in strength and durability tests, and it was verified that peak stress was reduced and that sheet thickness could be reduced in those areas.

This technology will first be applied in the 2014 model year FIT, following which its use will be successively expanded. It is believed that its use will contribute to the realization of weight savings.

References

(1) Doira, K., Ohoka, H., Umeno, K., Fukumoto, M., Okamura, K., Ueda, H.: Development of Resistance

Spot Welding Simulation Technology, Honda R&D Technical Review, Vol. 18, No. 1, p. 185-192
(2) Japanese Industrial Standards, JIS Z 3140:1989, Method of Inspection for Spot Weld

■ Author ■


Hisayasu OOKA


Atsushi SUZUKI


Mitsushige GOTO


Keita OTSUKA


Yasumasa OKADA

Application of Model-based Development to MICU

Noboru UJIGAWA* Shuhei KINOSHITA* Masayuki YAMAZAKI*

ABSTRACT

The introduction of model-based development is being promoted to increase specification quality in the development of software for body electrical parts. This introduction requires model-based development processes and development tools. Therefore, a model-based development process was constructed that covers from analysis of requirements in the early stages of development to definition of the methods for achieving those requirements. In addition, the tools needed to efficiently promote development were developed. The constructed process was applied to trial development of a Multiplex Integrated Control Unit, and resulted in a 35% reduction in incompleteness (undefined, conflicting or ambiguous specifications) compared to control specifications created using the previous development process.

1. Introduction

As the importance of electronic control technology in automobiles increases, the scale and complexity of software is increasing steadily[(1)]. However, demands to increase quality, shorten the development time, and reduce the cost of electronic control units are also increasing. Amidst these circumstances, the introduction of model-based development (MBD) is recently being promoted to increase the quality of software mounted in vehicles[(2)-(4)].

The control specifications for Multiplex Integrated Control Units (MICU) that perform integrated control of body electrical functions such as door locks, wipers, headlights, turn signal lamps and hazard lamps are presented to suppliers, and suppliers develop parts based on those specifications.

However, issues concerning the control specifications presented to suppliers included clearly defining the requirements and specifications that form the basis of the specification definitions, how to ascertain the compatibility of common use design specifications, and performing unambiguous design.

An MBD process was constructed and trial MICU development was performed to address the above issues. This paper describes the constructed process and developed tools, and the effects obtained from trial development.

2. Goals of Process Construction

The goals of constructing an MBD process were established as follows.

(1) Creating a system that enables separation of requirements and specifications, analysis of requirements from multiple viewpoints, and detection of insufficient requirement definitions
(2) Creating a system that allows clear expression of the relationships between requirements and specifications, and association of the reasons and other information concerning those relationships.
(3) Creating a system that enables reduction of specification ambiguity by using a semi-formal specification description language

3. Construction of the Development Process

3.1. Process Overview

The constructed MBD process consists of analysis viewpoints and levels (Fig. 1).

3.1.1. Viewpoints

Analysis is performed from multiple viewpoints to enable detection of insufficient requirement definitions in the early stages of development. These analysis viewpoints are as follows.

- Behavior: The required behavior and state transitions of the system are defined.
- Structure: The static composition and structure of the system are defined.
- Requirement: The required contents of the system are defined.

3.1.2. Levels

(1) System definition: The subject of development (what) is clarified and the system for which requirements are to be

* Automobile R&D Center

defined is specified. The system scope, role, functions and relationships with other systems are defined in this level.

(2) Requirement definition: The demanded behavior, structure and requirements of the specified system are defined.

(3) Method definition: The specific methods (how) for realizing the system are defined. These methods are associated with the behavior, structure and requirements defined by the requirement definition, and each is assigned a reason (why).

3.1.3. Work product

Figure 2 shows the work product created for each viewpoint and level. These work products are created mainly using System Modeling Language (SysML)[5] diagrams, MATLAB/Simulink and Stateflow[6]. Here, the minimum work product required for each analysis viewpoint and level is selected from the multiple diagrams defined by SysML.

3.2. Process Details

Figure 3 shows the detailed workflow for the process configured by the analysis viewpoint and level framework.

3.2.1. System definition

(1) Definition of development scope: The system to be developed is specified using a use case diagram. In addition, the users and other systems related to the specified system are defined (Fig. 4).

- Definition of system users: Persons (e.g., drivers) and things (e.g., other systems) that use the system are defined as actors.
- Definition of system functions: Functions required of the system from the viewpoints of the actors are defined as use cases.
- Definition of relationship between system users and functions: Use cases and the actors that execute (use) those use cases are associated.
- Definition of system boundaries: Use cases are enclosed by system boundary frames, and the system to be developed is defined.

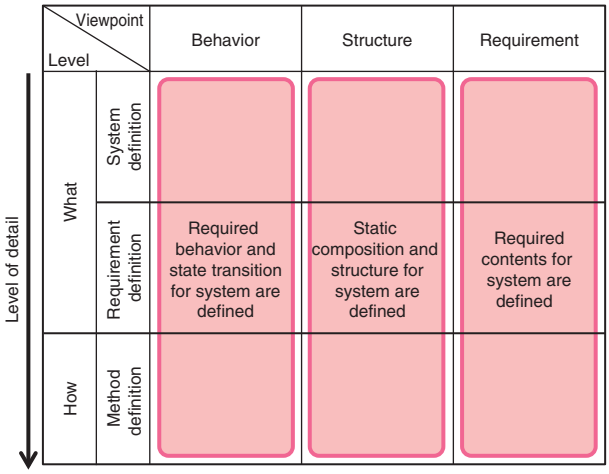


Fig. 1 Relationship between process and analysis viewpoints

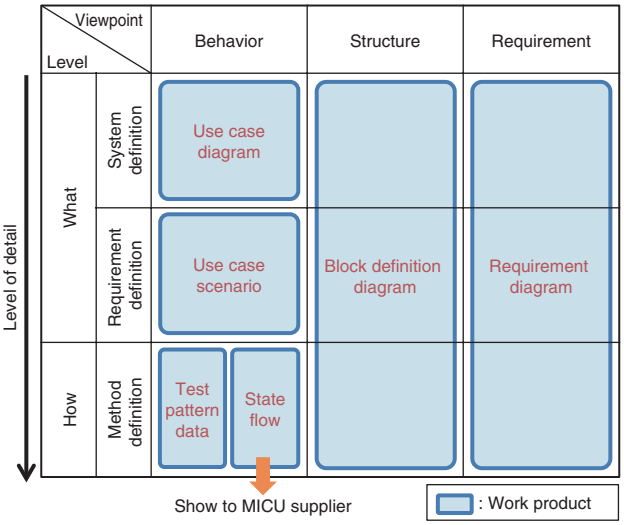


Fig. 2 Work product of each viewpoint and level

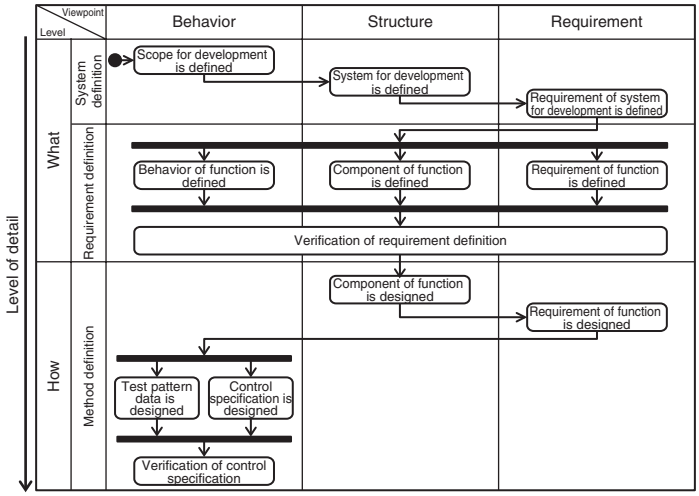


Fig. 3 Workflow of development

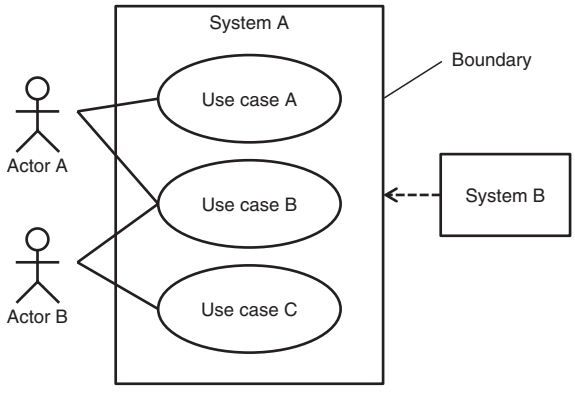


Fig. 4 Example of use case diagram

(2) Definition of system to be developed: The system to be developed is defined as a block definition diagram based on the use case diagram (Fig. 5).
- Boundary frames in the use case diagram are defined as the structure blocks in the block definition diagram, and information such as the system overview and body type is assigned.

(3) Definition of requirements of system to be developed: The requirements of the system to be developed are defined as a requirement diagram based on the use case diagram (Fig. 5).
- The use cases in the use case diagram are defined as the requirement blocks in the requirement diagram.

3.2.2. Requirement definition

(1) Analysis and definition of function behavior: Function behaviors are defined using scenarios based on the use case diagram (Fig. 6).
Scenarios define the interactions between the actors appearing in the use case diagram and the system, and the system behavior at that time. In this step the behavior is defined in various situations that can be conceived for the system.
- Definition of basic scenarios: The interactions between related actors and the system are defined as the basic scenario for each use case.
- Definition of expanded scenarios: Different patterns of precondition and post-condition, procedures leading to the post-condition, and actors for a basic scenario are derived and defined as the expanded scenario.

(2) Definition of function elements: The required system elements are defined in a block definition diagram based on the block definition diagram defined in the system definition process (Fig. 7).
The elements comprising the system are defined as structure blocks. In addition, the relationship between structure blocks is also defined. The definition process is as follows.
- The system elements needed to satisfy the requirements are defined as structure blocks from the viewpoints of input, control and output.
- The defined structure blocks are associated according to the relationship between upper and lower structures.
- The information exchanged between structure blocks

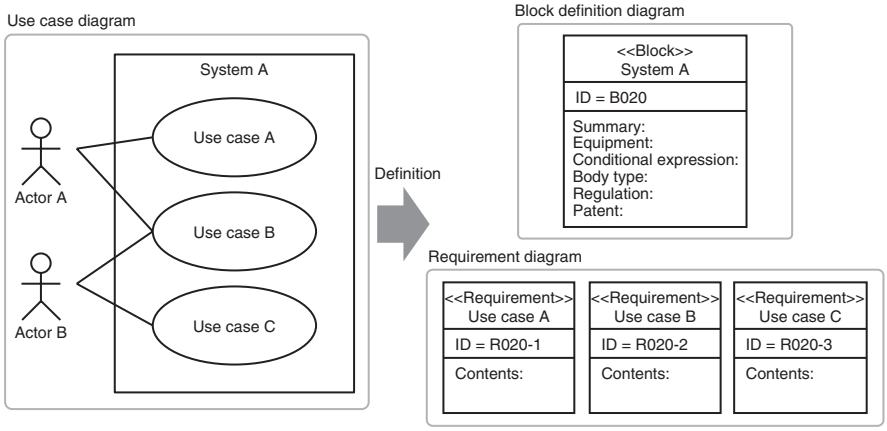


Fig. 5 Relationship of each diagram in system definition process

Scenario	
ID	UC020-1-1
Summary	···
Actor	Driver
Order	Contents
Precondition	Ignition is OFF
1	Driver turns on ignition
2	System outputs relay
3	End of Scenario
Postcondition	Relay is ON

Fig. 6 Example of use case scenario

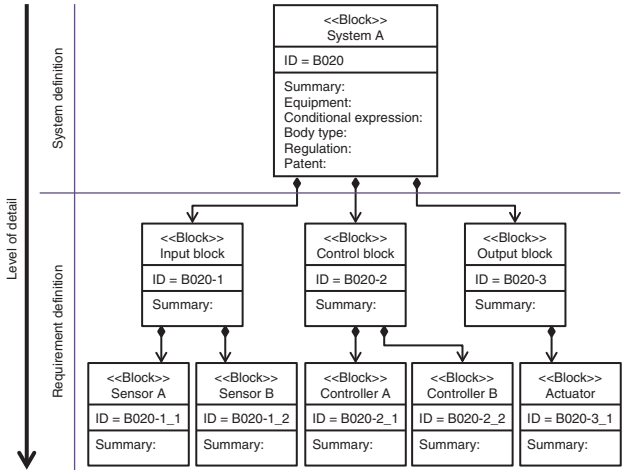


Fig. 7 Example of block definition diagram in requirement definition process

is defined in each structure block as input and output information (Fig. 8).

(3) Analysis and definition of function requirements: The requirements for each function are defined in a requirement diagram based on the requirement diagram defined in the system definition process (Fig. 9).
The requirements of each function are defined as requirement blocks, and the relationship between requirement blocks is defined. The definition procedure is shown below.
- The detailed requirements (e.g., operations, conditions, output, priority ranking in case of requirement conflict) of the use cases defined in the system definition process are extracted in consideration of system use scenarios, and defined as requirement blocks.
- The defined requirement blocks are associated according to the relationship between upper and lower requirements.
- The reason for each requirement is associated.

(4) Verification of requirement definition: The work products created in the requirement definition process are compared as shown in Fig. 10 and verified from the following viewpoints.
(a) Comparison of requirement diagram and scenarios
- Are the requirements needed to satisfy the scenario defined?
- Are all scenarios associated with requirements?

(b) Comparison of scenarios and block definition diagram
- Are the structures needed to satisfy the scenarios defined?
- Is the input and output information needed to satisfy the scenarios defined?

(c) Comparison of block definition diagram and requirement diagram
- Are the structures needed to satisfy the requirements defined?
- Are all requirements associated with structures?
- Is the input and output information needed to satisfy the requirements defined?

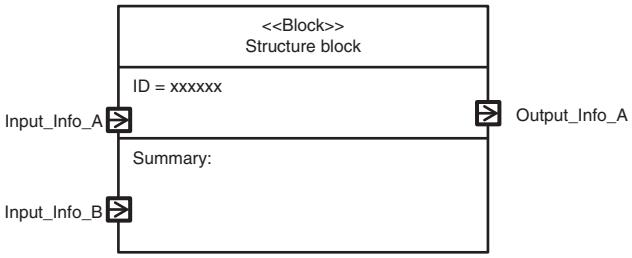


Fig. 8 Example of definition of input and output information to structure block

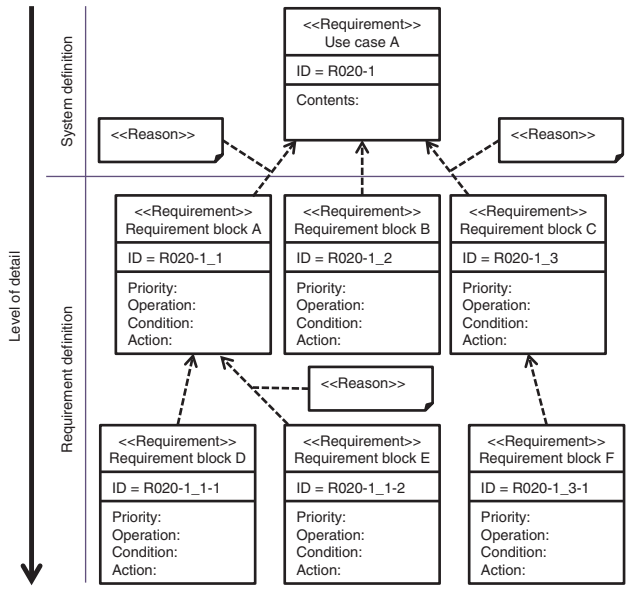


Fig. 9 Example of requirement diagram in requirement definition process

3.2.3. Method definition

(1) Specification of function elements: The specific components are defined in a block definition diagram based on the block definition diagram defined in the requirement definition process (Fig. 11). The definition procedure is shown below.
- The specific components (e.g., switches, ECU, actuators) are defined as structure blocks for the structure blocks defined from the input, control and output viewpoints in the requirement definition process. At this time the information and evidence indicating the reason for selection are associated with the structure block. This associated information enables ascertaining of the compatibility of common

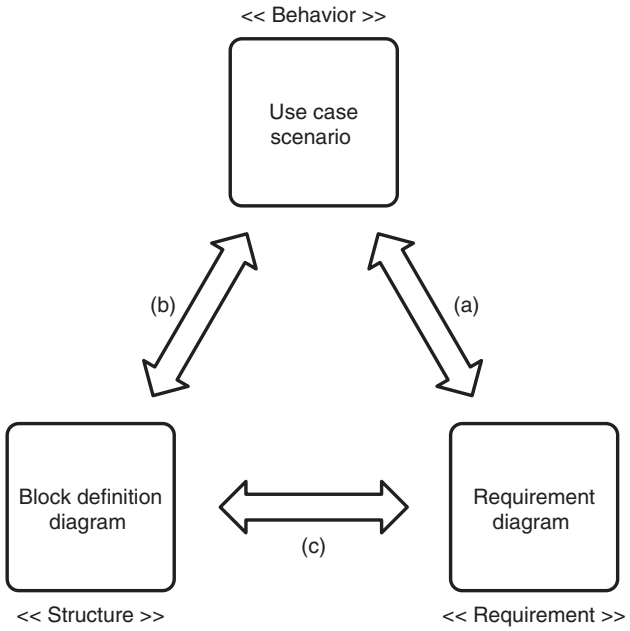


Fig. 10 Verification of work product

use design specifications in case of differential development such as minor changes or specification changes for each destination.
- Software elements are defined as structure blocks for the structure blocks defined from the control viewpoint in the requirement definition process.
- The defined structure blocks are associated according to the relationship between upper and lower structures.
- Electrical characteristics and other data are defined as attribute information for each defined structure block.
- The input and output information is defined for each structure block.

(2) Specification of function requirements: Methods are investigated and associated with the requirements in the requirement diagram based on the block definition diagram and requirement diagram defined in the requirement definition process.
Methods for the operations, conditions and outputs defined in the requirement diagram are defined in requirement blocks in consideration of restrictions arising from the hardware configuration and software processing methods, and these methods are associated with the requirements. In addition, the reasons for the methods are associated with the requirement blocks.

(3) Creation of test patterns: Test patterns are created on the basis of the scenarios defined in the requirement definition process and the input and output information defined in the block definition diagram (Fig. 12).

(4) Creation of control specifications: The Stateflow is defined on the basis of the requirement diagram and block definition diagram created thus far (Fig. 13).
The detailed events required for control and the states that arise when events occur are defined using the states and transition conditions.
- Definition of states
  Of the input and output information defined in the structure blocks of the block definition diagram, the output information is extracted as the states.
- Definition of transition conditions
  Each condition described in the requirement blocks defined in the requirement diagram is defined as a condition for transition between states.
- States and transition conditions are added and deleted as necessary.

The Stateflow created here is based on description rules established for other process models as a result of hearings to collect requests from suppliers in order to present control specifications to suppliers.

(5) Verification of control: The Stateflow and test patterns are compared to verify the defined control specifications.

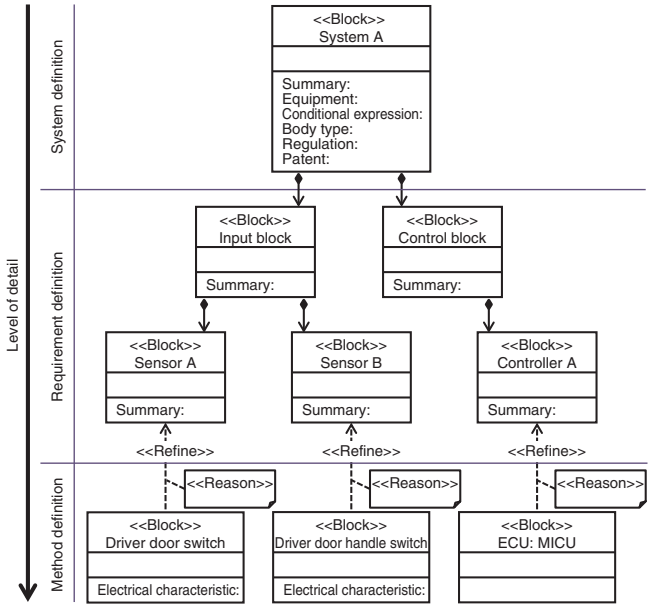


Fig. 11 Example of block definition diagram in method definition process

Time (sec)	Signal						
	Input					Output	
	Signal_A	Signal_B	Signal_C	Signal_D	Signal_E	Signal_F	Signal_G
0	0	0	0	0	1	0	0
1.00	0	1	0	0	1	0	0
2.00	0	1	0	0	1	0	0
3.00	0	0	0	0	1	0	0
4.00	0	0	0	0	1	0	0
5.00	0	0	0	0	1	1	0
6.00	0	0	0	0	1	1	0
7.00	0	0	2	0	1	0	1
8.00	0	0	2	0	1	0	1
9.00	0	0	2	0	1	0	0
10.00	0	0	2	0	1	0	0

: Change point of value

Fig. 12 Example of test pattern data

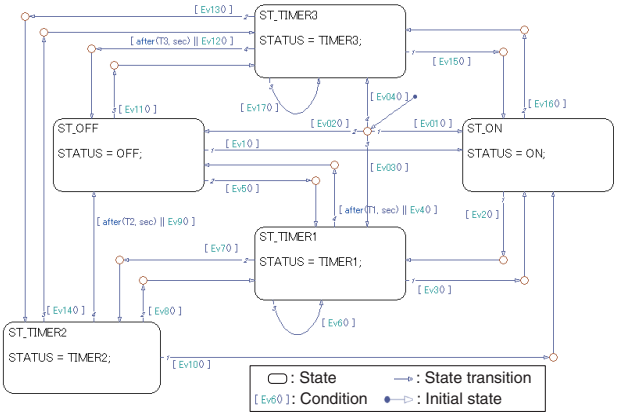


Fig. 13 Example of Stateflow

4. Construction of Development Tools

4.1. Synchronization of Input and Output Information

The input and output information of each block is defined in the structure blocks of the block definition diagram. However, many attributes such as name, direction, meaning, possible value, and initial value are assigned to input and output information, and it was a burden to describe the attributes for each input and output information in the model. In addition, complex procedures were also required to display the attribute information when examining the detailed description contents.

Therefore, a tool was developed that can edit the input and output attribute information and reflect the edited contents to the model using a list format user interface. This tool can also be used to output the model contents in list format (Fig. 14).

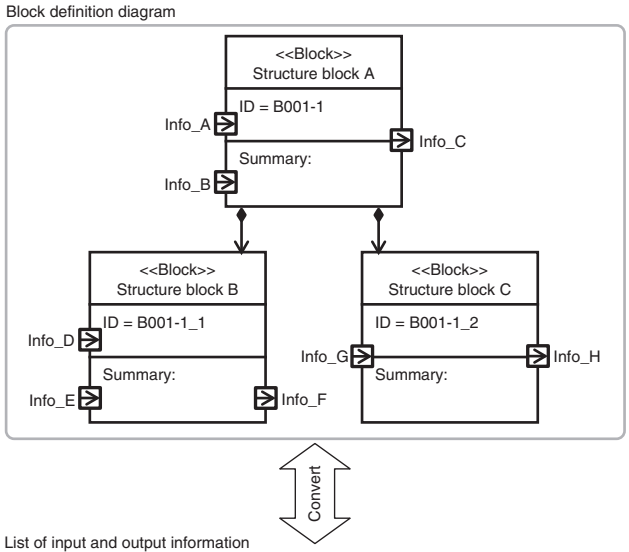
This tool enabled reduction of the work time required to assign input and output information to 1/5 that prior to tool introduction.

4.2. Automatic Assignment of IDs to Demands and Structural Elements

Unique IDs were assigned to requirement blocks and structure blocks. However, the number of blocks increases in proportion with the size of the system, so much work time was required to define the IDs one by one in the model. In addition, repeated changes to models resulted in ID overlap.

Therefore, a tool was constructed that automatically assigns a unique ID to each block, enabling automation of the tasks of “Redefine all IDs,” “Define IDs only for elements (requirement and structure blocks) without ID definition,” and “Delete all IDs.”

This tool enabled complete prevention of ID duplication and shortened the work time required to assign IDs to 1/2 that prior to introduction.



List of input and output information

Structure ID	Structure name	Signal name	In/Out	Value	Initial value	Description
B001-1	Structure block A	Info_A	In	···	···	···
B001-1	Structure block A	Info_B	In	···	···	···
B001-1	Structure block A	Info_C	Out	···	···	···
B001-1_1	Structure block B	Info_D	In	···	···	···
B001-1_1	Structure block B	Info_E	In	···	···	···
B001-1_1	Structure block B	Info_F	Out	···	···	···
B001-1_2	Structure block C	Info_G	In	···	···	···
B001-1_2	Structure block C	Info_H	Out	···	···	···

Fig. 14 Synchronous tool of input and output information

5. Verification of the Process

Trial MICU development was performed in accordance with the MBD process to verify the constructed process. The number of specification checks from the supplier for the control specifications was used as the evaluation scale used to judge the advantages and disadvantages of the constructed process.

The condition was that if the number of specification checks classified as undefined and undescribed, conflicting, or ambiguous (multiple interpretations possible) in the breakdown of specification checks from the supplier could be reduced, the constructed process would be judged to have higher development quality than the previous development process.

The cooperation of the MICU supplier was obtained, and the control specification created using the MBD process was checked by the supplier from the same viewpoints as the previous development. As a result, the number of specification checks classified as undefined and undescribed, conflicting, or ambiguous decreased by 35%.

6. Conclusion

The newly constructed MBD process enabled organizing of the purpose of the system, the system configuration, and how each system element behaves, by analyzing the system from the three viewpoints of behavior, structure and requirements. Furthermore, the requirement quality could be increased by organizing and comparing each work product. In addition, association of requirements, reasons for requirements, and methods for achieving requirements enabled ascertaining of the compatibility of common use design specifications.

In the future, the constructed development process will be applied to mass-production development in order to steadily increase quality as well as continue to promote enhancements from the viewpoint of efficiency. In addition, efforts will also be made to establish rules governing the use of work products by multiple divisions, and to popularize the MBD process.

References

(1) Shasai sofuto kyodaikani tachimukau, Nikkei

Automotive Technology, 2007-11, Nikkei Business Publications, p. 82-83 (2007) (in Japanese)
(2) http://sec.ipa.go.jp/reports/20120323.html, 2012/8/23
(3) Mizutani, M., Yahata, Y., Kamei, Y., Hayase, K., Kaneda, M.: Application of model-based development to body-system mass-produced ECU, Mitsubishi Motors Technical Review, No. 22, p. 56-59 (2010)
(4) Watanabe, S., Yoshino, H., Shionoya, Y., Seki, T.: New MBD Software Development Process for Electronic Control AWD System, Honda R&D Technical Review, Vol. 23, No. 1, p. 23-29
(5) http://www.omgsysml.org/
(6) http://www.mathworks.co.jp/products/

■ Author ■


Noboru UJIGAWA


Shuhei KINOSHITA


Masayuki YAMAZAKI

Design Appearance Evaluation Tool for Non-prototype Development

Daisuke IDE* Ryosuke SAITO** Hajime KUBO**

ABSTRACT

The aim with this paper is to achieve a tool for non-prototype automotive development that is faster, simpler, and enables judgment equivalent to that with a physical model. Evaluation by the computer graphics to convey the appeal of shapes by means of artistic effects is commonly used. In non-prototype development, computer graphic output effects allowing the same judgment as with a physical model are required, and this approach has to yield output for evaluation with highly accurate results and by a realistic amount of calculation time without depending on the skills of individuals.

The computer graphic software named Total Objective and Physical Simulation was developed in order to achieve the required computer graphic output with a reasonable amount of calculation time. It was decided that the software would not use manual adjustment of environment and material parameters, but instead handle only data measured from actual objects. In addition, Monte Carlo path tracing specialized for parallel Graphic Processing Units was adopted for the calculation technique. This tool achieved physically correct rendering based on measurement data with a high level of performance.

1. Introduction

There are at present increasing requirements for non-prototype approaches to automobile development in order to shorten development time.

In the design field, mockups are fabricated and evaluated in order to judge styling design quality. However the judgment of styling design quality at the final stages leading to mass production requires to confirm the accurate appearance that includes the functional components involved. This is referred to as design appearance evaluation. Design appearance evaluation needs judgment of a prototype car, and taking into consideration the process until completion of a prototype car, it poses a major issue for the shortening of development time.

This development will describe the features and results from workplace use of the computer graphics (CG) software known as Total Objective and Physical Simulation (TOPS), which has been under development to enable CG confirmation as an alternative to the prototype car in design appearance evaluation.

2. Development Goals

2.1. Differences from Conventional CG Software

Conventionally, the role of CG software in design development was mainly in the area of concept design in the initial stages of development. This area calls for effective rendering of the appeal of the design concept and shape intended by the designers. In many cases, therefore, this would convey the appeal of the shape by depicting it in ways that are not to be found in reality, as seen in Fig. 1(a). Consequently, these images are modified by tuning in many ways. Specialized personnel with advanced CG skills are also needed to implement the tuning.

However, in order for the appeal intended by the designers to be carried over into mass production, not only the appeal of the shape, but also the appearance when fabricated as a physical model need to be confirmed. Conventionally, this was done using mockups and prototype cars. In non-prototype development, however, a final check using a physical model cannot be performed, and so this needs to be done using CG. For this kind of confirmation, the output should not be the kind of presentation in Fig. 1(a), should accurately depict the physical model as though in a photograph, in Fig. 1(b). In addition, enabling judgment equal to that of a physical model should not depend on skills, should keep consistent uniformity. Software that satisfied this requirement did not exist, and so it was decided to develop new software.

2.2. Requirements for Design Appearance Evaluation

Conventionally, design appearance evaluation was implemented with imagery data processed using CATIA,

* HG Administration Division

** Automobile R&D Center

and this method clarify brought numerous issues. On many of the points identified, however, judgment cannot be readily made on the basis of imagery data, and many points require a physical model in order to make a judgment. Consequently, confirmation is made in combination with the use of a prototype car. The identified items were therefore analyzed, and they were found to be subject to tendency classification as shown in Fig. 2.

Particular items tending to require an actual vehicle to enable judgment were found to be summarized as (1) glass reflections and refractions, (2) reflections matching the material and appearance of the internal looks through gaps, and (3) shade on fit and gap areas (Fig. 3). These areas revealed conspicuous differences in appearance between CATIA and an actual vehicle, so that proper design appearance evaluation could not be readily performed. These points in particular, therefore, require rendering that presents their appearance accurately.



(a) Artistic (b) Real

Fig. 1 Artistic and Real

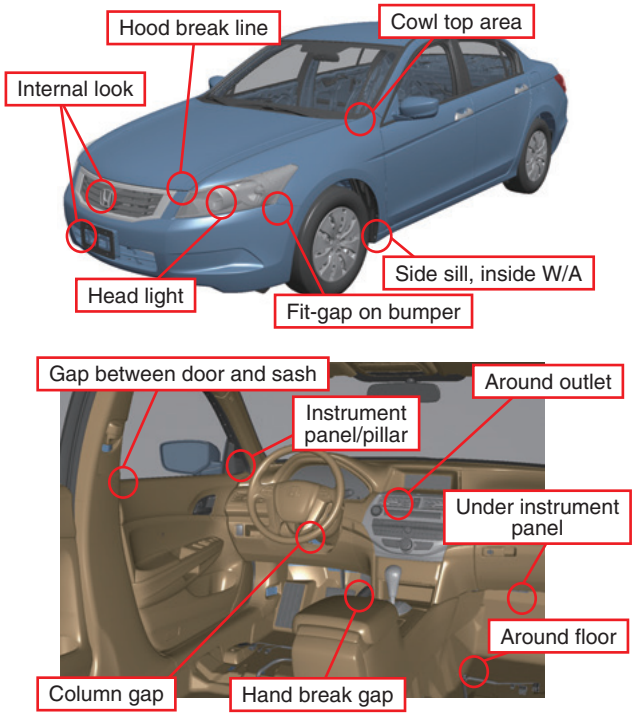


Fig. 2 Issues reported as “Physical model required”

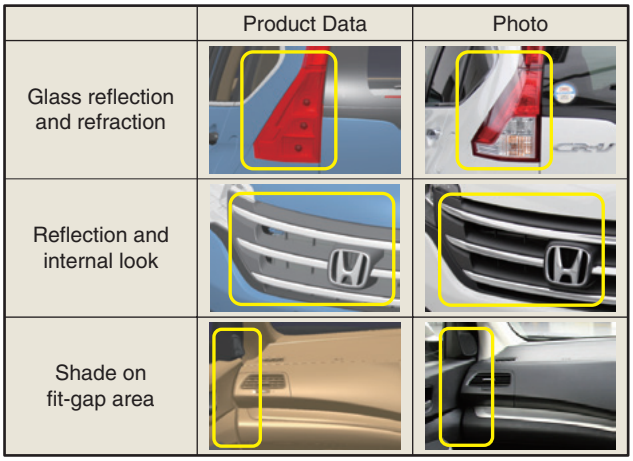


Fig. 3 Points of attention for physical model check

3. Technology to Achieve Goals

3.1. Technical Issues

In order to use technological means to achieve the desired requirements, accurate simulations of light and material objects are needed. This, first of all, needs accurate shape data on the vehicle. It additionally needs an environment model that is accurately rendered in the same way as an actual space, and a material model that accurately renders surface characteristics in the same way as a physical model.

Simulation of light behavior is performed using the above three (Fig. 4), but since this entails a massive amount of calculation, conventional CG software uses many arbitrary approximation methods to obtain its results. In order to render the physical model, however, it is necessary to eliminate arbitrary approximation processing and to perform accurate calculation in detail. Considering also that this is being used in the automotive development workplace, a system that outputs results interactively in response to user operations is sought. It is also necessary to

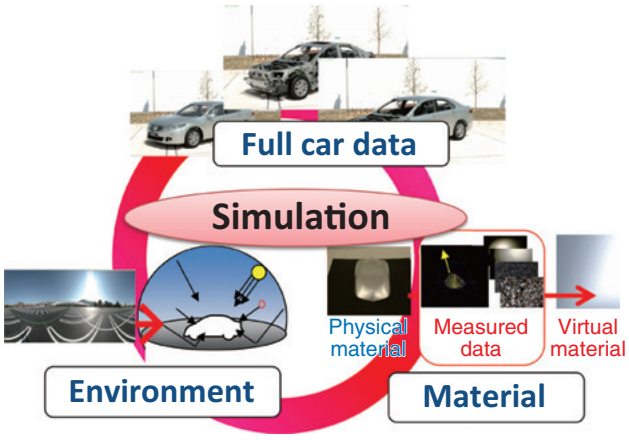


Fig. 4 TOPS overall structure

produce results within a short calculating time, even if the calculations are massive.

To summarize, the technical issues needing to be overcome were (1) technology for rendering material properties, (2) technology for rendering environment characteristics, and (3) computing technology for completing the processing quickly.

3.2. Technology for Rendering Material Properties

Three technologies were used to render material properties: a measuring instrument for obtaining the reflection characteristics (Bidirectional Reflectance Distribution Function: BRDF)[1] for all angles of incidence and reflection angles; a microscope for measuring minute light behavior of flakes and so on included in coatings; and a highly accurate scanner for measuring surface texture and other large patterns. The BRDF in particular is an important element in representing material properties. However, commercial measuring instruments do not readily provide accurate measurement data for certain areas, such as in a regular reflection direction and at angles close to the horizontal.

The physical properties were therefore obtained from coated surfaces, plastic, glass, and other such compositions, and matching material models were created. As regards elements of importance for material properties, such as materials, processing methods, and so on, information was available on those materials that are used within Honda, and this allowed the formation of models specialized for the use of those materials. This enables compensation for measuring instrument error and accurate material rendering (Fig. 5).

3.3. Technology for Rendering Environment Characteristics

Measurement of the environment needs accurate measurement of light intensity and hue. For that purpose, a camera that captures High Dynamic Range (HDR) imagery containing more color information than ordinary imagery was used together with an actinometer that measures absolute values of light intensity. In addition, gamma value correction and white balance correction matched to the camera characteristics were performed, and an environment model with well-adjusted light intensity and color balance was created (Fig. 6).

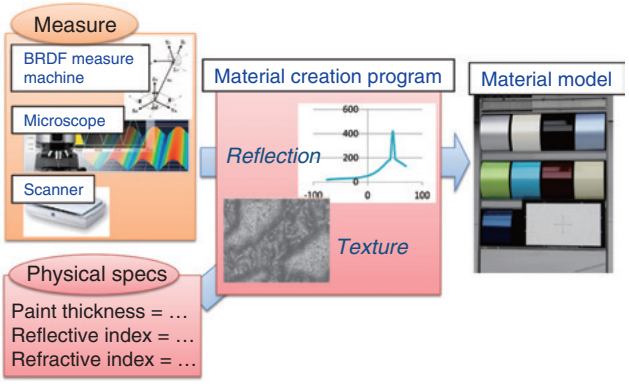


Fig. 5 TOPS material creation

3.4. Computing Technology

The method adopted for calculation of the simulation is called Path Tracing[2], which performs light calculations all together without approximations. This method does not separate the categories of direct light and indirect light. The calculations of light from the environment falling on material objects are performed all together.

In high-precision CG software, a method called Ray Tracing[3] is often used. This performs calculations only of direct light, which can be done at greater speed. This method alone is unable to render shadows accurately, so it is used together with a variety of methods known as Global Illumination[4, 5] that handle indirect light, which involves enormous amounts of calculation, by rendering approximations. This can render an appearance that is similar to that produced by indirect light calculation. However, the rendering requires large amounts of manual tuning, which has a major influence on the output results.

In Path Tracing, by contrast, indirect light is also calculated as part of the whole so that indirect light can be rendered accurately and manual tuning is not needed (Fig. 7). The amount of calculation becomes massive, however, and in order to achieve higher calculation speed, TOPS focused on the GPU, which has shown rapidly increasing performance in recent years.

GPU is generally a processing unit that is specialized for graphics processing. Compared to a central processing unit (CPU), which is commonly used to calculate simulations, the GPU enables fast calculations at lower cost. However, the GPU is not well suited to branch processing and other such more complex calculations, and achieving high calculating capability has to involve simplification and

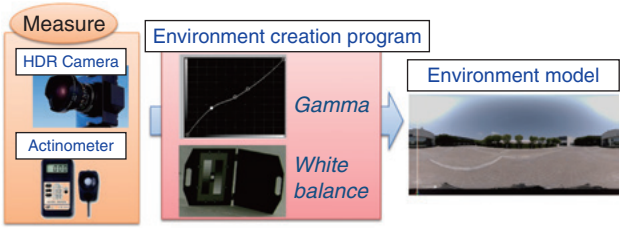


Fig. 6 TOPS environment creation

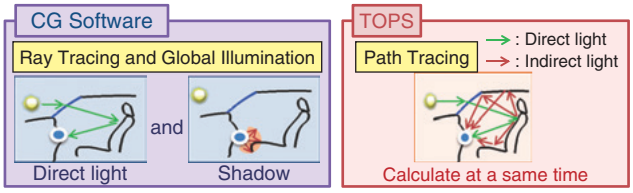


Fig. 7 TOPS rendering engine

parallelization of individual calculations.

The Monte Carlo method, which performs simulations in a probabilistic manner, was therefore adopted for TOPS, and it was implemented to employ parallel processing specialized for the GPU. The Monte Carlo method performs repeated calculations using random numbers, and each calculation is independent. This makes it more readily adaptable to parallelization, and suits this method to calculation using a GPU.

4. Results

Figures 8 and 9 show actual vehicle photographs and TOPS output results. The actual vehicle photographs also indicate points of attention for design appearance evaluation. All the environment and material information was created from measured data, and these results achieve rendering with an appearance identical to photographs.

These results can be considered to yield output on a par with photographs with regard to the visual points that need confirmation using an actual vehicle. The openings and inside of the wheel house in Fig. 8 appear to be lighter than on the actual vehicle. This is because the fin shapes, surface processing, and other details of functional components inside the openings are areas that were not included in the drawing issue data, so they were not reflected in the rendering data and they therefore present a different appearance. In order to obtain a more accurate appearance, therefore, more accurate shape rendering is necessary.

Figure 10 shows TOPS output results for different materials. Since differences in material have a large impact

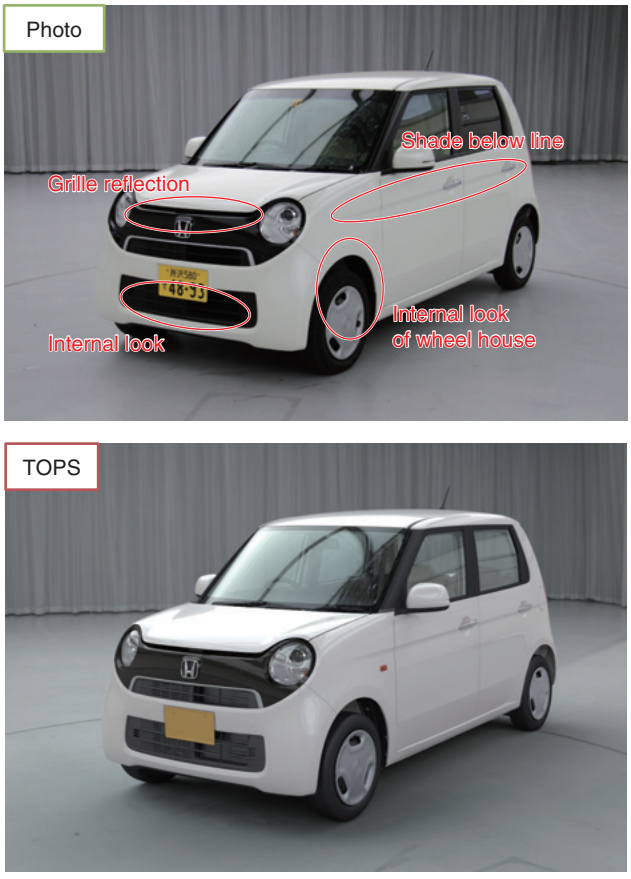


Fig. 8 TOPS result (Exterior)

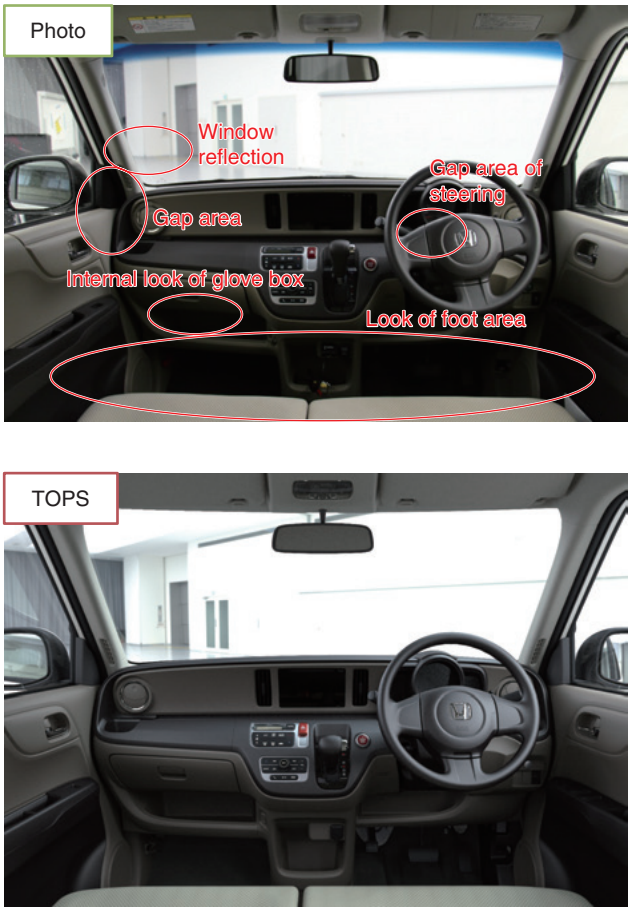


Fig. 9 TOPS result (Interior)



Fig. 10 TOPS result (Appearance difference by material)

on the appearance, TOPS calculates the various material properties and renders the way highlights and shadows appear according to the material.

Next, regarding calculation time, TOPS maximizes use of an arrangement specialized for the GPU by mounting eight high-performance GPUs (seven NVIDIA Tesla K10 chips and one NVIDIA Tesla M2070Q) in a single computer.

Calculation time increases according to how many times reflection and refraction phenomena appear. Consequently, the vehicle lights that involve calculation of appearance seen through more complex lenses are the parts that take the most calculation time. Figure 11 shows the results from rendering the lights in Full HD (1920×1080) resolution. The Monte Carlo method initially yields results that contain considerable noise, but then these gradually resolve. The result after 0.1 second is extremely noisy, but after five seconds the image generally resolves. Stable results are obtained in about 60 seconds.

Even in those areas that take the most time, therefore, approximate results can be obtained in about five seconds. This can be considered to have achieved sufficient calculation speed to enable interactive operation.

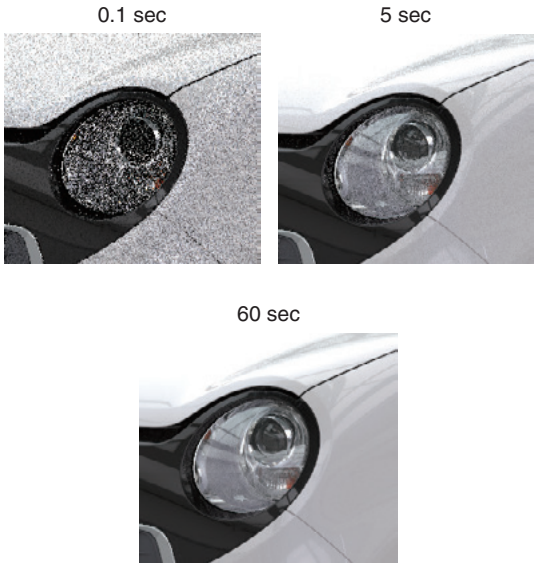


Fig. 11 TOPS result (Performance)

5. Conclusion and Future Outlook

In moving toward non-prototype development, development of TOPS has been pursued with the aim of achieving design appearance evaluation by CG that is equivalent to use of a physical model. TOPS differs from conventional CG software in that it creates all the data for rendering environment and material from measured data, and in that it calculates accurate simulations of light at high speed. This was able to produce rendering results that are equivalent to use of a physical model. This approach achieved a degree of accuracy in rendering data that is adequate for design appearance evaluation of items that, until now, could only be checked using a prototype car.

However, the appearance equivalent to a photograph that was achieved here cannot be considered equal to the appearance of a physical model in actual human eyes. Human eyes automatically apply compensation to input information, and they can see things that are not visible in a photograph.

Figure 12 shows photographs that are all taken of actual cars. In the case of photographs, when they are taken so that the darker areas are visible, the lighter areas are washed out, and when they are taken so the lighter areas are visible, the darker areas turn all black. To the actual human eye, however, both seem to be visible simultaneously. The use of CG to render an image for judgment that can completely replace the physical model in design appearance evaluation will depend on consideration of rendering methods that are faithful to reality and that can adequately reproduce the effects of the human eye.

Advanced rendering methods will be necessary in order to move forward from photographic quality to physical model quality. First, it is necessary to obtain real-time calculation performance to capture shapes dynamically. Since the TOPS calculation method can be readily parallelized, it achieves higher levels of scalability with respect to hardware enhancement, and it is capable of reaching that next step.

Second, it is necessary to enhance display devices. The present effort used standard display devices with Full HD resolution and 24-bit color resolution, but devices with still more advanced resolution and color resolution have been coming on the market. Higher color resolution can be considered particularly effective in enhancing reproducibility. In addition, the use of calibration matched to the display device can be expected to render output that is identical to the actual appearance of the space being viewed.

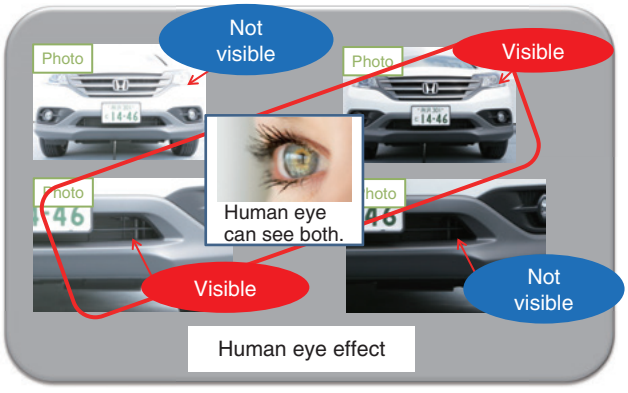


Fig. 12 Photo realistic and real

Third, Rendering of three-dimensional space will also be necessary. That will require highly accurate 3D display devices that can render an accurate sense of distance, so future evolutions of technology will be explored.

In conjunction with that, verification of the correlation with the actual vehicle will be performed repeatedly by comparing actual vehicles side by side with TOPS output in order to confirm whether output equal to the physical model is being obtained. This will investigate human evaluation methods and uncover requirements.

Our intention is to continue pursuing further development and deployment in order to build systems that will contribute to non-prototype development.

References

(1) Nicodemus, F. E., Richmond, J. C., Hsia, J. J, Ginsberg, I. W., Limperis, T.: Geometrical Considerations and Nomenclature for Reflectance, National Bureau of Standards monograph 161 (1977)
(2) Kajiya, J. T.: The rendering equation, Computer Graphics, ACM SIGGRAPH Computer Graphics, Vol. 20, Issue 4, p.143-150 (1986)
(3) Whitted, T.: An improved illumination model for shaded display, Communications of ACM, Vol. 23, No. 6, p. 343-349, (1980)
(4) Ward, G. J., Rubinstein, F. M. W., Clear, R. D.: A ray tracing solution for diffuse interreflection, ACM SIGGRAPH Computer Graphics, Vol. 22, Issue 4, p. 85-92 (1988)
(5) Ward, G. J., Heckbert, P. S.: Irradiance gradients, Third Eurographics Workshop on Rendering, p. 85-98 (1992)

■ Author ■


Daisuke IDE


Ryosuke SAITO


Hajime KUBO

Report of Field Test Results Using Electric Vehicle and Plug-in Hybrid Vehicle Prototypes

Yoshitaka TAKASUKA* Toru KIMURA* Junya TUNEISHI*
Akihito OHTSU* Naoki FUJIHARA* Yoshiko TAKAHASHI*

ABSTRACT

With the aim of realizing the joy and freedom of mobility and a sustainable society where people can enjoy life, Honda intends to produce electricity from the sunlight and other forms of renewable energy, manufacture next-generation mobilities that use this electricity as energy, and provide these mobilities to users. As the first stage of these efforts, courses were set domestically in Kumamoto and Saitama Prefectures and overseas in Guangzhou City in the People's Republic of China, and driving tests were performed. As a result of these tests, data of the actual electric vehicle driving range and actual plug-in hybrid vehicle all-electric range was obtained, and CO_2 emissions and annual fuel cost reduction effects were confirmed. In addition, based on the results of these driving tests, the next stage of joint field tests with local governments was determined to be is feasible.

1. Introduction

Automobile manufacturers are currently promoting the research and practical use of alternative energy in order to reduce CO_2 emissions aimed at prevention of global warming, and in consideration of depletion of petroleum resources. These efforts include the market introduction of electrified vehicles such as plug-in hybrid vehicles (PHEV), electric vehicles (EV) and fuel cell electric vehicles (FCV) in place of internal combustion vehicles such as gasoline vehicles and diesel vehicles. However, these electrified vehicles are more expensive than internal combustion vehicles such as gasoline vehicles, and sufficient social infrastructure including charging stations and hydrogen stations has not yet been constructed, so popularization of such vehicles is lagging.

In April 2010, the Japanese Ministry of Economy, Trade and Industry (METI) announced six strategies (Overall strategy, Battery strategy, Resource strategy, Infrastructure strategy, Systems strategy, International Standards strategy) as its Next Generation Vehicle Strategy, and set the goal of increasing the ratio of EV and PHEV as a percentage of new vehicle sales to 15% to 20% by 2020 and 20% to 30% by 2030. In conjunction with this, METI also set the goal of installing two million standard chargers and 5,000 quick chargers throughout the country by 2020. Furthermore, following the 2011 Great East Japan Earthquake, EV and FCV have come to be considered as a means of emergency energy storage, and methods of use other than as a simple means of transportation are gathering attention.

The Chinese government announced its "Ten Cities Thousand Vehicles" program in September 2008. This program slated for 2008 to 2012 aimed to install charging facilities in major metropolises in parallel with having 1,000 or more new energy vehicles (EV, PHEV and FCV) operating in each city[(1)]. Furthermore, the Auto Industry Development Program (2009-2011) announced in March 2009 presented goals of expanding the electric vehicle (EV, PHEV, hybrid vehicles (hereafter, HEV)) production scale (500,000 units/year) and increasing the ratio of new-energy vehicles as a percentage of passenger car sales (5% of the total). In addition, the Automobile Development Plan (2010-2012) for energy-saving vehicles (HEV) and new-energy vehicles (EV, PHEV, FCV) announced in April 2012 also stated the goal of over five million new-energy vehicles on the road by 2020.

Amidst these circumstances, Honda commenced social field tests using EV and PHEV from 2010 with the aim of realizing the joy and freedom of mobility and a sustainable society where people can enjoy life. As the first stage of these efforts, driving courses were determined and driven by Honda staff to gather vehicle data and other necessary data. These results confirmed the EV and PHEV ranges and the CO_2 emissions reduction and driving cost reduction

* Automobile R&D Center

effects in actual traffic environments. In addition, the next stage of tests was determined to be feasible based on these results. This next stage consists of determining specific operation procedures, loaning vehicles to local government employees and typical users, and having these users perform daily driving to collect data and verify ease of use. This paper reports the results of these driving tests conducted by Honda staff in Japan and China.

2. Overall Concept of Field Test and Vehicles Used in the Test

2.1. Overall Concept of Field Test

The overall concept of the Honda field test is Honda Electric Mobility Synergy aimed at realizing the joy and freedom of mobility and a sustainable society where people can enjoy life. This is done by using Information and Communication Technology (ICT) to link systems such as photovoltaic charging stations that produce electricity from renewable energy with the next-generation personal mobilities group as shown in Fig. 1 to enable the ideal energy management for both separate regions and society overall.

EV and PHEV were used as the personal mobilities in the tests, ICT was used as assist technology, and electricity was supplied from photovoltaic charging stations and other facilities. The goal was to understand the actual performance and issues of each technology, propose optimum methods of use based on those results, and to verify technologies and systems that can lead to new business in the coming electric vehicle popularization period and also create new value following popularization.

2.2. Position of Field Test Using Prototype Vehicles

Driving by Honda staff was performed from May 2011 to May 2012, and focused on the following items:

(1) Understanding actual vehicle performance such as actual driving distances; and

(2) Confirming the feasibility of field tests performed by local governments, which are planned next.

The following results were obtained.

2.3. Vehicle Specifications

Figure 2 shows external views of the vehicles used, and Table 1 and Table 2 list the specifications. The EV prototype vehicle was created by installing an electric

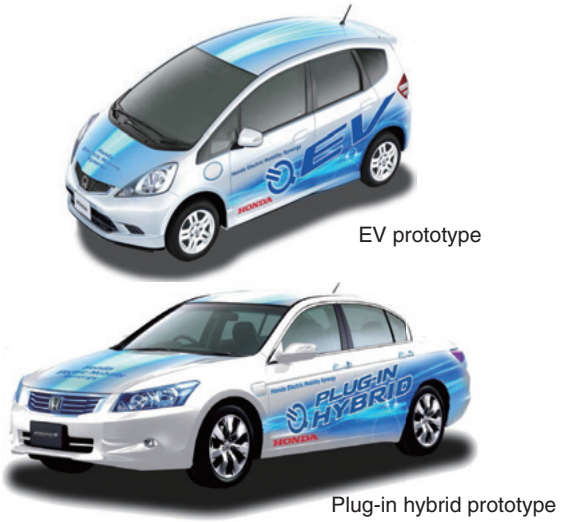


Fig. 2 Test vehicle external view

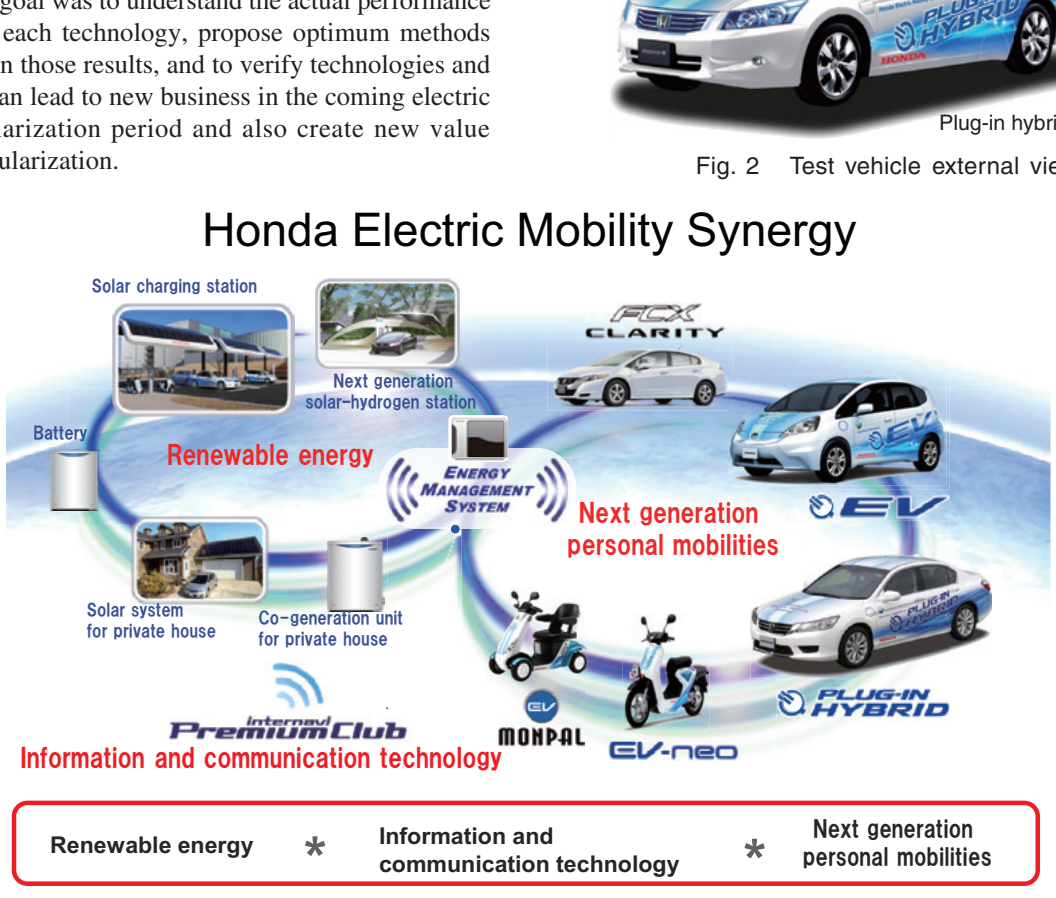


Fig. 1 Honda concept

Table 1 EV specifications

	Japanese model	Chinese model
Motor type	Coaxial motor with gear box (same as FCX Clarity)	Same as Japanese model
Motor max. output	92 kW	Same as Japanese model
Motor max. torque	256 Nm (26.1 kgfm)	Same as Japanese model
Driving range	Over 160 km *1	Over 150 km *3
Max. vehicle speed	144 km/h	Same as Japanese model
Battery type (manufacturer)	Lithium-ion battery (TOSHIBA)	Same as Japanese model
Charging time	100 V: less than 12 hours, 200 V: less than 6 hours, Quick charge *2: approximately 20 min	220 V: less than 6 hours

*1 Honda test result in JC08 mode *2 CHAdeMO specification *3 Honda test result in NEDC mode

Table 2 PHEV specifications

Engine	Atkinson cycle 4-cylinder 2.0 L with i-VTEC
Transmission	Electric CVT
Motor	Two-motor system (drive and regeneration / generation)
Motor max. output	120 kW
Battery type (manufacturer)	6 kWh lithium-ion battery (Blue Energy)
Max. driving range	Over 1,000 km *1
All electric range	25 km *2
Max. vehicle speed as EV	100 km/h
Charging time	100 V: less than 4 hours, 200 V: less than 1.5 hours

*1, 2 Honda test result in JC08 mode

vehicle system in a mass-production FIT body, and the PHEV prototype vehicle was created by installing a plug-in hybrid vehicle system in a mass-production INSPIRE body. Vehicle registration plates were obtained through modified vehicle application, and the vehicles were driven on ordinary roads. The Chinese field test was conducted using only EV. Like the Japanese field test, the EV prototype vehicle was created by installing an electric vehicle system in a mass-production FIT body. A vehicle permit was obtained and driving was performed as a product sample.

3. Field Tests in Japan

Saitama Prefecture and Kumamoto Prefecture were selected as field test partners as these prefectures are the locations of Honda factories and were also selected as second-phase regions for the "EV & PHEV Town Initiative" directed by METI's Automobile Division. In addition, an agreement was concluded and field tests were also conducted with Saitama City, which is a government ordinance city that is promoting its own E-KIZUNA Project and electrification.

3.1. Driving Courses

3.1.1. Saitama Prefecture and Saitama City area

In Saitama Prefecture and the government ordinance city of Saitama City, the area inside the Saitama City limits that is part of the metropolitan area, the area around Kagohara Station as a residential suburb of the greater metropolitan area, and the expressways used to travel to resort areas on weekends, were thought to represent typical metropolitan areas. Therefore, the following driving courses were set.

(1) Two daily use courses used by the residents of the greater metropolitan area (Saitama City) to drive through urban areas
(2) One park-and-ride use course used by suburban residents to drive to the nearest station in order to commute to the greater metropolitan area
(3) Two weekend use courses used by residents of the greater metropolitan area to travel to resort areas on weekends using expressways

Table 3 shows the driving distance and major via points of each course.

3.1.2. Kumamoto Prefecture area

In Kumamoto Prefecture, Kumamoto City, which is

Table 3 Driving routes and distance in Saitama Pref.

(1) Commuting driving routes in Saitama City area

Route Name	Driving Route	Distance	Via Points
Saitama urban route 1	Saitama ward offices, North-South area	54 km	Chuou, Kita and Minami ward offices
Saitama urban route 2	Saitama ward offices, East-West area	57 km	Sakura, Iwatsuki and Midori ward offices

(2) Park-and-ride driving routes in Kagohara Station area

Route Name	Driving Route	Distance	Via Points
Kagohara route	Park-and-ride	30 km	Yoriichou, Kagohara Station

(3) Weekend highway driving routes

Route Name	Driving Route	Distance	Via Points
Highway route 1	Tokyo Gaikan Expressway	64 km	Wako IC, Souka IC, Koshigaya Lake Town
Highway route 2	Metropolitan Expressway	76 km	Wako IC, Itabashi JCT, Gaien IC

Table 4 Driving routes and distance in Kumamoto Pref.

(1) Commute driving routes in Kumamoto City area

Route Name	Driving Route	Distance	Via Points
Urban route	Inside Kumamoto City	52 km	Pref. office, castle, station
Suburban route	In and around Kumamoto City	61 km	Kumamoto University, Mt. Kinpou

(2) Sightseeing driving routes in Aso City area

Route Name	Driving Route	Distance	Via Points
Mountain route 1	Mt. Aso winding road (870 m elevation, 3.9% gradient)	65 km	Road station Aso, Aso farm land
Mountain route 2	Mt. Aso winding road (1057 m elevation, 4.8% gradient)	70 km	Top of Mt. Aso
Mountain route 3	Mt. Aso winding road (1057 m elevation, 4.6% gradient)	80 km	Top of Mt. Aso

(3) Daily driving routes in Amakusa island area

Route Name	Driving Route	Distance	Via Points
Amakusa urban route	Inside Amakusa City	16 km	Amakusa City office
Suburban route 1	North area to Amakusa City area	66 km	Itsuwacho branch, City office
Suburban route 2	Mid area to Amakusa City area	80 km	Amakusacho branch, City office
Suburban route 3	South area to Amakusa City area	96 km	Ushibukacho branch, City office
Suburban route 4	Southeast offshore area to Amakusa City area	101 km	Shinwachou branch, City office
Suburban route 5	Kamishima island south area to Amakusa City area	44 km	Kumumotocho branch, City office
Suburban route 6	Honda base suburban area residence	75 km	Ariakecho branch, City office

the location of the prefectural office and also a hub city for the prefecture at the time of the field test; Aso City, which includes many sightseeing spots such as Mt. Aso; and Amakusa City, which is an isolated island and has established a life sphere within a limited area were thought to represent typical Japanese local areas. Therefore, the following driving courses were set.

(1) Two commuting use courses used by residents of a regional urban center (Kumamoto City) to drive to work places within the city and surrounding areas

(2) Three sightseeing courses used by tourists and others to drive from the airport within the area centering on Aso City

(3) Seven daily use courses used by residents of an isolated island to drive within the island for daily life.

Table 4 shows the driving distance and major via points of each course.

3.2. Driving Results and Observations

Figures 3 and 4 show the driving results. The total driving distance from May 2011 to May 2012 for two EVs (one EV each in Saitama Prefecture and Kumamoto Prefecture) reached 35,000 km, and for four PHEVs (two PHEVs each in Saitama Prefecture and Kumamoto Prefecture) reached 71,000 km.

The EV range per full charge averaged 132 km, which is more than 80% of the in-house test result of 160 km in JC08 mode. The PHEV all-electric range (AER) averaged 17.5 km, which is approximately 70% of the in-house test result of 25 km in JC08 mode. The EV range results were good in consideration of the effects of changes in actual outdoor temperatures and road conditions compared to JC08 mode driving. Figure 5 shows the PHEV driving distances in AER and HEV modes. This shows that the AER was shorter for sightseeing use (climbing Mt. Aso) and city driving in Saitama City compared to other driving routes. This is inferred to be due to the effects of uphill gradients and the frequency of stopping due to traffic congestion, which are not present in JC08 mode. As such, the PHEV AER result is also thought to be reasonable.

Figures 6 and 7 show the results of estimating the EV CO_2 emissions and driving cost reduction effects, and Figs. 8 and 9 show the results of estimating the PHEV CO_2 emissions and driving cost reduction effects based on these driving results.

Assuming an annual driving distance of 10,000 km, EV provide CO_2 emissions reduction effects of 55% compared to a 2000 year model FIT inertia weight class gasoline vehicle, which is equivalent to the amount of CO_2 absorbed

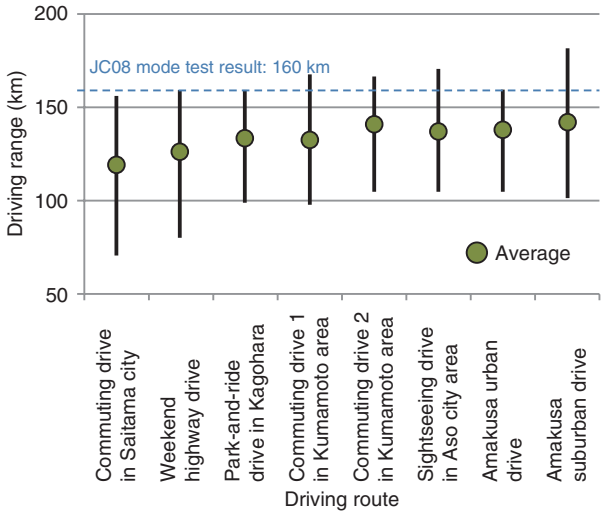


Fig. 3 EV driving range test result

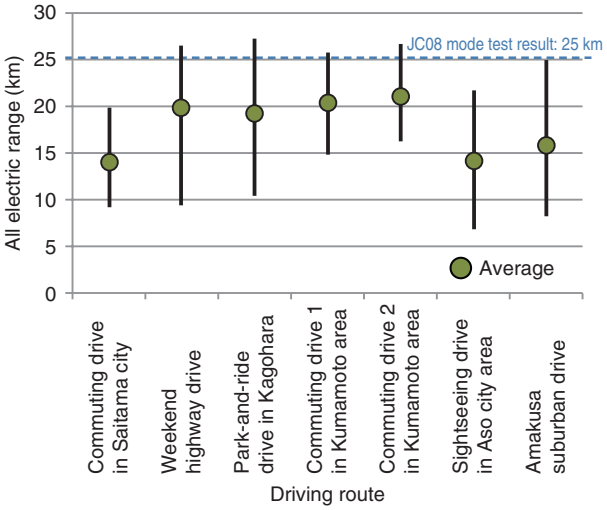


Fig. 4 PHEV AER test result

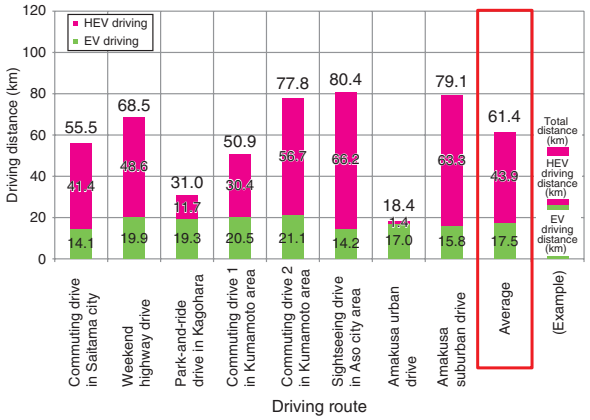


Fig. 5 PHEV EV and HEV mode driving comparison

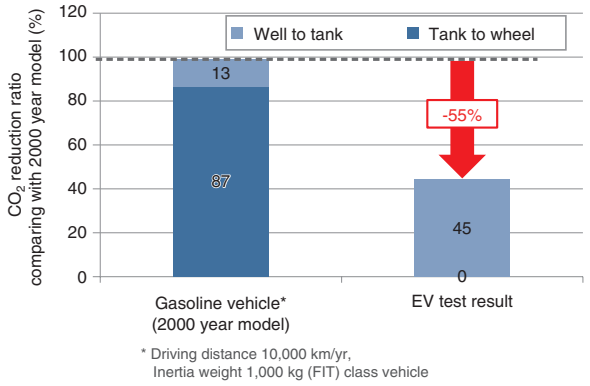


Fig. 6 CO_2 reduction ratio by EV

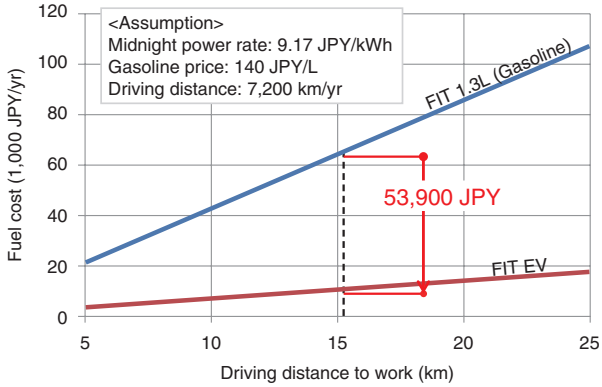


Fig. 7 Fuel cost reduction by EV

by approximately 68 cedar trees in one year. In addition, there are also fuel cost reduction effects of approximately 54,000 yen assuming a commuting distance of 15 km each way and 240 days of use per year (annual driving distance 7,200 km).

Likewise assuming an annual driving distance of 10,000 km, PHEV provide CO_2 emissions reduction effects of 42% compared to a 2000 year model Accord inertia weight class gasoline vehicle, which is equivalent to the amount of CO_2 absorbed by approximately 69 cedar trees in one year. In addition, there are also fuel cost reduction effects of approximately 56,000 yen assuming a commuting distance of 15 km each way, 240 days of use per year, and charging only at night. When charging is also performed at the workplace during the day in addition to at night, the fuel cost reduction effect increases to approximately 60,000 yen. If the price difference between an EV and a gasoline vehicle is to be recovered by only the fuel cost over six years of use, a vehicle price difference of approximately 320,000 yen in the FIT class is thought to be a realistic number. A similar calculation for PHEV yields a vehicle price difference of approximately 360,000 yen in the Accord class. In reality, however, price differences with gasoline vehicles of the same class currently exceed 1.5 million yen, which makes it a challenge to recover the price difference by only the fuel cost, even in consideration of government and other subsidies (1 million yen or less).

The test results show that the average EV range per full charge is approximately 132 km, but in consideration of even harsher driving conditions (road congestion, road gradient, air conditioner (A/C), lights and other power consumption) and assuming return to the start (departure) point, it is necessary to install a quick charger every approximately 70 to 80 km.

Many public quick chargers and general quick chargers have already been installed in Saitama Prefecture centering on Saitama City and National road No. 17 as shown in Fig. 10, and can cover driving within the prefecture. In Kumamoto Prefecture, drawing approximately 80 km-radius circles centering on currently (as of the end of fiscal year 2011) installed public quick chargers and quick chargers operated by automobile dealers and others as

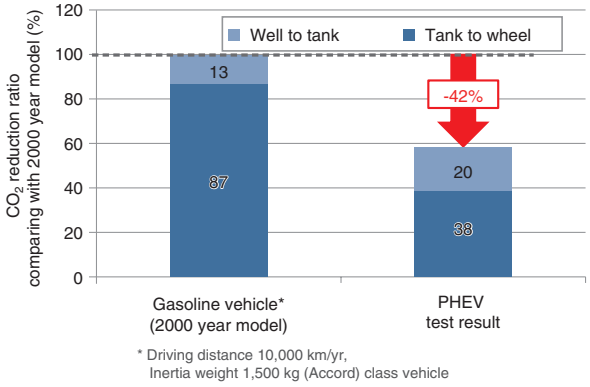


Fig. 8 CO_2 reduction ratio by PHEV

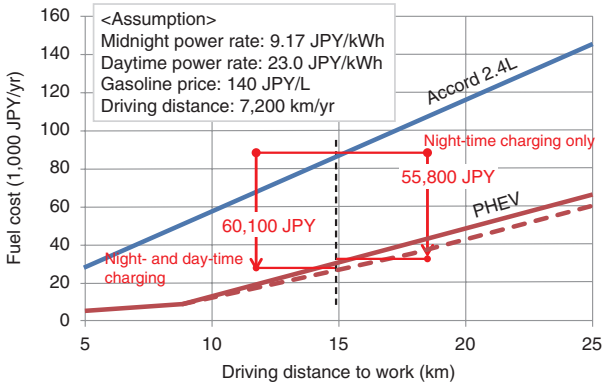


Fig. 9 Fuel cost reduction by PHEV

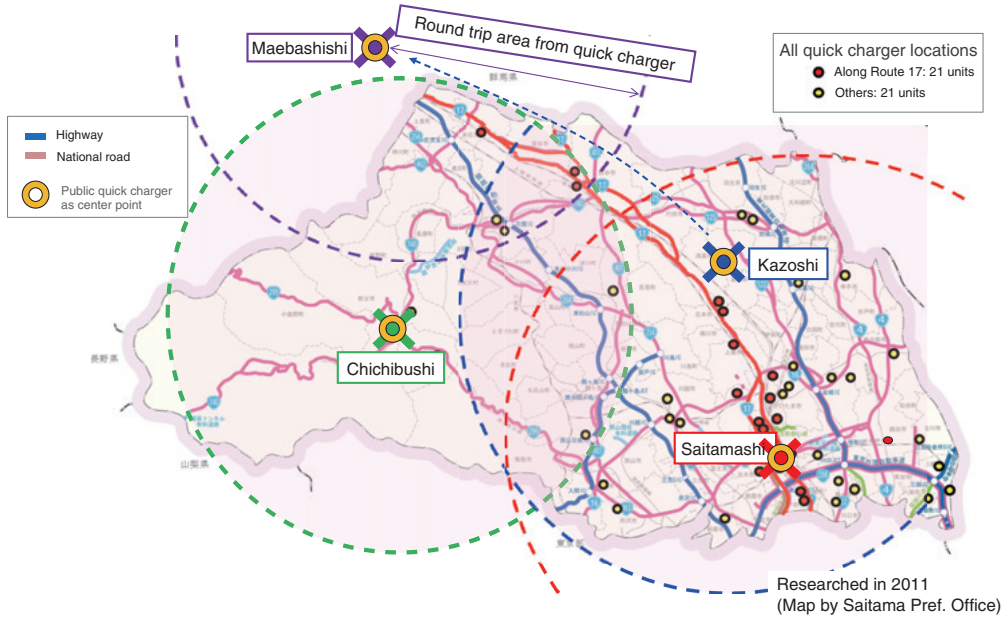


Fig. 10 Quick charger covered area in Saitama Pref.

shown in Fig. 11 shows that the entire prefecture can be covered except for one part along the border with Miyazaki Prefecture. Furthermore, almost the entire prefecture can be covered simply by installing public quick chargers in the Hitoyoshi and Yatsushiro districts in the future. However, quick chargers require approximately 20 minutes (charging time after the charge warning lamp lights until 80% of the battery capacity is reached), so as the number of EV increase, consideration should also be given to increasing the number of chargers installed in each location.

There were approximately 37,000 gas stations throughout Japan as of the end of fiscal year 2011[(2)]. In contrast, the number of charging stations is much less at approximately 1,700 quick chargers and approximately 6,200 standard chargers[(3)], and business hours are short (many public charging stations operate from 09:00 to 18:00). Furthermore, many public quick chargers are installed at prefectural offices, ward offices and other public facilities, which cannot be said to be good location conditions compared to gas stations located alongside roads. Therefore, urgent measures that address this inconvenience due to a lack of charging infrastructure are thought necessary in consideration of future EV popularization.

3.3. Photovoltaic Charging Station

Photovoltaic charging stations such as shown in Fig. 12 were constructed within the Honda Wako Head Office Building premises and the Honda Kumamoto Factory premises to demonstrate the use of renewable energy in this field test.

The goal for these photovoltaic charging stations was to generate the electric energy needed to drive four EVs 40 km per day from the sunlight, and to supply this energy for 365 days. Each charging station uses 84 pieces of 125W-CIGS thin-film solar cells made by Honda Soltec Co., Ltd., and has three 200 V standard chargers and one 50 kWh quick charger. The goal was to generate photovoltaic power of approximately 30 kWh per day and 11,000 kWh over one year, and the amount of generated power was confirmed for the one-year period from August 2011 through July 2012. Figure 13 shows the results. The average daily generated

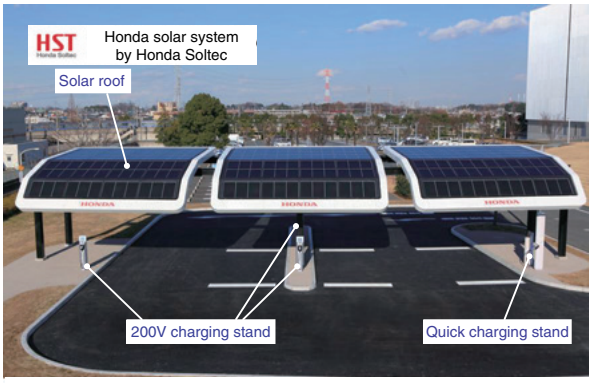


Fig. 12 Photovoltaic charging station in Wako

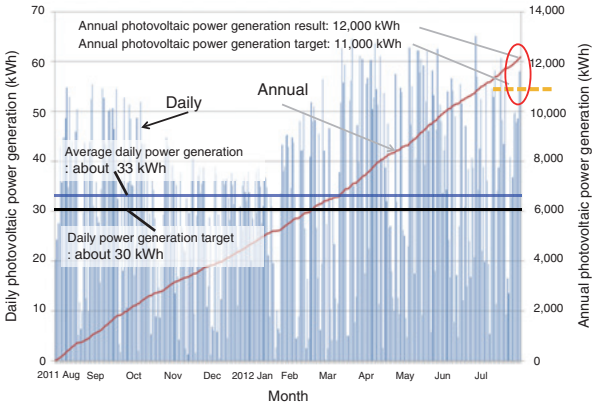


Fig. 13 Photovoltaic power generation result

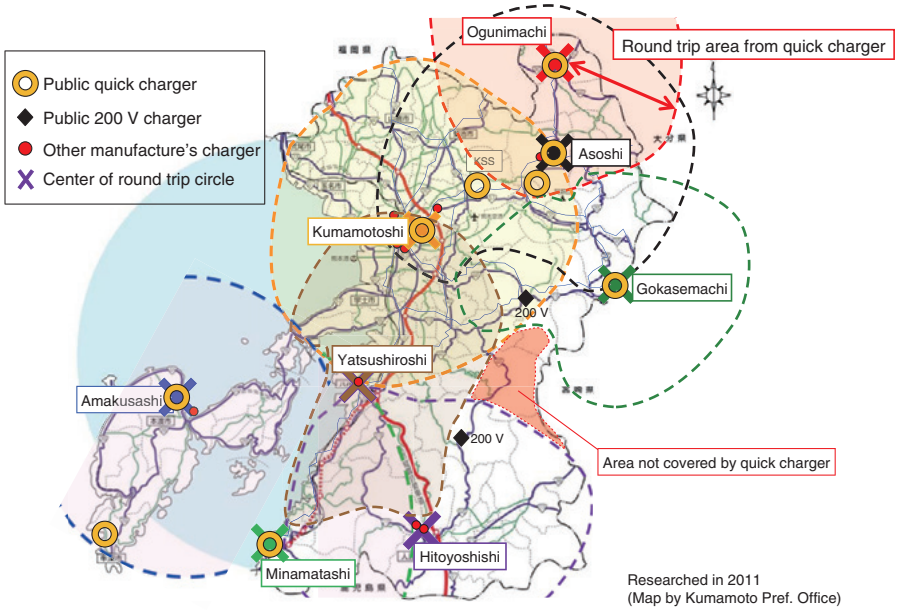


Fig. 11 Quick charger covered area in Kumamoto Pref.

Table 5 Driving routes and distance in Guangzhou area

(1) Traffic jams routes in Guangzhou City

Route Name	Driving Route	Distance	Via Points
Traffic jam route 1	Inside Guangzhou City area	20 km	Pearl River
Traffic jam route 2	Inside Guangzhou Cityarea	14 km	Garden hotel
Traffic jam route 3	Inside Guangzhou City area	31 km	LiuHuaHu Gong Yuan, Pearl River
Traffic jam route 4	Inside Guangzhou City area	32 km	LiuHuaHu Gong Yuan, Garden hotel

(2) Commuting to work place

Route Name	Driving Route	Distance	Via Points
Commuting route	Guangzhou City to work place	58 km	Guangzhou Honda factory

(3) Guangzhou Baiyun Airport via highway

Route Name	Driving Route	Distance	Via Points
Airport route 1	Guangzhou City to Baiyun Airport via highway	76 km	Garden hotel, Baiyun Airport
Airport route 2	Guangzhou City to Guangzhou Honda factory via Baiyun Airport on highway	130 km	Garden hotel, Baiyun Airport, Guangzhou Honda factory

energy was approximately 33 kWh, which achieved the target, and the annual generated energy was approximately 12,000 kWh, which also achieved the target. However, this graph shows that the daily generated energy varies greatly according to the weather and other factors, so it is thought that an energy storage system such as a stationary battery is also needed to augment the driving energy provided only by electricity obtained by photovoltaic power generation.

4. Field Test in China

Agreements were concluded with the Guangzhou Automobile Group Co. Ltd. (GAC Group), which operates a joint venture with Honda, and with Guangzhou City, which is home to the GAC Group factory, as the field test partners in China, and the field test was commenced from December 2011 using only the EV planned for local production.

4.1. Guangzhou City Area

Urban areas in China experience chronic traffic congestion, and many factories and other work places are located in the suburbs, so much commuting is done by car. An additional special circumstance is that foreigners with international driving licenses cannot drive an automobile in China, so people are frequently driven to and from airports. Therefore, the following driving courses were set as typical driving courses in China.

(1) Four courses driving through congested urban areas
(2) One course commuting from the inner city to the suburbs
(3) Two courses driving back and forth between the inner city and the airport using highways

Table 5 lists the driving distances on each course.

4.2. Driving Results and Observations

Figure 14 shows the driving results. The total annual driving distance for three EV reached 41,600 km. The EV range per full charge indicated an average value of 169 km, compared to the in-house test result of 150 km in the New European Driving Cycle (NEDC) mode. This value is better than the driving result in Japan (132 km), and is thought to be due to the following three factors.

(1) There is relatively little congestion when commuting to the suburbs or driving to the airport via the highway, so driving could be performed smoothly.
(2) Guangzhou is warm throughout the year (outside temperature 10°C to 40°C), so the heater power consumption during the winter is low as shown in Fig. 15. In addition, the summer is hotter than in Japan, but the cooler power consumption becomes saturated at 0.5 kW as shown in Fig. 16, so there is little increase in

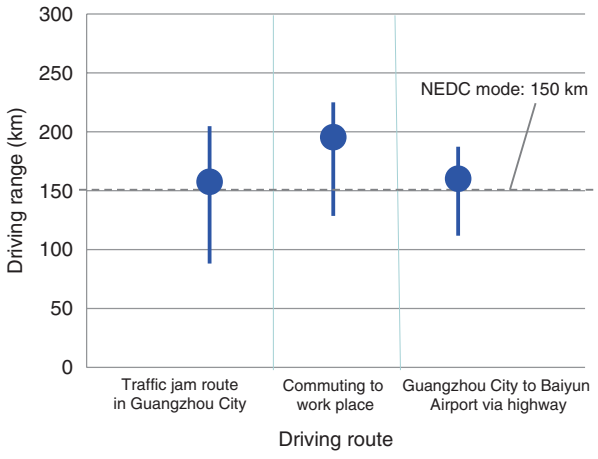


Fig. 14 EV driving range test result

power consumption due to air conditioning.

(3) Most of the roads around Guangzhou City are flat and there was no driving course with a large gradient such as the Mt. Aso winding road driving courses in Japan.

Figures 17 and 18 show the results of estimating the CO_2 emissions and driving cost reduction effects in China based on these driving results. EV provide CO_2 emissions reduction effects of 64% compared to a 2008 year model FIT 1.3 L gasoline vehicle, which is equivalent to the amount of CO_2 absorbed by approximately 88 cedar trees in one year. In addition, there are also fuel cost reduction effects of approximately CNY 5,600 assuming a commuting distance of 30 km each way and 240 days of use per year (annual driving distance 14,400 km). CO_2 emissions intensity, electricity rates and gasoline prices differ from those in Japan, but this shows that EV can also contribute to reducing CO_2 emissions and fuel costs in China.

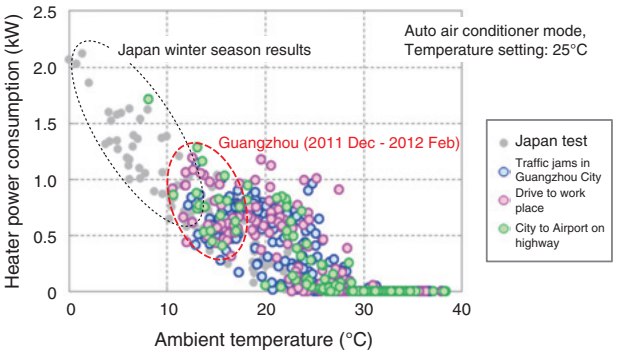


Fig. 15 Heater power consumption

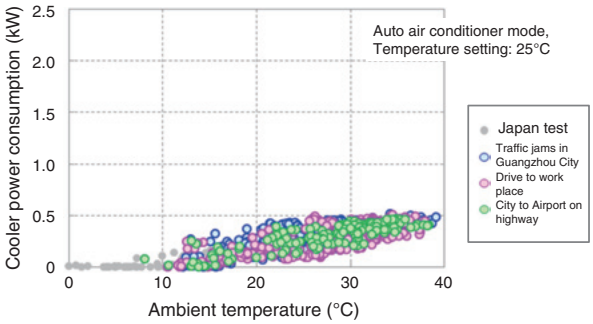


Fig. 16 Cooler power consumption

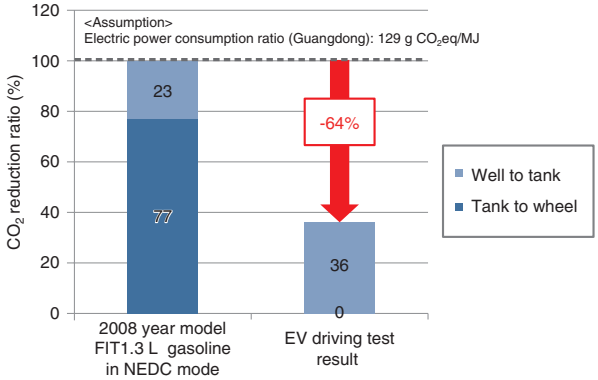


Fig. 17 CO_2 reduction ratio by EV in China

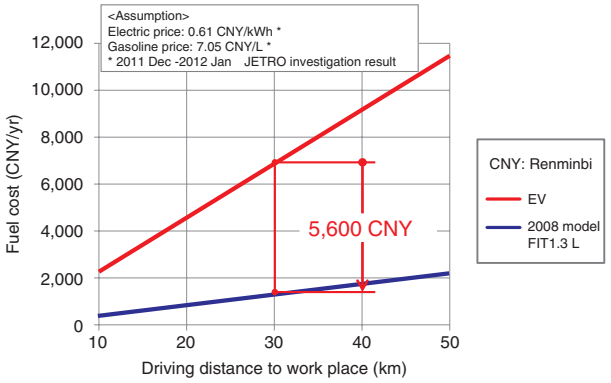


Fig. 18 Fuel cost reduction by EV in China

5. Field Tests by Local Governments

5.1. Proposal for Field Tests by Local Governments

Saitama Prefecture has set a goal of using EV and PHEV to promote measures to prevent global warming and increase the convenience of movement. In accordance with this goal, the prefecture has proposed the following four items.

(1) Sharing use as official local government vehicles by government employees based at prefectural offices and other locations

(2) Park-and-ride use combined with photovoltaic charging stations

(3) Rail and ride-type rent-a-car use in sightseeing areas centering on Chichibu

(4) Owner-type sharing use that assumes personal ownership

In addition, Saitama City has proposed the following three items with the aim of demonstrating the receptivity of EV in a metropolitan area through cooperation with stakeholders centering on Saitama City and realizing a low-carbon society.

(1) Sharing use that combines personal vehicle use by local government employees with official local government vehicle specifications

(2) Verification of lifestyle enhancement through use of next-generation mobilities that employ ICT in combination with other companies spanning different industrial sectors

(3) Use of a free-range system whereby different vehicles are used according to the driving distance, with EV used for normal driving and gasoline vehicles used for longer distances

Kumamoto Prefecture has set a goal of using EV and PHEV to reduce CO_2 emissions and to vitalize and enhance the quality of life (QOL) of provincial cities. In accordance with this goal, the prefecture has proposed the following four items.

(1) Sharing use as official local government vehicles by government employees based at prefectural offices and other locations

(2) Rent-a-car use for sightseeing that makes the most

of sightseeing facilities around Aso City and within Kumamoto City
(3) Elderly welfare bus use in the form of ride sharing by multiple people in isolated island areas
(4) Sharing use within hot springs associations as tourist courtesy cars

5.2. Feasibility Judgment for Field Tests by Local Governments

The abovementioned field test items to be performed by local governments assume a driving distance of 10 km to 120 km per day, and presuppose charging partway along the route or at night when driving for longer distances. This means that sufficient driving can be performed given the EV range per full charge and the PHEV AER obtained from the field tests reported in this paper. In addition, a quick charger is installed every approximately 80 km in both Kumamoto and Saitama Prefectures, and 200 V standard chargers or quick chargers are also installed at locations that serve as vehicle sharing bases, so it was judged that each field test could be performed without running out of electricity.

6. Conclusion

EV and PHEV were actually driven in Japan (Saitama Prefecture and Kumamoto Prefecture) and China (Guangzhou City), and the following results were obtained.

(1) Actual vehicle performance such as actual driving distances was understood.
The EV ranges in actual traffic environments were as follows.
Japan: 132 km (JC08 mode in-house measurement value: 160 km)
China: 169 km
In addition, the PHEV AER was as follows.
Japan: 17.5 km (JC08 mode in-house measurement value: 25 km)
The EV range is short at approximately one-third the gasoline vehicle range, but can be said to be a level that enables market use if the applications are narrowed down sufficiently. In addition, the PHEV AER can also be said to be a sufficiently effective range for short-distance applications such as commuting.
The CO_2 emission reduction effects were as follows.
Japan: EV: 55% reduction (compared to a 2000 year model FIT inertia weight class gasoline vehicle)
PHEV: 42% reduction (compared to a 2000 year model Accord inertia weight class gasoline vehicle)
China: EV: 64% reduction (compared to a 2008 year model FIT 1.3 L vehicle)
CO_2 emissions of both EV and PHEV are approximately one-half those of gasoline vehicles and renewable energy can also be used, so EV and PHEV are effective means of preventing global warming and reducing use of petroleum resources.
The annual fuel cost reduction effects were as follows.
Japan: EV 53,900 yen (compared to a 2008 year model FIT 1.3L vehicle)
PHEV 55,800 yen (charging only at night) (compared to 2008 year model Accord 2.4L vehicle)
60,100 yen (charging two times: once during the day and once at night)
China: EV CNY 5,600 (compared to a 2008 year model FIT 1.3L vehicle)

(2) Feasibility of subsequent field tests by local governments
Each planned field test can be performed within the actual ranges without running out of electricity, and sufficient CO_2 reduction effects can also be expected, so field tests by local governments were judged to be feasible.

7. Acknowledgements

The authors wish to express their deep thanks to all related parties in the Industry Support Division of the Kumamoto Prefectural Government, the Air Environment Division and Industry Support Division of the Saitama Prefecture Prefectural Government, and the Office for Environmental Future City Promotion of the Saitama City government for their cooperation with these market driving tests.

References

(1) Ministry of Science and Technology of the People's Republic of China: http://www.most.gov.cn/tztg/200902/t20090211_67363.htm, (2009) (in Chinese)
(2) Agency for Natural Resources and Energy: Kihatsuyu hanbaigyousha suu oyobi kyuuyusho suu no suii (2012) (in Japanese)
(3) http://ev.gogo.gs

■ Author ■


Yoshitaka TAKASUKA


Toru KIMURA


Junya TUNEISHI


Akihito OHTSU


Naoki FUJIHARA


Yoshiko TAKAHASHI

Research on Combustion Improvement Techniques by Intake Valve Offset and Squish Effect

Takamori SHIRASUNA* Hideki SAITO* Tomokazu NOMURA*

ABSTRACT

Reported in this paper are the technologies for improvement of combustion efficiency by applying two simple methods to a single cylinder, 110 cm^3 displacement, four-stroke, two-valve gasoline engine.

In the first attempt, we tried to improve combustion efficiency by increasing tumble of the air-fuel mixture flow. To increase tumble, we devised an offset intake valve design in which a part of the intake valve was located outside of the cylinder bore. With this offset intake valve configuration, a part of the inlet port perimeter was blocked causing disturbance of air-fuel mixture flow along the cylinder wall that resulted in a strong turbulence. The increased turbulence permitted lean burn at an air-fuel ratio leaner by two points, reducing Indicated Specific Fuel Consumption by 4.8% from that of the base engine. With the intake valve shifted outwards against the cylinder bore, the spacing next to the exhaust valve increased, allowing the intake valve diameter to be enlarged to compensate for the deterioration of the maximum power.

In the second attempt, we tried to improve combustion efficiency by increasing the reversed squish flow of the air-fuel mixture. As the means to increase reversed squish flow, we employed a slant-parallel squish configuration. With the application of this squish arrangement, the margin against knocking generation was enhanced and the compression ratio was increased to 9.5 from the original 9.0 while reducing the Indicated Specific Fuel Consumption by 2.6%.

The offset intake valve design coupled with the high compression ratio produced by the slant-parallel squish design lowered the Indicated Specific Fuel Consumption by 6.0% compared to the base engine.

1. Introduction

Recent years have seen increasing demands to reduce CO_2 emissions to cope with global warming. In the field of mobility, fuel economy improvement therefore has been a key theme for research. Various research and developments for fuel economy improvement have been currently conducted in the field of small motorcycles, which account for more than 90% of the world's motorcycle sales. Gasoline engines for motorcycles require simple methods of improvement of fuel economy. Extension of the lean burn range and/or increase of the compression ratio by controlling knocking are some of the effective ways to satisfy the requirement. To extend the lean burn range, it is known that such options as a multi-spark ignition system[(1)] that strengthens ignition, application of a sub combustion chamber[(2)], in-cylinder turbulence to accelerate combustion, etc. are effective for the said purpose. For example, with respect to in-cylinder turbulence, research has been conducted using a tumble generator valve[(3)] or a swirl generator valve[(4)]. Application of such a device, however, requires additional parts and control devices.

In the meantime, research has been conducted for other options such as reshaping of the intake port[(5)] and use of masking[(6)] to intensify tumble flow from a simple mechanical arrangement without using additional parts. However, such an option tends to increase resistance in the intake passage, causing reduction of intake air volume. There have been only a few cases of research on improvement of fuel economy from intensified tumble flow.

In this research, we defined the partially open throttle tumble ratio as a new indicator of tumble flow intensity, and clarified the relationship between tumble flow intensity and fuel economy improvement through basic experiments using stationary tumble generator flaps (hereafter referred to as "flap") of various sizes. The tumble flow was further intensified to extend the lean burn range by the use of masking effects from the intake valve offset to improve fuel economy, at the same time increasing the intake valve diameter was to prevent lowering of maximum power resulting from reduced intake air volume.

Such ways as improvement of combustion chamber cooling, reduction of residual gas, application of squish zone, etc. are known to control knocking when the compression ratio is raised. Among these, application of

* Motorcycle R&D Center

squish is a simple construction without using any device. Many studies on squish have been reported[7), (8)]. With a squish zone created, burning velocity increases regionally in the far end of the combustion chamber due to the reversed-squish flow of mixture that enters the squish zone when the piston descends after passing TDC. From that effect, flame propagation reaches the unburnt mixture in the far end of the combustion chamber before the knocking occurs, which is considered to be the reason squish helps to control knocking[(9)]. Also, it is considered that slant-parallel squish is the shape of the squish zone effective in creating reversed-squish flow. Such knowledge, however, are obtained from research on four valves per cylinder engines. There are only a few cases of research in single cylinder, two-valve engines (two valves per cylinder) on the effective squish shape, contribution of the squish shape to the control of knocking, and increase of compression ratio permitted by the control of knocking. Using CFD, we analyzed the reversed-squish flow in various types of squish shape in the two-valve per cylinder, small displacement engine. We then conducted tests to clarify the correlation between intensity of reversed squish flow and knocking using actual engines. Moreover, we conducted combustion analysis to clarify how squish helped to control knocking.

Lastly, we conducted tests on the combined configuration of offset intake valve and squish, and investigated the degree of influence on fuel economy and power output for extension of the lean-burn range and increase of the compression ratio in accordance with the respective goals of the aforementioned configuration measures.

2. Test Engine and Test Conditions

2.1. Major Specifications of Test Engine

A commercially available engine for small motorcycles was used for the tests. Table 1 shows the major specifications of the test engine. The engine was an air-cooled, four-stroke, single cylinder, two-valve gasoline engine with a displacement of 109.2 cm^3. Fuel was supplied by a carburetor. It should be noted, however, that in the tests to alter the air-fuel ratio (A/F), the pressure in the carburetor float chamber was regulated to control A/F. A rotary encoder was positioned on the crankshaft to obtain crank angle signals of 360 pulses per revolution. For measurement of the pressure in the cylinder, a piezoelectric pressure transducer (Kistler 6041A) was used. The engine was linked with the dynamometer via the transmission system, and controlled at constant engine speeds and loads. Testing on the unit engine was conducted at a constant transmission ratio.

2.2. Conditions of Test Operations

To measure the benefits of the combustion improvement, the lean burn limit, combustion analysis and fuel economy benefits were assessed under partially loaded conditions, and the power output and the knocking were assessed at wide open throttle conditions. The operation conditions are:

Table 1 Specifications of experimental engine

Engine type	Air cooled, four stroke, single cylinder, gasoline engine
Bore × Stroke [mm]	50.0 × 55.6
Displacement [cm^3]	109.2
Compression ratio	9.0
Valve diameter [mm x number]	Intake: 25.5 × 1
	Exhaust: 21.0 × 1
Valve lift [mm]	Intake: 5.8
	Exhaust: 5.6
Ignition system	Electronically controlled capacitor discharge ignition
Fuel system	Carburetor
Fuel type Research octane number (RON)	Regular gasoline 90
Maximum brake power output	6.27 kW at 8000 r/min
Maximum brake torque	8.72 Nm at 6000 r/min

Partially loaded condition: Engine speed: 3750 r/min; BMEP400 kPa; MBT
Fully loaded condition: Engine speed: 3000-8500 r/min; Throttle: Wide open throttle; A/F 12.4

2.3. Lean-burn Limit of Test Engine

Figure 1 shows the Indicated Specific Fuel Consumption (ISFC) and the Coefficient of Variation of Indicated Mean Effective Pressure (COV_{IMEP}) when the A/F is altered under partially loaded condition. The A/F that indicated the lowest ISFC was 16.5 in the test engine. Also, the COV_{IMEP} at A/F of 16.5 was 5%. As an increase of COV_{IMEP} occurred if the A/F was further shifted to the lean side, a further reduction of ISFC was thought difficult. To further lower ISFC, an extension of the lean burn range by an increase of turbulence in the cylinder, etc. was necessary. As the means to extend lean burn range, we focused our attention on the intensity of tumbling.

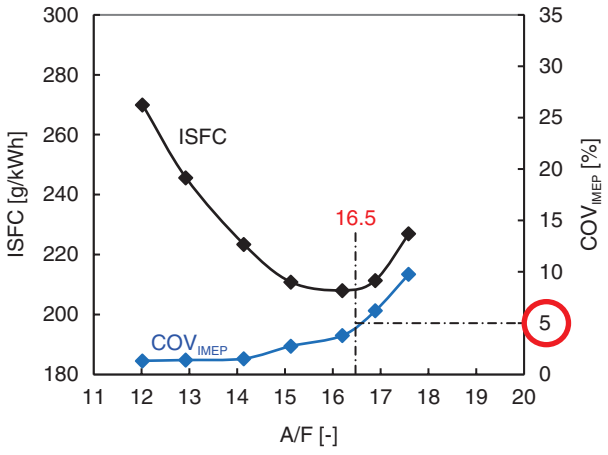


Fig. 1 ISFC and COV_{IMEP}

3. Indicator of Tumble Flow Intensity and Prospective Output in Constant Flow Tests

In this research, tumble ratio (*TR*) was used as the indicator of intensity of tumble flow. Also, as indicator of prospective power output, the integrated value of effective intake valve opening area over the crank angle (Z_i) was used. These indicators were measured in the steady flow rig tests.

3.1. Definition of Tumble Ratio

TR is expressed by the ratio of the tumbling angular velocity (ω_R) of the air in the cylinder against the angular velocity of the crankshaft (ω_E) when the charging of mixture is completed, and defined by Eqs. (1), (2) and (3)[7].

In this research, since *TR* was estimated by relative value instead of absolute value, volumetric efficiency (η_v) was simply treated as 1.

$$TR = \frac{\omega_R}{\omega_E} = \frac{L_d \eta_v \int_{\alpha 1}^{\alpha 2} C_f N_r d\alpha}{(\int_{\alpha 1}^{\alpha 2} C_f d\alpha)^2} \quad (1)$$

$$L_d = \frac{BS}{n_v D_v^2} \quad (2)$$

Where,

TR: Tumble ratio
ω_R: Tumble angular velocity
ω_E: Angular velocity of crankshaft
L_d: Engine shape factor
η_v: Volumetric efficiency
$\alpha 1$: Crank angle at inlet valve opening
$\alpha 2$: Crank angle at inlet valve closing
C_f: Flow coefficient
N_r: Non-dimensional rig tumble
B: Cylinder bore
S: Engine stroke
n_v: Number of intake valves
D_v: Intake valve diameter

N_r is expressed by the ratio of tumbling angular velocity against flow velocity in the intake port.

$$N_r = \frac{\omega_R B}{V_0} = \frac{8M}{\dot{m} V_0 B} \quad (3)$$

Where,

V_0: Theoretical intake flow velocity
M: Torque measured by tumble flow meter
$\dot{m}$: Air mass flow rate through port

TR was assessed by the two methods of actual measurement in the steady flow rig and CFD analysis that simulated steady flow testing.

Figure 2 shows the test equipment used for the steady flow tests. Table 2 shows the conditions of the steady flow tests.

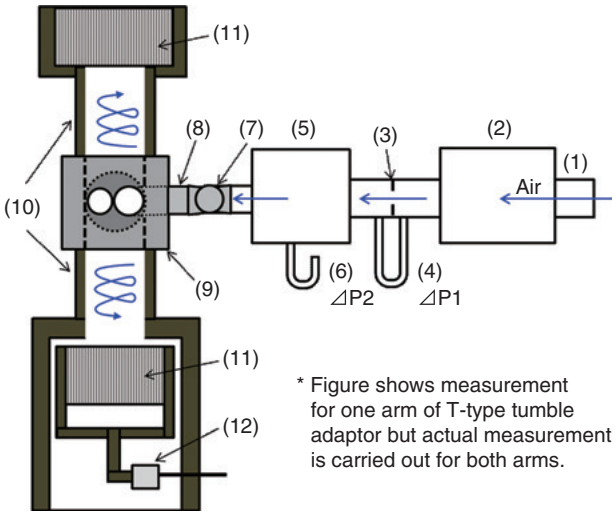
In this research, *TR* was also assessed at partial throttle openings. As the intake resistance increases at a partial opening, the *TR* lowers. It was therefore necessary to improve accuracy of *TR* measurement. A compact impulse tumble meter for exclusive use was prepared, and the experiment was conducted.

Table 2 Conditions of steady flow test

Valve lift [mm]	1, 2, 3, 4, 5, 6
Throat diameter [mm]	0.535, 1.31, 2.75
Pressure of surge tank B (ΔP2) [kPa]	5
Load cell rated capacity [N]	0.5
Rated torque [Nm]	5×10^{-3}

Also, actual measurements of *TR* were conducted two times with the branch pipe reversed. The total of each *TR* measured on the left and right sides was evaluated as the representative *TR*.

Figure 3 shows the CFD analysis model used for *TR*



(1) Air pump	(7) Carburetor
(2) Surge tank A	(8) Inlet pipe
(3) Throat	(9) Cylinder head
(4) Digital manometer (ΔP1)	(10) T-type tumble adaptor
(5) Surge tank B	(11) Honeycomb matrix
(6) Digital manometer (ΔP2)	(12) Load transducer

Fig. 2 Flow test rig

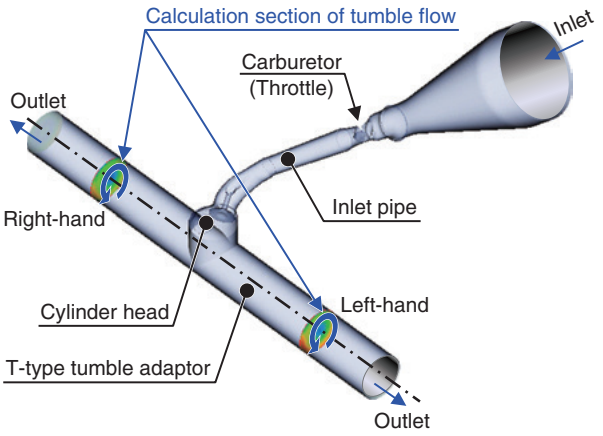


Fig. 3 CFD model for tumble ratio calculation

Table 3 CFD conditions for steady flow test

Software name	SCRYU/Tetra
Solution type	Steady state flow
Valve lift [mm]	1, 2, 3, 4, 5, 6
Pressure difference of Inlet and outlet [kPa]	5
Cell type	Tetrahedron
Boundary cell type [mm × layers]	Prism 0.3 × 2
Number of cells	4,500,000
Differencing scheme	MUSCL scheme
Pressure velocity coupling	SIMPLEC
Turbulent model	Standard k-ε

calculation. Table 3 shows the calculation conditions of CFD analysis.

3.2. Prospective Power Output Indicator

The factor most influential for engine power output is the amount of air drawn into the combustion chamber in a cycle. As an indicator for assessment of the amount of intake air, Z_i in the steady flow tests is effective, and is defined by the Eq. (4). On the other hand, Z_i is defined by Eq. (5) at the CFD analysis[11]. And Fig. 4 shows a conceptual diagram of Z_i. In this research, Z_i was used as an indicator of prospective power output.

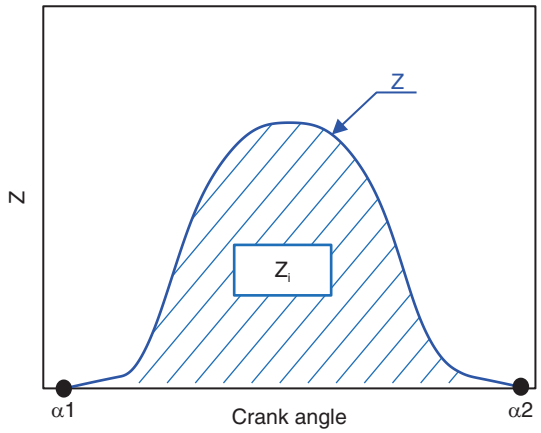


Fig. 4 Definition of Z_i

$$Z_i = \int_{\alpha 1}^{\alpha 2} Z d\alpha = \int_{\alpha 1}^{\alpha 2} \beta A \sqrt{\frac{\Delta P1}{\Delta P2}}\, d\alpha \quad (4)$$

Where,

Z_i: Integrated value of effective intake valve opening area over crank angle

Z: Effective intake valve opening area

β: Flow coefficient of throat

A: Cross section of throat

$\Delta P1$: Pressure difference of throat

$\Delta P2$: Pressure of surge tank B

$$Z_i = \int_{\alpha 1}^{\alpha 2} Z d\alpha = \int_{\alpha 1}^{\alpha 2} C_f A_v d\alpha \quad (5)$$

Where,

A_v: Intake valve opening area

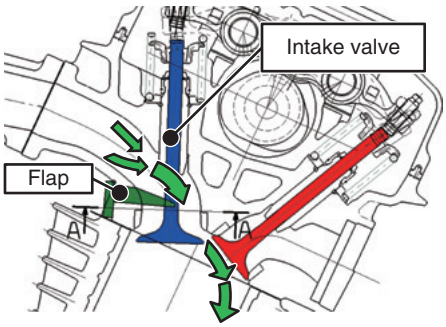
4. Correlation between Tumble Flow Intensity and Fuel Economy Improvement

Regarding the relationship between tumble flow intensity and fuel economy improvement, only a few examples have been reported up to now. In an attempt to identify this relationship, four types of flap were installed to alter tumble flow intensity in the intake port, and conducted CFD analysis and research on the actual engine. We also identified issues that could arise when the fuel economy was improved by intensifying of tumble flow.

4.1. Intensifying of Tumble Flow by Tumble Flow Generator Flap

To intensify tumble flow, protruding flaps of various size were positioned inside of the intake port. We analyzed how the flap affects Z_i and TR by CFD analysis that simulated constant flow tests. Figure 5 shows the installed flap and these shapes. The areas protruding in the intake port were increased respectively in the order of A, B, C and D.

Figure 6 shows Z_i and TR calculated in the CFD analysis. The tendency was that TR increased along with an increase of surface area of the flap, which meant that the flap effectively generated tumble flow. No decrease of Z_i at an identical throttle opening was seen in the small throttle opening range regardless of the flap size. As the throttle opening increased,



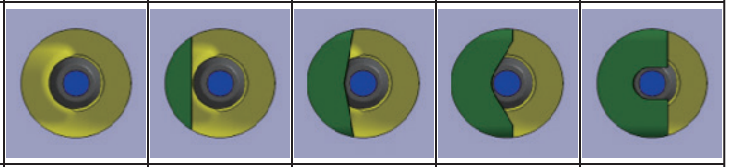
Name	Base (Without flap)	Flap A	Flap B	Flap C	Flap D
Flap shape (Section A-A)					
Flap area ratio [%]	0	19.4	36.0	48.6	60.9

Fig. 5 Installed flaps and shapes

however, the tendency was that Z_i at an identical throttle opening decreased proportionally to the flap size. The reason could be considered that when the throttle opening is small, as the throttle valve determined the minimum cross-sectional area of intake passage, the installation of a flap has no effect on the suction resistance. It could be considered that when the throttle opening was large, the cross-sectional area of intake passage became smallest where the flap was installed, causing an increase of suction resistance and lowering of Z_i.

Figure 7 shows Z_i and *TR* actually measured in the steady flow tests. The data shows the same tendency as in the CFD analysis shown in Fig. 6, even in the partial opening in addition to the wide open throttle (WOT). It was confirmed that the assessment by CFD analysis was appropriate for relative comparison of Z_i and *TR*. Thus, we decided to assess Z_i and *TR* later by CFD analysis data. *TR* at a throttle opening of 15 degrees, which was the typical operating condition, was also defined as the partially open throttle *TR* (POT TR).

Figure 8 shows CFD analysis data indicating distribution of flow velocity in the intake port and cylinder. The data was calculated at a throttle opening of 15 degrees and valve lift of 4.5 mm. The flow of air in the intake port was directed to the exhaust valve side by the flap. The directed air entered the cylinder at a high flow velocity, and induced strong tumble flow. Along with an increase in size, the flap restricted flow of air into the cylinder from the cylinder sleeve side of the intake valve, preventing induction of inverse tumble flow. These effects contributed to the increase of POT TR.

4.2. Intensity of Tumble Flow and Fuel Economy Improvement

The impact of four types of flap on fuel economy

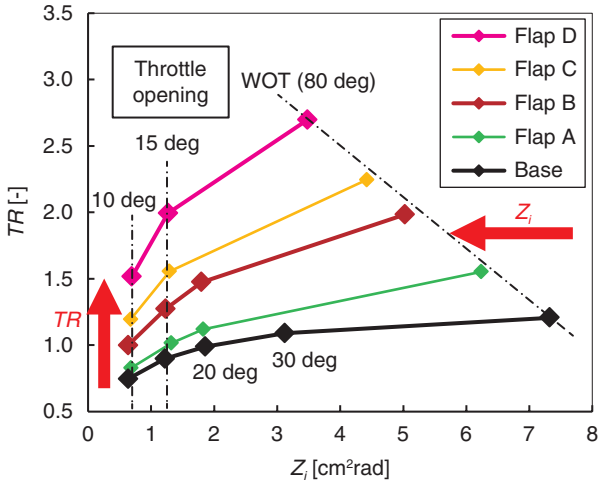


Fig. 6 Z_i and *TR* (CFD)

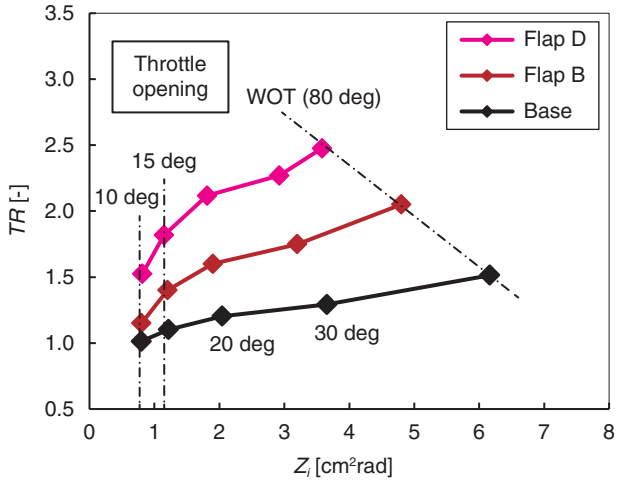


Fig. 7 Z_i and *TR* (Actual measurement)

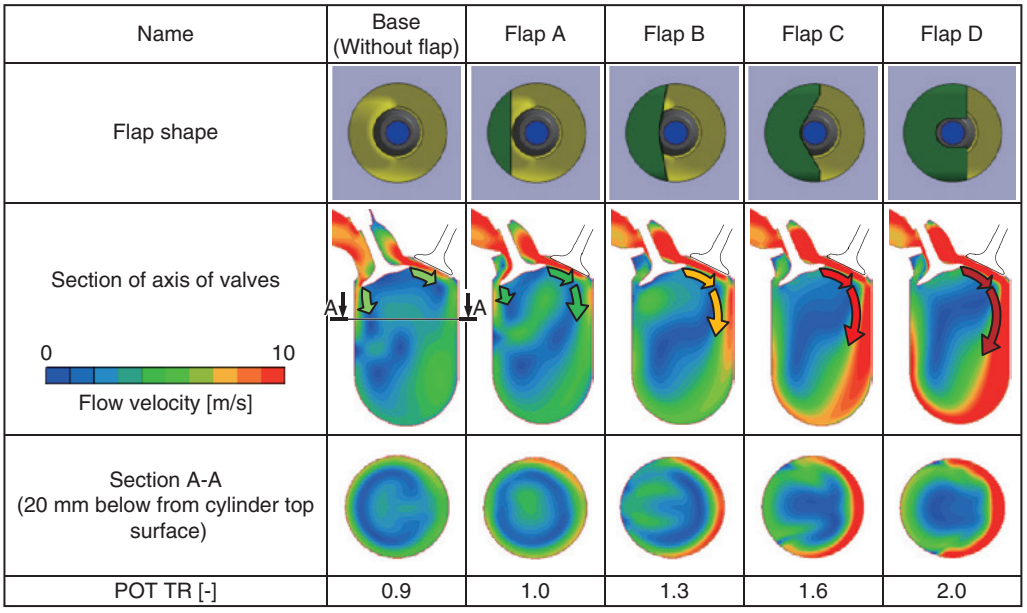


Fig. 8 CFD calculation (in-cylinder flow)

improvement was analyzed by experiments. Figure 9 shows the relationship between A/F and ISFC under the typical operating conditions in IDC. Figures 10, 11, 12 and 13 show results of the combustion analysis. In addition, the crank angle from ignition to the Mass Fraction Burn of 10% was defined as the initial combustion period ($MFB_{0\text{-}10\%}$), and the crank angle from the Mass Fraction Burn of 10% to 90% was defined as the main combustion period ($MFB_{10\text{-}90\%}$).

Compared to the basic design, the design equipped with the flap showed a tendency for the ISFC in the lean range to lower along with an increase of flap surface area. It has been clarified from the combustion analysis that in the basic design, $MFB_{10\text{-}90\%}$ increased rapidly and the degree of constant volume also lowered rapidly along with the leaning of A/F. Also, COV_{IMEP} increased rapidly from near an A/F of 17, indicating that the combustion became unstable.

Accordingly, lowering of ISFC with the basic design is unattainable in the range of A/F leaner than 17.

Meanwhile in the flap-equipped design, $MFB_{0\text{-}10\%}$ and $MFB_{10\text{-}90\%}$ were reduced in all A/F zones. Also, the steep increase of $MFB_{10\text{-}90\%}$ along with the leaning of A/F was lessened. Thus, both the steep lowering of the degree of constant volume and the steep increase of COV_{IMEP} in the lean range were alleviated. Consequently, the lean burn limit has been extended, making it possible to lower the ISFC.

Figure 14 shows the relationship between POT TR and ISFC lowering ratio. The ISFC lowering ratio was calculated

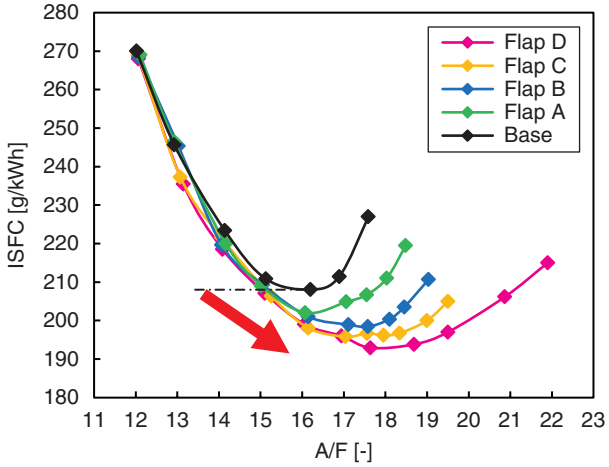


Fig. 9 Relationship between A/F and ISFC

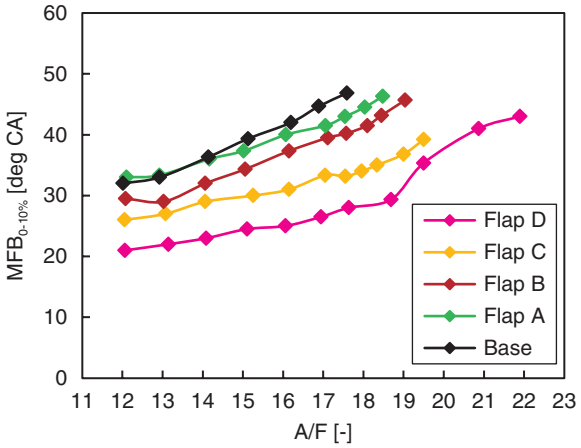


Fig. 10 Relationship between A/F and $MFB_{0\text{-}10\%}$

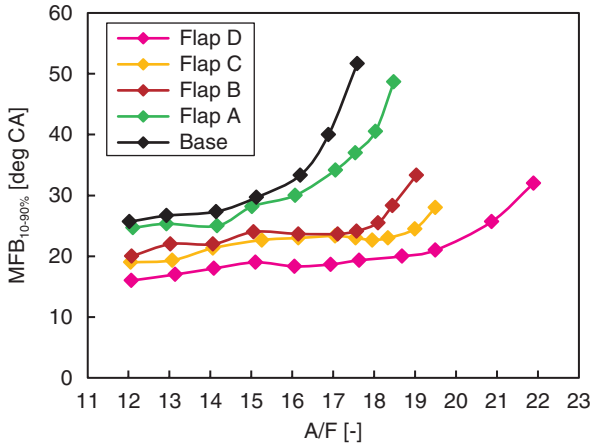


Fig. 11 Relationship between A/F and $MFB_{10\text{-}90\%}$

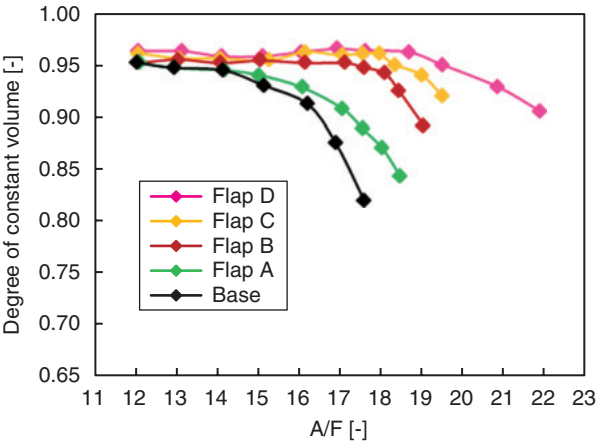


Fig. 12 Relationship between A/F and degree of constant volume

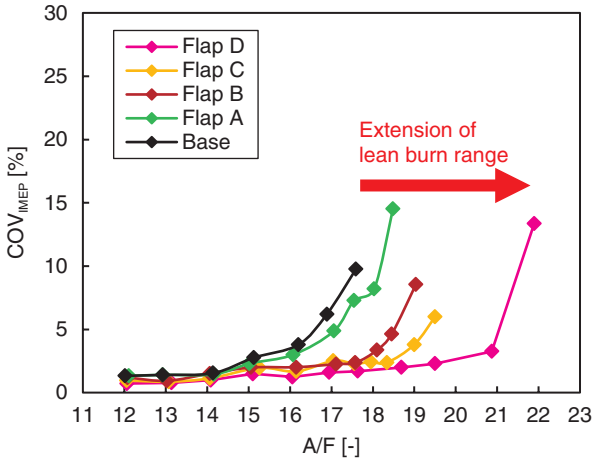


Fig. 13 Relationship between A/F and COV_{IMEP}

using the lowest ISFC when each flap was equipped in Fig. 9. It could be understood that the ISFC lowering ratio was correlated to the POT TR, and we therefore concluded that the POT TR is an effective indicator of lowering of ISFC.

Figure 15 shows the relationship between the POT TR and the maximum power. Although the intensifying of tumble flow with a flap was effective in reduction of ISFC, as the Z_i was lowered at the same time, the maximum power decreased along with an increase of POT TR, which meant that there is a trade-off between the so-called fuel economy and the maximum power.

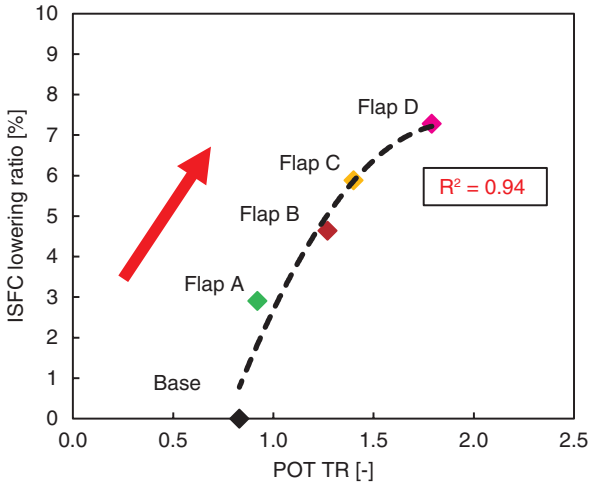


Fig. 14 Relationship between POT TR and ISFC lowering ratio

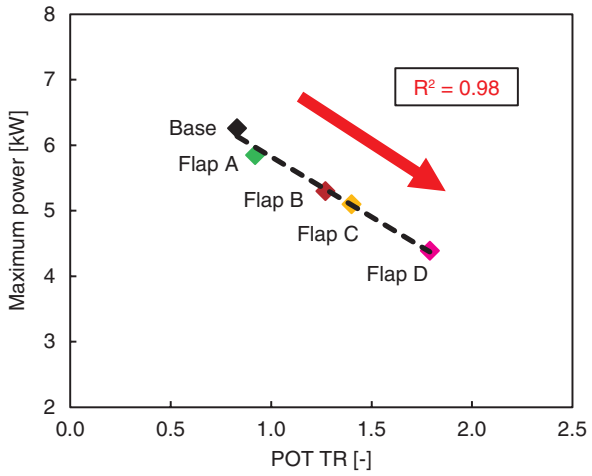


Fig. 15 Relationship between POT TR and maximum power

5. Strengthening of Tumble Flow and Prevention of Lowering of Maximum Power by Offsetting of Intake Valve

The lowering of maximum power due to reduced intake air volume was a concern when a flap was used. To cope with this issue, we have invented a way to reduce lowering of intake air volume while controlling flow of intake air from the cylinder sleeve side of the intake valve.

5.1. Mechanical Arrangement of Intake Valve Offset

We worked out a new way to intensify tumbling while reducing lowering of maximum power output.

In an attempt to intensify tumble flow while reducing lowering of maximum power, we created a new way to realize vigorous tumble flow. Figure 16 shows the mechanical arrangement. The new design features a part of the intake valve jutting out beyond the perimeter of the cylinder bore. A recess was created by machining the top of the cylinder sleeve on the intake valve side. The recess prevented interference with the intake valve. The flow of mixture into the cylinder from the cylinder sleeve side was disturbed by masking effects from the recess. From these effects, vigorous tumble flow identical to fitting a stationary tumble generator flap was induced. With the intake valve located outside, the clearance between the intake valve and the exhaust valve increases, which allows enlarging of the diameter of the intake valve, preventing lowering of maximum power. This method is hereafter referred to as “intake valve offset.”

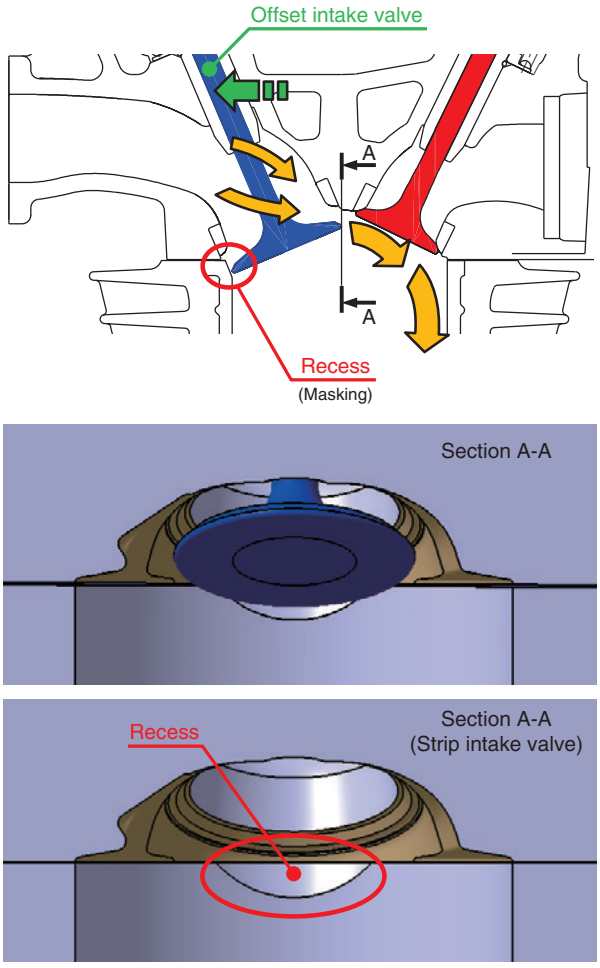


Fig. 16 Offset intake valve design

The parameters other than the intake valve were fixed when designing the amount of intake valve offset and increasing valve diameter. Preconditions when designing are shown as follows.

Compared to the base engine:

(1) No change in valve included angle
(2) No change in exhaust valve layout
(3) No change in piston ring location (height)
(4) No change in valve timing & valve lift
(5) Relocation of intake valve should be parallel to cylinder head gasket surface and toward outside of cylinder bore

Under the above-described preconditions, the intake valve offset was determined by the following steps. The amount of intake valve offset is interrelated to how far away the intake valve is relocated and the intake valve diameter. Accordingly, how far away the intake valve should be relocated was determined first. Then, an extension of the intake valve diameter was considered.

The details of designing of intake valve offset are as follows.

(1) How far away the intake valve should be relocated

To attain maximum masking effects from the intake valve and the cylinder sleeve, the recess was designed to allow for maximum intake valve relocation. The recess was set at the location that allows retention of the minimum necessary space [Fig. 17(1)] between the bottom of the recess and the top of the top ring when the piston was at top dead center. After that, the clearance between the intake valve and the recess was determined at the minimum necessary amount to prevent interference of both parts in order to obtain maximum masking effects [Fig. 17(2)].

(2) Extension of intake valve diameter

When the clearance between the intake valve and the exhaust valve was the same as in the basic design, it was possible to extend the intake valve diameter by a maximum of 3 mm from the basic design as per (1). It should be noted, however, that in this instance, as a step occurred on the combustion chamber wall [Fig. 17(3)], the flow of drawn mixture was disturbed in the exhaust valve side by the step, causing possible lowering of Z_i or TR. Such a step increased along with an extension of intake valve diameter.

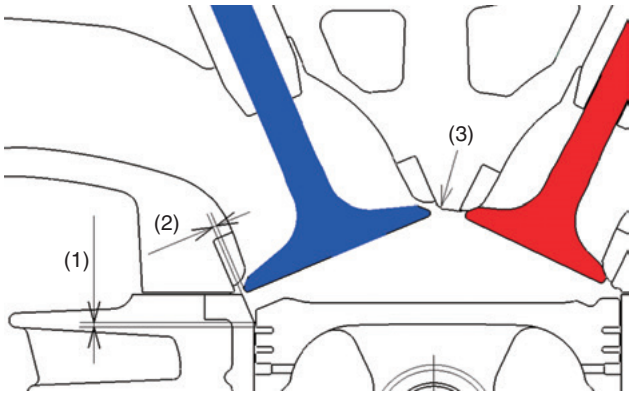


Fig. 17 Steps to determine intake valve offset

Therefore, allowable intake valve diameter free of negative impacts was investigated by CFD analysis. Thus, the intake valve diameter was finally extended by 2 mm. At that time, the offset of the intake valve was 2.3 mm from that of the basic model.

Figure 18 shows the combustion chambers of the base engine, one with the intake valve diameter increased by 2 mm by offsetting of the intake valve, and the other with the intake valve diameter increased by 3 mm by offsetting of the intake valve.

5.2. Analysis for Effects of Intake Valve Offset by CFD

The impact of intake valve offset on POT TR and Z_i was analyzed using CFD.

First, the N_r per valve lift was calculated at a throttle opening of 15 degrees. Figure 19 shows the results. When the intake valve was offset, the N_r increased in the full range

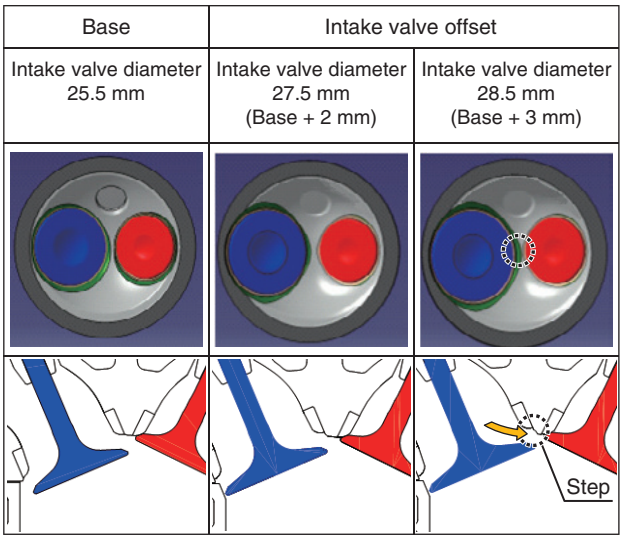


Fig. 18 Combustion chamber with intake valve offset

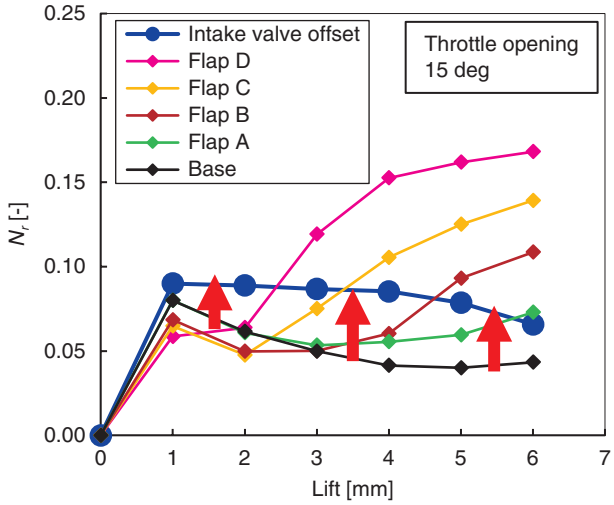


Fig. 19 Relationship between valve lift and N_r

of valve lift when compared to the basic design. Also, with the intake valve offset, the N_r tended to increase in the range where the valve lift was low compared to the flap. This was because the recess was placed close to the intake valve seat, allowing achievement of greater tumble effect than the flap in the low valve lift range.

Next, the C_f per valve lift was calculated at WOT. Figure 20 shows the results. When the C_f of intake valve offset and that of flap B were compared, the C_f values were nearly the same when the valve lift is less than 4 mm. When the valve lift was more than 4 mm, however, the C_f value was higher in the intake valve offset than in flap B. This was because the masking effect was reduced in the high valve lift range when intake valve offset was applied. As a result, C_f increased.

Figure 21 shows the relationship between valve lift and Z. When Z in the offset intake valve was compared to that of flap B, Z in the offset intake valve tended to increase relative to Z of flap B more than in the comparison of C_f. As indicated by the preceding Eq. (5), Z is defined as a product of C_f and A_v. In the intake valve offset design, as the intake valve diameter was increased by 2 mm from the basic design, A_v increased, resulting in an increase of Z.

TR and Z_i are calculated from N_r, C_f and Z. Figure 22 shows the results. In the intake valve offset design, POT TR of 1.3, which is the same level as in flap B, was attained. Also, in the intake valve offset design, the Z_i at WOT was more than in flap B although it was lower than in the basic design. Thus, the new design was expected to allow an escape from the trade-off between fuel economy and maximum power.

In this connection, when only offsetting of the intake valve was applied without increasing the intake valve diameter, Z_i decreased by approximately 8% from 6.67 cm^2·rad to 6.15 cm^2·rad, although POT TR did not decrease. Figure 23 shows the results of CFD analysis of flow velocity distribution in the intake port and in the

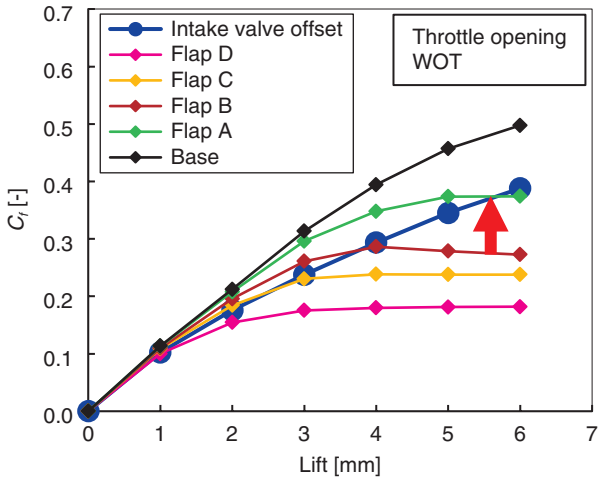


Fig. 20 Relationship between valve lift and C_f

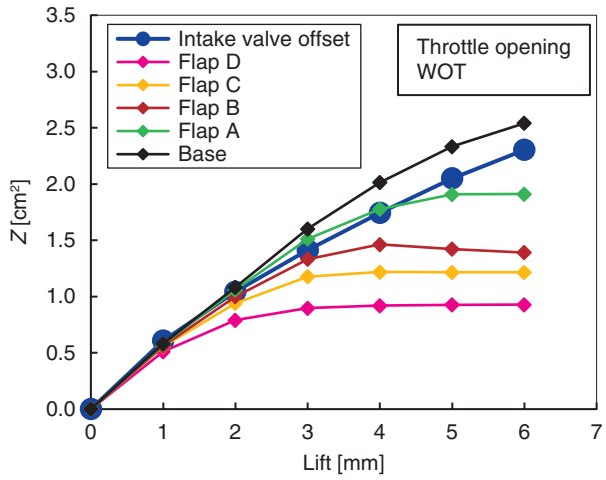


Fig. 21 Relationship between valve lift and Z

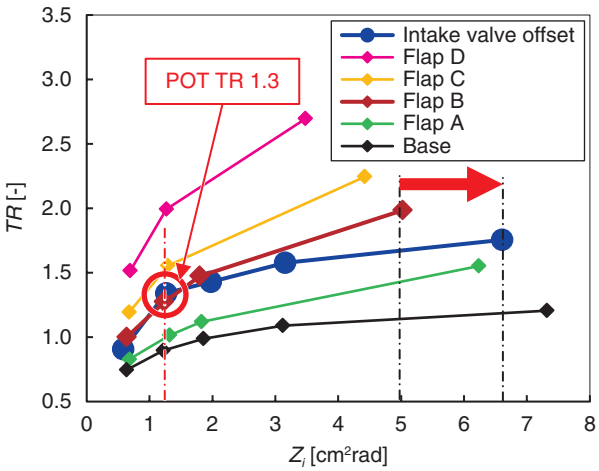


Fig. 22 Relationship between Z_i and TR

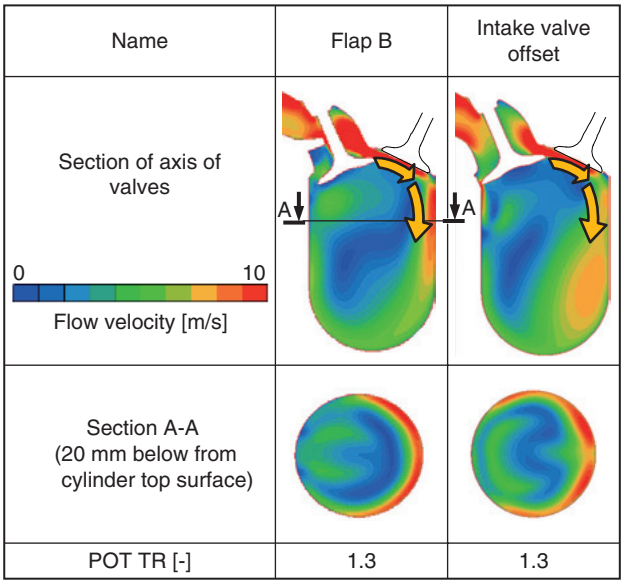


Fig. 23 Flow velocity distribution analyzed by CFD

cylinder. The calculation was conducted at a throttle opening of 15 degrees and valve lift of 4.5 mm, which was where N_r of intake valve offset intersects with that of flap B in Fig. 19. Due to the masking effects from the intake valve offset, the flow of mixture from the cylinder sleeve wall side of the intake valve was disturbed, and the flow from the exhaust valve side to the cylinder became vigorous. Thus, the intake valve offset induced vigorous tumble flow in the cylinder, allowing attainment of the same POT TR as with flap B.

5.3. Fuel Economy Improvement and Prevention of Lowering of Maximum Power

Using the engine incorporating intake valve offset, fuel economy improvement and prevention of lowering of maximum power were verified by experiments. Figure 24 shows the relationship between A/F and ISFC under the typical operating conditions in IDC. Figures 25, 26, 27 and 28 show the results of combustion analyses.

The lowering of ISFC in the lean range was confirmed as the effect of intake valve offset, similar to the case of fitting of a flap in the intake port. When compared with the minimum value of ISFC, the rate of lowering was 4.8%. This rate of lowering of ISFC was equivalent to that of flap B having almost equal POT TR value. The results of combustion analysis showed the shortening of $MFB_{0\text{-}10\%}$ and

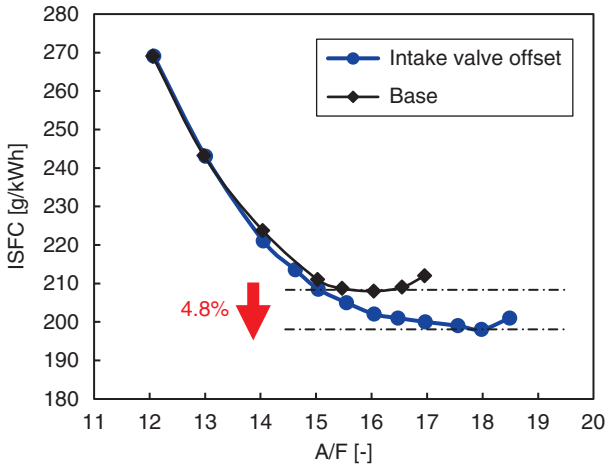


Fig. 24 Relationship between A/F and ISFC

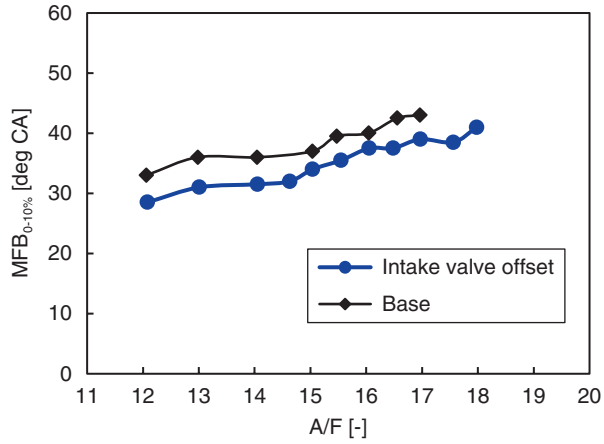


Fig. 25 Relationship between A/F and $MFB_{0\text{-}10\%}$

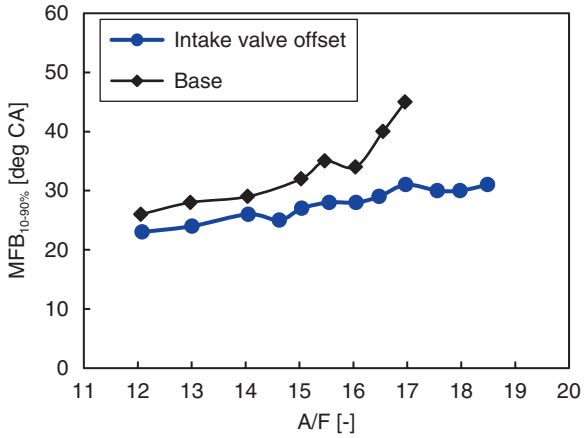


Fig. 26 Relationship between A/F and $MFB_{10\text{-}90\%}$

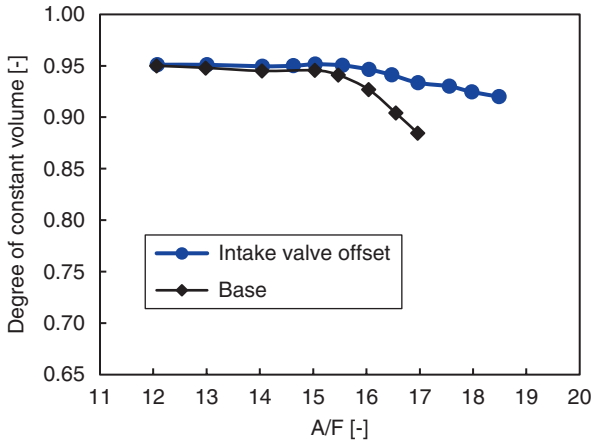


Fig. 27 Relationship between A/F and degree of constant volume

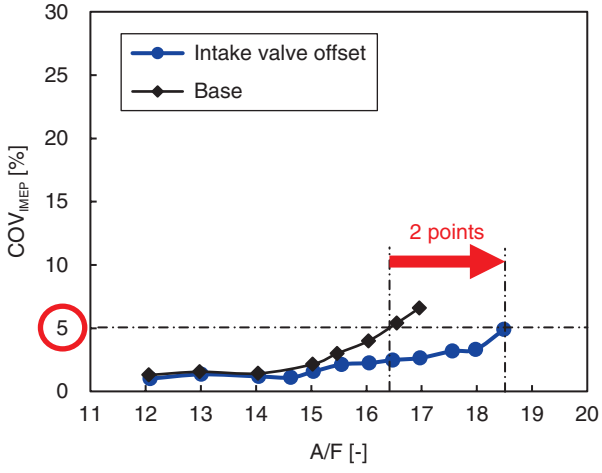


Fig. 28 Relationship between A/F and COV_{IMEP}

$MFB_{10\text{-}90\%}$ and the increase of degree of constant volume in the engine incorporating intake valve offset. When A/F where COV_{IMEP} reached 5% was defined as a lean burn limit, the lean burn limit of intake valve offset shifted 2 points to the lean side compared to the base engine.

Figure 29 shows power output at wide open throttle. The drop in maximum power of the engine was suppressed to 4% when intake valve offset was applied, while it declined by 15% compared to the base engine when flap B was used.

Figure 30 shows the relationship between POT TR and maximum power. It can be observed that the point showing the status with application of intake valve offset lies outside the trade-off line between POT TR and maximum power when different shapes of flap were equipped.

Consequently, it was confirmed that the trade-off relationship between ISFC and maximum output power was mitigated without using complicated mechanisms, like variable devices, by applying this technique.

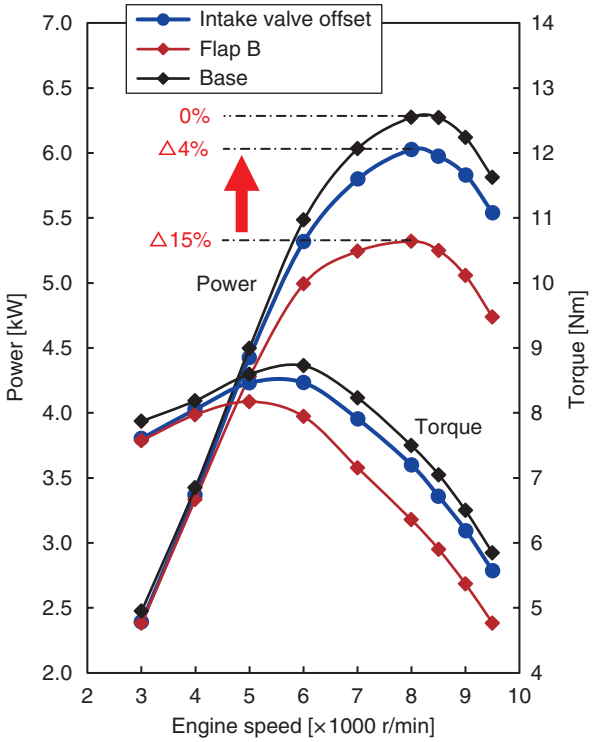


Fig. 29 Power output at wide open throttle

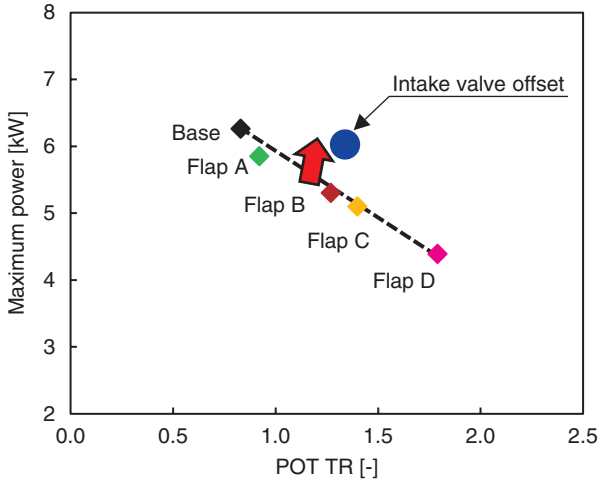


Fig. 30 Relationship between *TR* and maximum power

6. Control of Knocking by Squish and Improvement of Fuel Economy from Increased Compression

The following have been analyzed through CFD analysis and actual tests of two-valve per cylinder engines.

- Squish zone shape that is effective for creation of reversed squish flow
- Controlling of knocking by squish
- Fuel economy from increased compression realized by control of knocking

Figure 31 shows the specifications of the test engine. The rate of projected squish surface area indicates the rate of squish surface area against the bore surface area viewed from the cylinder head gasket side.

6.1. Intensity of Reversed Squish Flow from Various Squish Shapes and Impacts to Margin to Knocking Occurrence

To clarify the relationship between the reversed squish flow, which is considered effective for control of knocking, and the shape of squish zone, we conducted CFD analysis. Reversed squish flow occurs when the piston descends after passing TDC. Figure 32 shows the in-cylinder pressure waveform when knocking occurs in the actual engine (wide open throttle, Ne 3000 r/min, 50 cycles). Knocking occurred at the crank angle of 5-10 degrees ATDC. In view of this, we chose the crank angle of 5 degrees ATDC for assessment of intensity of reversed squish flow by CFD analysis.

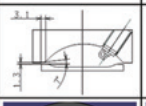
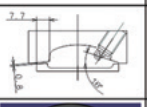
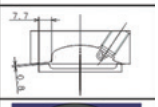
		Base	Sq-A	Sq-B
Squish shape	Plug side	NA	Taper	Slant-parallel
	Opposite side	Taper	Slant-parallel	Slant-parallel
Squish height [mm]		1.3	0.8	0.8
Projected area of squish [%]		12.3	26.9	26.9
Compression ratio		9.0	9.0	9.0
Cross sectional view (Section A-A)				
Squish shape				

Fig. 31 Specifications of squish

Figure 33 shows the results of CFD analysis. The vector shows the direction and intensity of the flow.

The differences in the flow speeds of the reversed squish between the tapered squish and the slant-parallel squish were compared at the plug side and at its opposite side. In the opposite side of the spark plug, the speed of reversed squish flow that enters the squish zone was higher in the area of the slant-parallel shape (Sq-A and Sq-B) than in that of the tapered shape (basic design). In addition, in the spark plug side, the speed of reversed squish flow was higher in the area of the slant-parallel shape (Sq-B) than in that of the tapered shape (Sq-A). From the above-mentioned findings, it was determined that the slant-parallel squish is effective to intensify reversed squish flow.

To clarify the influence of intensity of reversed squish flow on knocking, the ignition timing when knocking occurred and the MBT were measured through experiments. Here, the variance of crank angle between the ignition timing when knocking occurs and the MBT is defined as "margin to knocking occurrence" for assessment of knocking control.

Figure 34 shows the ignition timing when knocking has occurred, Fig. 35 shows MBT, and Fig. 36 shows margin to knocking occurrence. It can be understood from Fig. 34 that the ignition timing when the knocking occurred

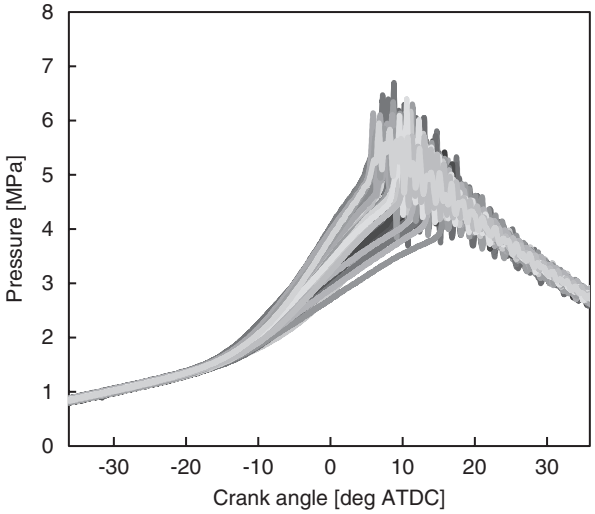


Fig. 32 Pressure waveform with knocking occurrence

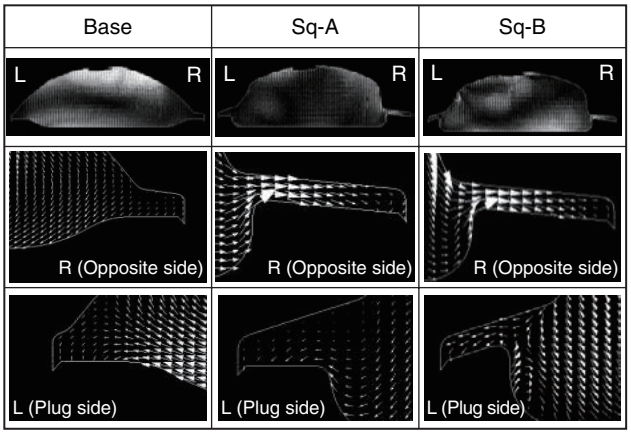


Fig. 33 Effect of squish area location on squish flow formation (5 deg ATDC CA)

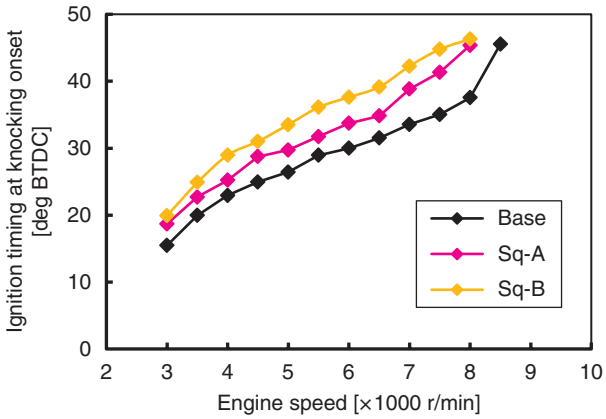


Fig. 34 Effect of squish on ignition timing at knocking onset

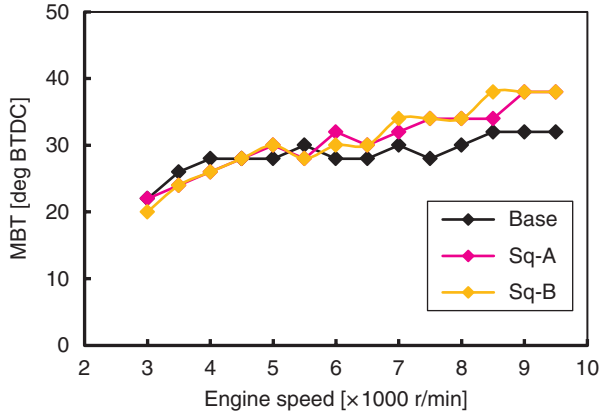


Fig. 35 Effect of squish on MBT

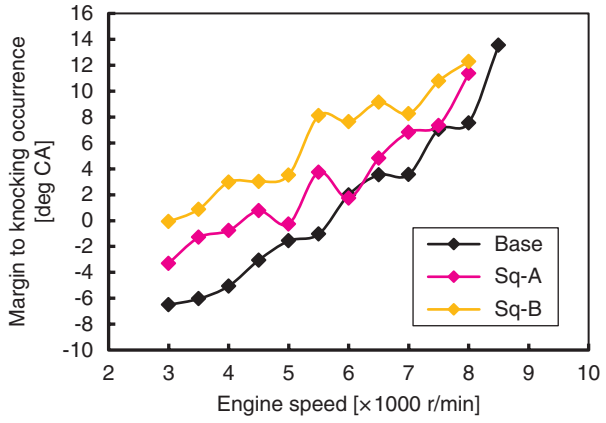


Fig. 36 Effect of squish on margin of knocking occurrence

advanced in the order of basic design, Sq-A, Sq-B along with the intensifying of reversed squish flow. Since there was no large difference in MBT as shown in Fig. 35, the margin to knocking occurrence increased in the order of Sq-A, Sq-B when compared to the basic design as Fig. 36 shows.

The following has been found from the application of squish to the two-valve per cylinder, small displacement engine.

- The slant-parallel squish is effective for intensifying of reversed squish flow
- The intensity of reversed squish flow is correlated to the margin to knocking occurrence.

6.2. Increase of Compression Ratio to Take Advantage of Squish Effect

We attempted to increase compression ratio to take advantage of the margin to knocking occurrence from squish effects. The compression ratio ε for the same margin to knocking occurrence as the basic design was 9.5 (0.5 higher than the basic design). The compression ratio was raised by changing the piston crown height without altering the squish shape from Sq-B. This design is defined as Sq-B$_{(\varepsilon+0.5)}$. The ignition timing when the knocking occurred, the MBT and the margin to knocking occurrence of Sq-B$_{(\varepsilon+0.5)}$ are shown respectively in Figs. 37, 38, and 39. Figure 37 shows that the ignition timing when the knocking occurred in Sq-B$_{(\varepsilon+0.5)}$ was retarded from that of Sq-B, and is the same as that of the basic design. Also, Fig. 38 shows that the MBT was the same as that of the basic design and Sq-B. Accordingly as Fig. 39 shows, the margin to knocking occurrence was lower than Sq-B, and the same as in the basic design.

6.3. Changes of Heat Generation Rate Caused by Squish

To clarify factors that increase margin to knocking occurrence by the application of squish, we conducted combustion analysis. (Analysis conditions: Engine speed: 6000 r/min; Throttle: wide open throttle; A/F 12.4)

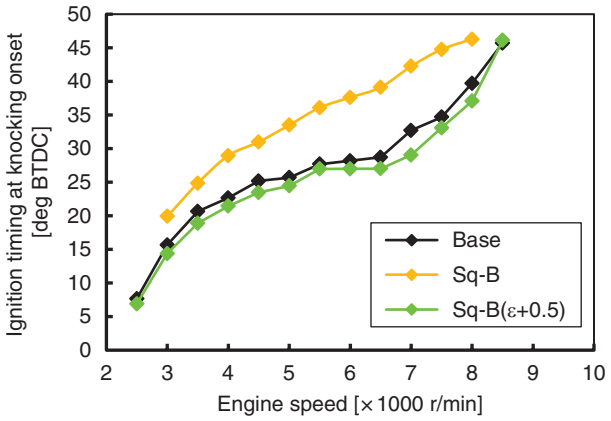


Fig. 37 Effect of compression ratio on ignition timing at knocking onset

Figure 40 shows the rate of heat release and the in-cylinder pressure at various crank angles. The Pmax of Sq-B with the increased margin to knocking occurrence was the same as that of the basic design. When the rate of

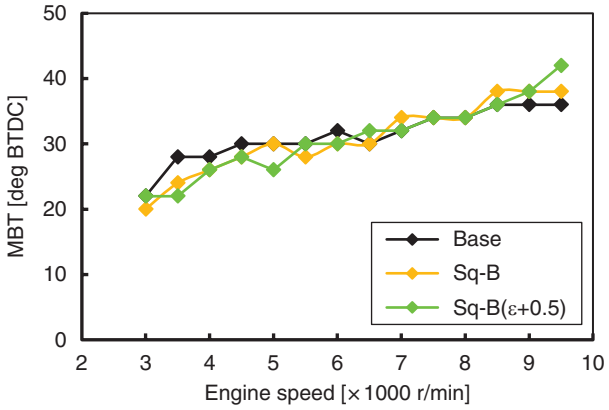


Fig. 38 Effect of compression ratio on MBT

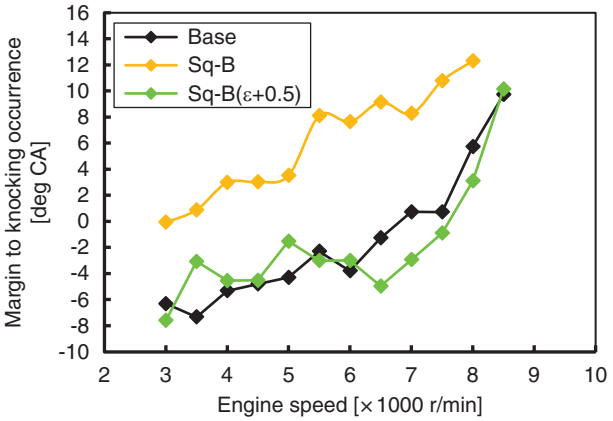


Fig. 39 Effect of compression ratio on margin to knocking occurrence

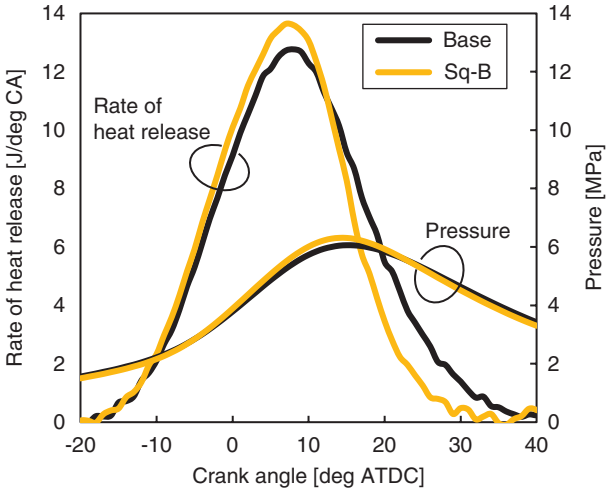


Fig. 40 Comparison of rate of heat release and pressure

heat release was compared, the rate of heat release of Sq-B was higher than in the basic design near the crank angle of 5 degrees ATDC where CFD analysis shows differences in the intensity of reversed squish flow. It can be considered that the accelerated combustion in that period from the squish effect is a factor of the increased margin to knocking occurrence.

6.4. Improvement of Fuel Economy by Control of Knocking Using Squish

Figure 41 shows the ISFC and the $MFB_{50\text{-}90\%}$ in the latter combustion period in Sq-B and Sq-$B_{(\varepsilon+0.5)}$ at A/F of 16.5, where the ISFC of the basic design became lowest under the partially loaded conditions. Compared to the basic design, the ISFC lowered by 1.3% in Sq-B, and the $MFB_{50\text{-}90\%}$ was shortened by 5 degrees (from 24 degrees to 19 degrees). In Sq-$B_{(\varepsilon+0.5)}$, the ISFC was lowered by 2.6% from the basic design, and the $MFB_{50\text{-}90\%}$ was shortened by 5 degrees (from 24 degrees to 19 degrees). It can be considered that the ISFC of Sq-B lowered because of the shortened $MFB_{50\text{-}90\%}$. Also, the ISFC of Sq-$B_{(\varepsilon+0.5)}$ lowered because of the improvement of theoretical thermal efficiency due to the increased compression ratio in addition to the shortening of $MFB_{50\text{-}90\%}$.

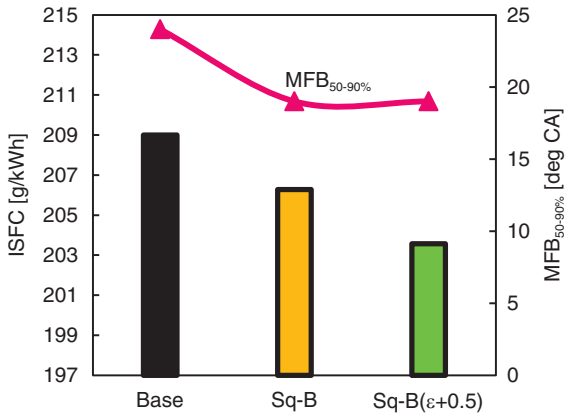


Fig. 41 Comparison of ISFC and $MFB_{50\text{-}90\%}$

7. Effectiveness of Combination of Offset Intake Valve and Squish

As mentioned above, the offset intake valve has extended the lean burn range by the intensifying of tumble effects. Also, the squish allowed increase of compression ratio by intensified reversed squish flow. With these concepts combined, the performance was investigated using the specs shown in Fig. 42.

Figure 43 shows COV vs A/F. In the intake valve offset Sq-$B_{(\varepsilon+0.5)}$, the lean burn range was extended by 2 points in A/F from the basic design just like the offset intake valve. Figure 44 shows the ignition timing when the knocking occurred, and Fig. 45 shows the MBT. The angles were

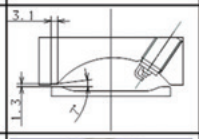
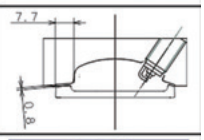
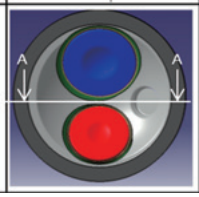
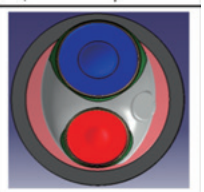
		Base	Intake valve offset Sq-$B_{(\varepsilon+0.5)}$
Intake valve offset		NA	Applied
Intake valve diameter [mm]		25.5	27.5
Squish shape	Plug side	NA	Slant-parallel
	Opposite side	Taper	Slant-parallel
Squish height [mm]		1.3	0.8
Compression ratio		9.0	9.5
Cross sectional view (Section A-A)			
Squish shape			

Fig. 42 Specifications of intake valve offset Sq-$B_{(\varepsilon+0.5)}$

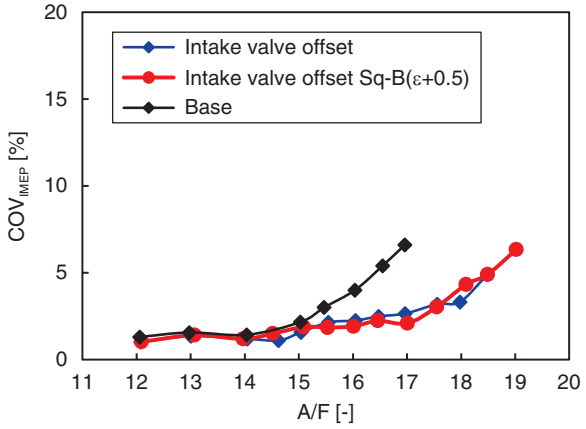


Fig. 43 Relationship between A/F and COV_{IMEP}

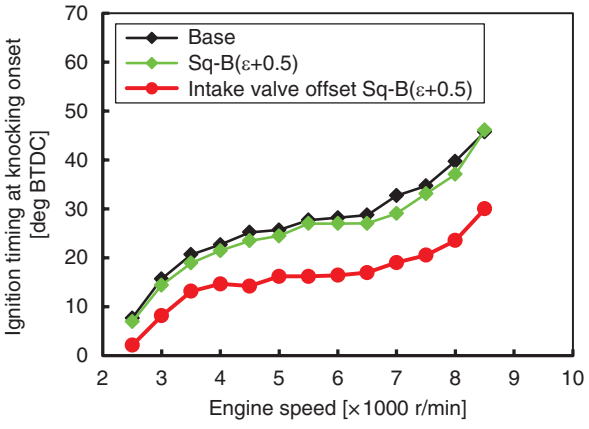


Fig. 44 Comparison of ignition timing at knocking onset

retarded from the basic design both in the ignition timing when the knocking occurred and in the MBT. As Fig. 46 shows, the margin to knocking occurrence of the intake valve offset Sq-$B_{(\varepsilon+0.5)}$ was the same as in the basic design. It is considered that the reason why the ignition timing when the knocking occurred and the MBT in the intake valve offset Sq-$B_{(\varepsilon+0.5)}$ were retarded from the basic design was the shortening of the principal combustion period $MFB_{10\text{-}90\%}$ in the offset intake valve design due to the intensified tumbling as shown in Fig. 26.

From the above findings, it has been clarified that effectiveness of both ideas is individually attainable even when the combustion improvement from extension of lean burn range by off-setting of the intake valve is combined with that from increased margin to knocking occurrence by the squish effects.

Figure 47 shows the power output when the throttle is opened widely. Figure 48 shows ISFC vs A/F. Although the maximum power output in the intake valve offset Sq-$B_{(\varepsilon+0.5)}$ decreased by 3% from the basic design, the minimum ISFC has been lowered by 6.0%.

Figure 49 shows the relationship between the lowering ratio of ISFC and the maximum power output under the partially loaded conditions. Each rate of lowering ratio of ISFC when the four kinds of tumble generator flap were equipped was calculated from Fig. 12. If the 6.0% reduction

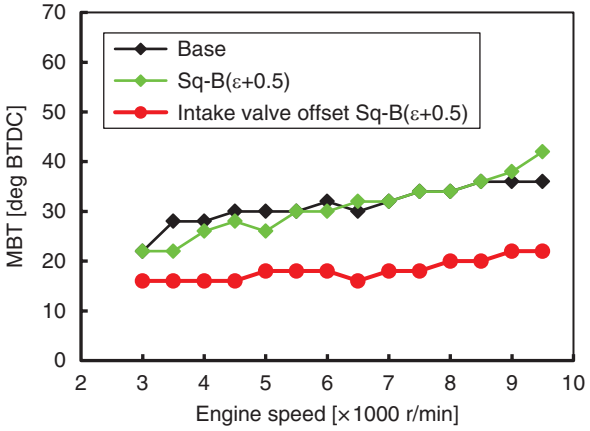


Fig. 45 Comparison of MBT

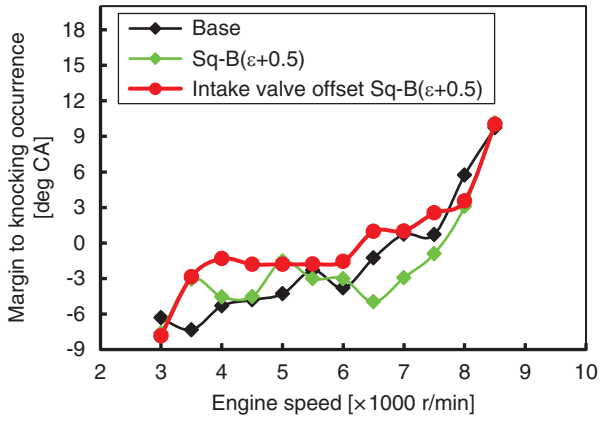


Fig. 46 Comparison of margin to knocking occurrence

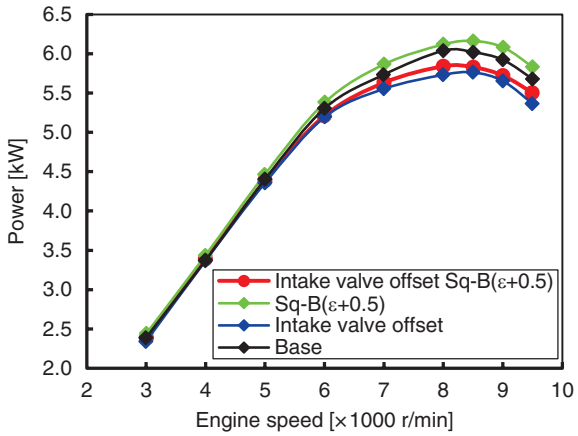


Fig. 47 Power output at wide open throttle

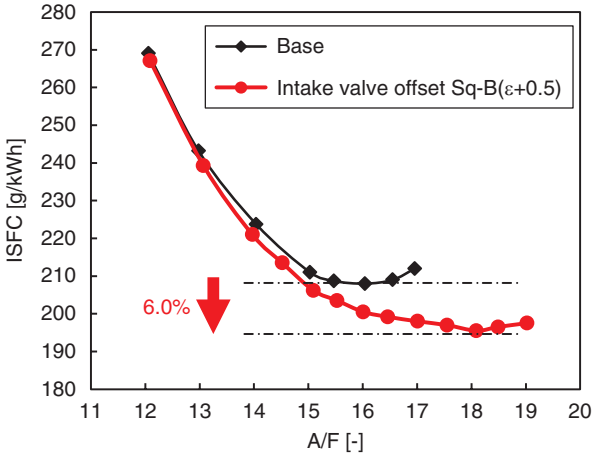


Fig. 48 Relationship between A/F and ISFC

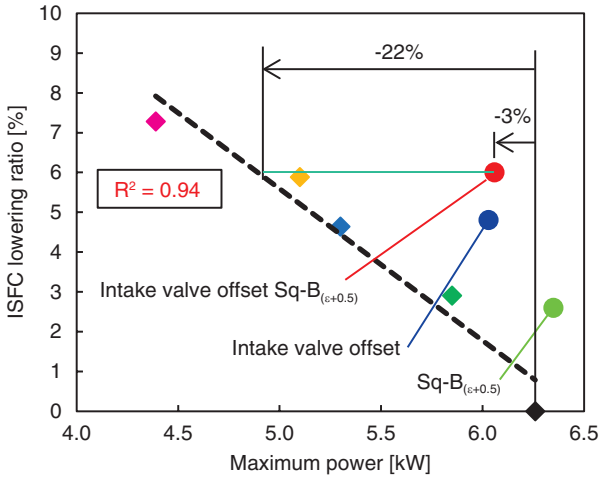


Fig. 49 Relationship between maximum power and ISFC lowering ratio

of ISFC realized by the intake valve offset Sq-$B_{(\varepsilon+0.5)}$ were attained only by use of the flap, the maximum power output would be lowered by 22% (from 6.3 kW to 4.9 kW). When the intake valve offset Sq-$B_{(\varepsilon+0.5)}$ was used, however, the decrease in maximum power output was only 3% (from 6.3 kW to 6.1 kW).

Based on the results of combined measures mentioned above, it was confirmed that the trade-off relationship between ISFC and the maximum output power could be successfully mitigated without using complicated mechanisms such as variable devices.

8. Conclusion

The extension of lean-burn range by offset intake valve and increased compression ratio using squish have improved ISFC while preventing reduction of the maximum power output.

(1) It has been clarified that the POT TR is correlated to the rate of ISFC reduction in the partially loaded conditions, which are subjected to these studies. Thus, it has been determined that the POT TR can serve as an index of ISFC reduction.

(2) The following two principles, which have been clarified in the four-valve per cylinder engine for automobiles are also confirmed in the small displacement, two-valve per cylinder engine for motorcycles.
   (i) The intensity of reversed squish flow is correlated to the control of knocking.
   (ii) The slant-parallel squish is effective to intensify reversed squish flow.

(3) With the intake valve off-set, the POT TR increased, and the lean burn limit has been extended by two points in A/F compared to the basic design. Thus, the ISFC under the partially loaded conditions has been reduced by 4.8% from the basic design.

(4) The slant-parallel squish controls knocking, allowing an increase of compression ratio (from 9.0 to 9.5), which has reduced the ISFC by 2.6% from the basic design under the partially loaded conditions.

(5) By the combination of the offset intake valve mentioned in (3) and the increased compression ratio using the slant-parallel squish mentioned in (4), the minimum ISFC under the partially loaded conditions has been reduced by 6.0% from the basic design while keeping the decrease in maximum power output to as little as 3% (from 6.3kW to 6.1kW).

References

(1) Nakayama, Y., Suzuki, M., Iwata, Y., Yamano, J.: Development of a 1.3L 2-Plug Engine for the 2002 Model 'Fit', Honda R&D Technical Review, Vol. 13, No. 2, p. 43-52

(2) Toulson, E., Huisjen, A., Chen, X., Squibb, C., Zhu, G., Schock, H., Attard, W.: Visualization of Propane and Natural Gas Spark Ignition and Turbulent Jet Ignition Combustion, SAE Technical Paper 2012-32-0002 / JSAE Paper 20129002 (2012)

(3) Mochizuki, K., Kashima, T., Kakinuma, A.: Improvement of Combustion in an SI Engine with Tumble Generator Valve, Journal of Society of Automotive Engineers of Japan, Vol. 50, No. 9, p.38-43 (1996)

(4) Iijima, S., Kubota, R., Kikuchi, K.: Development of Technologies for Improving Fuel Economy of Small Motorcycle Engines, SAE Technical Paper 2009-32-0083 / JSAE Paper 20097083 (2009)

(5) Falfari, S., Brusiani, F., Bianchi, G. M.: Assessment of the Influence of Intake Duct Geometrical Parameters on the Tumble Motion Generation in a Small Gasoline Engine, SAE Technical Paper 2012-32-0095 / JSAE Paper 20129095 (2012)

(6) Iwai, K., Narahara, K., Fujimoto, M., Tabata, M.: Effect of the Intake Valve Lift on Tumble Flow and Combustion Characteristics in an S.I. Engine, JSAE Transaction, Vol. 36, No. 1, January, p. 33-38 (2005)

(7) Tabata, M., Fujimoto, M., Iwai, K.: Knocking Improvement by Tumble Flow and Reverse Squish Flow, Matsuda Technical Reviews, No.21, p.192-198 (2003)

(8) Miyamoto, K., Hoshiba, Y., Hosono, K., Hirao, S.: Enhancement of Combustion by Means of Squish Pistons, Mitsubishi Motors Technical Reviews, No. 18, p.32-41 (2006)

(9) Ueda, T., Okumura, T., Sugiura, S., Kojima, S.: Effects of Squish Area Shape on Knocking, 1998 JSAE Annual Congress Proceedings, No. 982 (9832369) p.99-102

(10) Wotton, C. R. N.: Steady State Flow Bench Port Performance Measurement and Analysis, Ricardo Report DP93/0704 (1993)

(11) Furuhama, S., et al.: Enjinnojiten, Asakura Publishing Co., Ltd., ISBN 4-254-23073-7, p.123-125 (1994) (in Japanese)

■ Author ■


Takamori SHIRASUNA


Hideki SAITO


Tomokazu NOMURA

Technique for Prediction of Automotive Transmission Lubrication Performance

Daiki SAEGUSA* Shinji KAWAI*

ABSTRACT

A technique was created for rapidly and accurately predicting oil flow within a transmission.

This research employs the finite difference method to perform analysis, and handles wall boundaries by the method of assigning boundary information to cells and reproducing the object shape. This enabled the gear rotation and engagement that shape oil flows to be handled more readily, and also reduced the calculation cost.

This analytical technique was applied to a manual transmission, and the results show that the calculation of oil flows that takes approximately 26 days by the conventional technique was shortened to approximately four days. In terms of accuracy, it was further confirmed that the technique also enabled prediction of the state of lubrication in an actual transmission.

1. Introduction

The purpose of the transmission is to convert the power output from the engine to an optimal driving force and speed and transmit it to the driveshaft. The gears, bearings, and other component parts that form the route for transmitting that power are subject to damage or deterioration from wear and heat generation. In order to limit these factors, a continuous supply of oil needs to be unfailingly delivered to every part while it is in operation. On the other hand, when the amount of oil is increased to enhance the lubrication, the resistance torque increases because of oil agitation and shear. This resistance torque becomes a direct power loss and affects vehicle fuel efficiency. For this reason, transmission design seeks to enhance the housing in order to enhance oil flows, and baffles are placed in the area around each gear as ways to achieve a balance between lubricating ability and loss reduction. However, the techniques for confirming the effects of such measures at the design stage are not adequate, and as things actually stand, the process depends on such things as the experience of the people in charge of development and confirmation performed after first having fabricated prototypes for endurance testing, tests using flow visibility, and so on. With visibility testing, as well, it is often the case that interior flows cannot be adequately confirmed because they are hidden by parts or by oil adhering to the inside wall of the housing.

Simulation is used today for a variety of reasons, including the shortening of development time, reduction in prototype expenses, and grasping phenomena that are not readily analyzed through testing on actual machinery. This is also the case with oil flows inside the transmission, for which analysis of flow phenomena using Computational Fluid Dynamics (CFD) is gradually becoming the norm. CFD includes a variety of different methods, and the methods are selected according to the intended use. Many issues still remain, however, with regard to analysis for the purpose of predicting lubrication performance and loss, which are mutually exclusive in performance, throughout the interior of the transmission, and methods for the purpose have not yet been established.

In the interior of the transmission, oil is agitated by multiple gears and other such rotating bodies. Unsteady and more complex flows are also formed by oil and air mixing together, and the calculation cost becomes immense. There are also minute droplets and sudden pressure fluctuations where gears are engaged, and it is no simple matter to apprehend the behavior of fluid surfaces.

This article reports on the creation of a technique for predicting the state of lubrication in terms of oil flows of these kinds inside a transmission within a practical length of calculating time.

2. Research Aims

Prediction of oil flows in the interior of the transmission calls for the ability to reproduce both the movement of bodies such as rotating gears and the behavior of fluids

* Automobile R&D Center

induced by those movements. Representative methods of CFD include the finite volume method and the finite element method. In these methods, the region that is calculated is converted to meshes that are treated as minute fluid elements and the behavior of the fluid is calculated. When this is done, the usual approach is to generate the meshes to follow object shapes. Since the calculation applies to both gas and liquid, this method can perform calculation that takes into account the air entrainment that has such a large influence on oil flows at high rotational speeds. In a transmission, however, this approach needs to handle fluid regions such as engagement of gears that change form from moment to moment while the calculation is underway, and this therefore calls for a special approach that will be described below. The dynamic mesh model[(1)] automatically regenerates meshes in conjunction with the rotation of a body, while the sliding mesh model[(2)] simulates gear movements by taking the region around a gear centered on the axis of rotation, dividing it into cylindrical domains, and rotating those cylindrical areas. In the dynamic mesh model, however, it is a virtually insuperable challenge to continue maintaining mesh quality during the process of calculation, and the calculation can readily become unstable. In the sliding mesh model, the rotating meshes need to be kept from interfering one with the other, so this approach cannot take the engagement of gears into consideration. Also, the dynamic mesh model and sliding mesh model both need enormous amounts of time for generating meshes and for calculations when they handle large numbers of parts.

At the same time, however, attention is also being given to the particle method of analysis[(3)], which converts oil and other fluids into particles for calculation. Compared to methods that use meshes, this has the advantage of higher calculating speeds because it calculates only particulated fluids. However, it cannot readily take into account the effects of air entrainment and negative pressure on oil flows, so that, under present conditions, application of this method is limited to oil flows at low rotational speeds that are less affected by those factors.

Given these circumstances, the aim of this research was defined as the creation of a technique that can predict transmission lubrication performance and that satisfies the following conditions:

(1) It can reproduce gear rotation, including engaged portions, and calculate the oil flows formed by those movements, thus predicting the state of lubrication in each part
(2) It has a calculating time that is practically usable in development
(3) It can take into consideration the effects on oil flows from air entrainment and negative pressure

3. Analysis Objects and Methods

3.1. Analysis Objects

In order to judge whether oil flows induced by rotating bodies are accurately grasped, the object was defined as an automotive manual transmission that does not include hydraulic circuits (Fig. 1).

3.2. Calculation Method

This research was based on the finite difference method, which uses meshes in the calculation domains, in order to enable consideration of the effects on oil flows from air entrainment and negative pressure. In order to address the issue of how to handle gear engagement, it applied the approach not of meshes generated according to shapes, but rather of incorporating information on gear shape and status of movement in cells (individual elements delimited by meshes) (Fig. 2)[(4)]. The rotation of a gear is reproduced not by changing the shapes of cells but by providing that information again. This approach is able to reproduce the engagement of gears without diminishing mesh quality, unlike the dynamic mesh model. This approach is able to reproduce the engagement of gears without diminishing mesh quality, as in the dynamic mesh model. In addition,

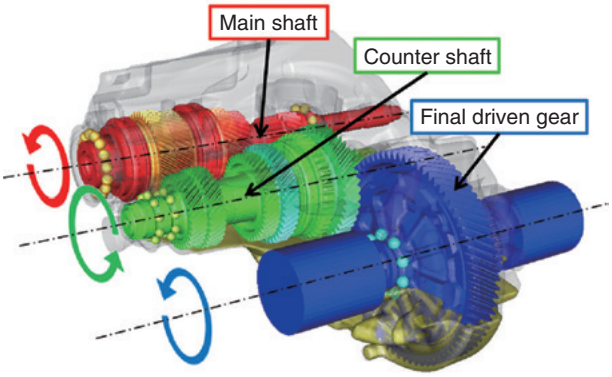


Fig. 1 Mechanical components of automotive manual transmission

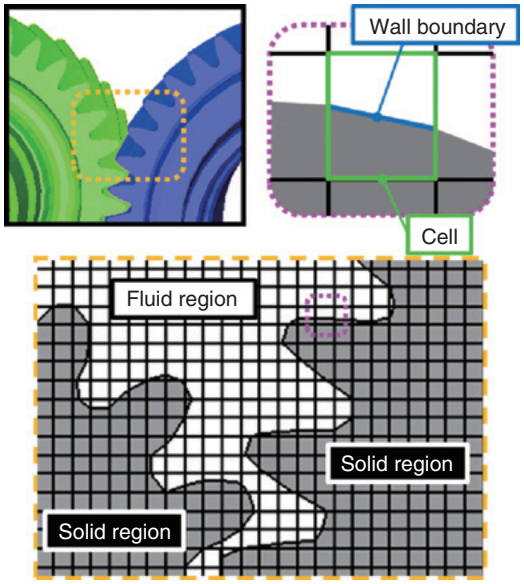


Fig. 2 Wall boundary treatment

this approach can shorten the calculating time as well as the time taken to prepare for analysis because it does not need to generate meshes according to shapes.

The behavior of fluid surfaces was calculated using the Volume of Fluid (VOF)[5] method.

Large Eddy Simulation (LES)[6] was used for the turbulence model because this approach is suited to accurately grasping highly nonstationary phenomena such as oil churning.

These methods are being applied as a way of achieving a balance between increased speed and accuracy of calculation.

4. Accuracy Validation

4.1. Validation Method

Compared to conventional methods in which the meshes are created to match the shapes, the reproducibility of object shapes is lower with this method. Consequently, the influence on the accuracy of calculations needs to be checked. The following steps were therefore taken to verify the accuracy of this method:

Step 1. Accuracy of flow field formed by single-phase flows and moving wall boundary

Step 2. Accuracy of flow path formed by multi-phase flows and moving wall boundary

4.2. Accuracy Verification of Flow Field Formed by Single-Phase Flows and Moving Wall Boundary

In order to confirm that a velocity field formed by rotating bodies within a fluid was analyzed accurately, actual measurements were made of flow velocity distribution using Particle Image Velocimetry (PIV)[7, 8] as an experiment in single-phase flows (Fig. 3). The measurement object was an oil flow by agitation created by a Rushton turbine (Fig. 4) in a cylindrical tank. The use of stereo PIV, which employs two cameras, further enabled measurement of the vertical component of flow velocity with reference to a laser sheet surface. Measurements were taken under three conditions, at a rotational speed of 375 rpm, 525 rpm, and 750 rpm.

Figure 5 shows a comparison between the measurement

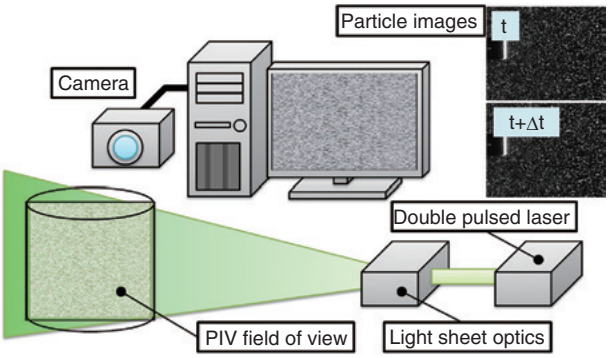


Fig. 3 PIV experiment system

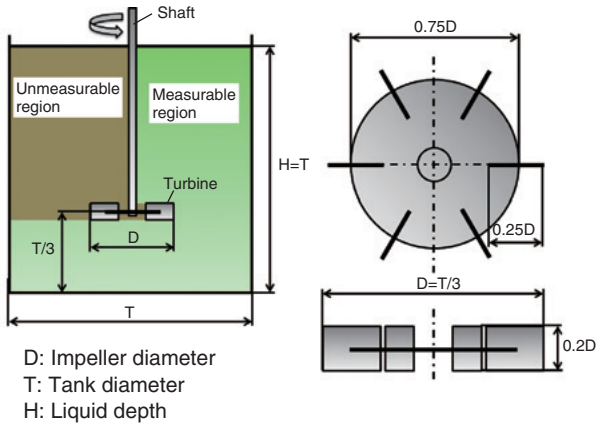


Fig. 4 Rushton turbine blade

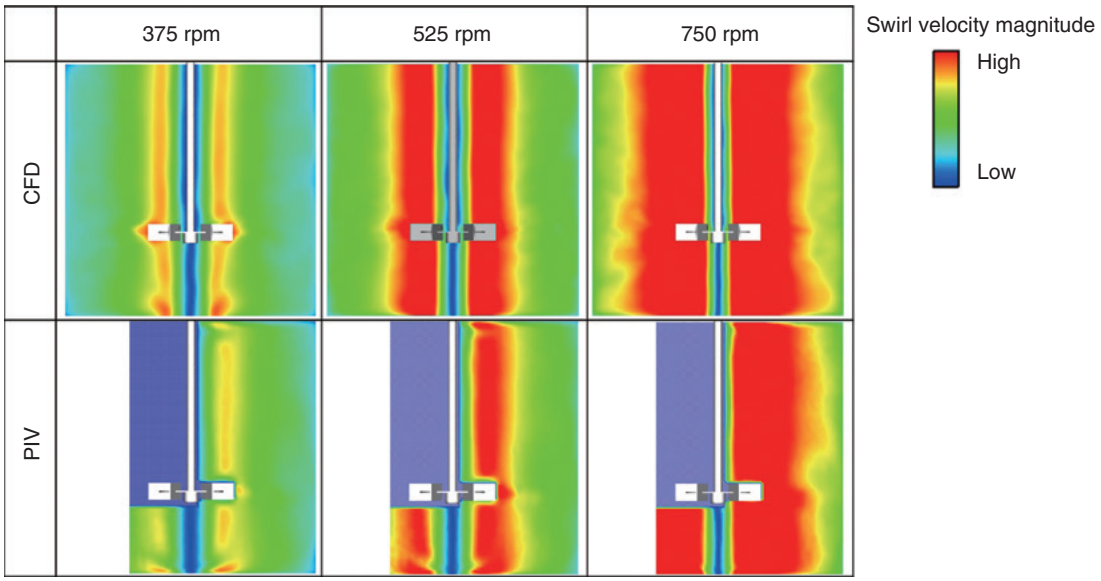


Fig. 5 Comparison of swirl velocity magnitude distribution between CFD and PIV experiment

results and CFD for the distribution of swirl velocity magnitude. The colors represent time averages of flow velocity, with red indicating higher velocity areas that shade into blue where the velocity is lower. Figure 6 shows a comparison of quantified velocities at different positions in a radial direction. It is apparent that changes in flow velocity due to differences in rotational speed as well as the decline in flow velocity at increasing distances from a rotating body in a radial direction are captured correctly in quantitative terms, as well.

4.3. Accuracy Validation of Flow Path Formed by Multi-Phase Flows and Moving Wall Boundary

Next, a gearbox composed of only one pair of gears as shown in Fig. 7 was used to conduct an agitation experiment, and this was taken as the object of comparison in order to confirm the reproducibility of gas-liquid flows using this method. The housing was made of transparent acrylic resin and the device was arranged to enable visual confirmation of the oil trajectories caused by rotation of the gears.

Figure 8 shows a comparison between the experiment results and CFD for trajectories. Rotational speed conditions of 200 rpm, 400 rpm, and 800 rpm were used. The reproducibility of oil trajectories resulting from different rotational speeds was verified.

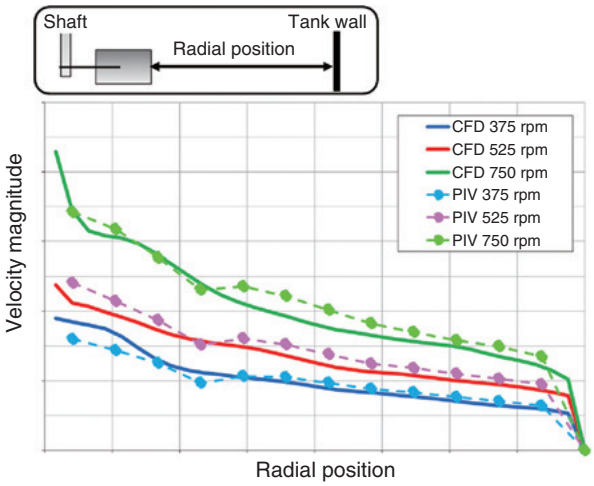


Fig. 6 Comparison of velocity magnitude distribution of radial position between CFD and PIV experiment

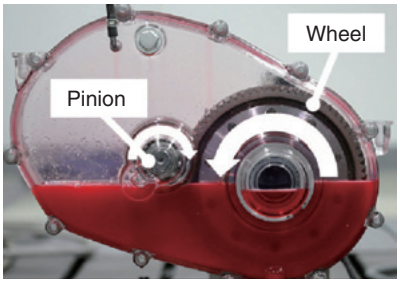


Fig. 7 PIV experiment system

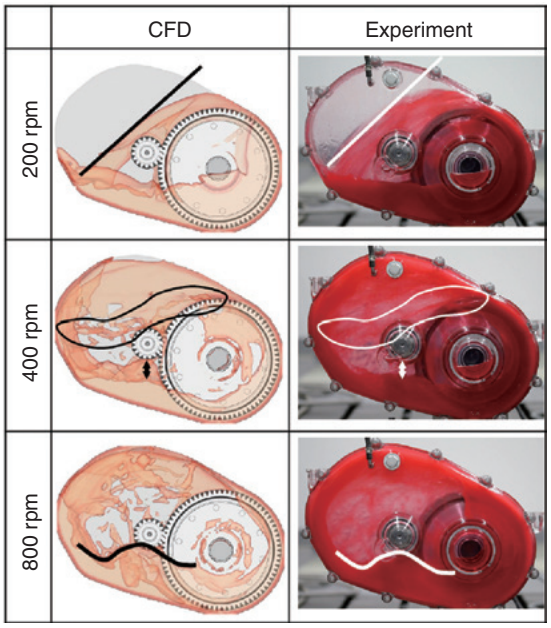


Fig. 8 Comparison of oil trajectory between CFD and experiment

First, at 200 rpm, the trajectories of oil lifted by the wheel are in close agreement. There is also close agreement at 400 rpm, showing a portion of the oil that has been thrown off by the wheel and separated from the main flow of oil, and also showing it in contact with the pinion. There is agreement again at 800 rpm, showing an increase in the flow velocity of the component moving in the direction of the gear rotation, oil being pressed against the outer periphery, and the appearance of the fluid surface of the oil sump. The fluid surface that was not in contact with the pinion at 400 rpm has come into contact with it at 800 rpm, and the behavior of the fluid surface is in close agreement at all rotational speeds.

5. Application to Automotive Transmission

Oil flows inside an automotive manual transmission were analyzed using this method, and the flow characteristics were compared with those in imagery from visibility experiments using an acrylic case. Evaluation was performed under three conditions of gear rotational velocity, set at vehicle speeds of 15 km/h, 30 km/h, and 60 km/h.

Figures 9 and 10 show comparisons of the results of analysis using CFD and oil flows confirmed by visibility experiment at each vehicle speed. The element that has an important influence on flows inside the transmission is the gear. The final driven gear, in particular, has a large external diameter, is located at the lowest position, and has the greatest influence on oil flows. Attention was therefore focused on this area. The characteristics by vehicle speed were, first of all, at 15 km/h, that oil in the vicinity of the gear was lifted only as high as the red

dotted line in Fig. 11. When the speed rises to 30 km/h, it is apparent that the oil that is lifted as high as the top of the gear passes through the channels placed in the case interior walls and is supplied to the bearings at both ends that support the final driven gear. At 60 km/h, a larger amount of oil is transported by agitation, and there is an increase in the drops that are visible where they are thrown to the top of the housing and in oil adhering to the wall surface.

The characteristics of the flows described above are also similarly found in the analysis results. This method does capture the changes in fluidity that accompany changes in vehicle speed.

When the conditions of flow are confirmed from a different viewpoint, the experiment results and the analysis results both confirm that the amount of oil adhering to the wall surface increases as the vehicle speed increases.

It is apparent from the above results that this method accurately reproduces oil flow experiment results and that it will be effective in investigating oil flows at the design stage.

Taking the analysis at 30 km/h as an example for calculation time, the time taken by analysis to reach the quasistationary state at 3.0 sec was 3.57 days (performing calculations in parallel using 12 CPUs). This achieved a time approximately 1/7 that taken for an equivalent analysis performed using a conventional technique (Fig. 12). This is a practical calculation time for predicting lubrication performance at the design stage.

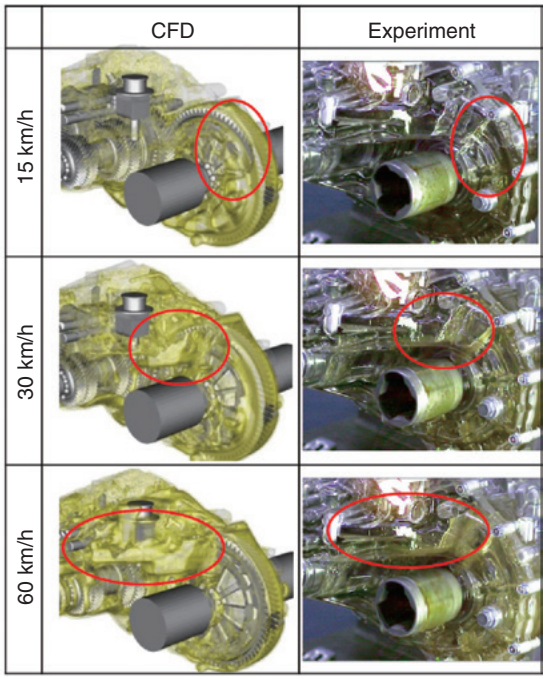


Fig. 9 Comparison of oil trajectory between CFD and experiment: rear view

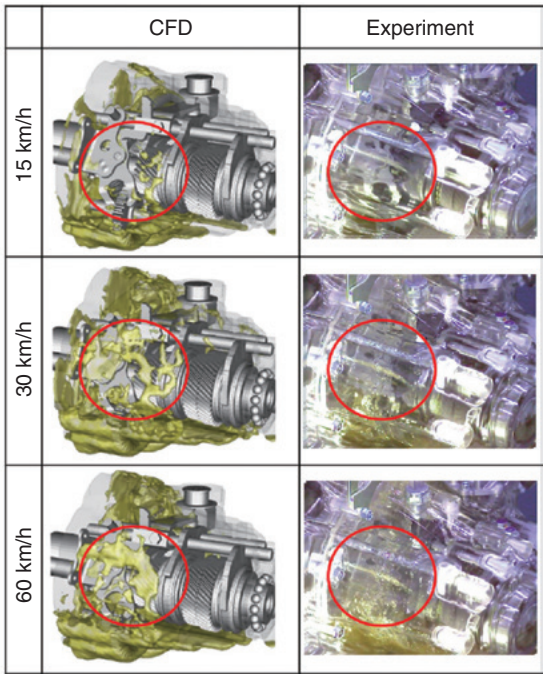


Fig. 10 Comparison of oil trajectory between CFD and experiment: front view

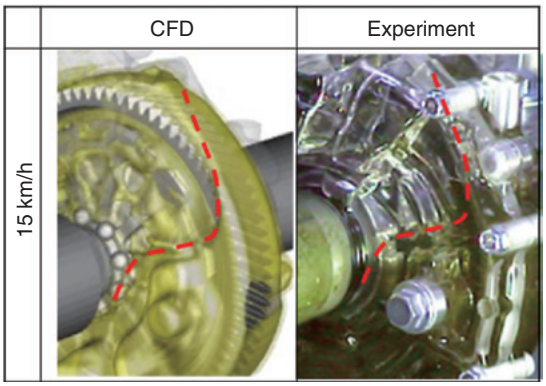


Fig. 11 Comparison of oil trajectory between CFD and experiment: detailed view at 15 km/h

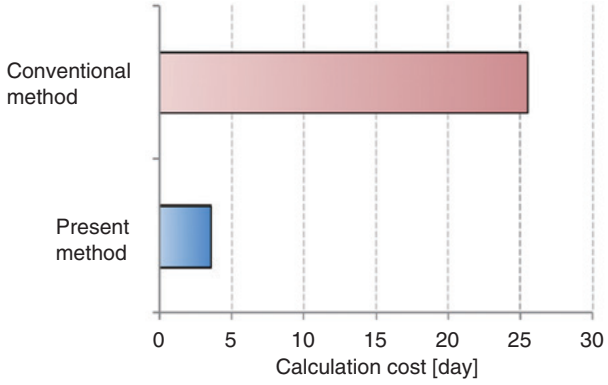


Fig. 12 Comparison of calculation cost between conventional method and present method

6. Conclusion

A technique was created for rapidly and accurately predicting oil flow within a transmission.

This technique is premised on the use of meshes in calculation domains to enable consideration of air entrainment and negative pressure, and it uses the finite difference method as a discretization method. For shapes of bodies and status of movement, it takes the approach of incorporating information in cells. This enabled the gear rotation and gear engagement portions that shape oil flows to be handled more readily and also reduced the calculation cost. In order to capture the behavior of fluid surfaces accurately, this approach uses the VOF method, while for its turbulence model it adopts LES. This enhanced its accuracy.

This technique was applied to oil flows inside an automotive manual transmission, and it was able to achieve prediction results for lubrication performance that have a close correlation with actual transmissions. The technique was also able to shorten calculation time to the point where results could be obtained in a practical length of calculation time at the design investigation stage.

References

(1) Li, L., Versteeg, H., Hargrave, G., Potter, T., Halse, C.: Numerical Investigation on Fluid Flow of Gear Lubrication, SAE Int. J. Fuels Lubr., Vol. 1, Issue 1, p. 1056-1062, (2009)
(2) Moshammer, T., Mayr, F., Kargl, K., Honeger, C.: Simulation of Oil Flow in Gear Box Housing, SAE Technical Paper, 2006-01-1574, (2006)
(3) Muto, K., Sakai, I., Ozaki, N.: Prediction of the Fluid Resistance in Stirred Fluid Using Particle Method, JSAE Annual Congress (Spring), 352-20095482, (2009)
(4) Hirt, C. W., Sicilian, J. M.: A Porosity Technique for the Definition of Obstacles in Rectangular Cell Meshes, International Conference on Numerical Ship Hydrodynamics, 4th, p. 450-468, (1985)
(5) Hirt, C. W., Nichols, B. D.: Volume of Fluid (VOF) Method for the Dynamics of Free Boundaries, Journal of Computational Physics, Vol. 39, p.201-225, (1981)
(6) Derksen, J., Van den Akker, H. E. A.: Large Eddy Simulations on the Flow Driven by a Rushton Turbine, AIChE Journal, Vol. 45, No, 2, p.209-221, (1999)
(7) Visualization Society of Japan: PIV Handbook, 328p, Morikita Publishing Co., Ltd. , (2002)
(8) Nishino, K.: Fukuzatsu Ranryu no Zenba Keisoku - Ranryu Moderu Keisan tono Hikaku ni Mukete -, Saikin no Kagaku Kougaku 57 [Ryushi / Ryutai Kaiseki, Suuchi Shimyureeshon no Tenbou to Jissen Jirei] Kagaku Kogakkai Hen, p.24-36, (2007) (in Japanese)

■ Author ■



Daiki SAEGUSA



Shinji KAWAI

Study of Seal Structure of High-differential-pressure Water Electrolysis Cell

Nobuyuki KAWASAKI* Eiji HARYU* Hiroyuki ISHIKAWA*
Koji NAKAZAWA* Masanori OKABE*

ABSTRACT

A study was conducted of a method of realizing airtightness for high-pressure hydrogen in an electrolysis cell using high differential pressure water electrolysis, a high-pressure (35 MPa) hydrogen production technology. When conducting high differential pressure water electrolysis in an electrolysis cell using a proton exchange membrane, the maintenance of airtightness against high-pressure hydrogen via the membrane, an elastic part, represents an issue. To resolve this issue, the effect of the use conditions of the membrane on changes in the thickness of the membrane was studied. The results indicated that it was necessary to set the holding loads in the cells so as to help ensure that the surface pressure of the membranes maintaining airtightness around the cathode space was greater than the pressure of the high-pressure hydrogen, and to select the hardness of the seal parts with consideration of the gaps occurring due to the state of wetness or dryness of the membrane. Evaluation of the durability of a high differential pressure water electrolysis stack applying the findings of this study verified that airtightness was maintained over the long term.

1. Introduction

Using hydrogen as fuel and emitting only water, the fuel cell electric vehicle represents the ultimate clean car. The provision of infrastructure for the supply of the hydrogen used as fuel by fuel cell electric vehicles is an important factor in promoting their more widespread use. As one means of supplying hydrogen, Honda has proposed the Solar Hydrogen Station (SHS), at which fuel cell electric vehicles can be filled with hydrogen produced by water electrolysis using electricity generated by solar cells.

In the initial phase of its development, the SHS stored the hydrogen produced by water electrolysis under pressure for supply to vehicle hydrogen tanks, using a mechanical compressor. However, this method presented the issue that the power consumed by the mechanical compressor reduced operating efficiency[1), (2)].

The development of a high differential pressure water electrolysis technology that pressurizes hydrogen at the same time as electrolyzing water increased system efficiency by 25% and reduced volume by 60% against the system using the mechanical compressor[(3)]. The SHS2, a second-generation hydrogen station using this technology, has been demonstrated in Japan and U.S.[(4)].

The characteristics demanded of the electrolytic unit used in this high differential pressure water electrolysis can be classified into electrolysis performance, ability of sustaining differential pressure, and airtightness performance. Of these, the results of tests concerning electrolysis performance and ability of sustaining differential pressure have already been reported[(5)]. With regard to airtightness performance, the system uses a combination of elastic parts, a proton exchange membrane (PEM) and O-rings, in order to realize a structure that seals in high-pressure hydrogen. This is the same airtight structure that is standard for fuel cells that have an internal pressure close to atmospheric pressure, and for water electrolysis at atmospheric pressure. However, the thickness of the PEM varies in response to pressure on the membrane or the state of wetness or dryness of the membrane. This property represents an issue for the seal structure in high differential pressure water electrolysis. It is therefore necessary for the O-rings, one of the seal parts, to maintain the seal even in conditions under which the thickness of the PEM changes.

In response to this issue, this paper will discuss research that measured the changes in the thickness of the PEM under moist, high-pressure conditions to clarify its behavior in an actual operating environment, and that studied the conditions necessary for the holding loads in the cells and the O-ring sealing parts. The ability of a stack manufactured with consideration of the results of these studies to maintain airtightness was verified in durability tests.

* Automobile R&D Center

2. Characteristics of High Differential Pressure Water Electrolysis

2.1. Structure of High Differential Pressure Water Electrolysis Cell

2.1.1. Basic principle and airtight structure

The basic principle of high-pressure water electrolysis is electrolysis of water using a PEM. If the flow of hydrogen, the product of the electrolysis, in the downstream direction is controlled, pressure will increase as the volume of hydrogen produced increases. By comparison with equal pressure systems, in which pressure increases simultaneously at both the cathode and the anode, differential pressure systems increase pressure only at the cathode, making it possible to reduce the size of the unit. A differential pressure system was therefore adopted in the present research. Figure 1 shows a schematic diagram of a high differential pressure water electrolysis cell.

In this cell, the PEM does not simply separate the cathode space and the anode space, but together with the O-ring seals in the outer circumference of the electrolysis section, also plays a role as a part that maintains the airtightness of the water electrolysis cell. This high differential pressure water electrolysis cell structure has the same structure as a normal atmospheric pressure water electrolysis cell using a PEM, but a higher holding load is employed in order to seal in the high-pressure hydrogen.

2.1.2. Electrode holding structure

It is necessary for the holding force pushing on the electrodes in the electrolysis cell to be greater than the repulsion force due to internal pressure. As an example, if the surface area of the bottom of the cathode space is assumed to be 100 cm^2, at a hydrogen pressure of 35 MPa, the repulsion force is 350 kN. There are two methods of generating this holding force: A method that uses the elasticity of metal in the form of the axial force of springs or bolts [Fig. 2(a)], and a method using a piston [Fig. 2(b)], in which the piston is pushed down by the high-pressure hydrogen produced by water electrolysis to provide the holding force. Elastic parts are also employed in the cylinder in the piston method in order to help ensure the necessary holding force at atmospheric pressure and the contact surface pressure at the electrolytic surfaces necessary for electrolysis to occur[5]. In the method shown in Fig. 2(a), when the pressure of the product hydrogen increases, the force holding the electrodes declines as a result of the repulsion force produced by internal pressure. This makes it necessary to initially set an excessive holding load. By contrast, in the method shown in Fig. 2(b), which uses a piston, the holding force increases in proportion with internal pressure, and it is therefore possible to set the minimum necessary initial load. Figure 3 shows the holding power in relation to internal pressure and the changes in the surface pressure of the seal section of the PEM sandwiched between the anode and cathode parts. As Fig. 3(a) shows, in order to maintain a specified PEM surface pressure when the hydrogen is under high pressure, the surface pressure of the PEM is high from the stage of low hydrogen pressure. Because of this, the PEM undergoes a high degree of static deformation, and because the load produced by the elastic parts declines, it is necessary to set the initial load at an even higher level. Imparting this type

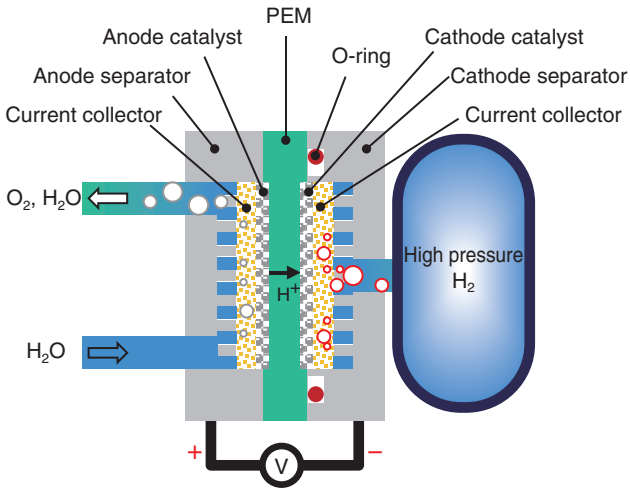
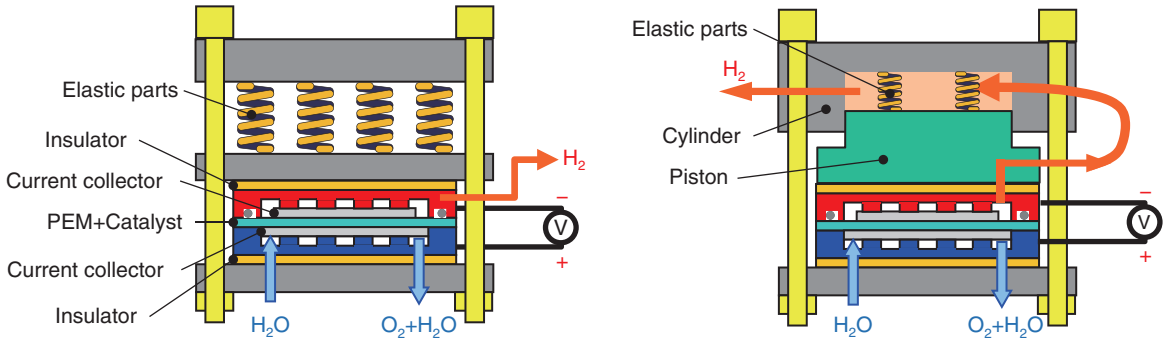


Fig. 1 Schematic of high-differential-pressure water electrolysis cell



(a) Holding structure using elastic parts (b) Holding structure using piston

Fig. 2 Holding structure of electrolysis cell

of load necessitates the use of large springs as the elastic parts, increasing the size of the unit. By contrast, in the system shown in Fig. 3(b), the surface pressure of the PEM is appropriate irrespective of the hydrogen pressure. For this reason, the present research employed the piston method, as shown in Fig. 3(b).

2.2. Study of Airtightness

In the structure of the high differential pressure water electrolysis cell, the PEM, together with the O-rings, fulfills the role of maintaining airtightness. O-rings are normally used as seals between solid, non-deformable parts. In this structure, however, because the PEM with which the O-rings make contact deforms under loads, the characteristics of the PEM affect airtightness. The fluorine-based PEM used in the present development has a comparatively low elastic modulus, and therefore deforms easily, and its swelling ratio when it absorbs water is also high. In order to maintain airtightness, it is therefore necessary to study the appropriate load settings and evaluate changes in the thickness of the PEM in response to load and conditions of wetness and dryness.

2.2.1. Study of holding load in cell

In order to impart the optimum surface pressure to the PEM in both the electrolysis section and the seal section of the electrolysis cell, it is essential to set the optimum diameter for the piston that generates the holding load. The load generated by internal pressure is determined by the pressurized area of the piston. If the diameter is large, the piston will be capable of generating a large load, but this would increase the size of the unit and might result in excessive increase in the surface pressure of the PEM. Because of this, it is necessary to set the appropriate load with the aim of realizing the minimum necessary size.

The holding load on the piston is expressed by Eq. (1).

$$F_{pis} = S_{pis} \cdot P_H + F_{sp} \quad (1)$$

F_{pis} : Piston holding load (N)
S_{pis} : Piston pressurized area (mm^2)
P_H : Hydrogen pressure (MPa)
F_{sp} : Load generated by elastic parts in cylinder (N)

The necessary surface pressure for electrolysis to occur in the electrolysis section is 5 MPa, as determined from contact resistance and membrane resistance[5]. This surface pressure is imparted to the entire range of the effective surface area of the PEM based on the setting of F_{sp}, without consideration of the hydrogen pressure.

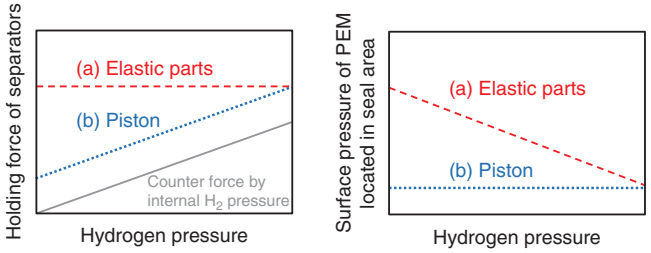


Fig. 3 Comparison of holding force of separators and surface pressure of PEM located in seal area

2.2.2. Study of specifications of seal parts

Standard criteria for the selection of O-rings as seals are provided by JIS[6], but because the O-rings will be in contact with PEM in the case of the high differential pressure water electrolysis configuration, a special selection criterion is necessary. This is the gap produced by the change in the thickness of the membrane due to the amount of expansion that occurs when there is a difference in the state of wetness and dryness of the PEM in the seal section. Figure 4 shows channels for the flow of hydrogen in the exterior of the electrolysis section when the cells are layered. These are areas in which it is assumed that extrusion of the O-rings. The seals on these channels are also formed by the PEM and O-rings. In these areas, the PEM swells at the inner sides of the O-rings due to the water content of the product hydrogen. However, at the outer sides of the O-rings, the PEM is exposed to the air and is therefore dry, resulting in the occurrence of gaps in the outer sides of the O-rings due to differences in membrane thickness, as shown in Fig. 5. It is therefore necessary to select the O-rings used in these areas with consideration of these gaps.

With regard to the twin issues of setting the holding load in the cells and responding to the gaps that form in the O-rings, the change in the state of the PEM under high pressure – a phenomenon unique to high differential pressure water electrolysis – is a factor in the settings for the seal structure. The clarification of the changes in the

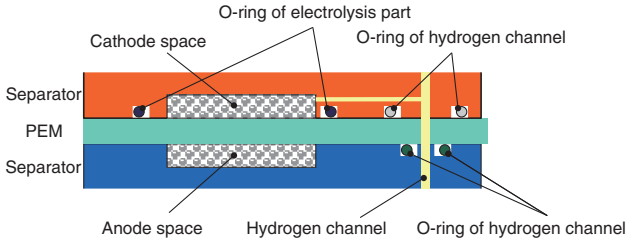


Fig. 4 Schematic of hydrogen channel designed on outside of electrolysis part

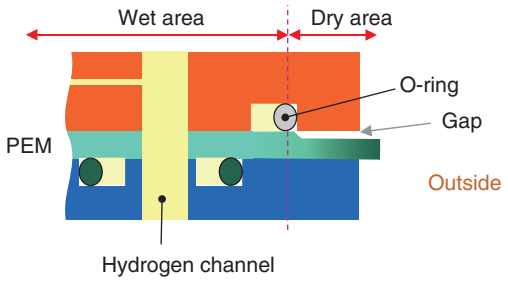


Fig. 5 Generation of gap by dryness of PEM of seal area

thickness of the PEM membrane under actual operating conditions helped to resolve these issues. The airtightness of a stack in which the outcomes of these studies were applied was verified in long-term durability tests.

3. Test Methods

3.1. PEM Compression Characteristic Test

Compression tests were conducted to study the thickness change characteristic of the PEM under moist, high-pressure conditions. The sample PEM was immersed in water prior to the test and allowed to swell until saturation. It was then pressed using an indenter of a specified surface area, and displacement and load were measured. The strain characteristic of the device was measured in advance, and the measured values were corrected on this basis. The atmosphere for the measurements was based on conditions for electrolysis; the temperature range was 35˚ to 80˚C, and the humidity was set at 95% RH in order to maintain the moist state of the PEM. Pressure was applied repeatedly to the sample, and it was immersed in 25˚C water in order to rehydrate, following which the amount of displacement in the membrane was measured.

3.2. Electrolysis Test using Piston-type High Pressure Water Electrolysis Cell

Figures 6(a) and 6(b) show schematic diagrams of electrolysis cells. To verify the optimum setting of piston load, changes in the PEM were studied based on behavior during electrolysis for pistons with two different pressurized areas (S_{pis}): In (a), S_{pis} is equal to the surface area of the bottom of the cathode space, S_H, the minimum setting; while in (b), S_{pis} corresponds to S_H plus S_{seal}, the surface area of the seal section.

The basic structure of the electrolysis cell was the same as that of an atmospheric-pressure cell, and the body of the cell was constructed of a titanium alloy. The spring load inside the piston was set to produce the 5 MPa surface pressure necessary for electrolysis under high pressure. The stiffness of the supporting column connecting the upper cylinder and the bottom section was set to help ensure that the deformation produced by the repulsion force generated by the product hydrogen did not affect the spring load inside the piston. A fluorine-based electrolytic membrane was used for the PEM, and a Ru-Ir-Fe complex oxide catalyst was used at the anode and a platinum black catalyst was used at the cathode. Sintered metal current collectors were used at both electrodes.

Electrolysis voltage, E_{we}, during high differential pressure water electrolysis was used as the indicator in evaluating electrolysis performance. This parameter is found using Eq. (2)[7].

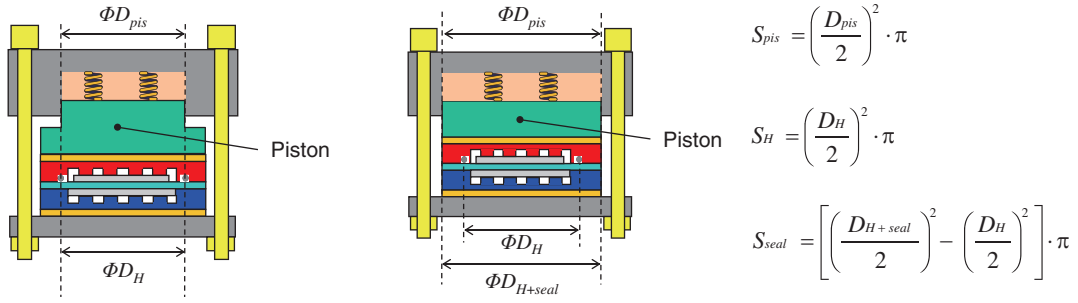
$$E_{WE} = E_0 + \frac{RT}{2F} \ln \frac{P_1}{P_2} + ir \qquad (2)$$

E_0 : Theoretical operating voltage (V)
T : Absolute temperature (K)
R : Gas constant (J/mol · K)
P_1 : High-pressure side hydrogen partial pressure (MPa)
P_2 : Low-pressure side hydrogen partial pressure (MPa)
ir : DC resistance voltage (V)
F : Faraday constant (C/mol)

The second term in the equation corresponds to the potential arising from the difference in hydrogen concentration in a gas concentration cell.

3.3. Durability Tests of Stack Structure

The high differential pressure water electrolysis stack was subjected to durability operation using the test apparatus shown in Fig. 7 in order to verify its durability. The stack was put through continuous high differential pressure electrolysis, and was operated with repeated pressure increase and decrease: Pressure was increased, maintained at 35MPa, and decreased to atmospheric pressure. Current efficiency, calculated from the flow rate of the hydrogen produced by the stack, can be used as a numerical indicator of seal performance. Current efficiency is calculated using Eq. (3). This parameter was calculated based on measurements of the amount of hydrogen produced per hour by high differential pressure electrolysis, taken using a gas meter.



(a) Piston area is equal to base area of cathode space

(b) Piston area is equal to sum of base area of cathode space and seal partial area

Fig. 6 Structure of piston type high-differential-pressure water electrolysis cells

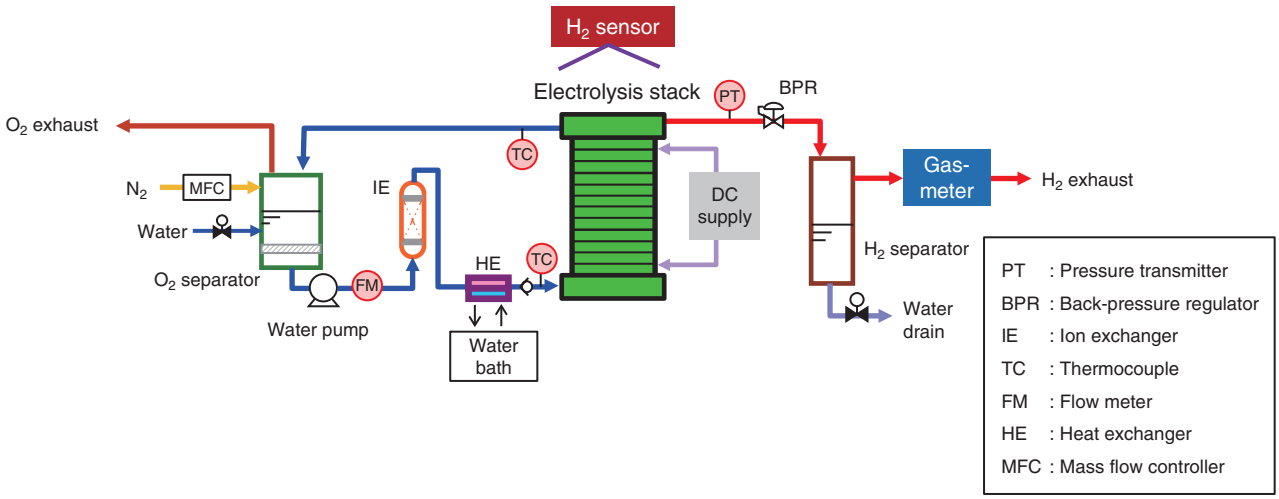


Fig. 7 Evaluation system of electrolysis stack

$$\eta_A = Q \cdot \left(\frac{I_{WE} \cdot 3600}{F} \cdot \frac{1}{2} \right)^{-1} \times 100 \qquad (3)$$

η_A : Current efficiency (%)
Q : Amount of hydrogen produced (mol/hr)
I_{WE} : Electrolysis current (A)

A hydrogen sensor was positioned close to the stack, and verified that there were no leaks of hydrogen to the exterior.

4. Results and Considerations

4.1. Setting Cell Holding Load

4.1.1. PEM compression characteristic

When the PEM employed in the high differential pressure water electrolysis cell is compressed under high pressure, its thickness declines. This is due to the compression of the base material and the expulsion under high pressure of the water that has swollen the membrane due to the constant presence of water as an electrolyte at the anode. Figure 8 shows the results of measurements of the rate of decline in thickness in response to the application of surface pressure to the PEM under moist conditions, taken using a compression tester. The degree of displacement changes significantly at close to 5 MPa, irrespective of the measurement temperature, and increases as surface pressure increases.

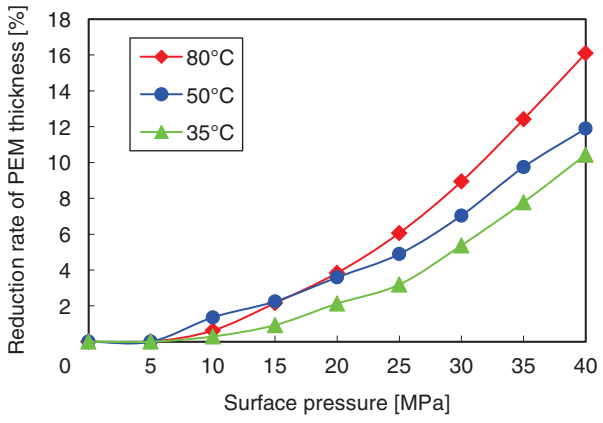


Fig. 8 Reduction rate of PEM thickness to surface pressure

4.1.2. Evaluation using electrolysis cells

Figure 9 shows changes in cell voltage against the pressure of the hydrogen produced in electrolysis tests of the electrolysis cells shown in Fig. 6. In the results shown as (a), for the cell with a piston pressurized area corresponding to the area of the bottom of the cathode space, cell voltage increases rapidly from close to 15 MPa; in the results shown as (b), for the cell with a piston pressurized area corresponding to the area of the piston in (a) plus the surface area of the seal section, the cell voltage almost conforms to the electrolysis voltage calculated using Eq. (2). The increase in cell voltage shown in (a) is due to a decline in the contact surface pressure between the current collector and the catalyst at the electrolysis surface[5].

The factors behind this decline in surface pressure will

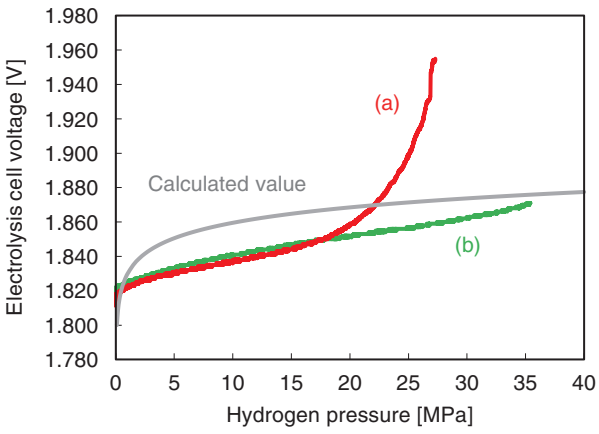


Fig. 9 Comparison of electrolysis cell voltage change

be considered from the perspective of the surface pressure of the section of the PEM acting as a seal on the external circumference, designated P_{seal}. P_{seal} is expressed by Eq. (4), using the piston load found by means of Eq. (1), the repulsion force generated by the high-pressure hydrogen, and the surface area of the seal.

$$P_{seal} = (S_{pis} \cdot P_H + F_{sp} - S_H \cdot P_H) / S_{seal} \quad (4)$$

In the results shown as (a) in Fig. 9, $S_{pis}=S_H$, and Eq. (4) therefore becomes Eq. (5), with P_{seal} becoming constant at 5 MPa due to the setting of F_{sp}.

$$P_{seal} = F_{sp} / S_{seal} = 5 \text{ [MPa]} \quad (5)$$

Because $S_{pis} = S_H + S_{seal}$ in the result shown as (b) in Fig. 9, Eq. (4) becomes Eq. (6), with Pseal varying as a linear function of hydrogen pressure.

$$P_{seal} = (S_{seal} \cdot P_H + F_{sp}) / S_{seal} = P_H + 5 \text{ [MPa]} \quad (6)$$

Figure 10 shows the surface pressure of the PEM in the cathode space, including the electrolysis section, and the seal section at the outer circumference for configuration (a) and configuration (b) in Fig. 9. In configuration (a), the difference in pressure between the cathode space and the seal section increases with increasing internal pressure. When this occurs, the thickness of the membrane in the cathode space including the electrolysis section declines in comparison to the thickness of the membrane in the surrounding seal sections, as shown schematically in Fig. 11. The reduction of contact surface pressure on the electrolysis surface resulting from this produces an increase in cell voltage. This phenomenon does not occur in configuration (b), because the surface pressure of the PEM in the seal section is set higher than the surface pressure of the PEM in the cathode space.

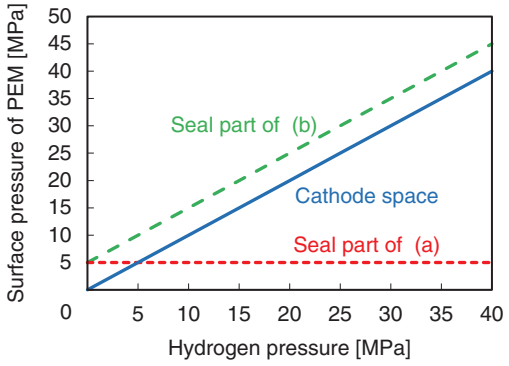


Fig. 10 Comparison of PEM surface pressure of cathode space and each seal part of (a) and (b)

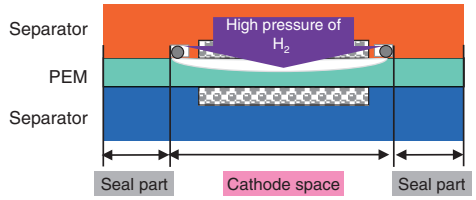


Fig. 11 Modification situation of PEM at time of high pressure in electrolysis cell (a)

This type of pressure difference produces O-ring deformation of the type shown in Fig. 12, which can act as a factor in reducing seal performance. This is because, when the PEM surface pressure on the exterior of the O-ring is lower than the hydrogen pressure in the cell, a force acts on the O-ring to push it towards the exterior.

Based on the considerations above, it can be seen to be necessary to set the piston load so as to help ensure that the surface pressure of the seal section of the PEM is greater than the pressure of the product hydrogen. In other words, it is necessary for the pressurized area of the piston, S_{pis}, to be greater than the sum of the surface area of the bottom of the cathode space, S_H, and the surface area of the seal section, S_{seal}.

4.2. Wetness and Dryness of PEM and Selection of Seal Parts

Section 4.1. discussed the reason for seeking to realize uniform compression deformation of the PEM in the high-pressure gas section and the surrounding seal sections. However, it is also necessary to select seal parts with consideration of the differences in membrane thickness occurring when there are differences in the state of wetness and dryness of the PEM.

Figure 13 shows the rate of change in the thickness of

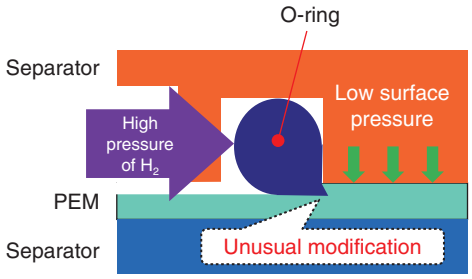


Fig. 12 Sectional view of seal portion

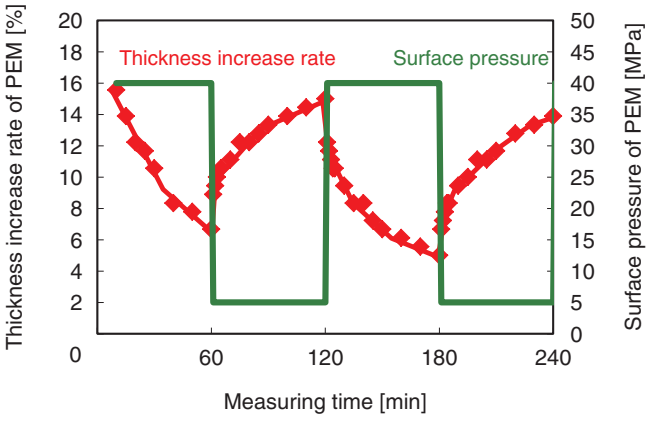


Fig. 13 Change of thickness increase rate of PEM to surface pressure change in humidification conditions

the membrane against a dry membrane when the surface pressure of the membrane is repeatedly alternated between the figure when electrolysis is not being conducted (5 MPa) and the figure when electrolysis is being conducted (40 MPa) under humid conditions. These results indicate that while the thickness of the membrane begins to decline simultaneously with the application of high pressure, because the speed of displacement is comparatively slow, specific conditions exist at the commencement of high-pressure operation under which the difference in thickness between the membrane when wet and when dry is at its maximum. Under these conditions, a maximum gap of 15% occurs in the membrane thickness. It is known that the maximum allowable gap is determined by the pressure on the O-rings and their hardness level. As allowable levels for planar seals at an internal pressure of 35 MPa, 20 μm is recommended for A80 seals and 55 μm for A90 seals[8]. For a membrane thickness of 100 μm, the gap would correspond to 15 μm, and an A80 seal could be used; for a membrane thickness of 200 μm, the gap would correspond to 30 μm, and it would be necessary to use an A90 seal.

4.3. Results of Durability Tests of Stack Structure

In order to obtain the necessary supply of hydrogen for the SHS2, it is necessary to layer the electrolysis cells to form a stack configuration. Based on the study of the characteristics of the PEM and the setting of the piston load and selection of the O-ring specifications described above, a stack of layered electrolysis cells was designed, and its durability was evaluated using the durability test set-up shown in Fig. 7. Because the volume of hydrogen measured will maintain a fixed value if airtightness is maintained during durability operation, measurement of changes in the volume of hydrogen flowing in the system can be used to judge whether an airtight structure has been realized in the high differential pressure water electrolysis stack.

Figure 14 shows current efficiency, an indicator of the volume of hydrogen produced, and hydrogen concentration as measured by a hydrogen sensor positioned close to the stack under conditions of 10000 hr of continuous electrolysis, with the pressure cycle electrolysis repeated 330 times. A loss of approximately 5% in current efficiency as the hydrogen passed through the PEM and passed the anode existed from the initial stages of operation, but this figure remained constant throughout the durability test; in addition, no hydrogen leaks were detected by the hydrogen sensor. These results demonstrate that the electrolysis cells maintain airtightness over the long term even when layered in a stack configuration.

5. Conclusion

A study of the airtightness of high differential pressure water electrolysis cells, a high-pressure (35 MPa) hydrogen production technology, produced the following results.

(1) The necessary holding load was obtained by using a piston, the cell holding structure, with a surface area greater than the sum of the surface areas of the bottom of the cathode space and the seal parts used in the outer circumference.

(2) Airtightness was maintained by setting the hardness of the O-rings with consideration of gaps occurring due to the state of wetness or dryness of the PEM.

Tests verified the long-term airtightness of a stack manufactured based on the findings of the study.

References

(1) Ueyama, M., Kita, M., Taguchi, S., Nakazawa, K., Nagaoka, H., Arakawa, S.: Introduction of Hydrogen Refueling Station with Photovoltaic Modules, Honda R&D Technical Review, Vol. 15, No. 2, p. 31-38

(2) Okabe, M., Nakazawa, K., Taruya, K., Handa K.: Verification Test of Solar-powered Hydrogen Station (SHS) with Photovoltaic Modules, Honda R&D Technical Review, Vol. 20, No. 1, p. 72-79

(3) Nakazawa, K., Nagaoka H., Takeuchi, J., Moburg, F., Yamashita, I., Okabe, M.: Introduction of High Differential Pressure Water Electrolysis-type Solar

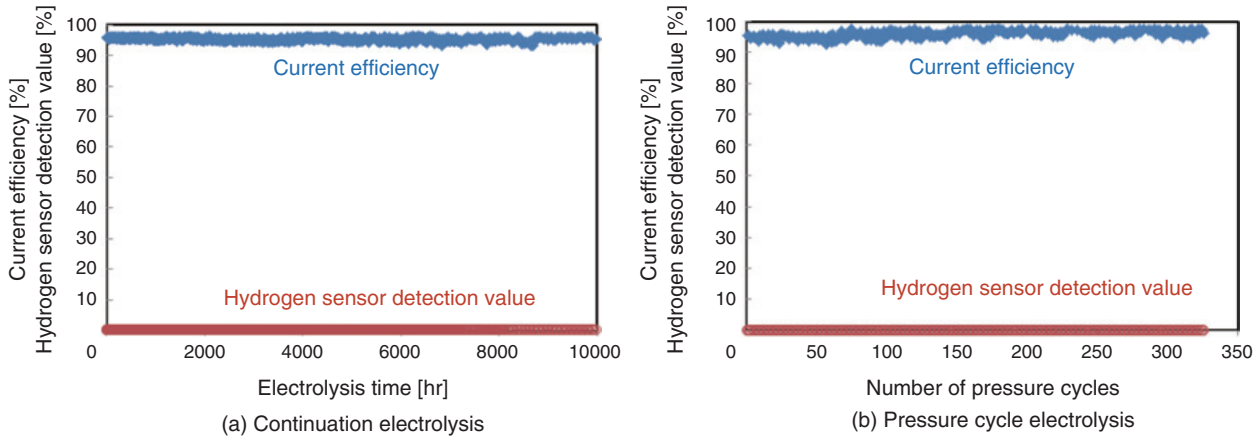


Fig. 14 Change of current efficiency and hydrogen sensor detection value at time of stack durable electrolysis

Hydrogen, Honda R&D Technical Review, Vol. 22, No. 2, p. 28-35
(4) Nagaoka, H., Yoshida, N., Cun, D., Yamashita, I., Okabe. M.: Verification Test of High Differential Pressure Water Electrolysis-type Solar Hydrogen Station (SHS2), Honda R&D Technical Review, Vol. 24, No. 2, p. 74-81
(5) Haryu, E., Nakazawa, K., Taruya, K., Ishikawa, H., Okabe, M.: Mechanical Structure and Performance Evaluation of High Differential Pressure Water Electrolysis Cell, Honda R&D Technical Review, Vol. 23, No. 2, p. 97-105
(6) JIS B2401: O-rings (2005)
(7) The Electrochemical Society of Japan: Electrochemical handbook, Vol. 5, p. 155 (2000)
(8) Japan Fluid Power Association (JFPA) standard: Guidelines for specification and selection of seals for hydraulic cylinders, JFPS 1003 (1999)

■ Author ■


Nobuyuki KAWASAKI


Eiji HARYU


Hiroyuki ISHIKAWA


Koji NAKAZAWA


Masanori OKABE

Development of Steel for High-strength Crankshaft by Precipitation Strengthening of Mn-nitride

Hiromasa TAKAHASHI* Hiroki MASUDA*
Shigefumi NISHITANI** Motoki TAKASUGA**

ABSTRACT

A high-strength gas soft-nitrided crankshaft steel that does not rely on the addition of rare metals has been developed. High strength is realized in Honda's conventional high-strength crankshaft steel through the addition of the rare metal molybdenum (Mo). By contrast, a high level of strength was achieved in the developed steel by making effective use of manganese (Mn), a universal component of steel, in the production process. High strength was realized by strengthening the ferrite phase using Mn content of 0.9 wt% or higher. It was determined that the strengthening mechanism was precipitation strengthening by means of Mn nitrides (η-Mn_3N_2) formed in the surface layer ferrite phase as a result of gas soft nitriding. Straightenability, a characteristic that is antagonistic to high strength, is also demanded from crankshaft steels following gas soft nitriding. This demand was responded to in the developed steel by increasing toughness through the reduction of carbon (C) content in order to increase the area ratio of the ferrite phase. The innovations described above have made it possible to reduce material costs by doing away with Mo while realizing an equivalent level of strength to the conventional high-strength steel. Strength has also been increased by 16% against crankshafts produced using the conventional standard steel, which contains no rare metals.

1. Introduction

Against the background of increasing demands from society for the realization of higher automotive fuel efficiency, automakers are pursuing the achievement of size and weight reductions in the crankshaft and other drivetrain parts in order to realize weight savings and reduce friction. A high level of fatigue strength is necessary in the crankshaft because it is constantly subject to repeated stress. A variety of mechanisms can be used to increase the strength of steel materials, including work hardening (dislocation strengthening), grain refinement strengthening, solid solution strengthening, and precipitation strengthening. Secondary strengthening methods used to elicit these strengthening mechanisms include induction hardening, roll processing, and gas soft nitriding (GSN)[(1)-(4)]. GSN is a method that increases hardness close to the surface of the material by diffusing nitrogen (N) from the surface to the inside. This method also makes it possible to increase the wear resistance of the sliding parts by means of the hard nitrogen compound layer (ε phase: $Fe_{2\text{-}3}N$; γ' phase: Fe_4N) that forms the surface. In many cases, rare metals such as Mo and vanadium (V) are added when GSN is used as a strengthening method[(5), (6)]. However, due to significant increases in the cost of rare metals and the instability of the procurement situation, manufacturers are today focusing attention on reducing rare metal content or eliminating the use of the metals altogether. For example, a method has been developed that makes it possible to achieve a high strength without adding rare metals by optimizing the copper (Cu) and chrome (Cr) content of the scrap using an electric furnace, promoting precipitation strengthening by means of the Cr and ferrite solid solution strengthening by means of the Cu[(7)]. The research discussed in this paper studied a method of achieving a high level of strength in steel produced in a blast furnace process without adding rare metals.

2. Development Goals

Following forging and machining, GSN is applied to Honda crankshafts for gasoline engines. Non-normalized steels, which eliminate the normalizing process following forging, are used as the crankshaft materials. Depending on the load levels of bending and twisting stress to which they will be subjected, standard steels and high-strength steels

* Automobile R&D Center
** Nippon Steel & Sumitomo Metal Corporation

used properly. Mo is added in order to realize a high level of strength in the high-strength material, and reducing the amount of this rare metal used therefore represents an issue. The present research studied a method of compensating for the decline in strength when Mo is not added by effectively using the basic elements composing the steel. At the same time, the crankshafts are prone to bending due to the heat stress produced during GSN, and bend reform is therefore performed in order to help ensure that the level of bending remains within specified limits. However, when the hardness of the surface increases following the application of GSN to increase strength, straightenability tends to decline. The present research therefore focused on the realization of a gas soft-nitrided steel for crankshaft use that could reconcile the antagonistic characteristics of high strength and straightenability without using rare metals by means of material design with the basic elements carbon (C) and Mn as a base.

In the development of the steel, material specifications were studied based on the following development aims:

(1) Equivalent level of fatigue strength to conventional high-strength steel
(2) Equivalent level of straightenability to conventional high-strength steel
(3) Equivalent cost to conventional standard steel

3. Concept of Material Composition Design

3.1. Concept of Strengthening of Microstructure

Non-normalized steels are employed in crankshafts to make it possible to rationalize the heat treatments used in the production process. The pinning effect of fine nitrides formed by the addition of nitrogen helps to control the coarsening of the microstructure during hot forging. The material displays a two-phase microstructure, with a hard pearlite microstructure and a soft ferrite phase. Figure 1 shows a standard microstructure and hardness profile for a non-normalized steel following GSN. GSN forms a hard compound layer at the surface of the material, and hardness of the nitrogen diffusion area is increased against the matrix.

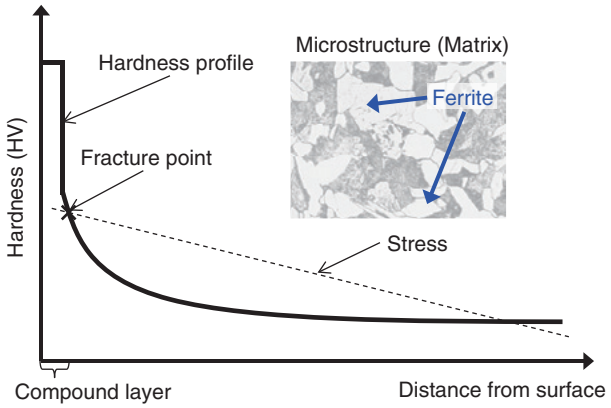


Fig. 1 Schematic of hardness profile after GSN

Controlling cracks is an important consideration in crankshafts, given the potential for fatigue failure resulting from repeated stress. Because cracks originate and develop in the ferrite phase directly below the compound layer when stress exceeds material strength, it is important to strengthen the ferrite phase in order to realize high strength.

The present research measured hardness at a depth of 50 μm from the surface layer using Vickers hardness tests in order to evaluate the effect of strengthening of the ferrite phase directly below the compound layer. This was defined as 50 μm depth hardness.

3.2. Study of Elements for the Realization of High Strength

The present development attempted to realize high strength through the effective use of basic elements in the steel as a substitute for the addition of rare metals. The basic elements present in steel are C, silicon (Si), Mn, sulfur (S), and phosphorous (P). Of these, Mn is known to be highly effective in strengthening the ferrite phase by means of solid solution strengthening. This strengthening mechanism occurs due to the fact that Mn atoms are a different size to Fe atoms, and when Mn exists in solid solution in Fe, it distorts the lattice arrangement of the Fe atoms, increasing deformation resistance. It was considered that the effective introduction of nitrogen by means of nitriding to a material with strain fields of this type would increase strength by further increasing deformation resistance.

It has also been reported that the fatigue strength of plasma-nitrided C-Mn alloys increases with an increasing additive amount of Mn, indicating the possibility that the mechanism of strengthening is precipitation strengthening due to nitrides[8].

In place of the conventional method of realizing high strength through the addition of Mo, the present research therefore sought to increase strength through nitrides, by means of increasing the additive amount of Mn, and studied the mechanism producing the effect.

3.3. Effect of Mn

The effect of the additive amount of Mn on fatigue strength was investigated as a preliminary study towards chemical composition design. Test specimens were produced by varying the additive amount of Mn between 0.5 wt% and 1.5 wt% in a 0.30-0.35 wt% carbon steel and applying GSN. Figure 2 shows the results of rotary bending tests. Fatigue strength increases with the addition of increasing amounts of Mn, and becomes equivalent to that of conventional high-strength steel at 0.9 wt% and above. This was therefore set as the necessary additive amount of Mn for the realization of high strength.

3.4. Concept of Realizing Straightenability

A method of increasing straightenability by controlling 50 μm depth hardness and increasing the area ratio of the ferrite phase has been reported[7]. Figure 3 shows the area

ratio of the ferrite phase, α, in a model alloy when the amount of C added is varied. The less C added the greater the increase in the ferrite phase. Chemical composition design in the present research sought to increase the area ratio of the ferrite by controlling the additive amount of C, a basic element, in order to help realize the target straightenability.

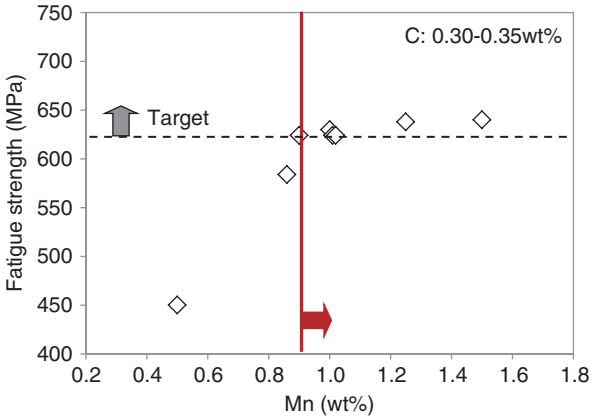
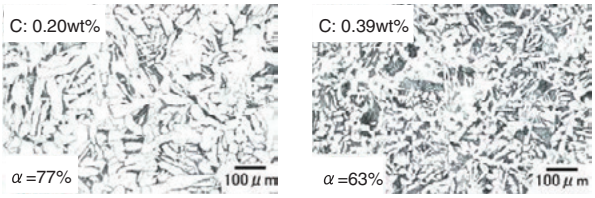


Fig. 2 Relationship between Mn and fatigue strength



(a) 0.20wt%C-0.03wt%Si-0.02wt%Mn (b) 0.39wt%C-0.02wt%Si-0.02wt%Mn

Fig. 3 Relationship between ferrite area ratio and C content

4. Chemical Composition Design

4.1. Setting Target Hardness

The range of 50 μm depth hardness following GSN to reconcile bending fatigue strength and straightenability was studied. Figure 4 shows the relationship between 50 μm depth hardness and bending fatigue strength. Fatigue strength standards were satisfied at hardness levels of 300 HV and above. Figure 5 shows the relationship between 50 μm depth hardness and straightenability. Straightenability standards were satisfied at 50 μm depth hardness of 360HV and below. The range of 50 μm depth hardness necessary to realize parts functions was therefore set at 300-360 HV.

4.2. Setting Components for Material under Development

In designing the chemical composition for the material under development, it was important to set a range for the components that would satisfy the 50 μm depth hardness set in Section 4.1. In doing so, it was necessary to establish an indicator, in consideration of the fact that the effect of each of the elements making up the steel differed. The equivalent amount of Mn (*Mneq*) was set as an indicator of the 50 μm depth hardness for the chemical composition of the material under development. *Mneq* is defined by Eq. (1). *Mneq* is obtained by converting the amount of the elements that have an effect on the 50 μm depth hardness following GSN into an amount of Mn, and is set using Mn, C, and Cr, which have a strong effect on hardness. Figure 6 shows the

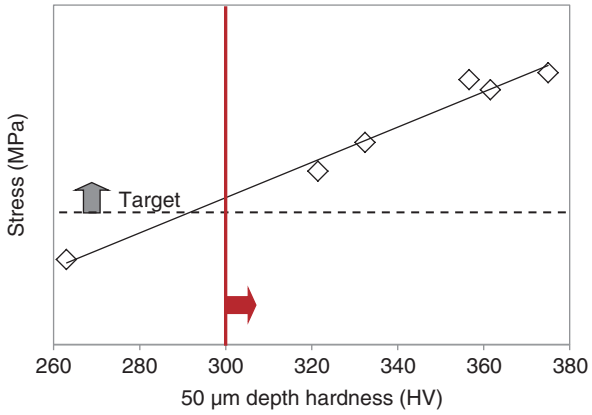


Fig. 4 Relationship between 50 μm depth hardness and bending fatigue strength

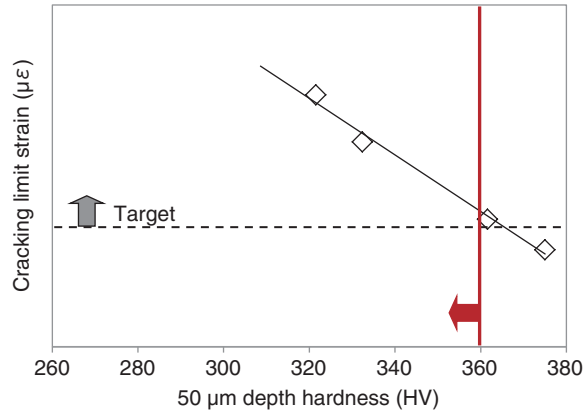


Fig. 5 Relationship between 50 μm depth hardness and cracking limit strain

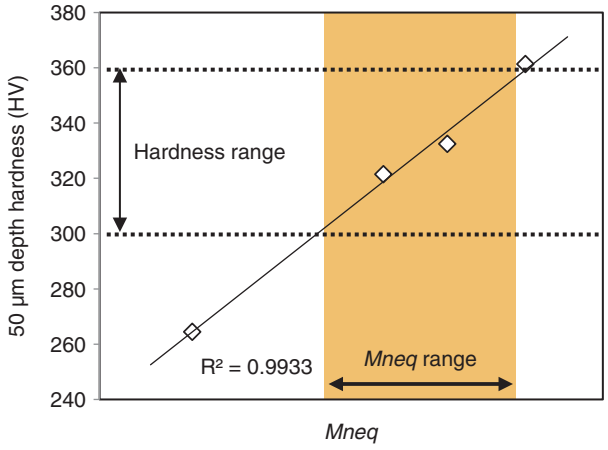


Fig. 6 Relationship between *Mneq* and 50 μm depth hardness

Table 1 Chemical composition of developed and conventional steel (wt%)

	C	Si	Mn	P	S	Cr	Mo
Developed high-strength steel	0.30	0.20	1.00	0.015	0.05	0.05	-
Conventional high-strength steel	0.37	0.20	0.82	0.015	0.07	0.05	0.16
Conventional standard steel	0.40	0.20	0.60	0.015	0.05	0.05	-

relationship between *Mneq* and the 50 µm depth hardness. As the figure shows, the 50 µm depth hardness increases proportionally with increase in *Mneq*, indicating the validity of the setting of *Mneq*. Using this relationship, a range for *Mneq* that would help to enable the realization of the target 50 µm depth hardness was set.

$$Mneq = \mathrm{Mn} + a1 \cdot \mathrm{C} + a2 \cdot \mathrm{Cr} \quad (1)$$

Mn, C, Cr: Amount of each element (wt%)
$a1$, $a2$: Constants

With the additive amount of Mn set in Section 3.3 (0.9 wt% and above) as a base, the chemical composition for the developed high-strength steel that would satisfy Eq. (1) was set. Table 1 shows representative chemical compositions.

The composition of the developed high-strength steel uses the composition of the conventional standard steel as a base, and eliminates the Mo content, increases the Mn content, and reduces the C content against the conventional high-strength steel. Because excessive reduction of the C content might result in a decline in wear resistance, C content was set at 0.3wt% for the developed high-strength steel.

5. Characteristics of Developed High-strength Steel

5.1. Material Characteristics

Figure 7 shows a cross-section of the microstructure close to the surface, Fig. 8 shows the nitrogen concentration profile, and Fig. 9 shows the hardness profile of the developed high-strength steel following gas soft nitriding. Figure 8 shows that the nitrogen concentration close to the surface of the developed high-strength steel is equivalent to that of the conventional high-strength steel. Figure 9 shows that the level of hardness of the inside of the developed high-strength steel is equivalent to that of the conventional standard steel, while gas soft nitriding has increased the surface hardness of the material to a level equivalent to that of the conventional high-strength steel. In other words, while the developed high-strength steel uses the same constituent elements as the conventional standard steel, it achieves a higher nitrogen concentration and a higher surface hardness. This is believed to be an effect of precipitation strengthening due to Mn nitrides formed as a result of the addition of an increased volume of Mn.

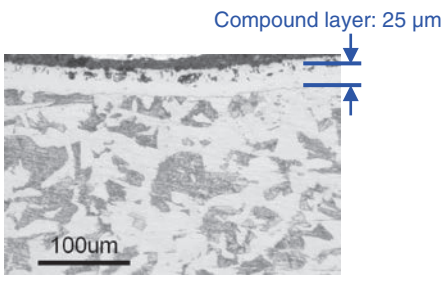


Fig. 7 Microstructure of developed steel after GSN

5.2. Characteristics of Crankshaft

A crankshaft for an inline 4-cylinder gasoline engine was produced using the developed high-strength steel, and the characteristics of the crankshaft in isolation were evaluated. Figure 10 compares the bending fatigue and straightenability of the developed steel with those of the conventional steels. The levels of these characteristics are shown as percentages, with the conventional high-strength steel as 100.

The fatigue strength of the developed high-strength steel is similar to that of the conventional high-strength steel, and 16% higher than that of the conventional standard steel. In terms of straightenability, while the developed high-strength steel falls behind the conventional standard steel, which has low surface hardness, its level is similar to that of the conventional high-strength steel.

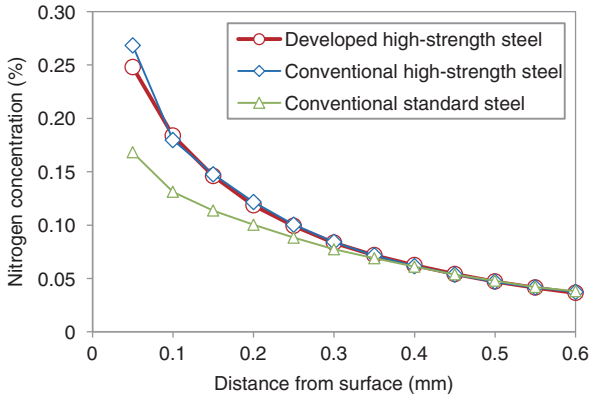


Fig. 8 Nitrogen concentration profile after GSN

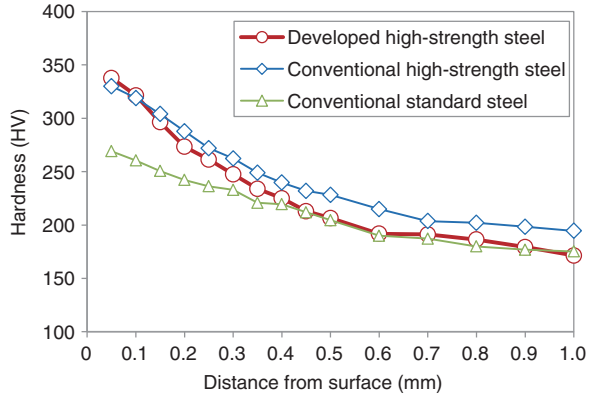
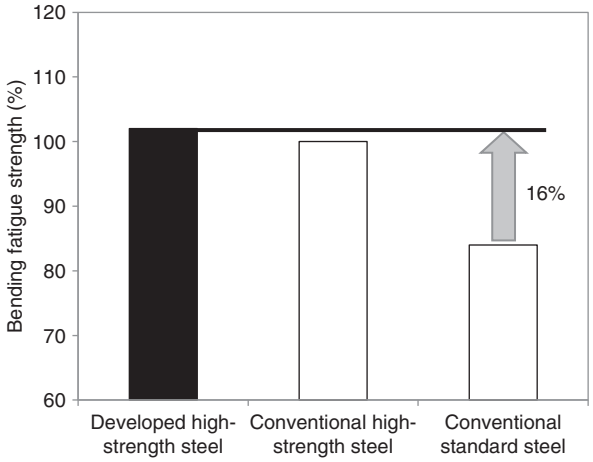
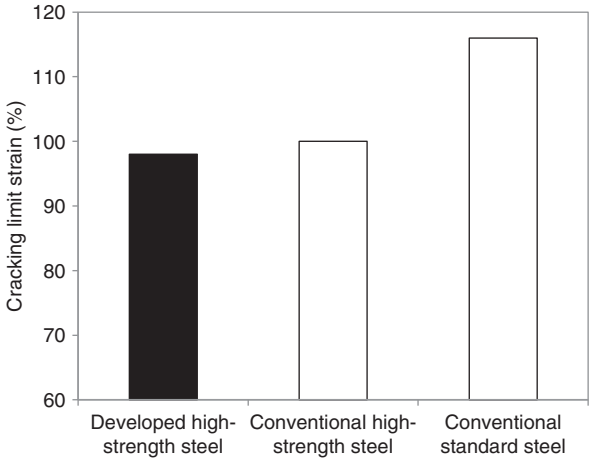


Fig. 9 Hardness profile after GSN



(a) Bending fatigue strength



(b) Cracking limit strain

Fig. 10 Crankshaft characteristic

Table 2 Chemical composition (wt%)

	C	Si	Mn	P	S
0.3C-0.5Mn	0.30	0.01	0.48	0.002	0.001
0.3C-1.0Mn	0.29	0.01	0.97	0.002	0.001
0.3C-1.5Mn	0.30	0.01	1.43	0.002	0.001
0.3C-2.0Mn	0.29	0.01	1.92	0.002	0.001

6. Analysis of High-Strengthening Mechanism

6.1. Test Specimen and Test Method

Model alloys of 0.3C-(0.5, 1.0, 1.5, 2.0)Mn were produced in order to clarify the high-strengthening mechanism via Mn (Fig. 11). Table 2 shows the chemical compositions of the model alloys used in the tests. The test materials were forged at 1250ºC to form round bars of ϕ50 mm, which were machined for use in rotary bending tests. Following GSN (using RX gas and NH_3 gas) at 600ºC for two hours, the test specimens were water-quenched. The microstructures of these test specimens were observed, and measurements of nitrogen concentration and hardness were conducted.

6.2. Effect of Mn on Material Characteristics

6.2.1. Effect of Mn on microstructure

Figure 12 shows photographs of cross-sectional microstructures of the model alloys close to the surface. Increasing the amount of Mn added increases the area ratio of the pearlite microstructure (the black regions in the photographs). The pearlite microstructure increases in proportion with increasing Mn content, and it is thought that hardness increases as a result, but in order to realize high strength it is necessary to increase the strength of the soft ferrite phase.

6.2.2. Effect of Mn on N concentration

Figure 13 shows the Mn content and nitrogen concentration of the test materials following GSN. The nitrogen concentration near the surface increases with increasing Mn content. It is believed that Mn effectively contributes to the diffusion of nitrogen in the inside of the material.

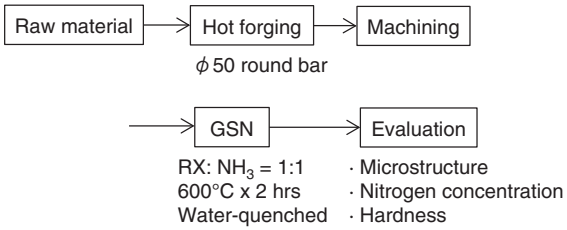


Fig. 11 Method of specimen preparation and property evaluation

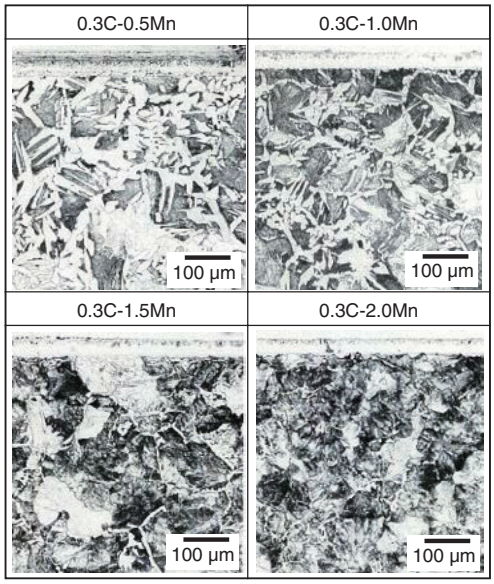


Fig. 12 Microstructure after GSN

6.2.3. Effect of Mn on hardness

Figure 14 shows measurement results for the 50 μm depth hardness following GSN. Hardness was measured by means of Vickers hardness tests using a 300 g indentation load. Vickers hardness increases with increasing Mn content. It is considered possible that this result originates in the hard pearlite microstructure, which increases as the Mn content increases. In order to study the effect of Mn on increasing the hardness of the soft ferrite phase, the hardness of the ferrite phase was measured by reducing the indentation load to 50 g and localizing the measurement area. The hardness of the ferrite phase increased with increasing Mn content. It is conjectured that the increase in fatigue strength with increased Mn content shown in Fig. 2 originates in an increase in the hardness of the ferrite phase.

6.3. Identification of Precipitates in Ferrite

The fine structure of the ferrite phase was observed using field emission-type transmission electron microscopy (FE-TEM) in order to study the strengthening mechanism by Mn. The 0.3C-1.0Mn material, having the same amount of C and Mn as was set in Section 4.2, was selected as the chemical composition for FE-TEM observation to clarify the strengthening mechanism. The test specimen was cut from the surface to the 50 μm depth hardness to allow observation of the ferrite phase directly below the compound layer. Figure 15(a) shows a bright-field image of the ferrite phase following GSN, while Fig. 15(b) shows the results of an element mapping analysis using scanning TEM energy-dispersive X-ray spectroscopy (STEM-EDS). Figure 15(b) shows that Mn is concentrated at the points at which nano-order acicular precipitates were observed in Fig. 15(a), indicating the formation of Mn precipitates. This demonstrates that precipitates are formed by the basic element Mn.

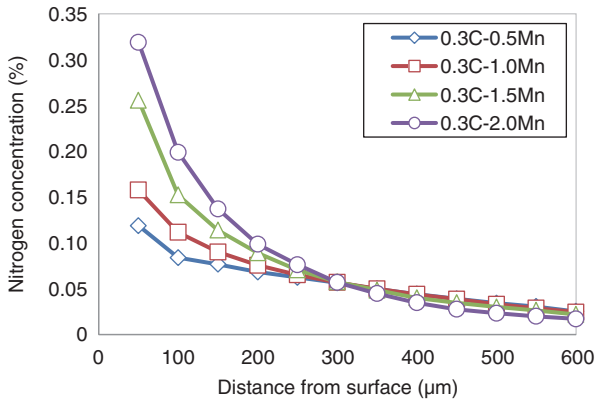


Fig. 13 Nitrogen concentration after GSN

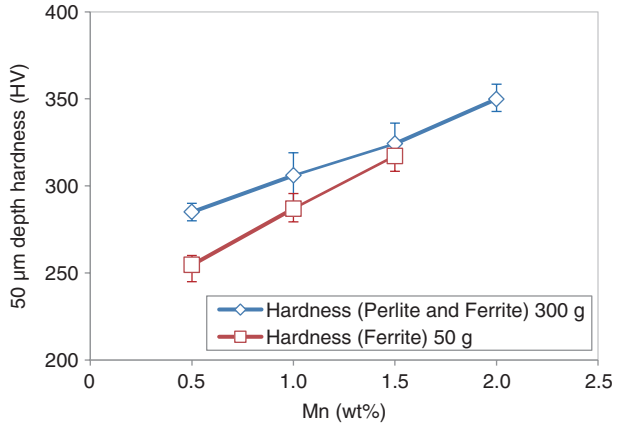


Fig. 14 50 μm depth hardness after GSN

6.4. Strengthening Mechanism by Precipitates

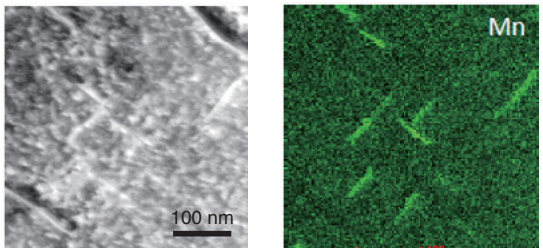
6.4.1. Precipitate structure

The structure of the precipitates shown in Fig. 15 was subjected to a detailed analysis. Figure 16 shows a TEM image and an electron diffraction pattern for the 0.3C-1.0Mn steel. In Fig. 16(a), precipitates ranging in length from 10 nm to 50 nm in a mutually orthogonal relationship can be seen in the field of observation. The diffraction pattern in Fig. 16(b) shows spot groups of iron, and groups of streak-shaped spots extending from the precipitates. Because the lattice formed by the precipitate spots displays a good correlation with the η-Mn_3N_2 crystal zone axis $[1\bar{1}0]_\eta$, the precipitates were identified as η-Mn_3N_2.

Figure 17 shows schematics of the mother phase Fe (α-Fe) and η-Mn_3N_2 unit cells. α-Fe is a cubic crystal with lattice constants of a=b=c=2.87Å. η-Mn_3N_2 is a tetragonal crystal with lattice constants of a=b=4.20Å and c=12.03Å.

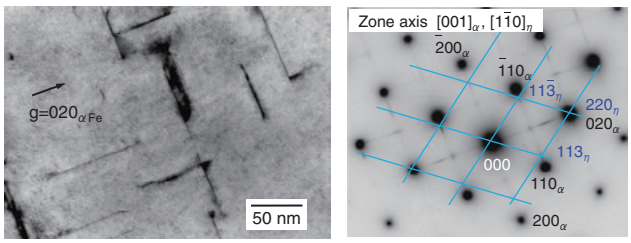
6.4.2. Precipitate morphology

The crystal zone axis shown in Fig. 16(b) is $[001]_\alpha$// $[1\bar{1}0]_\eta$, and the relationship $[020]_\alpha$//$[220]_\eta$ can be obtained



(a) STEM image (b) Elemental mapping of Mn

Fig. 15 STEM-EDS micrograph



(a) TEM image (b) Diffraction pattern

Fig. 16 Structure analysis of precipitation

from the diffraction pattern. In other words, Fe and η-Mn_3N_2 have a Baker-Nutting orientation relationship (B-N relationship). Figure 18 shows a schematic of the precipitate interfaces in the B-N orientation relationship. Figure 18(a) shows α-Fe on (001), while Fig. 18(b) shows η-Mn_3N_2 on (001). The precipitation morphology shown in Fig. 18(c) is a 45° rotation of the η-Mn_3N_2 on (001) with $[001]_\alpha$ and $[001]_\eta$ as the axes to produce $[001]_\alpha$// $[1\bar{1}0]_\eta$ and $[020]_\alpha$//$[220]_\eta$, against 2×2 α-Fe unit cells on (001). There is good overlap between Fe and Mn atoms. The misfit between the interatomic distances of the α-Fe atoms and the Mn atoms forming Mn_3N_2 precipitates is 3%, and consistency can therefore be considered good.

With the super-saturation of solid solution nitrogen as the driving force, the precipitates grow in such a way as to control the interface energy to a low level. Because of this, the growth of the precipitates increases the area of the $(001)_\eta$ plane (plane with low interface energy, perpendicular to the direction of the c axis), on which the Mn_3N_2 displays good consistency with the Fe atoms. In the case of growth in the direction of the C axis, it is believed that the precipitates double in thickness (to the equivalent of two unit cells) and form steps, at least in sections. It is conjectured that for plane other than $(001)_\eta$, because consistency with the Fe atoms is low (interface energy is high), the precipitates tend not to form steps, and precipitate growth in the direction of the c axis tends not to occur. It is therefore considered that because the Mn_3N_2 precipitates grow in this way in the directions of the a and b axes with one unit cell as the basic element, the precipitates are formed disk-shape in three dimensions.

Figure 19 shows a high-resolution TEM image of η-Mn_3N_2 precipitates. The precipitates marked by the arrows in Fig. 19(a) precipitated onto $(100)_\alpha$ and $(010)_\alpha$ in

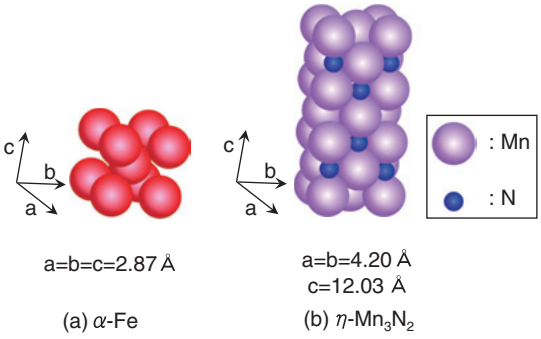
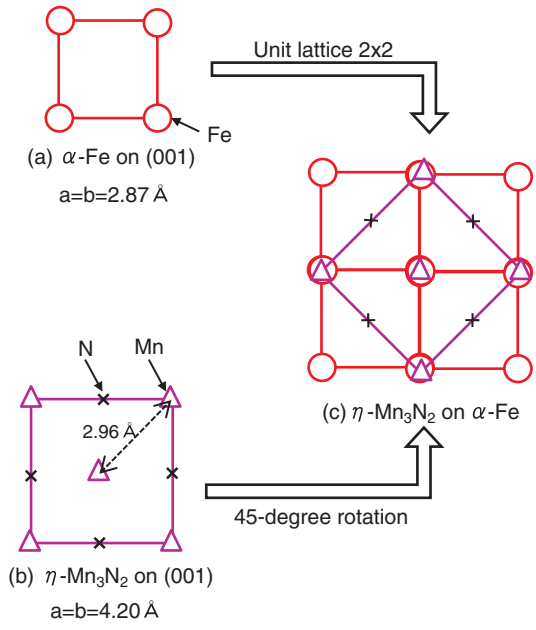


Fig. 17 Schematic of unit cell



$\varepsilon = (a_\eta - a_\alpha)/a_\alpha$
$= (2.96-2.87)/2.87 = 0.03$
ε : Misfit
a_α : Lattice constant for α-Fe
a_η : Lattice constant for η-Mn_3N_2

Fig. 18 Baker-Nutting orientation relationship between Fe and Mn_3N_2

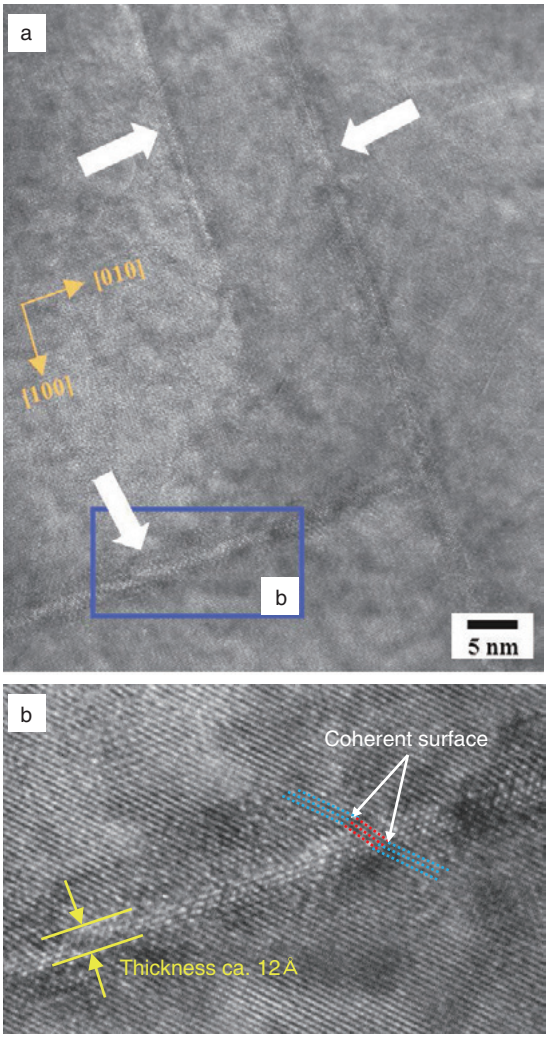


Fig. 19 High-resolution TEM image of Mn_3N_2

the ferrite phase. Figure 19(b) shows a magnified image of η-Mn_3N_2 that has precipitated onto a $(100)_\alpha$ (this is the area surrounded by the square in Fig. 19(a)). The thickness of this precipitate is 12Å, which corresponds well with the length of the η-Mn_3N_2 in the direction of the c axis (12.03 Å). This demonstrates that the observed precipitates grow anisotropically to specific planes, and the precipitate shown in Fig. 19(b) grows continuously (coherently) with the atomic arrangement of the mother phase. The strengthening mechanism of the developed steel by means of GSN is therefore conjectured to be strengthening through the formation of precipitates with a high degree of coherency in a B-N relationship (Fig. 18), which results in the formation of strain fields, increasing deformation resistance.

6.4.3. Precipitation behavior of precipitates

Figure 20 shows a schematic of the precipitation behavior of Mn_3N_2.

In Stage I, Mn exists as a solid solution in the ferrite phase (prior to GSN).

In Stage II, the application of GSN results in the diffusion of nitrogen in the ferrite phase, which forms a solid solution.

In Stage III, time of exposure to GSN has increased, resulting in increased nitrogen diffusion. In this state the precipitates display coherence with the mother phase, and this is believed to increase strength.

Stage IV represents the state of the precipitates in the ferrite phase when heat treatment for long periods or at excessively high temperatures has resulted in over-aging. In this case, the Mn_3N_2 precipitates become coarse. It is believed that some of the coarse precipitates become non-coherent, and their ability to strengthen the material therefore declines.

The results discussed above demonstrate that by contrast with the action of Mo in strengthening the conventional high-strength steel by clustering or concentrating the nitrogen surrounding it, the strengthening mechanism in the developed high-strength steel is the microscopic precipitation of η-Mn_3N_2 in the ferrite phase. In addition, it is conjectured that the precipitates formed in the developed high-strength steel are effective in strengthening the material because they display coherence with the mother phase, as shown in Stage III in Fig. 20.

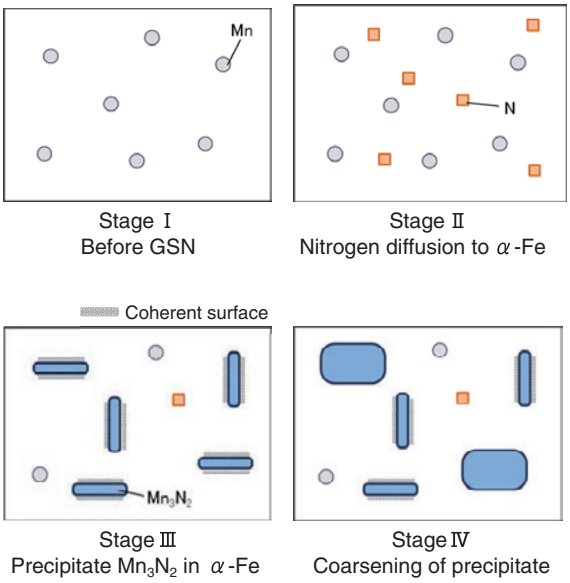


Fig. 20 Schematic of precipitate behavior

7. Conclusion

A high-strength blast furnace steel for crankshafts that eliminates the use of rare metals has been developed by optimizing the amount of Mn, a basic element composing steel. The developed high-strength steel is strengthened by the precipitation of η-Mn_3N_2, and by this means realizes equivalent strength to the conventional high-strength steel. Eliminating the addition of rare metals to the steel has reduced procurement risk and material costs. The development process produced the following results:

(1) It was possible to realize an equivalent level of fatigue strength to the conventional high-strength steel containing the rare metal Mo by increasing Mn content to 0.9 wt% in 0.30-0.35 wt%C carbon steels.

(2) The range of 50 μm depth hardness that made it possible to reconcile fatigue strength and straightenability was set. Taking into consideration the effect of each constituent element on 50 μm depth hardness, the equivalent amount of Mn (*Mneq*), based on the elements with the greatest effect on hardness (Mn, C, Cr), was introduced as a new indicator, and a range was set for this parameter.

(3) The formation of Mn nitrides was observed in a 1.0wt% Mn steel that had been gas soft nitrided. These were identified as η-Mn_3N_2 from their electron diffraction pattern.

(4) The strengthening mechanism with increased Mn is considered to be the precipitation strengthening of η-Mn_3N_2 with a B-N relationship in the ferrite phase.

The developed high-strength steel was first employed in the crankshaft for the 2013 model year CR-Z. The substitution of this crankshaft for a conventional standard steel crankshaft realized a 4 kW increase in power. Crankshafts produced using the developed steel will be employed successively in new gasoline engines.

References

(1) Onda, H., Asai, T., Fujiki, K., Kudo, H., Murofushi, K.: Development of High-strength Induction Hardened Crankshaft, Honda R&D Technical Review, Vol. 15, No. 2, p. 175-182

(2) Iwama, N.: Trend of special Steel for Automotive Parts, Journal of Society of Automotive Engineers of Japan, Vol. 55, No.10, p. 64-68 (2001)

(3) Mori, M., Koumoto, T., Harikago, T., Owaki, S., Iwama, N.: Development of High Fatigue Strength Microalloyed Steel Crankshaft, 2000 JSAE Annual Congress Proceedings, No. 47-00, p. 9-12
(4) Nagasaka, H., Mori, H., Araki, S., Ishibashi, Y., Hamada, T., Takami, M.: Fatigue Strength Improvement of Solid Type Crankshafts through Fillet Cold Rolling, Kobe Steel Engineering Reports, Vol. 48, No. 1, p. 68-71 (1998)
(5) Asai, T., Takitani, Y., Sano, N., Matsumoto, H.: Development of Non-normalized Nitrocarburized High Strength Crankshaft, Honda R&D Technical Review, Vol. 19, No. 1, p. 89-96
(6) Masuda, H., Matsuda, H., Yamazaki, A.: Development of High-strength and High-wear Resistance Nitrocarburizing Steel by Precipitation Strengthening of Mo-V Carbonitride, Honda R&D Technical Review, Vol. 24, No. 2, p. 117-125
(7) Takitani, Y., Saito, I., Miyazaki, T., Kamiya, K.: Development of Nitrocarburized High-strength Crankshaft with No Rare Metals Added, Honda R&D Technical Review, Vol. 23, No. 2, p. 70-75
(8) Hirukawa, H., Furuya, Y.: Effect of Mn Contents on Fatigue Properties of Plasma-Nitrided Fe-C-Mn Steels, Tetsu-to-Hagane, Vol. 98, No. 2, p. 69-74 (2012)

Author


Hiromasa TAKAHASHI


Hiroki MASUDA


Shigefumi NISHITANI


Motoki TAKASUGA

Development of Waterborne Primer Applicable to Different Plastics in Motorcycles

Tomoyuki INOUE* Akiko TANAKA*
Shinsuke MOCHIZUKI* Masanobu INOUE**

ABSTRACT

Most of the paint materials currently used for motorcycles contain a large amount of Volatile Organic Compounds. Volatile Organic Compounds are environmental load substances, and there is a strong demand for reducing their emissions in recent years. Many of a motorcycle's exterior parts are made of ABS plastics or PA plastics. These two plastic materials have different film adhesion mechanisms and adhesion strengths. Therefore it was necessary to use different conductive primers and it was one of the factors that caused a loss of time and materials in the painting processes. We challenged those two objectives, i.e., the reduction of Volatile Organic Compounds and the common use of the same conductive primer for different parts materials, by combining two kinds of resins originally designed individually, i.e., urethane resins with carboxylic acid groups and acrylic resins with amide groups, which have different properties. Many of the plastic parts used in motorcycles are painted manually because they have difficult areas to be painted by automated painting machines. Thus, the viscosity was adjusted to satisfy both the controllability of paint sagging and the surface smoothness to maintain the efficiency of paint workers' operations by using a thixotropic rheology control agent.

1. Introduction

1.1. Adoption of Waterborne Paint to Reduce VOCs

Recently, public concerns for environmental issues have been significantly growing. Chemical substances that are hazardous to the environment and/or health have been recognized as environmental load substances, and are now under regulations. Volatile Organic Compounds (VOCs) are a variety of those environmental load substances and are contained in the materials used in paints as well. "VOCs" is a general term for organic compounds that easily evaporate and remain as a gaseous body in the atmosphere, and VOCs are considered as a group of the substances that cause photochemical smog through photochemical reactions in the atmosphere. In some countries, regulations on VOCs have been enacted such as the Clean Air Act in the United States, TA-Luft in Germany and the Environmental Protection Act in the United Kingdom. In Japan, the Air Pollution Control Act was revised in April 2006 to include VOC regulations. This prompted the Japan Automobile Manufacturers Association (JAMA) to set a stricter target, aiming to reduce VOCs by 40%, compared to 2000, until 2010. Japanese automobile manufacturers have developed various technologies[(1), (2)] to meet this target. VOCs are contained in the organic solvents of painting materials and discharged during the painting processes in the automobile production lines. Since earlier times before JAMA set that target, great efforts had been made in Honda factories towards the improvement in painting efficiency, the retrieval of paint thinner and the adoption of high-solid-type solventborne paint. However, more efforts were needed to meet JAMA's target of a 40% reduction. Therefore, we had made further steps to adopt waterborne paint to achieve even larger reduction of VOC emissions.

1.2. Painting Materials to Be Changed into Waterborne Materials

The parts of a motorcycle that are painted are metal tanks, metal frames and plastic exterior parts such as cowls. Figure 1 shows proportions of VOC emissions per square meter from each part category in Honda's Kumamoto Factory. As can be seen from the graph, the greatest VOC emissions occur in the painting of the plastic exterior parts. To determine the details on the sources of the emissions, the VOC emissions for each layer of the painting materials were examined. The results are shown in Fig. 2. The paint layer structure has two layers composed of a primer and a top coat, which consists of a base coat and a clear coat, to give colored appearances. The primer is the main cause of such high VOC emissions generated during the painting process of the exterior parts. The chart in Fig. 2 shows that the primer emits

* Motorcycle R&D Center
** Nippon Bee Chemical Co., Ltd.

more VOCs than the base coat and clear coat. This is because the primer is a one-composite material and it cannot be produced as a high-solid type. Based on those circumstances, it was expected that a large reduction of VOCs could be achievable if the solvent-borne primers were replaced with waterborne primers, and a reduction of VOC rate in primers was realized from 70% to a few percentage points.

This expectation motivated us to make attempts to alter the solventborne primers currently used with the newly developed waterborne primer applicable to the plastic exterior parts.

1.3. Functions of Primers and Creation of One Common Primer

The primer is a film applied between a part and its top coat film used for a colored appearance. Its function is to apply conductivity for electrostatic spraying and to facilitate the adhesion between the top coat film and the parts.

The transfer efficiency in painting can be significantly improved by using the electrostatic spraying method in which large amounts of paint material are carried on to the parts to be painted with the help of electrostatic forces generated by electrical fields that are created by voltage applied between the paint spray gun and the parts. Non-electrostatic spraying has low transfer efficiency, because a large amount of the paint does not reach the target parts (Fig. 3). To apply the electrostatic spraying method, the target parts to be painted should have electrical conductivity, which is why conductive primers should be applied to plastic parts without conductivity when the top coat paint is electrostatically spray-painted.

Adhesion strength to a paint film varies from one plastic material to another. When the adhesion of the plastic is low, a primer with good adhesion characteristics to the plastic needs to be applied.

Figure 4 shows examples of plastic exterior parts of a motorcycle. Three different types of plastics are used for the

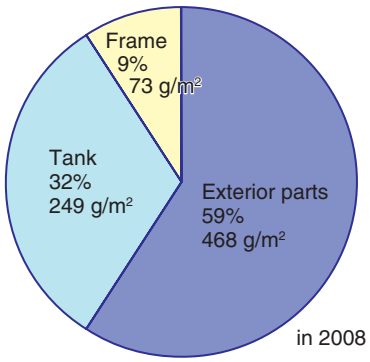


Fig. 1 Proportions of VOC emissions from each part category

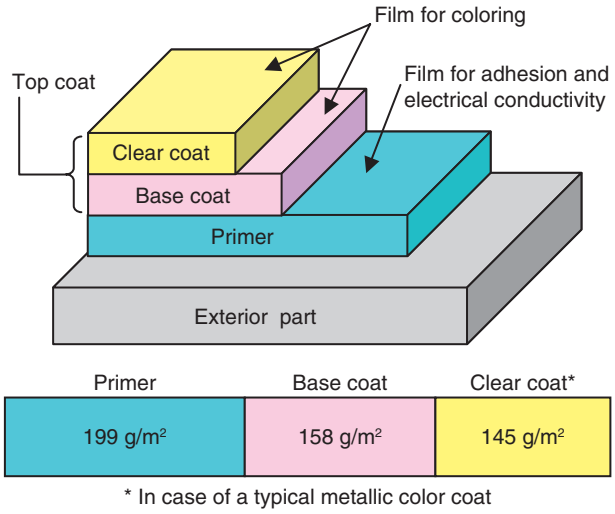


Fig. 2 Paint composition on exterior parts and VOC emission amount

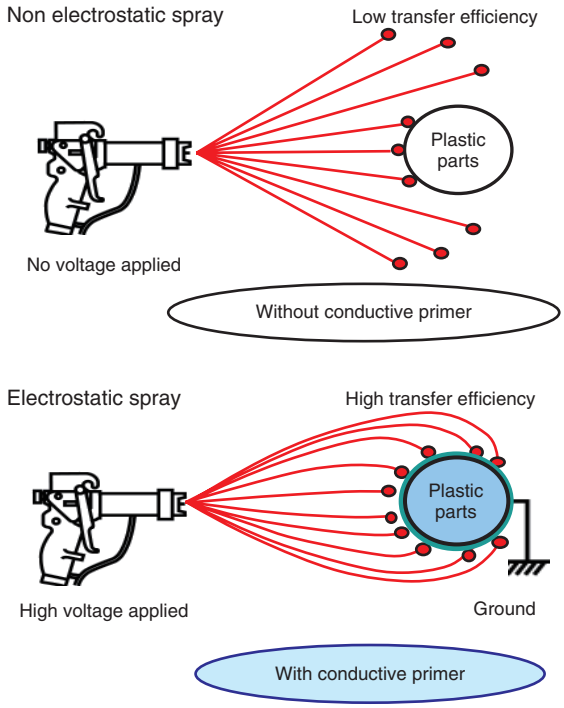


Fig. 3 Difference between non-electrostatic spray and electrostatic spray



Fig. 4 Plastic exterior parts of motorcycle

Table 1 Plastic type and features for applications

Plastic type	Features for applications
ABS	Easiness for painting
ABS+PE	Resistance against chemical agents
PA	Heat resistance

outer coverings of a motorcycle. Table 1 shows the features of the plastics to fulfill the requirements in motorcycle applications. The roles of the primers are outlined as follows. In the case of ABS and ABS with PE (Polyethylene) plastic (hereafter ABS+PE), the primer is used only to apply conductivity for electrostatic spraying, because two-package-type urethane acrylic paint adheres well to these plastics without primer.

In the case of PA plastic, on the other hand, the film does not adhere well. Therefore, a primer is required not only to provide conductivity, but also to ensure adhesion of the film to the parts. Thus, in this case, the primer plays the major role in preventing the film from peeling.

ABS and PA have different mechanisms of adhesion to primers and two different primers have to be separately used. This imposes on the necessity of management of time and material losses during the painting processes in our factories. These situations motivated us to develop a waterborne primer that can be used on both ABS and PA plastics.

Keeping the two objectives mentioned above in mind, we developed a waterborne conductive primer that could be used on different plastic materials of motorcycles, in order to reduce VOCs and simplify the painting process.

2. Requirements in Development

The requirements for our development of a waterborne conductive primer that could be used on different plastic materials were as follows:

(1) Organic solvent proportion (to whole primer quantity): Less than 3% (which is the amount to satisfy VOC emissions regulations)
(2) Surface electrical resistance: No more than 0.05 MΩcm (which is the value that fulfills the transfer efficiency requirement for electrostatic spraying)
(3) Substrate: ABS, ABS+PE and PA can be applied
(4) Paint film performances (initial adhesion, water resistance, humidity resistance, etc.): Equivalent to or better than current product
(5) Painting properties (sagging prevention management, surface smoothness of wet film, etc.): Equivalent to or better than current product
(6) Surface smoothness of dry film (LW, SW): Equivalent to or better than current product

3. Issues and Technical Measures

3.1. Adhesion to ABS and PA and Resin Design

ABS can be made to adhere to the paint film without difficulty by adding functional groups with polarity to the primer resins, because ABS contains nitrile groups with high polarity. Meanwhile, PA can not easily be made adhesive because it has less polarity with its crystallized structure. Therefore, regarding PA, the binding force for adhesion is mainly created by the intermolecular force of the alkyl chains between the primer resin and PA and by hydrogen bonding between the polar functional groups of the primer resin and the amide groups of PA. Moreover, in motorcycle applications, plastic parts are used even in high-temperature locations such as in the vicinity of an engine or an exhaust pipe. For those parts used under high temperatures, PA is usually selected because of its high melting point and being reinforced with glass filler. However, where the glass filler appears on the surface of the plastic (Fig. 5) the adhesion between the primer film and the plastic is further reduced.

Regarding adhesion strength between the top coat film and primer on ABS or PA, it does not become an issue because of the actions of polar functional groups contained both in the resin of the top coat film and in the resin of the primer film.

Because of these differences in adhesion mechanisms to the primer, a primer resin must be individually designed for each plastic. In those circumstances, we tried to select the appropriate principal chains and side chains in resins that adhered to ABS and PA and examine the suitable combination and the correct composition ratio. Table 2 shows the resins selected and their adhesion mechanisms. Figure 6 illustrates the adhesion mechanisms.

3.2. Decrease of Film Performance Due to Remaining Water and Increment of Solid Content Ratio*

A film of two-package-type urethane acrylic paint is formed by the reaction between the hydroxyl groups in the acrylic resin, the base resin, and the isocyanate groups in the isocyanate resin, the hardening agent, forming urethane bonds and creating a cross-linking reaction between them (Fig. 7). The hardening agent in the top coat paint also reacts with the hydroxyl groups in the primer resin, creating adhesion between the top coat film and the primer film.

Waterborne primer contains water as the solvent, and since water is less volatile, more water remains in the primer

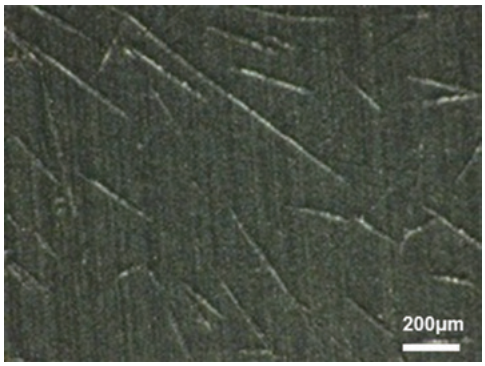


Fig. 5 Glass fillers appeared on surface of PA

Table 2 Resin type and adhesion mechanisms

Resin type		Target of adhesion	Adhesion mechanisms
Principal chain	Urethane emulsion	ABS PA	Dipolar interactions and hydrogen bonds between: (1) ABS; urethane bonds of urethane resin and nitrile groups of ABS (2) PA; urethane bonds of urethane resin and amide bond of PA
	Acrylic emulsion	PA	Intermolecular force of alkyl chains between acrylic resin and PA
Function group in side chain	Carboxylic acid groups	ABS PA	Dipolar interactions and hydrogen bonds between: (1) ABS; carboxylic acid groups and nitrile groups of ABS (2) PA; carboxylic acid groups and amide groups of PA
	Sulfonic acid groups	ABS PA	Dipolar interactions and hydrogen bonds between: (1) ABS; sulfonic acid groups and nitrile groups of ABS (2) PA; sulfonic acid groups and amide groups of PA
	Amide groups	PA	Dipolar interactions and hydrogen bonds between amide groups and amide groups of PA

film for a long time after it has been applied. If the top coat paint is applied while the primer still contains a large amount of water, the water from the primer will seep into the top coat paint. As the isocyanate groups in the hardening agent preferentially react with water than with the hydroxyl groups in the base resin, this interferes with the cross-linking reactions between the base resin and hardening agent, resulting in softening of the top coat film and the poor adhesion between the top coat film and the primer film (Fig. 8). Additionally bake-finishing after painting over primer containing water causes such deterioration in appearance as blisters in the film caused by vaporized water.

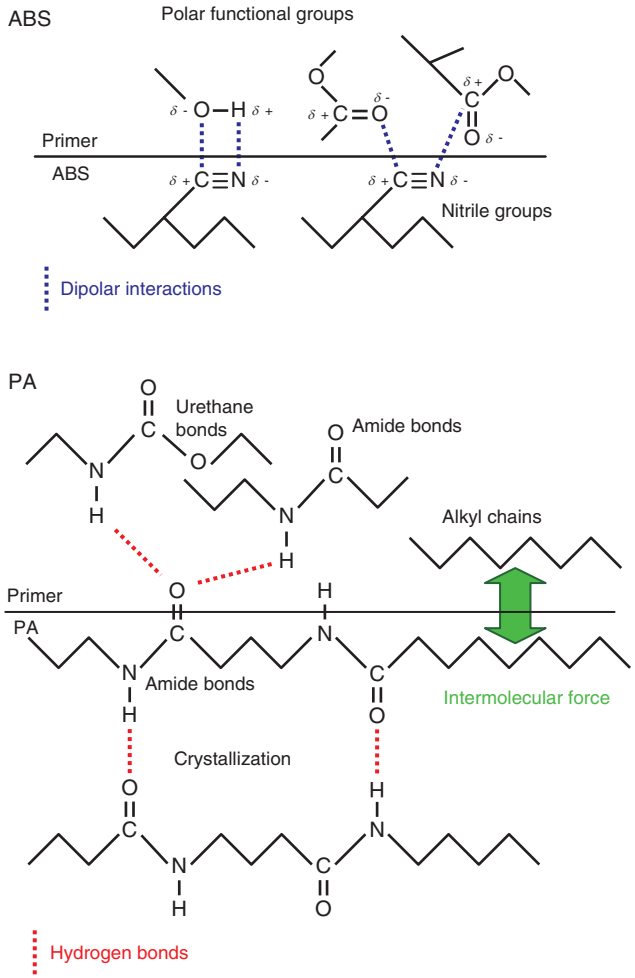


Fig. 6 Adhesion mechanism of primers to ABS and PA

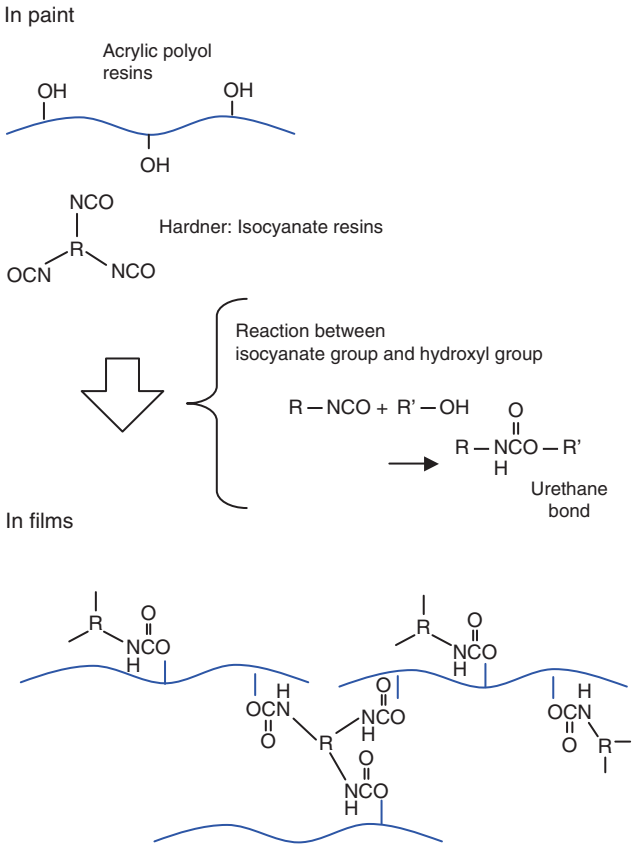


Fig. 7 Normal curing reactions

To avoid these defects, we added a preheating process between the processes of applying the primer and the top coat paint to release the water and increase the solid content ratio.

* Solid Content: The solid component containing no vaporizing substances such as water or solvent. In the case of painting materials, the solid content is the resin, body pigment, color pigment and additives. The solid content ratio is the ratio of the weight of the solid content to the overall weight, and is used both for a paint material before painting and for a wet film after painting.

3.3. Adjusting Viscosity to Stop Sagging While Maintaining Surface Smoothness

The solvent of the solventborne primer is made of organic material and has a high vaporization speed. Therefore, the solid content ratio goes up soon after the application and the viscosity increases as a result, contributing to the prevention of sagging during application. On the other hand, the solvent of the waterborne primer is water, which has a low vaporization speed. This leads to a low solid content ratio after the application, making it difficult to increase viscosity during application, and sagging occurs frequently as a result.

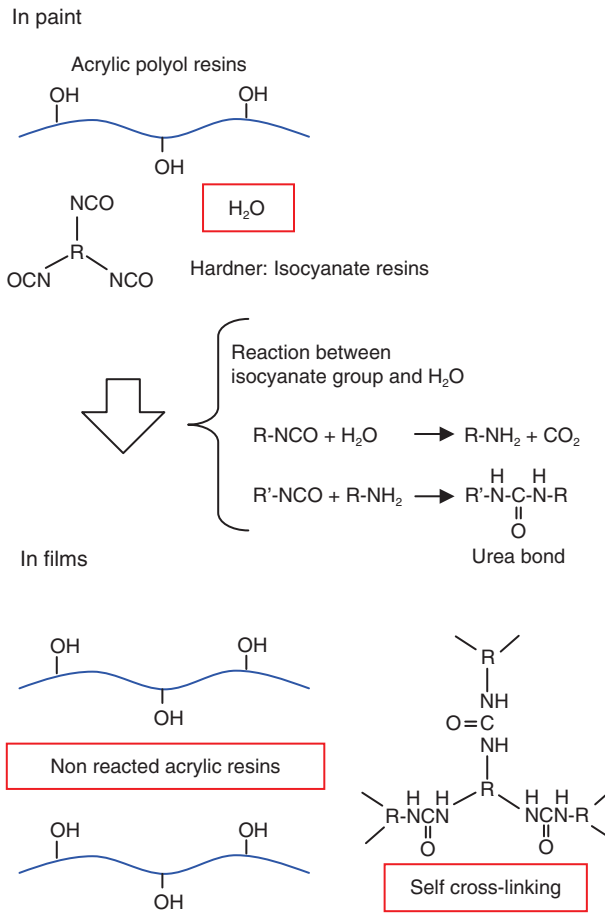


Fig. 8 Curing reactions with H_2O

The complexity in shapes of a motorcycle's plastic parts (Fig. 9) makes it difficult for an automated painting machine to follow the surfaces when applying the primer. This is why the primer tends to be applied unevenly or some portions even left unpainted with automated machines. Transfer efficiency and adhesion of the top coat film decrease if the primer film is uneven or missing. For those reasons, application of the primer requires painting work by hand. When the primer is applied by hand, the paint worker adjusts application conditions according to visual observations. The worker tends to apply paint repeatedly when he or she cannot get sufficient smoothness of the primer surface and that causes the film thickness to increase and results in sagging. Consequently, preventing sagging while maintaining the smoothness of the wet film is very important as requirements for manual painting.

One effective way to prevent sagging during application is to use a thixotropic rheology control agent to increase viscosity under low shear stress and decrease viscosity under high shear stress (Fig. 10). Therefore, in our development, we included an attempt to adjust viscosity by using a thixotropic rheology control agent in order to reduce sagging while maintaining surface smoothness.



Fig. 9 Example of motorcycle part with complex shape

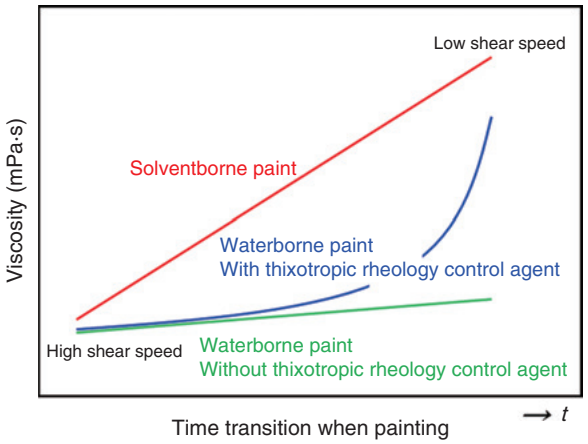


Fig. 10 Viscosity changes in painting process

4. Test Method

(1) Test pieces:
  (i) When tested with test panels:
  Flat panels made of ABS, ABS+PE, PA with dimensions of 150 × 70 × 3.0 mm
  (ii) When tested with actual parts:
  The front fender of the Honda VT750
(2) Test procedures
  (a) Adhesion Test:
  The grid test method (JIS K5400) was applied. The top coat film was carved into 100 cells with a utility knife. Adhesive tape was applied to those cells and then removed. The conditions of removals in the top coat film were checked by visual observation.
  (b) Water Resistance Test:
  The test pieces were immersed in 40°C water for a set time period and then checked for defects such as blistering or removal of film.
  (c) Humidity Resistance Test:
  The test pieces were kept at an ambient temperature of 50°C with 95% humidity for a set time period and then checked for defects such as blistering or removal of film.
  (d) Surface Smoothness Test:
    (i) Primer film in wet condition: By visual observation.
    (ii) Primer film in dry condition: By measuring Ra (roughness average) using a laser-type surface roughness measuring instrument. A cut off value: 0.8 mm.
    (iii) Top coat paint in dry condition: By measuring LW (long wave) and SW (short wave) using BYK-Gardner Wave Scan. The instrument measures the amplitude of filtered wave forms of a surface through a certain wavelength range. The measured value represents good surface smoothness when the value is small. The value of LW is for the wavelength range of 1.2 to 12 mm, and SW is for 0.3 to 1.2 mm.
  (e) Viscosity Test:
    (i) Paint viscosity: Brookfield viscometer with rotation speed of 6 rpm.
    (ii) Paint Viscosity of wet film: Cone plate viscometer with shear speed of $0.1sec^{-1}$.
  (f) Sagging Resistance Test:
  Primer was applied to a vertical test panel with a hole of 5 mm in diameter. Preheating was applied while keeping the panel vertically positioned. The sag limit thickness is defined as the film thickness that generates 5 mm of sagging.
  (g) Wettability Test:
  After top coat paint was dropped onto a dry film of primer, the contact angle was measured using a protractor. Measurements of the contact angle were taken after 30, 60 and 90 seconds, and this data was extrapolated to determine the contact angle immediately after the dropping of the top coat paint (0 seconds). A smaller contact angle means better wetness.

5. Results and Considerations

5.1. Designing Resin that Will Adhere to Both ABS and PA

In this development, emulsion type was selected as the mixture status of the waterborne primer resin, because of its high water resistance and high humidity resistance properties.

Four kinds of base resins were composed (shown in Table 3) with the combination of one selected principal chain, out of two kinds, and one selected functional group, out of three kinds, which were attached to side chains (shown in Table 2). Dispersion resins, additives and solvents were mixed with each base resin to make four kinds of primers, respectively, primer P-A, primer P-B, primer P-C, and primer P-D.

As the test pieces for paint substrates, three kinds of materials, ABS, ABS+PE and PA, were to be considered. Incidentally, ABS+PE is disadvantageous compared to ABS in respect of adhesion capability because ABS+PE contains PE by a few percentage points. Consequently, in these evaluation tests, only ABS+PE, which has greater difficulties in adhesion, was used to represent the tests for ABS and ABS+PE. In the next step, the primers prepared as above were painted onto the test pieces of ABS+PE and PA, the test pieces were preheated, and were painted with the top coat paint followed by bake-finishing. Adhesion tests were performed on those test pieces at the initial point of the entire tests followed by the adhesion tests after water resistance tests and humidity resistance tests.

The evaluation criteria for the adhesion test are: “good” if none of a hundred cells experienced exfoliations (denoted by circular symbol); “poor” if exfoliations occurred but less than 50% measured by area at any of the cells (denoted by triangular symbol); and “unacceptable” if any of the cells experienced exfoliations of more than 50% measured by area (denoted by cross symbol). The evaluation results are shown in Table 4.

The evaluation results of adhesion for Primer P-A and Primer P-B were good with ABS+PE, but unacceptable for PA. It was considered that these results came from the fact that carboxylic acid groups adhere well to ABS+PE but do not adhere well to PA. Primer P-C did not adhere well to ABS+PE but did adhere well to PA. It is predicted that adhesion occurred from dipolar interactions between the amide groups in Primer P-C and those in PA. Primer P-D did not adhere well to ABS+PE. The adhesion of Primer P-D with PA was evaluated as “good” but was considered as inappropriate for the final selection because swelling occurred after water resistance and humidity resistance tests. It was understood that the swelling occurred because of high water absorbency, in spite of good adhesion with PA, as sulfonic acids is more polar than carboxylic acids.

Table 3 Combination of principal chains and function groups in side chains

Base resin	Principal chain	Function group in side chain
A	Acrylic emulsion	Carboxylic acid group
B	Urethane emulsion	Carboxylic acid group
C	Acrylic emulsion	Amide group
D	Urethane emulsion	Sulfonic acid group

Table 4 Adhesion test results

Primer	Base resin	ABS+PE			PA		
		Initial	After WR	After HR	Initial	After WR	After HR
P-A	A	○	○	○	×	×	×
P-B	B	○	○	○	×	×	×
P-C	C	○	×	×	○	○	○
P-D	D	○	○	×	○	○(1)	○(1)

WR: Water resistance test, HR: Humidity resistance test
(1) Swelling, ○: Good, △: Poor (does not appear in this table), ×: Unacceptable

Table 5 Adhesion test results

Primer formula	Base resin			Compounding ratio (%)	ABS+PE			PA		
		Principal chain	Function group in side chain		Initial	After WR	After HR	Initial	After WR	After HR
P-AC1	A	Acrylic emulsion	Carboxylic acid group	50	○	○	○	×	△	○
	C	Acrylic emulsion	Amide group	50						
P-AC2	A	Same as above		25	○	○	○	○	○	△
	C			75						
P-BC1	B	Urethane emulsion	Carboxylic acid group	50	○	○	○	△	△	○
	C	Acrylic emulsion	Amide group	50						
P-BC2	B	Same as above		25	○	○	○	○	○	○
	C			75						

WR: Water resistance test, HR: Humidity resistance test, ○: Good, △: Poor, ×: Unacceptable

None of the four tested resins was qualified in both tests of adhesion to ABS+PE and to PA. Consequently, primer formulas P-AC1, P-AC2, P-BC1 and P-BC2 were made by mixing Base resin A or Base resin B, which have good adhesion characteristics to ABS+PE, with Base resin C, which have good adhesion characteristics to PA, while varying mixing ratios. Using these formulas, adhesion tests were conducted. Table 5 shows the mixing ratio of base resins and the results of adhesion tests.

All the Primer formulas in Table 5 satisfied the adhesion requirement to ABS+PE. However, the adhesion strength to PA varied from formula to formula. The adhesion strength was better in Formula P-AC2 when it was compared with Formula P-AC1, and was better in Formula P-BC2 when it was compared with Formula P-BC1. From these results, it was understood that the higher ratio of base resin C contributed to the higher adhesion strength to PA. In the comparisons of Formula P-AC1 with Formula P-BC1 and Formula P-AC2 with Formula P-BC2, the adhesion strength to PA was better in Formula P-BC1 and Formula P-BC2. It was considered that this was because the adhesion strength is improved when the urethane bonds in the urethane resin and the amide bonds in PA were attracted by the force of the hydrogen bonds.

These results showed that carboxylic acid groups contribute to adhesion to ABS+PE while amide groups and urethane resin contribute to adhesion to PA, and that a higher ratio of amide groups was needed to satisfy the adhesion requirements to PA. Through the evaluation processes mentioned above, Primer formula P-BC2 was eventually selected as the waterborne primer that was adhesive to both ABS+PE and PA.

5.2. Solid Content Ratio Control of Primer by Adding Preheating Process

The relationship between solid content ratio and paint performance was investigated, varying the temperature and the time of preheating processes, in order to get the solid content ratio of waterborne primer film that satisfies film requirements.

Test panels, mentioned in the Test Method section, were used for the test pieces. The setting time before the preheating was set at 3 minutes and preheating time was set at under 3 minutes, considering the paint hanger speed and the paint line length in the actual application to the manufacturing line. Four preheating (or drying) temperatures were set: room temperature, 40°C, 55°C and 70°C. Three

Table 6 Solid content ratio and film performance

Preheat condition	Primer		ABS						ABS+PE						PA						Judge-ment
	FT (μm)	SCR (%)	AP	AD	WR		HR		AP	AD	WR		HR		AP	AD	WR		HR		
					AP	AD	AP	AD			AP	AD	AP	AD			AP	AD	AP	AD	
RT×1 min	5	38.9	○	○	×	○	○	○	○	○	○	×	○	×	○	○	○	○	○	○	×
	9	33.5	○	○	×	○	×	×	○	○	○	×	×	×	○	○	○	○	×	×	×
	14	33	○	○	×	○	×	×	○	○	○	×	×	×	×	×	○	○	×	×	×
RT×2 min	5	43.5	○	○	○	○	○	○	○	○	○	○	○	×	○	○	○	○	○	○	×
	9	35.6	○	○	×	○	×	×	○	○	○	×	×	×	○	○	○	○	×	○	×
	14	35.1	○	○	×	○	×	×	○	○	○	×	×	×	○	○	○	○	×	○	×
RT×3 min	5	50.4	○	○	○	○	○	○	○	○	○	○	○	○	○	○	○	○	○	○	○
	9	38.1	○	○	○	○	×	○	○	○	○	×	×	×	○	○	○	○	×	○	×
	14	37.4	○	○	×	○	×	×	○	○	○	×	×	×	○	○	○	○	×	○	×
40°C×3 min	5	70.9	○	○	○	○	○	○	○	○	○	○	○	○	○	○	○	○	○	○	○
	13	63.3	○	○	○	○	○	○	○	○	○	○	○	○	○	○	○	○	○	○	○
	18	56.2	○	○	○	○	○	○	○	○	○	○	○	○	○	○	○	○	○	○	○
55°C×3 min	5	82.3	○	○	○	○	○	○	○	○	○	○	○	○	○	○	○	○	○	○	○
	10	74.7	○	○	○	○	○	○	○	○	○	○	○	○	○	○	○	○	○	○	○
	14	69.1	○	○	○	○	○	○	○	○	○	○	○	○	○	○	○	○	○	○	○
70°C×3 min	5	85.2	○	○	○	○	○	○	○	○	○	○	○	○	○	○	○	○	○	○	○
	12	80.3	○	○	○	○	○	○	○	○	○	○	○	○	○	○	○	○	○	○	○
	15	75.6	○	○	○	○	○	○	○	○	○	○	○	○	○	○	○	○	○	○	○

RT: 23°C, FT: Film thickness, SCR: Solid content ratio, AP: Appearance, AD: Adhesion test (Initial),
WR: Water resistance test, HR: Humidity resistance test, ○: Satisfactory, ×: Unsatisfactory

coating thicknesses were set: minimum required coating thickness, maximum thickness without sagging and average thickness of those two. The primer was applied to the test panels of ABS, ABS+PE and PA, and the panels were then preheated, painted with the top coat paint and bake-finished. Appearance evaluation and adhesion test were conducted at initial condition, at the conditions after water resistance tests and at the condition after humidity tests.

Table 6 shows the results. The results show that, when dried at room temperature, only the panels dried for three minutes with minimum film thickness met the paint requirements. It was also proved that all the test panels were satisfactory to the paint requirements when they were preheated at any temperature higher than room temperature.

As for solid content, it was revealed that the solid content ratio required for satisfactory film performance was 50% or more. As for the condition settings, the values finally decided for the actual production were 70°C for the preheating temperature and 3 minutes for preheating time, considering size and shapes of the actual production parts and the quality assurance under mass-production lines.

5.3. Adjusting Viscosity to Avoid Sagging While Maintaining Surface Smoothness

The sag resistance and the surface smoothness were evaluated while varying the viscosity by adding rheology control agents without changing solid content ratio. The surface smoothness was evaluated through visual observations by on-site paint workers, using a front fender of the motorcycle as a painting subject, and comparing, immediately after painting, the wet film of the waterborne primer with that of the solventborne primer currently used. Table 7 shows the results of the evaluations. In the evaluation of the sag resistance, when the viscosity was under 700 mPa·s, the higher the primer viscosity was, the larger the maximum film thickness against sagging became. However, when the viscosity got over 900 mPa·s, the sag limit thickness hardly increased. The required primer viscosity should be over 700 mPa·s for the sag limit thickness of 20 μm, which is needed as the minimum requirement for paint work.

For surface smoothness, the lower the primer viscosity was, the higher the surface smoothness of wet film became. However, the sagging occurred across the entire test panel if

Table 7 Sagging resistance and surface smoothness of painted wet film in changing primer viscosity

Primer viscosity (mPa·s)	Sag limit thickness (μm)	Surface smoothness of wet film
400	13	× (sagging across entire test panel)
700	21	◎
900	26	○
1800	27	△

◎: Better than current solventborne primer
○: Same as current solventborne primer
△: Worse than current solventborne primer
×: Out of permissible range

Table 8 Composition of waterborne conductive primer

Ingredients	Compounding ratio (wt%)	Function	
Water-soluble acrylic resin	1.3	Dispersion of pigments	Solid contents
Emulsion resin	13.2	Adhesion to substrate	
Pigments	10.4	Conductivity, Control of color	
Body pigments	0.8	Adhesion to glass filler	
Additives	1.6	Control of surface tension, Dispersion of pigments, Anti-bubble, Thixotrope	
Amine	0.2	Control of pH	Volatile contents
Water	70.3	Solvent	
Glycol	2.2	Coalescing agent	
Total	100		

the viscosity decreased to 400 mPa·s. The required viscosity ranged from 700 to 900 mPa·s to maintain equal or better surface smoothness of wet film compared to the current primers.

In conclusion, to satisfy the requirements of both sagging resistance and surface smoothness, the range of the primer viscosity should be between 700 and 900 mPa·s. 900 mPa·s was preferable in view of sagging resistance, while 700 mPa·s was preferable in view of surface smoothness. The primer viscosity was finally determined to be 900 mPa·s, because it should have been highly prioritized to maintain a larger tolerance for the paint workers' benefit.

Table 8 shows the final composition of the primer after resolving these three issues.

6. Achievements in Development

6.1. Reduction of VOC Emissions

The waterborne primer was developed to replace the current solventborne primers and was successfully applied to mass production. The waterborne primer contains 2.2% VOCs (Table 8) while solventborne primers contain around 70% VOCs. As a result, a 27% reduction of VOC emissions at the painting processes for plastic parts has been achieved. This contributed significantly to the 10 years of efforts in the Kumamoto factory for the total of 41% VOC reduction in the painting processes.

6.2. Unification of Primers for ABS and PA

The number of primers used in the painting processes were reduced from two to one and the work hours needed for the management and the administrative work for painting processes were significantly reduced. This also enabled the reduction of investment in facilities and equipment in the event of the installation of new painting lines.

Table 9 Surface smoothness of top coat paint

	LW(-)	SW(-)
On solventborne primer for ABS	14.3	40.5
On solventborne primer for PA	24.1	44.5
On waterborne primer	3.5	4.6

7. Secondary Benefits

This development was performed with the two objectives of the reduction of VOCs and the unification of primers for ABS and PA into one. However, other secondary benefits were obtained associated with those main objectives, such as the improvement in surface smoothness of the top coat film and the transfer efficiencies of the primer and the top coat paint. The details of those benefits are described below.

7.1. Enhancement in Surface Smoothness of Top Coat Film

To compare the surface smoothness of the top coat films on the currently used solventborne primer with that on the developed waterborne primer, surface smoothness (LW and SW) of the top coat films was evaluated. The results are shown in Table 9. From those results it was found that the surface smoothness of the top coat film on the waterborne primer was better than that on the solventborne primer was indicated in lower LW and SW values, ranging from 1/4 to 1/7 for LW and from 1/9 to 1/10 for SW, in spite of the viscosity adjustment (900 mPa·s) equalizing the surface smoothness of the wet films between the waterborne primer and the solventborne primer.

To investigate the reasons, the following points were evaluated.

(1) Surface smoothness (Ra) of the dry films of the primers without top coat films.
(2) Wettability (contact angle) of the top coat paint against the dry film of primers.
(3) Viscosity of the primers in the wet films
(4) Solid content ratio of the primers in wet films

The results are shown in Table 10. The waterborne primer showed smaller Ra with its dry film than the solvent-borne primer. This indicates that the surface smoothness of the dry films of the waterborne primer is greater than that of the solventborne primer. Moreover, the waterborne primer showed smaller contact angles with its dry film than the solvent-borne primer. This indicates that the wettability of the dry films of the waterborne primer is greater than that of the solventborne primer. From the above, we concluded that the surface smoothness of the top coat film had been improved by the superior surface smoothness and wettability of the dry film of the waterborne primer, when they were compared with the solventborne primers.

Table 10 Properties of primer films

	Dry film		Wet film	
	Ra (μm)	Contact angle (°)	Viscosity (mPa·s)	SCR (%)
Solventborne primer for ABS	0.20	47.6	394,000	55
Solventborne primer for PA	0.39	43.0	over 1×10^8 (out of range)	60
Waterborne primer	0.15	41.2	16,560	30

SCR: Solid Content Ratio (=Non volatile content tatio)

The reason why the waterborne primer can provide superior surface smoothness and wettability of the dry film is considered as follows.

As for the reason for the superior smoothness, the viscosity of the waterborne primers in the wet films showed smaller values than the solvent-borne primer from Table 10. Therefore, it is estimated that the fluidity of the waterborne primers is higher than that of the solventborne primers (Fig. 11). Moreover, the solid content ratio of the waterborne primers in the wet films showed smaller values than that of the solvent-borne primers. This means that the larger volume change occurred in the transition from the wet-film state to the dry-film state while preheating the waterborne primers than in the transitions of solvent-borne primers, and it is assumed that that improved the surface smoothness (Fig. 11).

As for the reason for the superior wettability, it is estimated that it was due to the small Ra and the high surface tension of the dry waterborne primer film, which has much higher polar functional groups compared with the solventborne primers.

7.2. Enhancement in Transfer Efficiency of Primer and Top Coat Paint

As another secondary benefit, a 9.5% efficiency enhancement of the primer transfer was observed in the waterborne primer compared to the solventborne primers. This can be explained by those reasons described below, which are presented as our assumptions.

Regarding the solventborne primers, which have high evaporation speed, the amount of flown-out and lost paint, without contacting the painting parts, is large because the paint particles lose their mass, and also there's a certain amount of paint that bounces back from the parts surfaces as the viscosity of the paint increases while the paint particles are travelling through the air. On the contrary, regarding

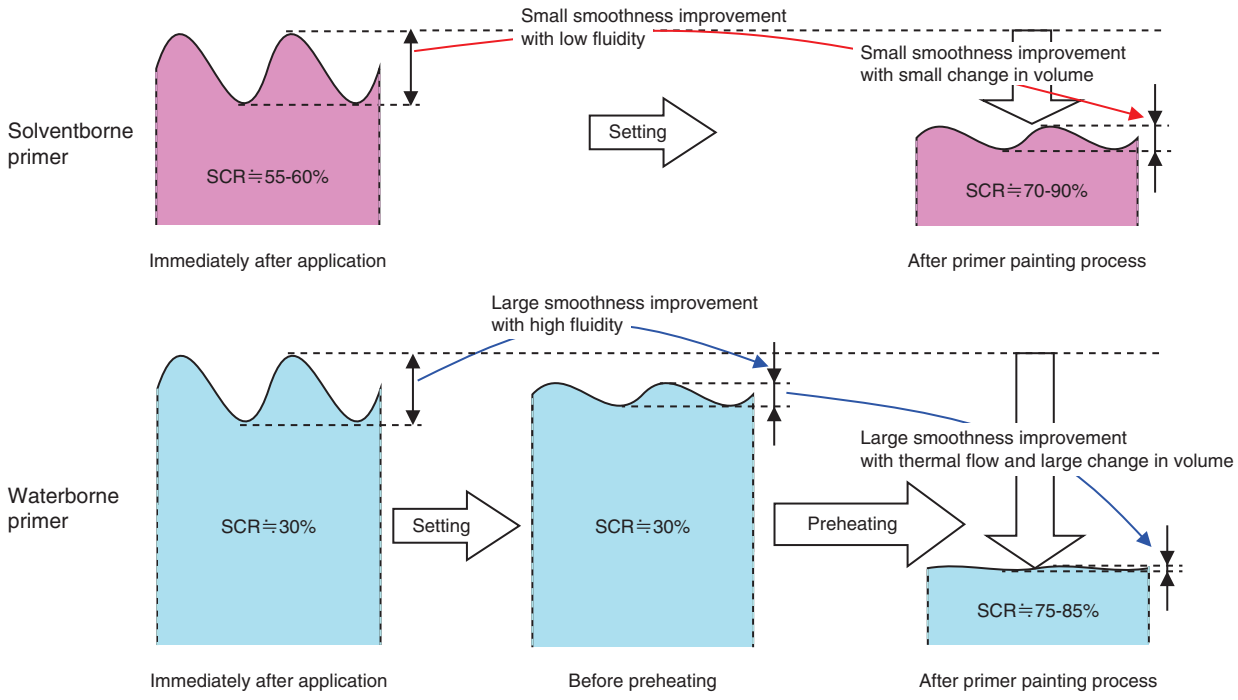


Fig. 11 Improvement of surface smoothness

the waterborne primers, which have low evaporation speed, the mass of the primer particles remains heavy, resulting in larger amounts of the primer reaching the painting parts, and the primer particles are easily captured at the surface of the painting parts and on the wet film formed in the process of painting as the viscosity of the paint remains low (Fig. 12).

The transfer efficiency of the top coat paint was enhanced as well on the waterborne primer compared to the solventborne primers. The reason can be understood that the top coat paint particles consecutively arriving at the primer coat surface are efficiently captured by the top coat paint already widely spread on the waterborne primer surface having good wettability, when compared with the solventborne primers.

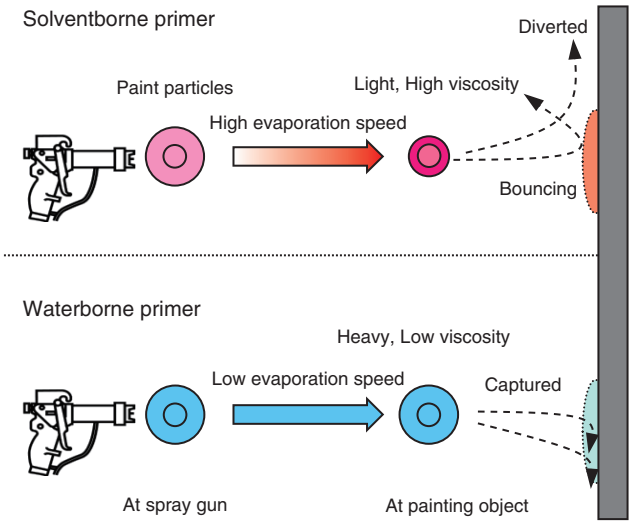


Fig. 12 Primer paint particles behavior

8. Summary

A primer that can be applied to both ABS and PA was successfully developed and the reduction of VOCs achieved by combining two different but dedicatedly designed waterborne resins. Through the application of this primer, a -40% reduction, which is the 2010 year reduction target of VOCs set by JAMA, was fulfilled. The application of this commonly usable primer enabled a reduction of the losses of time and materials in the painting lines. Moreover, thanks to the successful application of the waterborne primer, an enhancement of attractiveness in appearance was brought about by the enhanced surface smoothness, and the transfer efficiencies of the primer and the top coat paint were increased.

The primer developed here is already being applied in actual painting lines for plastic parts of motorcycle manufacturing in the Kumamoto Factory of Honda in Japan.

References

(1) Hashimoto, T., Ogawa, T.: Development of Chlorine-free Waterborne Primer for Bumper, Honda R&D Technical Review, Vol. 20, No. 2, p. 60-64
(2) Ihara, S.: Development of High-paintability Waterborne Primer Paint, Honda R&D Technical Review, Vol. 23, No. 1, p. 110-115

■ Author ■


Tomoyuki INOUE


Akiko TANAKA


Shinsuke MOCHIZUKI


Masanobu INOUE

Research on Photo-degradation Behavior of E-coat

Keisuke KOJIMA* Takamasa AOKI* Takeshi OGAWA*

ABSTRACT

An automotive paint process that remove the primer process has been developed in order to reduce the energy consumption and CO_2 emissions. An analysis method of the photo-degradation of the E-coat when the primer is removed was established, based on the changes in physical properties and chemical structures. As a result, the range of wavelength that cause peeling potential is under 550 nm. Based on these results, a layer to shield under 550 nm of light (1 base) was applied before the color development layer (2 base) without the drying process, enabling elimination of the primer process without limitation to color development.

1. Introduction

Recently, the need for the reduction of manufacturing energy costs and CO_2 emissions has been increasing, along with shortening of the automotive paint process. Conventionally, the application of body paint has mainly involved a four-coat/three-bake (4C3B) process, in which an E-coat is applied, after which a primer is applied and cured, following which a color base coat and a clear coat are applied and cured. Today, the use of a four-coat/two-bake (4C2B) process is becoming more widespread[(1)]. This process shortens the curing process from the primer process, with the topcoat being applied following drying of the primer. In addition, from around 2004, a three-coat/two-bake (3C2B) process began to be applied among European manufacturers. This process removed the primer process, and applied the topcoat following the application of the E-coat (Fig. 1). However, removing the primer process means that the light-shielding function fulfilled by the primer is also lost. As a result, the behavior of light transmission to the E-coat changes for each color, increasing the potential for peeling of the topcoat due to photo-degradation of the E-coat. This situation causes limitations on the color variations that can be developed. The research discussed in this paper therefore analyzed the photo-degradation behavior of the E-coat due to light transmission, and formulated a paint content able to reconcile the ability to remove the primer process with the ability to use a broader range of color variations. The details of the research are reported below.

2. Paint Quality Issues in the Removal of the Primer

Figure 2 shows the layers applied in the standard coating process, and Table 1 shows the role of each layer. The body paint is an E-coat applied to the steel sheets, which has the function of protecting the body from corrosion. The primer is applied to the E-coat for light shielding and stone chip resistance. After the base coat, which provides the color, the clear coat, which offers smoothness and weather durability, are applied. When the primer is removed, the functions that it conventionally fulfills are also lost. Because the qualities change for color

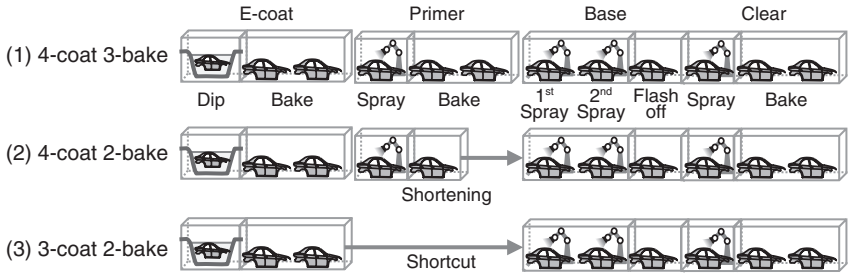


Fig. 1 Paint process of automobile

* Automobile R&D Center

Table 1 Function of each layer

Layer	Function
Clear	Appearance, Weather durability
Base	Coloring
Primer	Light interception, Chip resistance
E-coat	Corrosion control

changes such as hue and brightness, and their behavior with respect to absorption or transmission of light therefore changes, light transmission to the E-coat also changes with the removal of the primer. Figure 3 shows this effect. Light transmission behavior is dependent on the light absorption characteristic of the pigments in the base coat. White shows a low level of absorption for all wavelengths of visible light, and therefore transmits light easily, while black shows a high level of absorption for all wavelengths, and thus transmits almost no light. The chromatic color blue absorbs comparatively long wavelength from visible light, but is unable to absorb short wavelength, and they therefore tend to be transmitted to the E-coat. Light transmission is also affected by the film build, and thin films are not able to fully shield light rays. Because of this, when the primer is removed, the transmission of light to the E-coat is dependent on the pigments in and the film build of the base coat that provides each color. In terms of weather resistance, the E-coat is particularly prone to photo-degradation[2], and it is therefore necessary to limit the brightness and chroma of the base in order to stably shield the E-coat from light. In concrete terms, because the brightness L* value of general white pearl is around 90, to help ensure that the E-coat is stably shielded from light rays by the base coat only, it is necessary to reduce the brightness L* value of the base coat to between 75 and 80 through the addition of black or similar pigments that absorb more effectively. In order to maintain a high level of brightness, it is necessary to increase the thickness of the base coat, but this causes issues such as popping and sagging easily during application. The current project studied the photo-degradation behavior of the E-coat first, and discussed the method that would be able to achieve and maintain color variations.

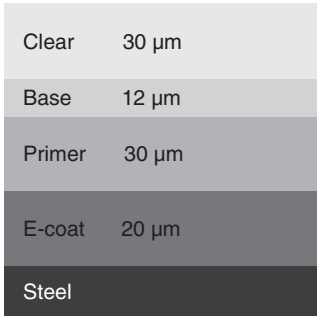


Fig. 2 Standard layer structure of body paint

3. Analysis of Photo-degradation of E-coat

3.1. Conditions of Photo-degradation

The main binder of the E-coat is generally an epoxy resin containing a bisphenol group. As Table 2[3] shows, the binder includes a variety of chemical bonds; the dissociation energy of these bonds is within the range of the irradiant energy of ultraviolet light, and the binder is therefore considered to be degraded by irradiation of UV light. Degradation of the surface of the epoxy resin due to the incidence of light of wavelengths of between 300 and 800 nm has been reported[4], but it is still not known which wavelength affect degradation.

The research first studied what kinds of effect the photo-degradation of the E-coat had on the automotive body paint. Panels that would allow the transmission of light to the E-coat were prepared and exposed outdoors, resulting in the type of peeling shown in Fig. 4. Figure 5 shows the results of observation of the form of peeling and elemental analysis around the areas of peeling using a scanning electron microscope (SEM). The fact that the results of elemental analysis of the areas of peeling designated α and β showed elements originating in the titanium dioxide in the E-coat demonstrated that the peeling of the topcoat occurred as a

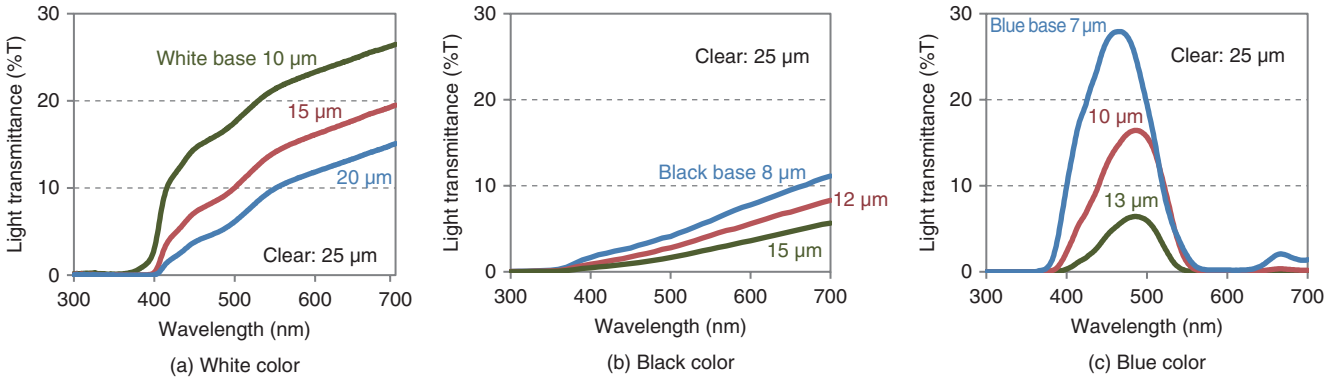


Fig. 3 Light transmittance of base and clear

Table 2 Bond-dissociation energy

Bond of E-coat	Bond-dissociation energy (kcal/mol)	Corresponding light wavelength (nm)
C-H	106	270
C-C	83	345
Ph-C	101	283
C=C	146	196
C-O	76	376
C=O	174	164
C-N	73	392
N-H	93	308
O-H	111	258

result of cohesion failure in the surface of the E-coat. This was considered to result from photo-degradation of the E-coat. In order to analyze the status of the degradation, changes in the chemical structure of the peeled areas as compared to a spare panel (a panel in the initial state) were analyzed using a Fourier transform infrared (FT-IR) spectrophotometer. The difference spectrum between initial state and peeling areas was studied in order to determine the changes in chemical structure by the FT-IR results. The results are shown in Fig. 6. The base peak in the difference spectrum was determined at 1510 cm^{-1}, in the absorption band of the aromatic rings originating in the bisphenol resin. By comparison with the initial state, the peeled areas showed a reduction in absorption bands that could

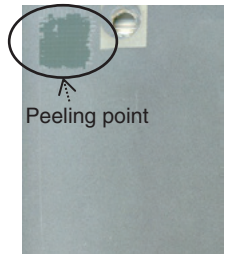
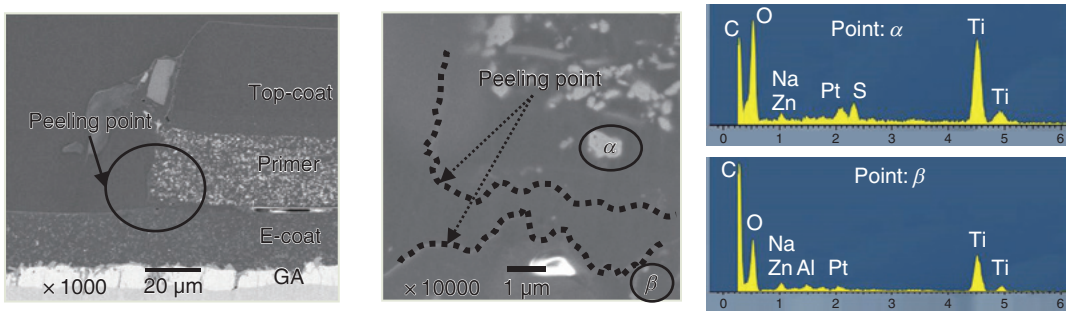


Fig. 4 Peeling of top coat after exposure test



(a) SEM image of peeling point (b) Close-up of peeling point (c) EDX results of α and β point

Fig. 5 Results of SEM-EDX

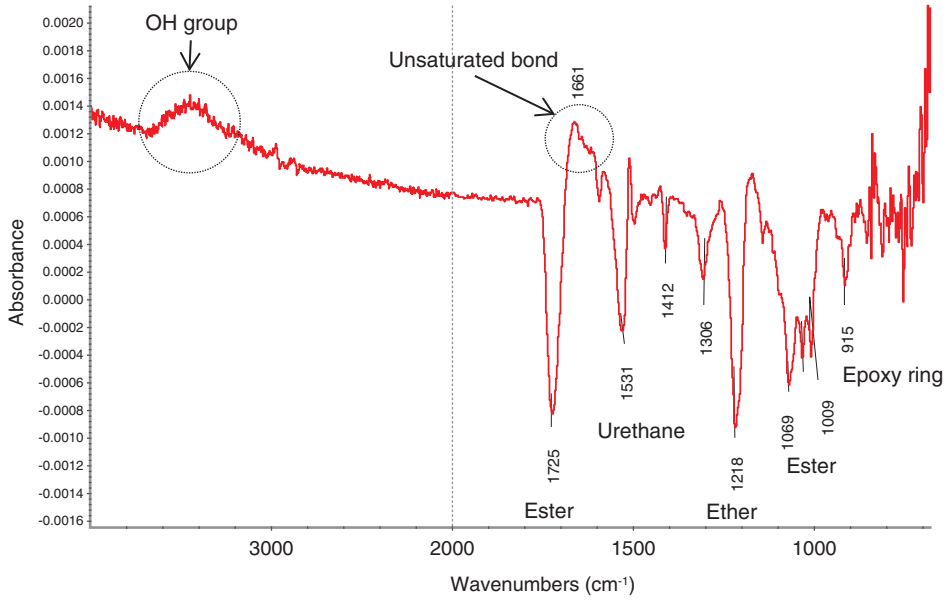


Fig. 6 Differential FT-IR spectrum of E-coat between initial sample and peeling point

be attributed to esters, urethane, and epoxy. In addition, an increase in OH groups with a peak at 3400 cm^{-1} and unsaturated bonds with a peak at 1661 cm^{-1} was observed. Based on these results, it was considered that the chemical structure of the E-coat changes due to photo-degradation, and as a result peeling occurs due to cohesion failure. Next, the wavelengths of light that degrade the E-coat were studied.

3.2. Method of Analysis of Light Wavelengths

In order to study the relationship between the wavelengths of light and the photo-degradation of the E-coat, an E-coat was irradiated in 10 nm intervals using a spectral aging testing machine. Because peeling occurs as a result of cohesion failure at the surface of the E-coat, as shown in Fig. 5(a) in Section 3.1, it was considered that photo-degradation would occur at the surface. Film strength was therefore measured at a depth of 2 μm from the surface in each irradiated area of the E-coat. It was measured using a surface and interfacial cutting analysis system (SAICAS), in order to determine the changes in physical properties due to irradiation. In addition, to provide confirmation of degradation, changes in chemical structure in each irradiated area were analyzed using FT-IR. Using these methods, it was possible to analyze photo-degradation behavior from both the physical and chemical perspectives. The panel used in the analysis was cured under the standard baking conditions at 170˚C for 30 minutes. Baking conditions and inclusions of iron ions can be considered as variable elements on automotive E-coating lines, and another panel, which had been cured at 220˚C for 15 minutes, the upper limit baking conditions such as the cross-linking density and physical properties of the coating, was therefore also used.

3.3. Results of Physical Analysis

With regard to the level of degradation, film strength after irradiation was expressed as a percentage, with the film strength of areas that had not been irradiated as 100. Figures of less than 100 indicated a decline in the film strength of the E-coat due to photo-degradation. Figure 7 shows the results. These results indicate that when a panel produced under standard baking conditions was irradiated by the spectral aging testing machine for 20 hours, film strength declined as a result of irradiation of wavelength of 400 nm and below. When the panel that had been cured at 220˚C was tested under the same conditions, a decline in film strength was observed at wavelength of 440 nm and below, and when the irradiated time was increased from 132 to 950 hours, film strength declined for wavelength of 450 nm and below. By contrast, no decline in film strength was observed for the wavelength range above 450 nm, irrespective of irradiated time. An FT-IR spectrum for the E-coat cured at 220˚C was obtained to determine the reason for this phenomenon (Fig. 8). This spectrum

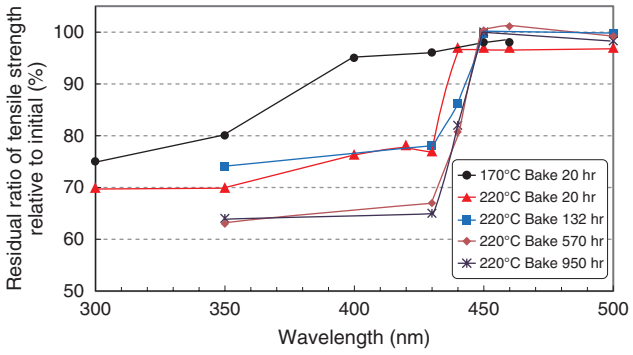


Fig. 7 Results of E-coat photo-degradation

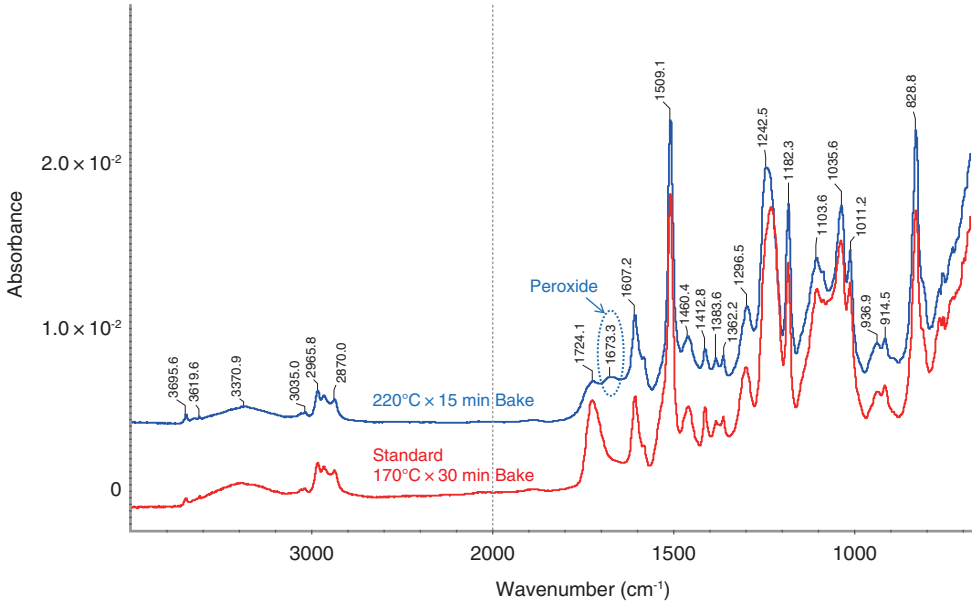


Fig. 8 FT-IR spectrum of E-coat baked at 220°C

showed a peak originating in peroxide. Because the bond dissociation energy of peroxide corresponds to a radiant energy of 447 nm[5], it is considered that the dissociation of the peroxide bonds produces organic radicals, promoting a degradation reaction, with the result that a decline in film strength is observed in areas upon which light of 450 nm and below was incident.

3.4. Results of Chemical Analysis

No decline in the film strength of the E-coat was observed for wavelength of above 450 nm. FT-IR analyses were next conducted to determine whether there was any change in the chemical structure of the E-coat. Figure 9 shows the results of measurements of areas upon which each wavelength was incident following 950 hours of irradiation from a spectral aging testing machine for the panel cured at 220°C. The 1510 cm^{-1} peak for the aromatic rings originating in bisphenol resin shows a tendency to decline at wavelength of above 450 nm. This indicates that at wavelength of over 450 nm, while there is no change in film strength, bisphenol chains in the surface of the E-coat have been subject to cleavage and have been reduced. In order to conduct a detailed study of the level of reduction of the bisphenol resin, the ratio of the areas of the 1510 cm^{-1} peak for aromatic rings originating in bisphenol resin and the 1610 cm^{-1} peak for aromatic rings in an area that had not been exposed to light was determined, and using this as a standard, a comparative analysis of the ratios of the areas of the 1510 cm^{-1} and 1610 cm^{-1} peaks for all wavelength of light for each irradiated time was conducted. The results are shown in Fig. 10. An area ratio of less than 1 on the vertical axis indicates a decline in bisphenol aromatic rings. The results show that it is wavelength of 550 nm and below at which this phenomenon occurs.

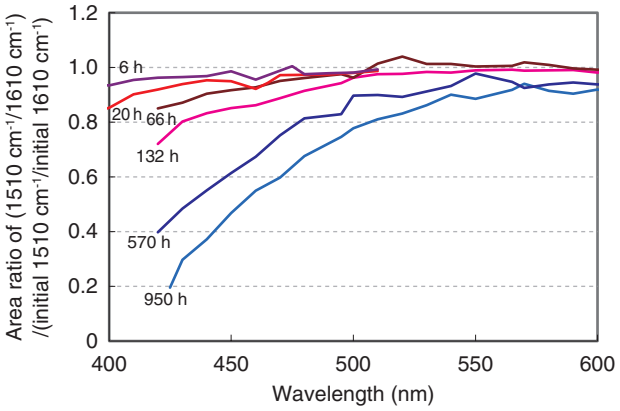


Fig. 10 Area ratio of before and after irradiation

4. Considerations

4.1. Considerations regarding Mechanism of Photo-degradation

At first it was hypothesized that photo-degradation of the E-coat occurred as a result of UV light, but the results shown in Figs. 9 and 10 indicated that the irradiation energy of visible light of wavelength between 450 nm and 550 nm also cleaves and dissociates the bonds in the binder. As causes of this phenomenon, it is possible to first consider the white pigment and corrosion inhibitor in the E-coat. However, because both are white powders, they reflect light rays of wavelength of 550 nm and below[6]. Carbon black is also included in the E-coat as a black pigment, but because it possesses a chemically stable structure[7], it is not considered to be a point of origin for degradation. FT-IR spectra were therefore studied before and after irradiation. As Fig. 11 shows, in addition to the production of peroxide and carbonyl as a result of degradation following irradiation,

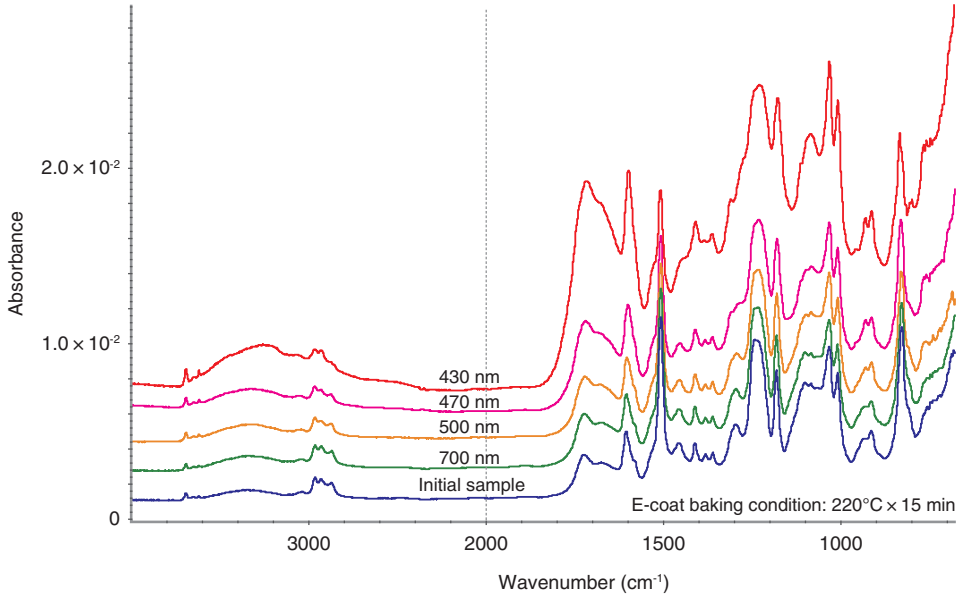


Fig. 9 FT-IR spectrum of E-coat photo-degradation (Irradiation time 950 hr)

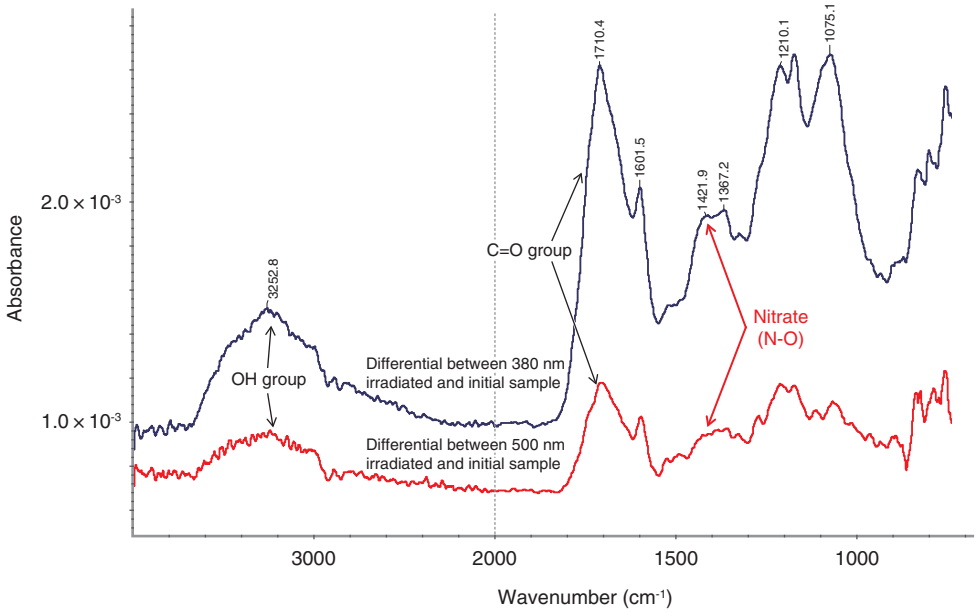


Fig. 11 Differential FT-IR spectrum of E-coat

there is also a slight peak close to 1400 cm^{-1} originating in NOx, and this NOx component is therefore considered to have an effect on degradation. Because NOx is highly prone to form radicals[8], there is considered to be a strong possibility that radicals produced from NOx as a result of irradiation to visible light of between 450 nm and 550 nm could result in cleavage of the bonds in the bisphenol resin. This NOx component is considered to become incorporated in the E-coat in small quantities as an impurity during curing.

4.2. Range of Light Wavelength That Affect Peeling

The results of the study discussed in Section 4.1. showed that light at wavelength of 450 nm and below resulted in degradation corresponding to a decline in the film strength of the E-coat, while light at wavelength of between 450 nm and 550 nm, despite the fact that no decline in film strength was observed, caused cleavage of the bonds in the bisphenol resin. While the form of degradation differs, because the peaks in areas on which light, for example of wavelength of 430 nm and 500 nm, was incident are similar (Fig. 9), it is considered that the only difference is the degree of cleavage of the bonds in the bisphenol resin. Bisphenol is the main binder of the E-coat, and it is therefore necessary to attempt to prevent its reduction by degradation. In addition, it is also considered to be necessary to intercept light of wavelength of 550 nm and below and attempt to prevent peeling of the topcoat in order to help prevent the production of the radicals that are thought to be the main factor in photo-degradation.

5. Countermeasure against Photo-degradation

5.1. Determination of Paint Content

Based on the analysis results discussed above, paint content was formulated in which a layer that intercepted light (1 base) was situated under the color-developing layer (2 base). In designing the 1 base, the ability to stably intercept light of wavelength of below 550 nm by means of management to produce a suitable film build was an important consideration. The design therefore made it possible to intercept light using a suitable film build with wide-ranging light absorption properties, from the UV range to the visible spectrum. The 2 base can be applied after application of the 1 base, with no drying or curing process, making it possible to remove the primer process. As a result, it has been possible to achieve a light interception function with color variations. Figure 12 shows the content of the paint. To provide an example of the interception function, Fig. 13 shows light transmittance when the 1 base is made of a neutral color.

5.2. Results of Verification of Weather Durability

The paint content designed in this research was subjected to an outdoor exposure test, and no peeling of the coating was observed (Fig. 14).

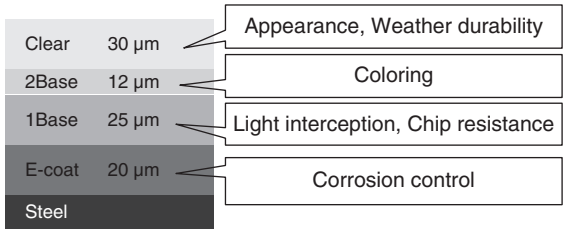
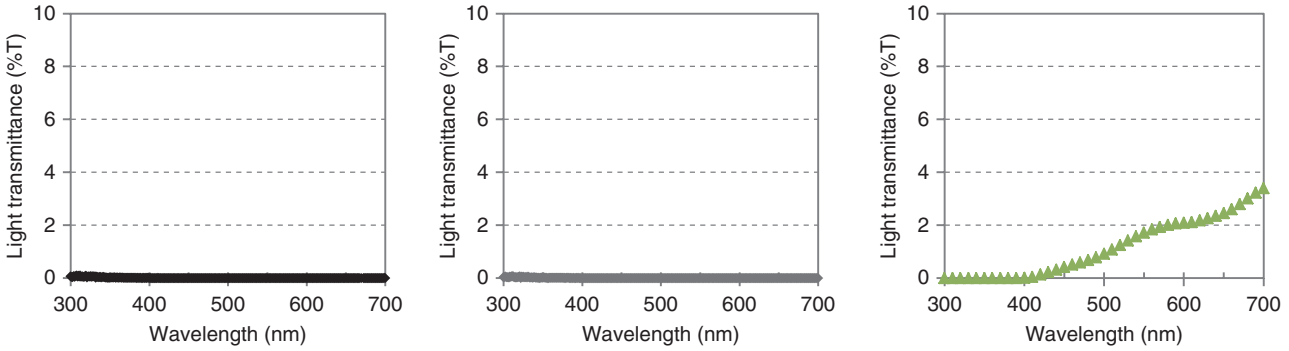
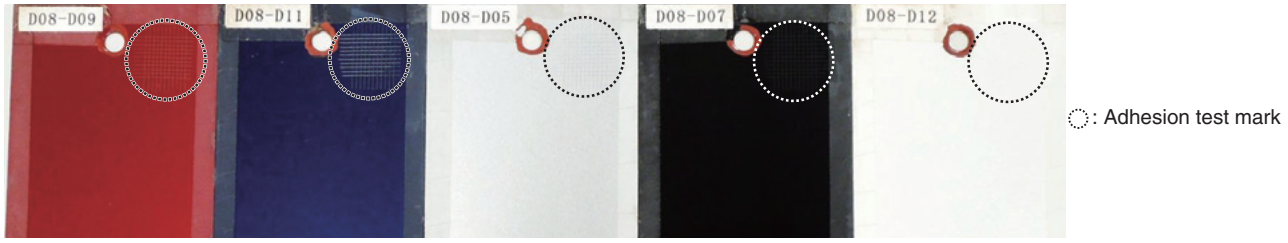


Fig. 12 Standard layer structure of 3C2B paint system of Honda



(a) Dark gray (L*=20, Film build 15 μm) (b) Middle gray (L*=50, Film build 15 μm) (c) Light gray (L*=80, Film build 20 μm)

Fig. 13 Light transmittance of 1BC



(a) Red (b) Blue (c) Silver (d) Black (e) White

Fig. 14 Result of exposure test

6. Conclusion

The photo-degradation behavior of an E-coat was analyzed and the countermeasure was determined. The results are as follows.

(1) A decline in the film strength of the E-coat was observed as a result of irradiated wavelength of 450 nm and below.
(2) Cleavage of the bonds in the bisphenol binder of the E-coat was observed as a result of irradiated wavelength of 550 nm and below.

Based on these results, a layer able to stably intercept light of wavelengths of below 550 nm (1 base) has been applied before the color-developing layer (2 base), making application possible without processes such as drying, reconciling the removal of the primer process with color variations. This has reduced both the length of the paint process and CO_2 emissions against the conventional paint process.

References

(1) Kadowaki, K., Endou, M., Hiramatsu, Y.: Development of Waterborne Automotive Coatings Applicable in 3 Wet System Aiming at Environmental Protection, Toryou no kenkyu, No. 144, p. 50-54 (2005) (in Japanese)
(2) Muramoto, H.: Multi-Layered Electrodeposition Paint and its Application to Automotive Coatings, TECHNO-COSMOS, Vol. 17, p. 2-7 (2004) (in Japanese)
(3) Fox, M. A., Whitesell, J. K.: Organic Chemistry I, Maruzen Publishing, 356p. (1999) (in Japanese)
(4) Monney, L., Belali, R., Vebrel, J., Dubois, C., Chambaudet, A.: Photochemical degradation study of an epoxy material by IR-ATR spectroscopy, Polymer Degradation and Stability, Vol. 62, No. 2, p. 353-359 (1998)
(5) Atlas Material Testing Technology LLC: Atlas Weathering Testing Guidebook, p. 14 (2003)
(6) Guo, B., Liu, Z., Hong, L., Jiang, H., Yan Lee J.: Photocatalytic effect of the sol-gel derived nanoporous TiO_2 transparent thin films, Thin Solid Films, Vol. 479, p. 310-315 (2005)
(7) Mochida, I.: Tansozai no kagaku to kougaku, Asakura Publishing, 248p., (1990) (in Japanese)
(8) Suzuki, H.: Chissosankabutsu no jiten, Maruzen Publishing, 484p., (2008) (in Japanese)

■ Author ■


Keisuke KOJIMA


Takamasa AOKI


Takeshi OGAWA

Study of High Smooth Electrodeposition Coating That Enables Primer Process-less Paint System

Katsuyoshi KANEKO* Toshikazu HIROBE*
Yusuke KAWADA* Tatsumasa HIDAKA*

ABSTRACT

A study was conducted on a high smooth electrodeposition coat that enables a 3-coat 2-bake primer process-less paint system. This study attempted to suppress the gas pinholes remaining in the deposition film before drying. The methods investigated were to suppress hydrogen gas generation by reducing the neutralizing acid concentration in the e-coat bath, and to enhance gas escape during electrodeposition by optimizing the deposition film viscosity. Application of these methods achieved a smoothness that enables a 3-coat 2-bake primer process-less paint system to secure a paint appearance equal to that provided by the current 4-coat 3-bake paint system.

1. Introduction

The purpose of automotive body paint is to secure anti-corrosion quality and color design. General automotive body paint uses a 4-coat 3-bake (4C3B) coating consisting of an electrodeposition coat (e-coat) that provides anti-corrosion functions, a primer coat that hides the surface roughness, provides chipping resistance (resistance to stone-chip paint damage) and blocks light to the e-coat, and a top coat consisting of a basecoat layer and clear layer that manifest the color design. Research based on this coat composition is proceeding for coating color design such as super-brilliant silver metallic coating[(1)], and also to achieve coat surfaces with high image clarity. Regarding high image clarity, numerous examples of technical development of coating materials aimed at increasing the coating surface smoothness have been reported since the 1980s, including the use of two primer layers, development of high-finish basecoat materials, and use of two clear coat layers[(2), (3)]. In addition, an example has also been reported of technology that enhances the paint appearance by using steel plate that achieves high image clarity by controlling the unevenness of the ground steel plate surface[(4)], and demands for paint appearance remain high.

On the other hand, amidst calls to prevent global warming, there are also demands to reduce CO_2 generated by the automobile production process, and development of new production technology is proceeding. A short-process paint system that integrates the primer and top coat processes has recently been introduced for body paint and use is spreading, but there are concerns about a drop in paint appearance (image clarity). A typical measure to address this is to change the clear coating to a high smooth type, but the use of high smooth-type coatings poses cost increase issues.

Previously, the hiding of surface roughness that affects paint appearance was performed by the primer coat (25 μm to 35 μm) present between the e-coat and top coat, and the e-coat (15 μm to 20 μm), which is applied to secure anti-corrosion quality, was not subject to high demands for smoothness. However, in the 3-coat 2-bake (3C2B) primer process-less paint system, the surface roughness-hiding function of the primer is performed by the e-coat and top coat (Fig. 1).

This study investigated the smoothness of the e-coat, which had mainly provided anti-corrosion functions thus far and was not the subject of attention for its contribution

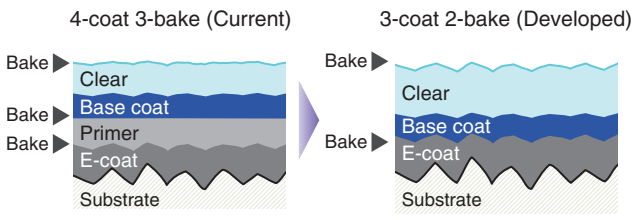


Fig. 1 Body paint structure

* Automobile R&D Center

to paint appearance. As a result, an e-coat smoothness was achieved that can secure a marketable paint appearance even without the use of a high smooth-type clear coating. This paper describes these details. The investigations in this study used a coat thickness of 15 μm, which is a strict condition for the e-coat thickness on outer panels that require good paint appearance.

2. Investigation of High Smooth Film Deposition Methods

The e-coat can be broadly divided into a coating resin component and a pigment component. Development of a new coating resin component affects the most important e-coat functions of anti-corrosion performance and throwing-power performance, so smoothing methods that do not involve a change in the resin component were investigated.

There are two possible methods as follows. The first method is to increase the ratio of the coating resin component that forms the coat. This reduces the ratio of the pigment component that impedes thermal flowing of the coat during drying, which enhances fluidity and makes it easier to form a smooth surface. However, enhancing the thermal fluidity brings about a drop in the melt viscosity, with the result that the coating coverage is insufficient at the edges of the coated object due to shrinkage stress during drying, making it easier for corrosion to occur (Fig. 2).

The second method is to reduce the surface conditioner, which is called an anti-crater additive. Oils and grease that could not be completely removed in the previous process or that were used in the various work processes may be adhered to the body on which e-coating is to be performed, or substances with properties that suppress thermal fluidity may be applied to maintain quality. This surface conditioner suppresses the fluidity of the coating in order to suppress the expansion of crater-shaped coat defects produced by contamination. This property conflicts with increasing the smoothness. In addition, reducing this surface conditioner not only lowers the crater resistance, but may also reduce the adhesion with the seam sealer and underbody coat.

The above two methods are subject to the previously described concerns.

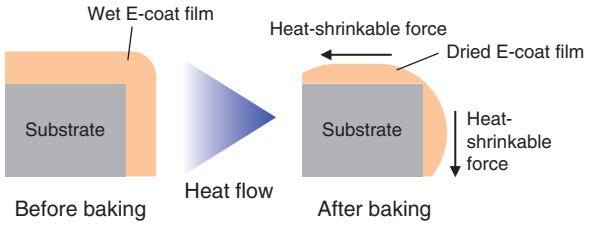


Fig. 2 Edge-covering property

Increasing the e-coat bath temperature and adding solvent are recognized as effective means of increasing the e-coat smoothness, but these detailed mechanisms have not yet been discussed. Increasing the e-coat bath temperature means that the behavior in the film deposition process is affected by the coat viscosity. Adding solvent increases the amount of solvent that transfers to the deposition film, which likewise means that the behavior in the film deposition process is affected by the coat viscosity. Hydrogen gas is produced on the steel substrate in the electrodeposition process, and this hydrogen gas escapes by passing through the film. The authors hypothesized that the increase in smoothness due to increasing the e-coat bath temperature and adding solvent is rooted in the behavior of the hydrogen gas produced during e-coat deposition. However, it was inconceivable that the hydrogen gas itself affected the film smoothness, so this study focused on the film, that is to say on the gas pinholes remaining in the film, after the hydrogen gas had escaped.

3. Reduction of Hydrogen Gas Pinholes

Equations (1) and (2) show the chemical formulas for the e-coat chemical reaction and deposition mechanism.

$$2H_2O + 2e^- \rightarrow H_2 + 2OH^- \quad (1)$$

$$RNH_3^+ + OH^- \rightarrow RNH_2 + H_2O \quad (2)$$

The water electrolysis shown in Eq. (1) occurs on the surface of the negatively charged substrate, with the result that OH radicals are generated on the steel surface. The OH radicals neutralize the acid that was suspended in the paint particles, so the paint particles lose their charge and deposit onto the steel surface as shown in Eq. (2) (Fig. 3)[5), 6)]. The hydrogen gas produced on the steel substrate by this electrodeposition process escapes intermittently from the film during e-coating, but traces of where the gas escaped exist as gas pinholes in the film. These gas pinholes cannot be completely repaired even in the thermal flowing process during drying, and remain as unevenness in the film surface. There are two possible methods as follows for reducing

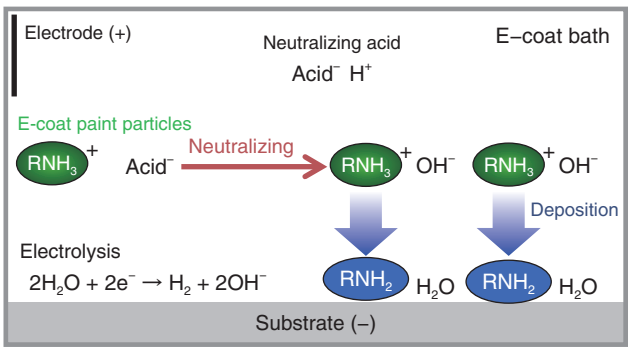


Fig. 3 Schematic image of E-coat

these hydrogen gas pinholes. The first is to increase the film deposition efficiency to reduce the amount of gas produced, and the second is to enhance the hydrogen gas escape. These two methods reduce the gas pinholes remaining in the film, so they can be expected to increase the film smoothness after drying (Fig. 4).

3.1. Increase in Deposition Efficiency

The amount of hydrogen gas is determined by the amount of electricity that flowed as shown in Eq. (1). That is to say, film deposition that uses less electricity also suppresses the amount of hydrogen gas produced. The deposition efficiency (film mass that can be deposited per unit coulomb) can be considered as an index for this purpose. Potential methods for increasing this deposition efficiency are to reduce the neutralizing acid concentration (MEQ) and to increase the solid concentration (NV) in the paint. This study attempted to reduce the MEQ. Positively charged paint particles are neutralized by acid and dispersed stably within the e-coat (Fig. 5), and the acid is then neutralized by OH radicals generated by water electrolysis. When using a high MEQ design created to stably disperse the paint particles, many OH radicals are consumed in neutralizing the acid, with the result that the amount of produced hydrogen gas increases. Therefore, it was thought that if a low MEQ design that was sufficient to neutralize the paint particles could be achieved, the film could be deposited using a smaller amount of electricity, which would reduce the amount of gas produced with the result that there would be fewer gas pinholes remaining and the smoothness would increase. This study compared high MEQ design and low MEQ design deposition films, and the results showed that, as expected, the low MEQ design reduced both the hydrogen gas pinholes remaining in the deposition film and the deposition film surface roughness, and also increased the film smoothness after drying (Fig. 6). Reducing the MEQ lowers the bath stability (dispersibility), but this issue was addressed by using a new high disassociation-type neutralizing acid.

3.2. Enhancement of Hydrogen Gas Escape

Reducing the film viscosity is thought to be an effective means of enhancing gas escape within the deposition film. The film viscosity is dependent on the temperature, so it is important to reduce the viscosity within the e-coat bath temperature range.

First, the relationship between the loss elastic modulus of the deposition film and the deposition film surface

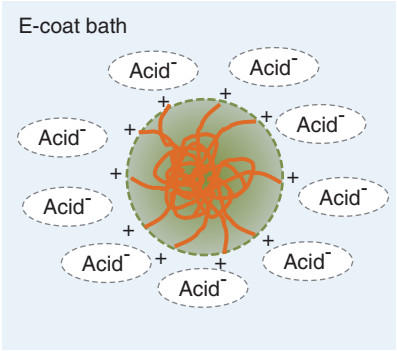


Fig. 5 Function of neutralizing acid

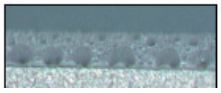
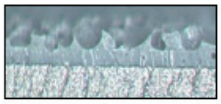
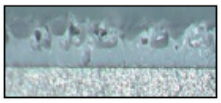
MEQ	High	Low
Beginning of deposition		
End of deposition		
Deposition film Ra	3.70	3.42
E-coat Ra (Dry)	0.17	0.15

Fig. 6 Cross-sectional view of wet film on high and low MEQ

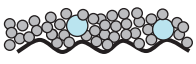
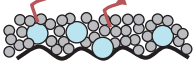
	Standard	High coulomb efficiency	High gas desorption speed
Beginning of deposition		 Lowering H_2 gas	 Easy to go out
End of deposition			
After baking			

Fig. 4 Schematic image of E-coat

roughness was investigated (Fig. 7). The loss elastic modulus is an index of deposition film viscosity, and can be used as a substitute to evaluate gas escape. The deposition film surface roughness was confirmed to decrease together with the loss elastic modulus. That is to say, enhancement of gas escape was proven to reduce surface unevenness. In addition, the deposition film surface roughness exhibited a fairly constant value at a loss elastic modulus of approximately 0.10 MPa or less. This means that there is an optimum value for this e-coat material. The solvent quantity was adjusted to achieve this optimum loss elastic modulus within the e-coat bath temperature range (26°C to 30°C). As a result, a stable deposition film surface roughness could be obtained within the entire temperature range (Fig. 8). The degree of solvent quantity adjustment was extremely small, and there was also no effect on the minimum melt viscosity during drying. This confirmed that the smoothness enhancing effect of solvent adjustment was not due to the reduction in melt viscosity during thermal flowing, and was instead a result of enhanced gas escape during film deposition, which reduced the gas pinholes.

4. Setting the Target

Next, the relationship between the paint appearance and the e-coat smoothness was investigated to determine the target value for the surface roughness-hiding function to be performed by the e-coat in the 3C2B primer process-less paint system. The correlation between the paint appearance index and the three cutoff regions of 0.8 mm, 2.5 mm and 0.8 mm to 8.0 mm was investigated using Ra (arithmetic mean estimation) as the e-coat smoothness index. The curve obtained by cutting off the waviness components longer than the prescribed wavelength from the film profile curve is called the roughness curve, and this wavelength is called the cutoff value. The results showed that the paint appearance index and surface roughness (cutoff 2.5) exhibit a high correlation (Fig. 9). Therefore, the film smoothness that can achieve the paint appearance target was set at Ra ≤ 0.25 (cutoff 2.5), compared to the current Ra ≤ 0.30 (cutoff 2.5) (Fig. 10).

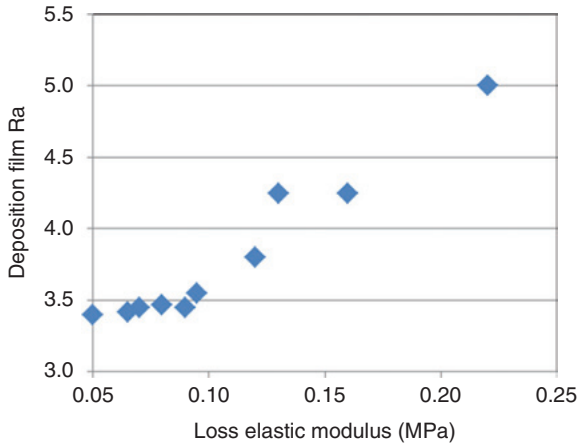


Fig. 7 Relationship between loss elastic modulus and deposition film Ra

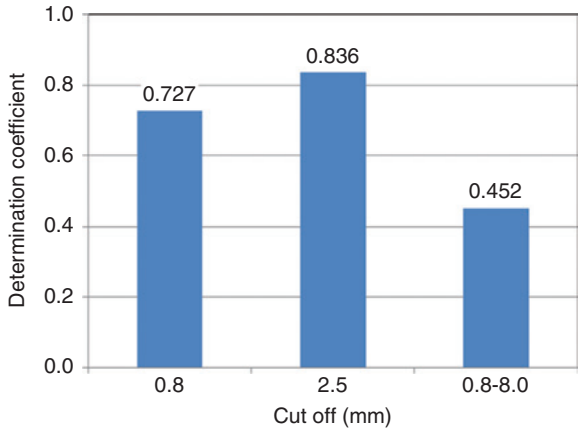


Fig. 9 Determination coefficient with paint appearance index and cut off values

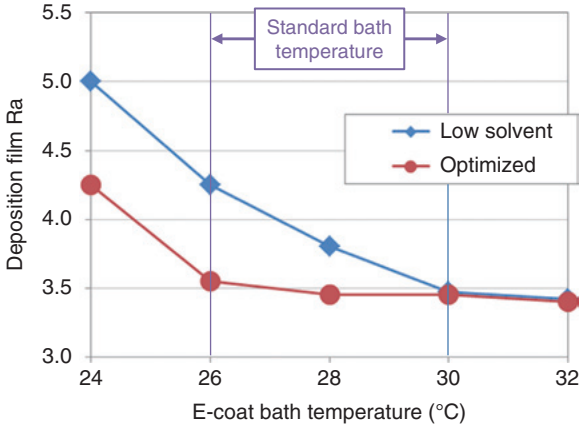


Fig. 8 E-coat bath temperature and deposition film Ra

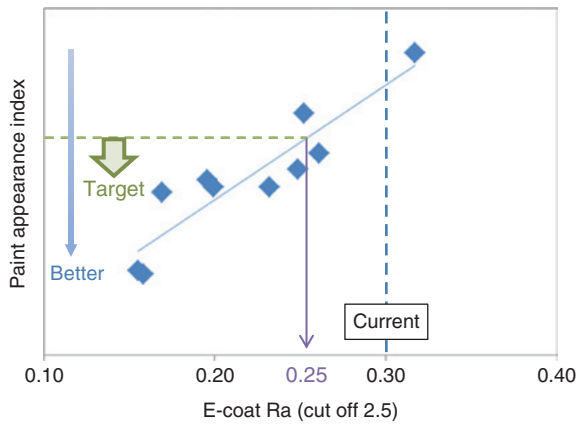


Fig. 10 Paint appearance and E-coat Ra

5. Verification of Effects

The effects were verified using an e-coat that employs the methods investigated in this study and steel sheets with different surface roughness (Fig. 11). The results were better than those for conventional materials within the control range of steel sheet surface roughness and secured a smoothness that satisfied the target value of Ra ≤ 0.25 (cutoff 2.5).

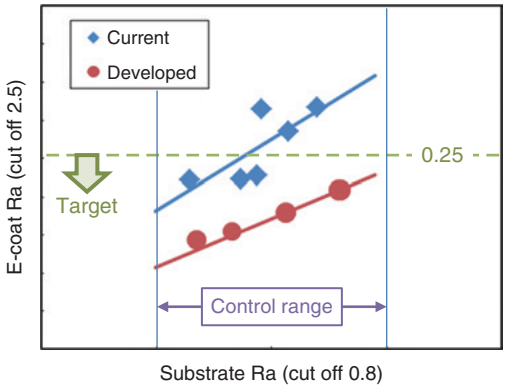


Fig. 11 E-coat Ra and substrate Ra

6. Conclusion

The e-coat smoothness can be increased to a level that supports the 3C2B primer process-less paint system by use of the following methods that reduce gas pinholes in the deposition film.

(1) The MEQ in the coat was reduced to reduce the amount of hydrogen gas produced.
(2) Gas pinholes were reduced by optimizing the deposition film viscosity to enhance gas escape within the deposition film.

An e-coat was developed by combining knowledge on how to increase smoothness obtained through this study with high throwing-power performance. Efforts are underway to promote the successive application of this e-coat to 3C2B primer process-less paint systems that require e-coat smoothness and to Honda's body painting lines.

References

(1) Ogawa, T., Ihara, S., Noumi, E., Kurata, Y.: Development of Super-brilliant Silver Metallic Coating, Honda R&D Technical Review, Vol. 18, No. 1, p. 166-171
(2) Asawa, T., Yamanaka, M., Unuma, A.: High luster and smoothing painting as laminated constitution, Journal of the Japan Society for Composite Materials, Vol. 14, No. 5, p. 181-187 (1988)
(3) Mori, J., Kubota, H., Shigenaga, T., Yamane, T., Kanda, T., Ohzeki, T., Tsuneoka, T.: Development of High Quality Appearance Basecoat, Mazda Technical Review, No. 25, p. 185-189 (2007)
(4) Furukawa, K., Tsunoyama, K., Imanaka, M., Kishida, A., Yamada, Y., Tsunekawa, H.: Development of High Image Clarity Steel Sheet LASERMIRROR, KAWASAKI STEEL GIHO, Vol. 20, No. 3, p. 203-209 (1988)
(5) Hayashi, H.: About Cationic Electrodeposition Coating Process, Journal of the Japan Society of Colour Material, Vol. 84, No. 8, p.283-287 (2011)
(6) Shigenaga, T., Yamada, M.: Development of Environmental-friendly High Throwing Power E-Coat, Mazda Technical Review, No. 24, p. 200-204 (2006)

■ Author ■


Katsuyoshi KANEKO


Toshikazu HIROBE


Yusuke KAWADA


Tatsumasa HIDAKA

Identification of Mechanism of Transmission of Flow-induced Noise through Glass for Vehicle Interior Noise Reduction

Kei AMBO* Kazuya MORISHITA*
Takashi YOSHINO* Minoru TERAMURA*

ABSTRACT

Seeking to identify the target for control to reduce vehicle interior noise, the research discussed in this paper determined the contribution ratio of convectional pressure and acoustic sound to high-frequency flow-induced noise (1 kHz-5 kHz) in the interior of a box modeling a vehicle interior, based on a model of cabin sound transmission from the pillar modeling the flow around the A-pillar. This study showed that the contribution ratio of acoustic sound to the overall value in the high-frequency range at the microphone in the box was approximately 93%, indicating that in the high-frequency range, acoustic sound is dominant in comparison to convectional pressure.

A comparison of the sound pressure distribution on the external surface of the front side glass of an actual vehicle, as estimated from surface pressure fluctuation and far-field sound, with the sound pressure distribution on the internal surface, as estimated from the vehicle interior sound level, showed that the difference between the sound pressure on the external and internal surfaces is almost exactly equal to the glass transmission loss. This result demonstrated that acoustic sound generated outside the vehicle is also dominant in sound transmission through the side glass in an actual vehicle, indicating that the reduction of acoustic sound generated outside the vehicle would be an effective means of increasing the comfort of the vehicle cabin in relation to high-frequency flow-induced noise.

1. Introduction

The achievement of increased fuel efficiency, looking towards the realization of a low-carbon society, and the achievement of increased driving stability and comfort as vehicles become faster are necessary elements in the further development of the automobile. The reduction of vehicle interior noise is one aspect of achieving increased automotive comfort. Sound sources for vehicle interior noise include noise from the engine, exhaust, and drive power transmission mechanism; road noise from the tires and the vibration of the suspension; noise from heating, ventilation and air conditioning (HVAC) systems; and flow-induced noise produced by air flow separation around each part of the vehicle. The electrification of powerplants is proceeding in order to realize increased fuel efficiency, and engine system noise is tending to decline as a consequence. In the FIT EV, for example, the ratio of flow-induced noise transmitted to the interior has increased with increased vehicle speed.

One of the technological issues in attempting to reduce flow-induced noise is determining how the noise is generated and how it comes to be heard inside the vehicle; it is necessary to identify the target for control in order to reduce vehicle interior noise. Among flow-induced noise, high-frequency flow-induced noise (1 kHz-5 kHz) generated around the A-pillar[(1)], including the door mirrors, is considered particularly important. This flow-induced noise is thought to be transmitted through the glass to the interior of the vehicle, but the mechanism of its generation and transmission has not been fully clarified.

The excitation force on the glass when noise is transmitted into the vehicle interior is thought to be made up of convectional pressure acting on the glass and acoustic sound generated by the fluctuations of vortices acting on the glass. In order to identify the control target for reducing vehicle interior noise, it is important to determine the contribution ratio of this convectional pressure and acoustic sound. Using wind tunnel tests of a vehicle interior noise measurement model fitted with a glass plate, Iida et al. showed that acoustic sound possess the property of passing readily to the interior of the vehicle[(2)]. However, the sound source was random noise, and this research did not identify the contribution ratio of convectional pressure and acoustic

* Fundamental Technology Research Center

sound originating in aerodynamic phenomena to vehicle interior noise.

The present research therefore sought to identify the control target for reducing vehicle interior noise. First, using a model of cabin sound transmission from the pillar modeling the flow around A-pillar that modeled the flow around the pillar (Fig. 1), the research identified the contribution ratio of convectional pressure and acoustic sound to vehicle interior noise when high-frequency flow-induced noise is transmitted to the cabin. Following this, it conducted a comparison of vehicle interior and vehicle exterior noise in an actual vehicle.

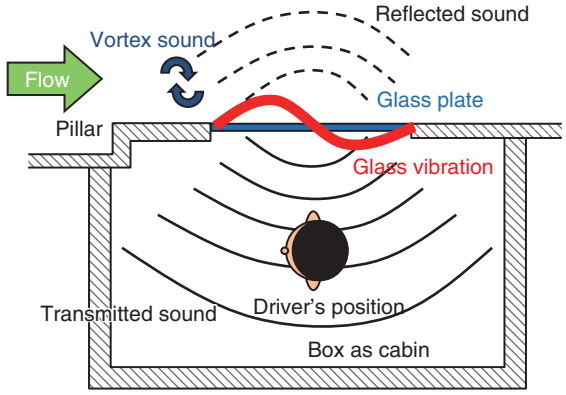


Fig. 1 Model of cabin sound transmission from pillar modeling flow around A-pillar

2. Determination of Glass Transmission Characteristics in Wind Tunnel Tests

Tests on the model of cabin sound transmission from the A-pillar were conducted in a closed loop low-noise wind tunnel of the specifications shown in Table 1 and Fig. 2(a). The model used a step, modeling a pillar, which connected the lower surface of the wind tunnel nozzle and the ground plate [Fig. 2(b)]. A glass plate was positioned on the downstream side of the step. As shown in Fig. 2(c), this glass plate had the same surface area as the front side windows in the FIT HYBRID. A box modeling a vehicle interior was positioned underneath the glass plate. To help eliminate the effect of acoustic resonance in the interior of the box, the entire box, other than the glass plate forming its roof, was covered in acoustic material to create an anechoic chamber. Measurements were conducted under the conditions shown in Table 2. Multi-field microphones, able to produce accurate measurement results in both reverberant and anechoic chambers, were used to measure far-field sound at a position of 1 m above the step as well as sound within the box (Fig. 3).

As Fig. 4 shows, differences in the thickness of the glass produce differences in the frequencies and sound pressure inside the box, indicating a different mechanism of transmission through the glass. In addition, while it was

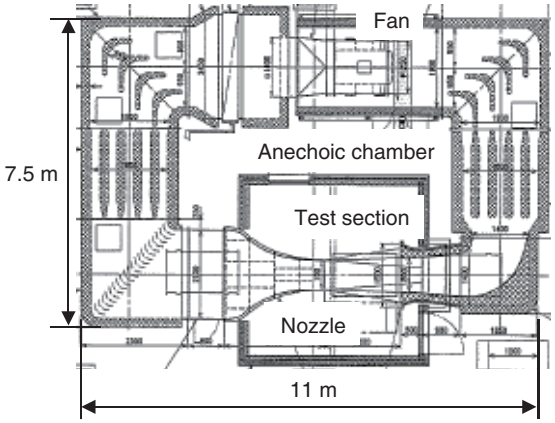
Table 1 Wind tunnel specifications

Maximum velocity	50 m/s
Background noise	54 dBA (30 m/s)
Nozzle exit size	0.7 × 0.7 m^2
Anechoic chamber size	4 × 4 × 3 m^3

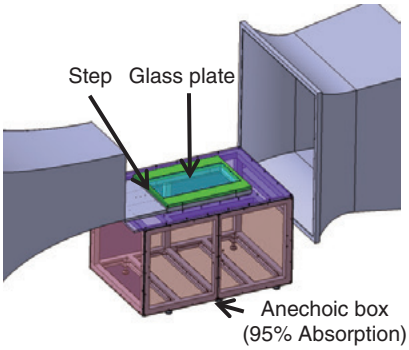
Table 2 Measurement conditions

Step height, H [mm]	30
Nozzle exit velocity, V [m/s]	33
Glass thickness [mm]	3, 4, 5
Microphone sampling frequency [Hz]	32000

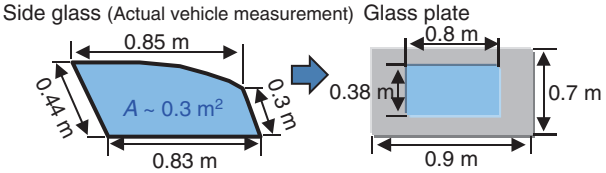
predicted that the vibration of the glass would change with its thickness, the fact that no change was observed in far-field sound for different thicknesses of glass indicates that the influence of vibration of the glass on far-field sound and the flow field is minimal.



(a) Schematic image of low-noise wind tunnel facility



(b) Schematic view of WT set-up



(c) Dimensions of glass plate

Fig. 2 Experimental set-up

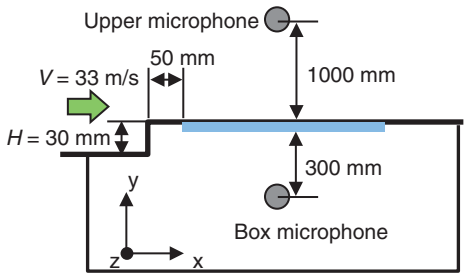


Fig. 3 Microphone positions

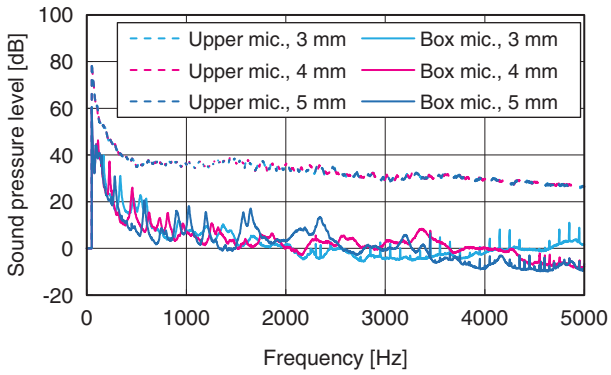


Fig. 4 Experimental results

3. Contribution ratio of Convectional Pressure and Acoustic Sound

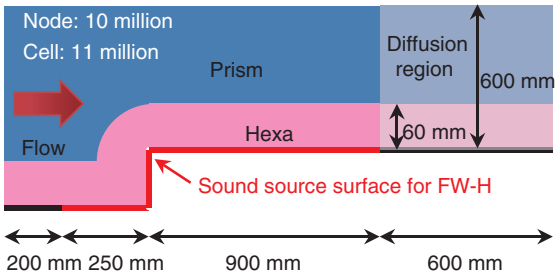
3.1. Method of Identification of Aeroacoustic Sound Source

Powell's theory of vortex sound locates the aeroacoustic sound source in the fluctuations of vortices generated in the vicinity of physical bodies[3]. Research has been conducted on the use of a statistical method (Stochastic Noise Generation and Radiation) in the identification of sound sources in order to reduce calculation cost[4], but the present research employed incompressible unsteady Large-Eddy Simulation (LES) in order to study the sound source, the vortex motion of the separation flow, in greater detail. A hexa mesh, consisting mainly of hexa and prism elements, was used in the analysis (Fig. 5). Table 3 shows the CFD calculation conditions.

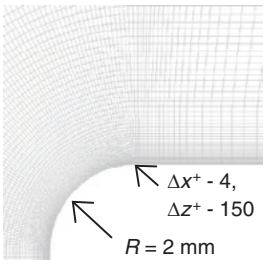
Far-field sound 1 m above the step was predicted based on pressure fluctuations in the sound source surface shown in Fig. 5(a) using the Ffowcs Williams-Hawkings (FW-H) method. Because the width in the direction of the span differed in the analysis and the test, the sound pressure in the analysis results was corrected using a correction formula proposed by Kato, et al.[5] Figure 6 shows a comparison of the predicted and measured values for the frequency distribution of far-field sound, in addition to the instantaneous vortex distribution on the hexa mesh. Figure 6(a) shows that the results for far-field sound obtained using the FW-H method correspond well with the

Table 3 CFD calculation conditions

Software	Fluent ver. 13.0 SP2
Inlet velocity, V [m/s]	33
Step height, H [mm]	30
Reynolds number [–]	66000

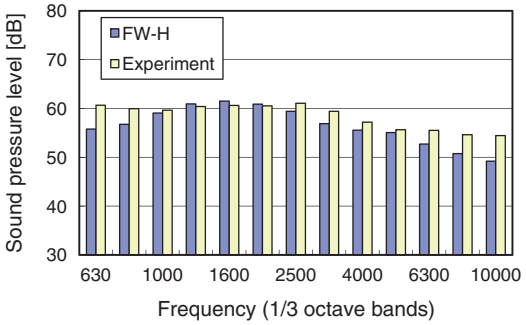


(a) Hexa/Prism mesh (Hexa mesh)

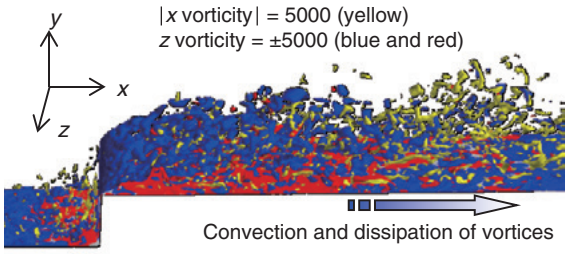


(b) Hexa mesh (enlarged view)

Fig. 5 CFD mesh



(a) Far-field sound spectra at 1 m above step



(b) Instantaneous vortex distribution

Fig. 6 CFD results

values obtained from the tests in the 1 kHz-5 kHz high-frequency flow-induced noise band. Figure 6(b) shows that directly following air-flow separation by the step, numerous horizontal vortices with Z-vorticity, (shown as blue and red) are produced, while following reattachment, numerous vertical vortices (yellow) with X-vorticity are produced, and the number of horizontal vortices declines.

3.2. Computational Aeroacoustic Analysis

Next, in order to identify the generation and propagation of acoustic sounds in the flow field using a decoupled solution, a computational aeroacoustics analysis (CAA)[7], in which the Lighthill equation[6], the governing equation, was discretized and solved using the finite element method, was employed. As shown in Fig. 7, an analytic mesh was generated in part of the flow field; a Lighthill tensor obtained from unsteady LES that extended the width in the direction of the span to 190 mm using hexa mesh was mapped as the sound source, and the status of generation and propagation of sound in the frequency domain was analyzed. A maximum mesh size of 5 mm was used in the CAA analysis, and the resolution for wavelengths of 5000 Hz was 10 points or more. Using infinite elements for the boundaries in the directions of the circumference and span, far-field sound was predicted using fifth-order extrapolation. Table 4 shows the calculation conditions for the CAA analysis.

Figure 8 shows a comparison of predicted and measured values for the directivity of far-field sound in the high-frequency range, in addition to the sound pressure distribution close to the step. Figure 8(a) shows that the results of predictions using CAA analysis display a better correspondence with results obtained from tests than predictions based on the FW-H method. This can be considered to result from the fact that CAA analysis is able to more accurately study the generation of quadripole sound by the fluctuations of the vortices and its process of propagation as dipole sound due to reflection and scattering at boundaries with physical body[8] than the FW-H method. An area of high acoustic pressure is conspicuous at the front of the region of air-flow separation at the step in Fig. 8(b). This area of high acoustic pressure corresponds to the area in which numerous horizontal vortices with Z-vorticity were shown to be produced in the comparison shown in Fig. 6(b).

Table 4 CAA calculation conditions

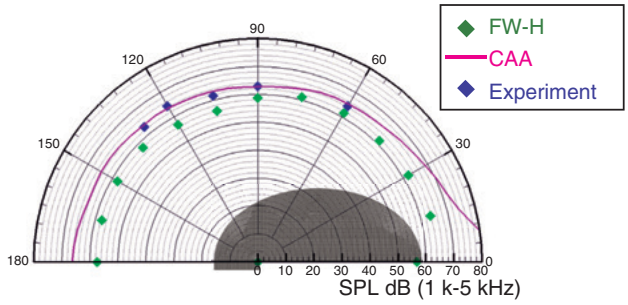
Software	ACTRAN/AA ver. 11.1
Sound source	Lighthill-Volume
Maximum frequency	f_{max} = 10752 Hz
Frequency filter	Δf = 14.3 Hz

Table 5 VA analysis calculation conditions

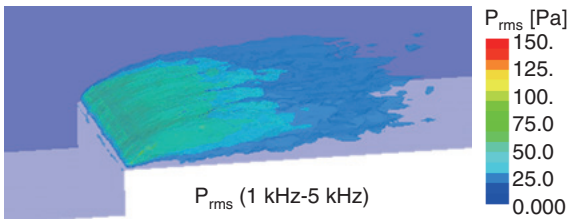
Software	ACTRAN/VA ver. 11.1
Vibration source	Acoustic and/or convectional pressure
Glass density	2500 kg/m^3
Glass Young's modulus	7.16 × 10^{10} (damping 3%)
Fixed point modeling as spring	Stiffness 90000 N/m
Maximum mesh size	5 mm (glass), 9.6 mm (air)
Maximum frequency	f_{max} = 10752 Hz
Frequency filter	Δf = 14.3 Hz

3.3. Method of Analysis of Vibro Acoustic

Far-field sound, the sound pressure distribution within the area under analysis, and the excitation force acting on the glass were determined from the CAA analysis discussed above. Here, a vibroacoustic (VA) analysis was conducted, as shown in Fig. 9. The glass excitation force was mapped as a vibration input, and the frequency response of the glass and a CAA analysis of the interior of a box modeling a vehicle interior were coupled for analysis. The influence of the coincidence effect, in which transmission loss declines at specific frequencies, was considered in the analysis of the frequency response of the glass. Prior to this analysis, the



(a) Far-field sound direction at 1 m from step



(b) Near-field sound distribution

Fig. 8 CAA results

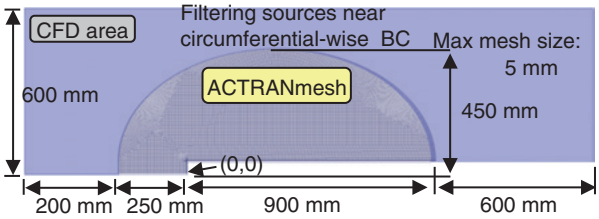


Fig. 7 CAA analysis

vibration mode of the glass and its acoustic transmission loss, as determined from the results of basic unit tests, were calibrated using the glass constraint conditions and damping rate as parameters[9]. Table 5 shows the calculation conditions for the VA analysis. The mesh size for the space inside the box was set as the wavelength of the frequency in the glass normal direction only, divided into six parts; infinite elements were used for boundary conditions, and the effect of rebound of interior sound was ignored.

Figure 10 compares predicted and measured values for the frequency distribution of far-field sound and box-interior sound. The excitation force employed included the convectional pressure and acoustic sound determined in the CAA analysis. While multiple samples were not used for the CAA analysis, and statistical variations therefore occur for each frequency, Fig. 10 shows that the results of prediction of sound pressure levels correspond well with measurement results. Table 6 shows a comparison of predicted and measured overall (OA) values (the total of sound pressure levels in the high-frequency range) for far-field and box-interior sound.

Table 6 shows that the sound pressure for the microphone positioned in the box in the CAA analysis is around 2 dB lower than the measured value, but because the same tendency can be observed for far-field sound, the main factor producing this result is thought to be the fact that the numerical analysis exclusively evaluates sound ideally transmitted from an aeroacoustic sound source, while the

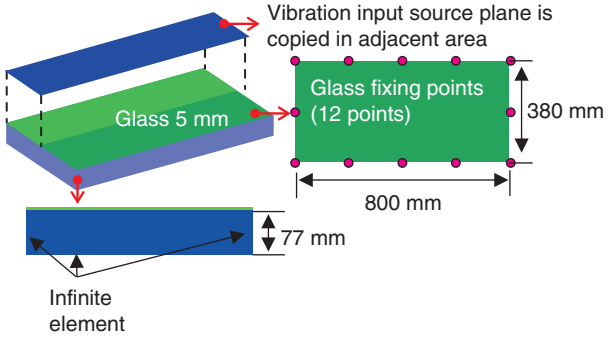


Fig. 9 VA analysis

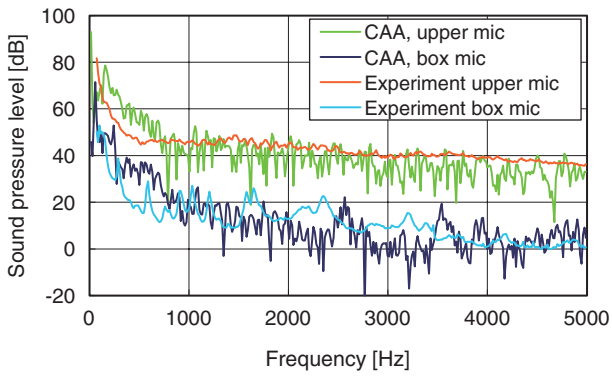


Fig. 10 Sound spectra at upper and box microphone positions (Glass 5 mm)

Table 6 Overall sound pressure level (1 kHz-5 kHz) at upper and box microphone

Microphone location	CAA [dB]	Experiment [dB]
Upper (far-field) mic	65.1	67.1
Box mic	36.6	38.9
Δ SPL (Transmission loss)	28.5	28.2

test results incorporate the effect of environmental noise. In addition, there is a good correspondence between values predicted using CAA analysis and measured values for the difference between far-field and box-interior sound (ΔSPL), which expresses glass transmission loss. This is considered to demonstrate that calibration based on the results of the basic unit tests of the glass plate made it possible to conduct an accurate VA analysis.

Verification of the method for identification of the aeroacoustic sound source and the CAA and VA analysis methods, as described above, demonstrated the realization of a level of analytic accuracy making it possible to achieve a good quantitative correlation with test results for high-frequency flow-induced noise, creating the potential for identification of the contribution ratio of convectional pressure and acoustic sound to noise in the vehicle interior using these technologies.

3.4. Determination of Contribution Ratio of Convectional Pressure and Acoustic Sound

The contribution ratio of convectional pressure and acoustic sound to sound pressure inside the box was determined by conducting a VA analysis of the type discussed in Section 3.3 while varying the excitation force acting on the glass.

Because the excitation force acting on the glass in Section 3.1 (Fig. 11) was determined using incompressible unsteady LES, it represents the excitation force due exclusively to convectional pressure. The excitation force acting on the glass in Section 3.2 (Fig. 12) is thought to incorporate acoustic excitation force produced by convectional pressure and acoustic sound. This is because a wave equation (the Lighthill equation) derived from the Navier-Stokes equation, the governing equation of the flow,

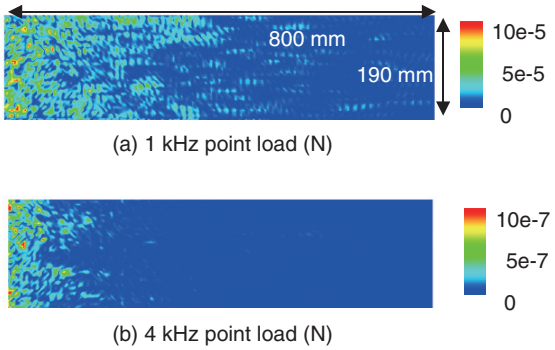
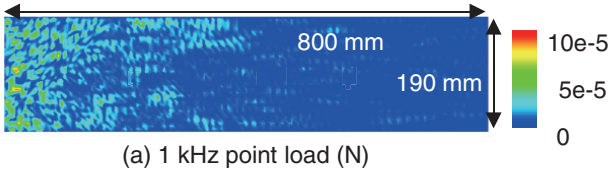


Fig. 11 Convectional pressure load (Glass 5 mm)

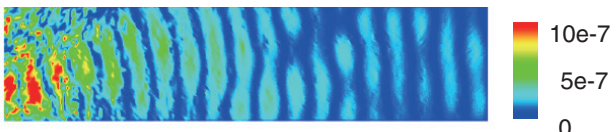
and a continuity equation, was employed as the governing equation. The pressure fluctuations in Section 3.1 and 3.2 were employed as the excitation force input for Section 3.3, and the box-interior sound in response to differences in the pressure fluctuations of the glass surface was determined.

In the case of box-interior sound when convectional pressure is used as the excitation force, the difference between calculated and measured values tends to become greater as the frequency increases (Fig. 13).

Determination of the difference between box-interior sound when the acoustic excitation force due to convectional pressure and acoustic sound is used as the glass excitation force and when convectional pressure is used as the glass excitation force made it possible to define the contribution ratio of acoustic sound. Figure 14 shows the frequency distribution for the contribution ratio of acoustic sound and the contribution ratio of acoustic sound at the OA value in the high-frequency range for the microphone in the box. In Fig. 14(a), while convectional pressure displays a contribution rate of around 10% between 1.0 kHz and 1.6 kHz, in the higher-frequency 2.5 kHz-5.0 kHz range, its contribution ratio is only several percent, and the contribution ratio of acoustic sound becomes dominant. In Fig. 14(b), the contribution ratio of acoustic sound at the OA value is approximately 93%, indicating that acoustic sound is dominant in the high-frequency range.



(a) 1 kHz point load (N)



(b) 4 kHz point load (N)

Fig. 12 Acoustic and convectional pressure load (Glass 5 mm)

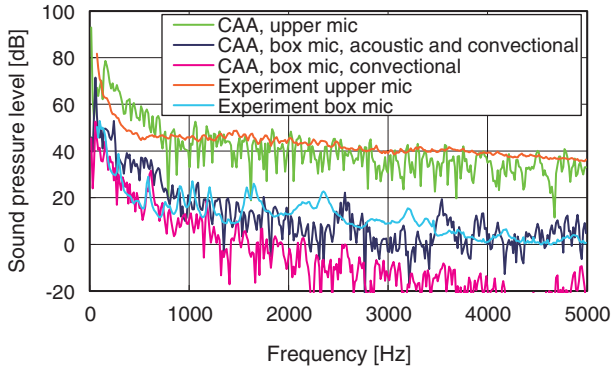
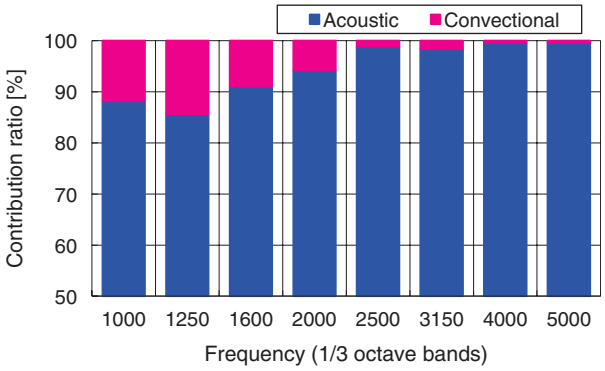
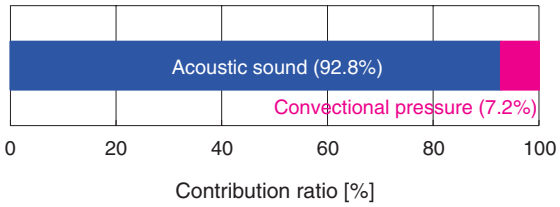


Fig. 13 Sound spectra at upper and box microphone positions

Figure 15 shows a sound propagation diagram[10] using pressure contours at 4 kHz, including the glass and the step. This figure also demonstrates that acoustic sound generated close to the step is propagated through the air, and transmitted into the interior of the box with no phase difference.



(a) Contribution ratio for 1/3 octave bands



(b) Overall sound pressure level (1 kHz-5 kHz)

Fig. 14 Contribution ratio of acoustic sound

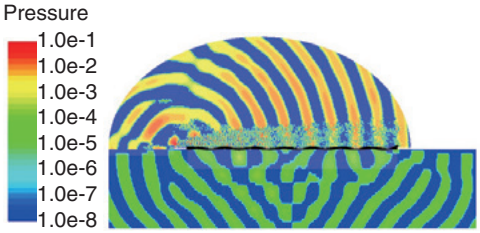


Fig. 15 Sound propagation at 4 kHz (Sound pressure [Pa])

4. Simultaneous Measurement of Interior and Exterior Acoustic Sound in an Actual Vehicle

Nouzawa, et al. studied the effect of acoustic noise in each frequency band on the vehicle interior[11], but research has not focused on sound generated by flow-induced noise passing through the side glass as a means of increasing interior comfort with respect to high-frequency flow-induced noise. The present research therefore attempted to clarify the relationship between the acoustic pressure at the glass surface, estimated from the far-field external noise, the pressure fluctuation on the glass surface, and the noise transmitted to the interior of the cabin.

Here,

Ps: Convectional pressure and acoustic sound

Pf: Acoustic sound

Pi: Sound pressure on the surface of the glass in the vehicle interior

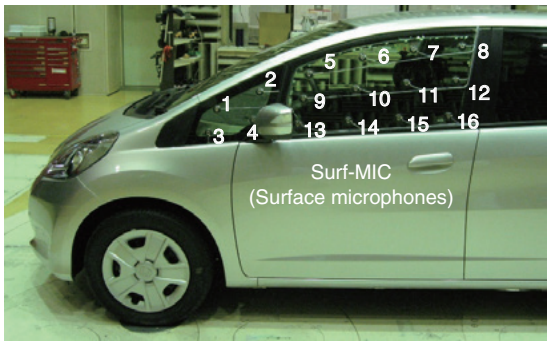
Table 7 shows an overview of the measurement equipment. Values measured using surface microphones attached to the external surface of the glass (Fig. 16) were used for *Ps*; for *Pf*, the acoustic pressure distribution at the side of the vehicle calculated using the beamforming method [Fig. 17(b)] from noise measurements taken by a planar microphone array positioned at a distance [Fig. 17(a)] was used. In order to evaluate sound transmitted to the vehicle interior, noise measurements were conducted using a spherical microphone array [Fig. 18(a)], and the distribution of *Pi* was calculated using the spherical beamforming method [Fig. 18(b)]. As Fig. 16(a) shows, the surface microphones were attached to the glass discretely. Because of this, for each physical quantity (*Ps*, *Pf*, and *Pi*), the values measured at the corresponding surface microphone measurement points (#1-#16) for two plates of side glass (plate thickness: 3.5 mm) fixed in place using different methods were made representative values, and their averages were used.

The relationship between the acoustic pressure at the surface of the side glass, estimated from the far-field external noise, the pressure fluctuation on the glass surface, and the noise transmitted to the interior of the cabin was determined using the following method: The values produced by subtracting the dB figures for *Pi* from the dB figures for *Ps* and *Pf*, respectively, and the transmission loss figures for the glass plates used in Chapter 2 (plate thickness: 3 mm and 4 mm) were compared (Fig. 19). The results for the transmission loss of the glass plates and the difference between *Pf* and *Pi* (*Pf* – *Pi*) are similar. By contrast, the results for the difference between *Ps* and *Pi* (*Ps* – *Pi*), which are equal to convectional pressure, are higher than the figures for glass transmission loss. Based on this result, it can be conjectured that there is almost no transmission of convectional pressure to the vehicle interior as sound pressure fluctuations.

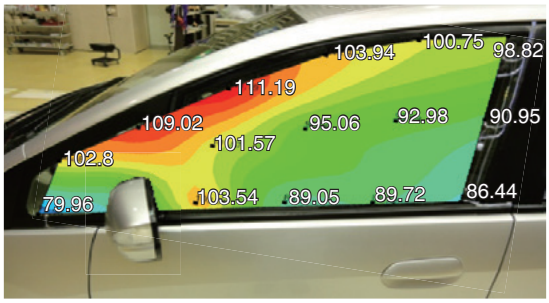
Both numerical analysis and vehicle tests showed that with regard to the transmission of noise through automotive window glass, it is the acoustic excitation force produced by acoustic sound, *Pf*, which is transmitted to become sound in the cabin due to the glass transmission loss.

Table 7 Experimental equipment

Manufacturer	Brüel & Kjær Sound & Vibration Measurement A/S
16-ch surface microphones (Surf-MIC)	4948 and 4949
42-ch half-wheel array microphones (BF)	Type 8608
50-ch spherical array microphones (SBF)	Type 8606



(a) Image of set-up

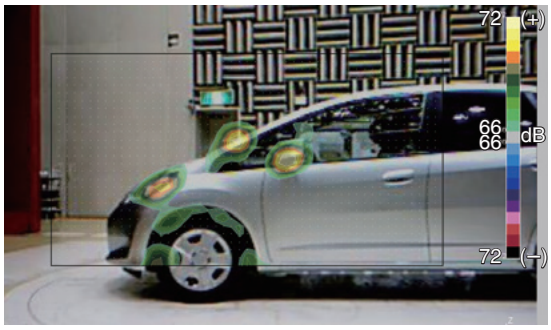


(b) Contour plot of sound pressure distribution (dB)

Fig. 16 Surface microphones



(a) Image of set-up

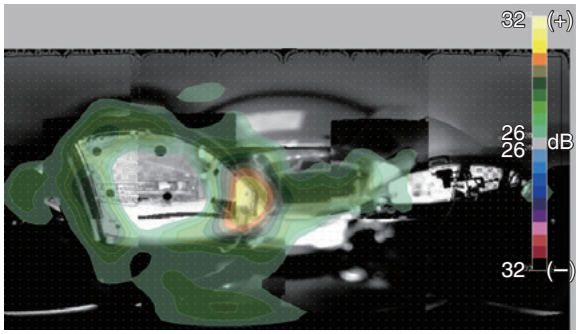


(b) 1/3-octave sound intensity map

Fig. 17 Beamforming



(a) Image of set-up



(b) Noise distribution within vehicle cabin

Fig. 18 Spherical beamforming

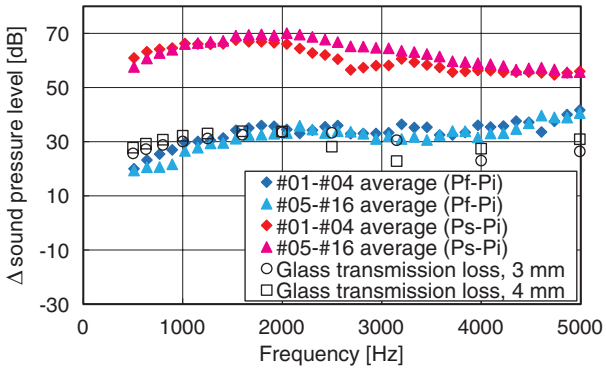


Fig. 19 Differences in sound spectra

5. Conclusion

Seeking to identify the target for control to reduce vehicle interior noise, the research discussed in this paper determined the contribution ratio of convectional pressure and acoustic sound to high-frequency flow-induced noise (1 kHz-5 kHz) in the interior of a box modeling a vehicle interior, based on a model of cabin sound transmission from the pillar modeling the flow around the A-pillar. This study showed that the contribution ratio of acoustic sound to the OA value in the high-frequency range at the microphone in the box was approximately 93%, indicating that in the high-frequency range, acoustic sound is dominant in comparison to convectional pressure.

A comparison of surface pressure fluctuations on the front side glass of an actual vehicle, the sound pressure distribution on the external surface of the front side glass, as estimated from far-field sound, and the sound pressure distribution on the internal surface of the front side glass, as estimated from the vehicle interior sound level, showed that the difference between the sound pressure on the external and internal surfaces is almost exactly equal to the glass transmission loss.

This result indicated that efforts to reduce acoustic sound generated by fluctuations in aerodynamic flow would be an effective means of reducing vehicle interior noise.

References

(1) Sumitani, K., Maeda, K., Ichinose, K.: Jidousya to Ryutairikigaku: Shyataimawarinagare to Kuurikitokusei, Nagare, Vol. 23, p. 445-454 (2004) (in Japanese)
(2) Iida, A.: Kuriki ni Kiinsuru Syanaisouon no Yosoku, Jidosyagijyutukai Sinpojiumu Tekisuto, Vol. 20124281, No. 18-11, p. 1-6 (2012) (in Japanese)
(3) Powell, A.: Theory of vortex sound, Journal of the Acoustical society of America, 36, p. 177-195 (1964)
(4) Kamatsuchi, T.: Linearized Euler Equation Niyoru Yokugatamawari no Nagare to Oto no Renseikaiseki, Nagare, Vol. 23, p. 285-294 (2004) (in Japanese)
(5) Kato, C., Takano, Y., Iida, A., Fujita, H., Ikegawa, M.: LES niyoru Ryutaion no Yosoku (Dai-ippou, Nijigen-enchu Karano Housyaon), TRANSACTIONS OF THE JAPAN SOCIETY OF MECHANICAL ENGINEERS Series B, Vol. 60, No.569, p. 126-132 (1994) (in Japanese)
(6) Lighthill, M. J.: On sound generated aerodynamically. I. general theory, Proceedings of the Royal society of London, Series A, vol. 211, p. 564-587 (1952)
(7) Caro, S., Ploumhans, P., Gallez, X., Morgenthaler, V., Mathey, F., Ciapa, G.: Identification of the Appropriate Parameters for Accurate CAA, 11th AIAA/CEAS Aeroacoustics Conference, vol. 4, p. 2407-2423 (2005)
(8) Mochiduki, O., Maruta, Y.: Nagare no Oto ha Dokokarakurunoka, Ryutaionkougakunyumon-Yutakana Otokankyo wo Motomete-, Asakura Publishing Co., Ltd., p. 74-97 (1996) (in Japanese)
(9) Anbo, K., Yoshino, T., Morishita, K., Teramura, M.: Transmission mechanism of flow-induced noise from the forward facing step through the glass plate, Actran Users Conference (2012)
(10) Ambo, K., Yoshino, T., Teramura, M.: Zenposteppu kara Hasseisuru Kazakirion no garasutoukamekanizumu, Nihon kikaigakkai ronbunshu Bhen, Vol. 79, No. 803 (2013) (in Japanese)

(11) Nouzawa, T., Li, Y., Kasaki N., Nakamura T.: Jidosyaniokeru kurikisouon no ongenkouzounitsuite, TRANSACTIONS OF THE JAPAN SOCIETY OF MECHANICAL ENGINEERS Series B, Vol. 75, No. 758, p. 101-107 (2009) (in Japanese)

■ Author ■


Kei AMBO


Kazuya MORISHITA


Takashi YOSHINO


Minoru TERAMURA

Honda R&D Co., Ltd.
Honda R&D Technical Paper Committee

Motorcycle R&D Center
Automobile R&D Center
Power Products R&D Center
Aircraft Engine R&D Center
Fundamental Technology Research Center
Honda R&D Americas

Editorial Afterword

In the two years since becoming a member of the Editorial Committee of the Honda R&D Technical Review, I have reviewed a large number of technical papers. Over the course of many years I have also attended presentations of papers at various events such as academic and technical meetings as well as reviewed such papers. During all these years, I have constantly been concerned that today's engineers are not as skilled in the crafting of technical papers as were earlier generations.

In my own case, I was a diligent reader from childhood. I encountered technical papers at university, and upon entering the world of work, I absorbed the essence of new technologies from these texts. To me, for an engineer, the writing of a technical paper or a test report or design standard corresponding to one was, in itself, the production of an outcome. Feeling this way and reviewing technical papers written by young engineers, or reading their finished manuscripts, I would consistently come upon cases of poor balance between placement of the main thesis of the discussion and the overall structure, as well as those in which the writing lacked elegance. The rise of the Internet and the "aliteracy" that has been much discussed in the media can be viewed as responsible for this. However, while the Japanese spend the least amount of time per day reading print media of any advanced nation, it is also reported that the number of books published continues to grow, and the reading rate among children is also on the rise following a slight drop in the 1990s. Email, blogs and the like have made writing an everyday process, and so it might also be said that young people have a more intimate acquaintanceship with the act of writing than people of my own age. Unexpectedly, when one looks one does not find factors promoting, or evidence for, increasing aliteracy among the young.

The postwar rote-learning style of education that stresses memorizing over thinking can be pointed to as standing behind the issues I have touched on above, but all currently working generations were subject to this type of education, and it would therefore be difficult to say that this alone is the culprit. Mutterings about the state of the young have been common throughout the world since the days of the Egyptian pharaohs. My grumblings here should be seen as no more than that, and based on groundless concerns.

Akihito Kasai

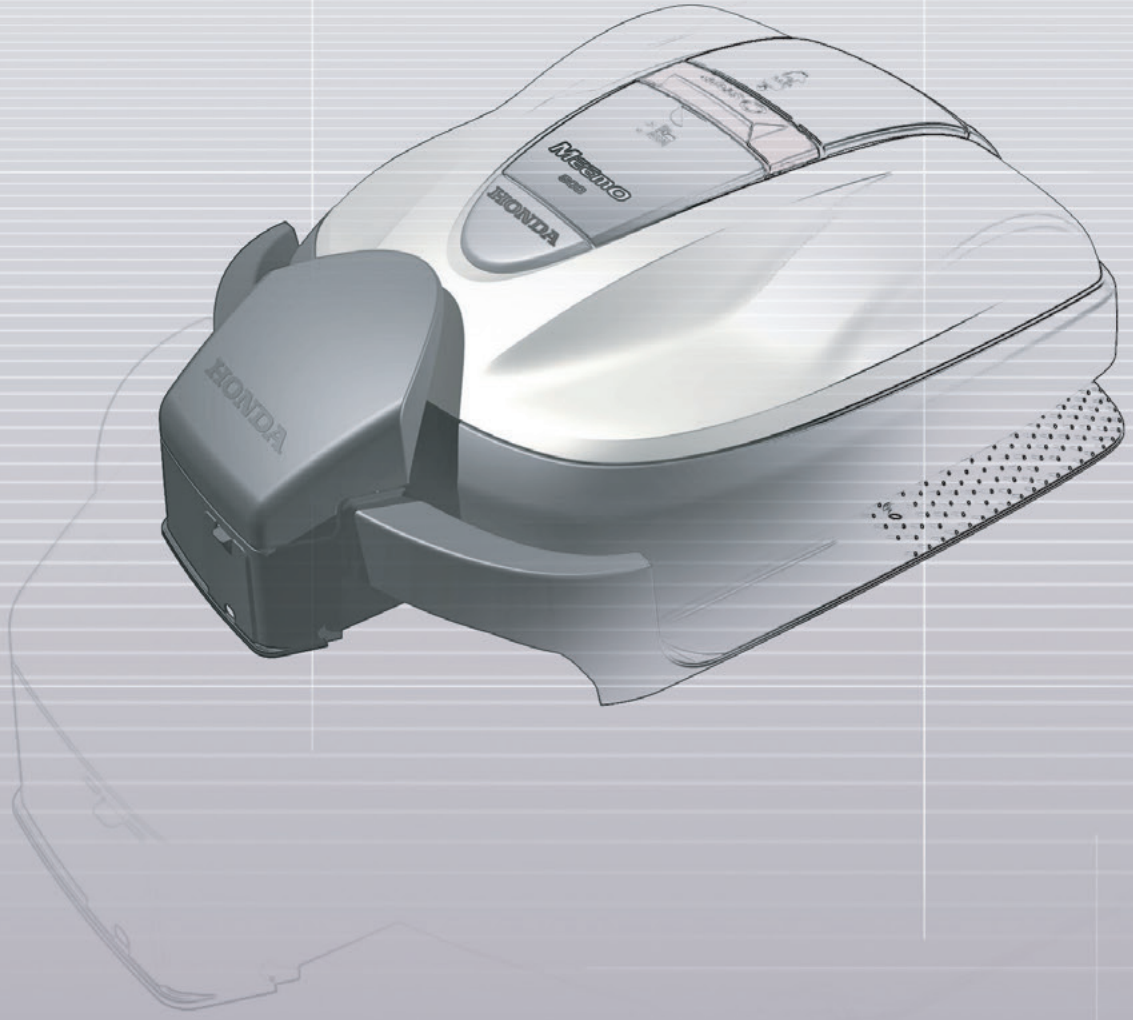
©2013 Honda Motor Co., Ltd. (All rights reserved)

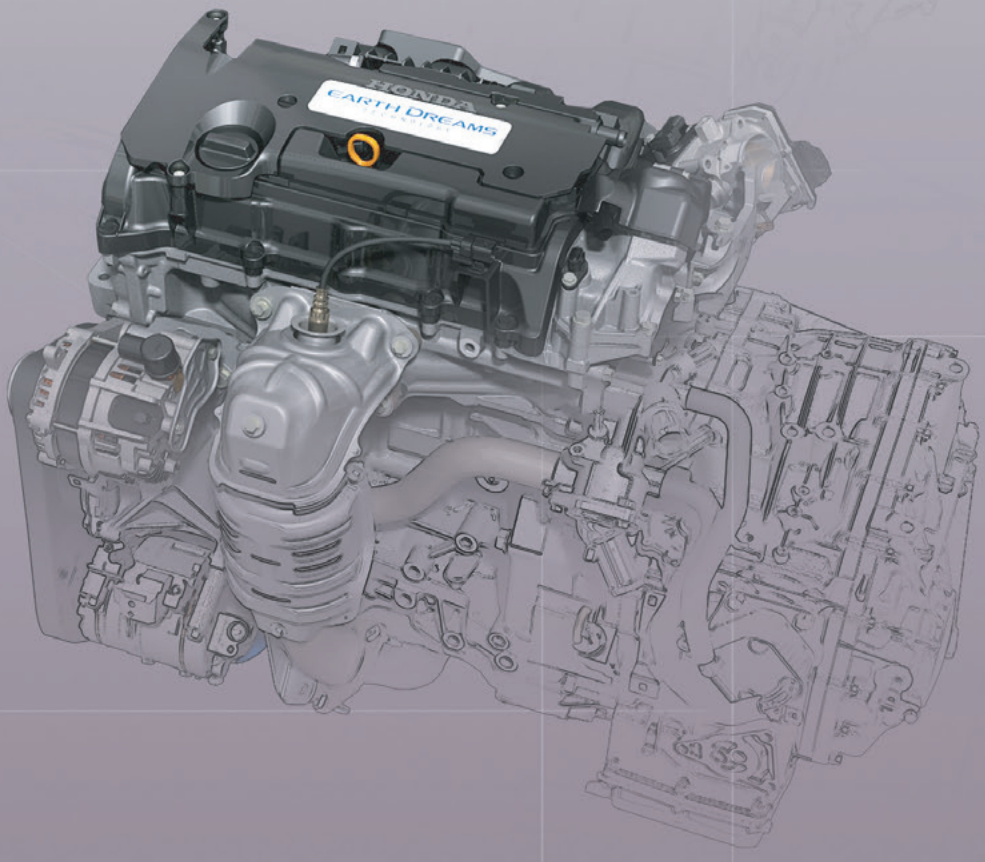
ISSN 1881-6223

Published by:
Honda Motor Co., Ltd.
2-1-1, Minami-Aoyama, Minato-ku,
Tokyo 107-8556, Japan

Edited by:
Honda R&D Co., Ltd.
Honda R&D Technical Paper Committee

Printed:
Sep. 1, 2013


HONDA
HONDA


HONDA
EARTH DREAMS